State-dependent potentials and clock ground-state cooling in an ytterbium quantum simulator

Tim Oliver Höhn

SIGILL: UNIVERSITAT: LUDOVIC: MAXIM:

München 2024

State-dependent potentials and clock ground-state cooling in an ytterbium quantum simulator

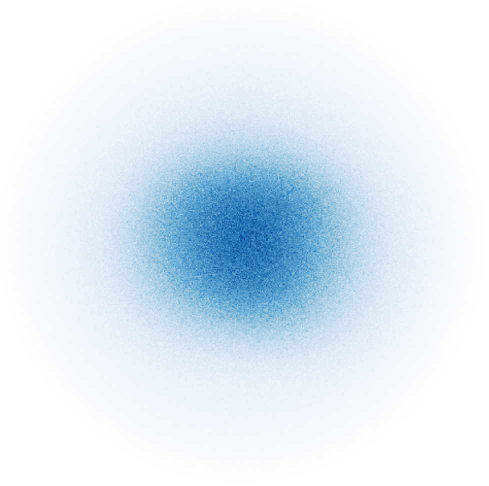

Dissertation an der Fakultät für Physik
Ludwig-Maximilians-Universität München

vorgelegt von

Tim Oliver Höhn

aus München

München, den 24. Juli 2024

Tag der mündlichen Prüfung: 4. September 2024

Erstgutachterin: Prof. Monika Aidelsburger

Zweitgutachter: Prof. Francesco Scazza

Weitere Prüfungskommissionsmitglieder: Prof. Thomas Birner, Prof. Tim Liedl

Zusammenfassung

In dieser Arbeit wird der Aufbau eines neuartigen experimentellen Systems beschrieben, das aus einer Kombination von dreidimensionalen optischen Gittern und optischen Pinzetten besteht und mithilfe dessen Quantensimulationsexperimente mit ultrakalten Ytterbium-Atomen in zustandsabhängigen Potentialen ermöglicht werden. Dabei stellt diese Arbeit die erste Beschreibung einer erfolgreichen Realisierung von Seitenbandkühlprozessen mithilfe des ultraschmalen Uhrenübergangs in bosonischen, spinlosen Elementen dar, die uns ermöglichen, gefangene Atome in einem ein- oder zweidimensionalen optischen Gitter bis auf den axialen Grundzustand herabzukühlen, und die auch das Erreichen des absolut niedrigsten Quantenzustands in allen drei Raumdimensionen möglich machen sollte. Zudem werden seitenbandunaufgelöste Molasse-Kühltechniken geschildert, die es uns erlauben, Fluoreszenzabbildungen von Atomen in optischen Pinzetten sowie Gittern bei jeweils unterschiedlichen Wellenlängen mit langen Belichtungszeiten vorzunehmen.

Hierbei ist das Einhalten von quasi-magischen Bedingungen entscheidend, um vergleichbare Fallentiefen für Atome im Grund- und angeregten Zustand unabhängig von der Position in der Falle oder der Intensität des Fallenlichts zu erreichen. Dies wird bei dem Molasse-Kühlen durch eine Verkippung der Magnetfeldrichtung, die die Quantisierungsachse festlegt, zu einem erstmals bestimmten magischen Winkel verwirklicht. Gleichsam erlaubt die Verwendung eines Gitters bei einer magischen Wellenlänge die hochpräzise Anregung von Atomen in den metastabilen Uhrenzustand, der als orbitaler Freiheitsgrad ein Schlüssel zur Simulation von komplexen Vielteilchensystemen darstellt. Durch spektroskopische Messungen bestimmen wir zwei weitere, zuvor unbestimmte magische Wellenlängen, die sich besonders für optische Pinzetten in Neutralatom-Quantencomputern eignen.

Um zudem das Spektrum der realisierbaren Quantensimulationsexperimente zu erweitern, messen wir auch potentialfreie Wellenlängen, bei denen die atomare Polarisierbarkeit und somit die Atom-Licht-Wechselwirkung verschwindet, sowohl für den Grund- als auch den Uhrenzustand mithilfe von periodischer Modulation, die zu parametrischem Heizen und kontrolliertem Teilchenverlust führt. Ergänzend illustrieren wir eine neuartige Messmethode, die auf thermometrischen Messungen des Seitenbandspektrums beruht. Dies stellt die erste Messung solcher Wellenlängen für Ytterbium und insbesondere die erste Beschreibung einer potentialfreien Wellenlänge für einen optisch angeregten Zustand überhaupt dar. Unterstützt wird dieses Resultat durch ein empirisches Modell, das die Polarisierbarkeiten der drei energetisch niedrigsten Zustände über den sichtbaren und infraroten Spektralbereich beschreibt und die gemessenen magischen und potentialfreien Wellenlängen miteinbezieht, um die Präzision des Modells zu verbessern.

Zudem führen wir in dieser Arbeit aus, wie optische Fallen bei ebendiesen Wellenlängen die Simulation von Gittereichtheorien in zwei räumlichen Dimensionen sowie die gezielte Neuanordnung von Atomen in Gittern mit geringen Abständen zwischen den Gitterplätzen ermöglichen können. Während Ersteres einen großen Schritt hin zu einem besseren Verständnis von komplizierten Feldtheorien bedeuten würde, erlaubt Letzteres die Initialisierung von beliebigen Anfangszuständen in optischen Gittern und eröffnet somit neue Möglichkeiten bei der Untersuchung von Vielteilchensystemen.

Abstract

This thesis reports on the construction of a novel experimental system based on a combination of a three-dimensional optical lattice and a tweezer array, which aims at the implementation of quantum simulation experiments with ultracold ytterbium atoms in state-dependent potentials. With large ground-state fractions as an essential prerequisite for most quantum simulation protocols, we describe the first realization of sideband cooling on the ultranarrow clock transition of spinless bosonic ytterbium atoms trapped in one- and two-dimensional optical lattices. This allows us to reach the lowest vibrational band along the strongly confined directions and is expected to provide us with a method to cool the atoms to the absolute motional ground state. In addition, we characterize a complementary molasses cooling method, enabling us to perform fluorescence imaging of atoms in optical tweezers and lattices at different trap wavelengths for long exposure times.

Here, it is instrumental to attain quasi-magic conditions to cancel differential light shifts, rendering the cooling efficient for all atoms irrespective of their position in the trap and its depth. To this end, we find a new magic angle for this cooling transition by tilting the magnetic field vector with respect to the lattice polarization. Moreover, we make use of a magic-wavelength lattice to excite atoms to the metastable clock state with high precision, which can thus be used as an orbital degree of freedom to simulate complex many-body systems. Conducting spectroscopic measurements of the wavelength-dependent ac Stark shift, we further determine two previously unknown magic wavelengths, which will likely find manifold applications in neutral-atom quantum computing systems.

To expand the toolbox for quantum simulation experiments, we also measure the tune-out wavelengths for the ground and clock state, where the respective ac polarizability and thus the atom-light coupling vanishes, by means of a modulation scheme to induce parametric heating and subsequent atom loss from the trap. Furthermore, we present a novel approach to detect tune-out wavelengths via sideband thermometry measurements. This represents the first report of such wavelengths for ytterbium and, in particular, the first time a tune-out wavelength for an excited state of an optical transition has been determined. We frame these results in an empirical model that describes the dynamical polarizabilities of the three lowest-lying states over the visible and infrared optical spectrum by taking the measured distinctive wavelengths into account, which leads to an enhanced predictive power of this model.

Additionally, we explicate on the facility of leveraging state-dependent potentials for the simulation of lattice gauge theories in one and two spatial dimensions as well as strategies for the dense rearrangement of atoms in lattices or tweezer arrays with minimal spacings. While the former would enable the unprecedented study of complicated field theories, the latter could pave the way for quantum simulation experiments with arbitrary initial states in optical lattices, opening up the possibility to study new phenomena in previously inaccessible many-body systems.

Contents

Introduction **1**

1 An ytterbium quantum simulator **6**
- 1.1 The alkaline-earth-like atom ytterbium . . . 6
  - 1.1.1 Level structure . . . 6
  - 1.1.2 The clock transition . . . 8
  - 1.1.3 Interactions . . . 11
- 1.2 AC polarizability . . . 14
  - 1.2.1 Far-detuned atom-light coupling . . . 14
  - 1.2.2 An empirical model for ytterbium light shifts . . . 19
- 1.3 Trapping atoms . . . 27
  - 1.3.1 Optical lattices . . . 28
  - 1.3.2 Optical tweezers . . . 31
- 1.4 Quantum simulation of lattice gauge theories . . . 32

2 Experimental design **38**
- 2.1 Vacuum chamber . . . 38
  - 2.1.1 Atom source . . . 39
  - 2.1.2 Science chamber . . . 42
  - 2.1.3 Glass cell . . . 42
- 2.2 Magnetic coils . . . 44
  - 2.2.1 Main coils . . . 45
  - 2.2.2 Transverse coils . . . 46
  - 2.2.3 Compensation coils . . . 47
  - 2.2.4 Shim coils . . . 48
- 2.3 Optical setup . . . 48
  - 2.3.1 Atom source setup . . . 49
  - 2.3.2 Intermediate setup . . . 50
  - 2.3.3 Hybrid tweezer-lattice setup . . . 53
- 2.4 Laser setups . . . 61
  - 2.4.1 Blue laser setup . . . 62
  - 2.4.2 Green laser setups . . . 63
  - 2.4.3 Clock laser setup . . . 65

2.4.4 Repump setup 65
2.4.5 Lattice laser setups 67
2.4.6 Loading tweezer setup 68
2.4.7 Tune-out laser setups 68
2.4.8 Frequency locks 70
2.5 MOT loading 74
2.5.1 Slowing beams 75
2.5.2 3D MOT 78
2.6 Lattice loading 80
2.6.1 1D lattice 80
2.6.2 2D lattice 85
2.6.3 Vertical lattice 86
2.6.4 3D lattice 91
2.7 Microscope objective 93
2.7.1 Objective mount 94
2.7.2 The bottom MOT beam 96
2.7.3 Objective performance 98
2.7.4 Tweezer loading 100
2.7.5 Fluorescence imaging 105

3 Ground-state cooling in a magic lattice **107**
3.1 Molasses cooling 108
3.1.1 Magic angle 109
3.1.2 Near-magic narrow-line cooling in a clock-magic 3D lattice 112
3.2 Resolved sideband cooling on the clock transition 114
3.2.1 Rethermalized 1D sideband cooling 116
3.2.2 2D sideband cooling 120
3.2.3 3D sideband cooling 125
3.3 Raman sideband cooling 127

4 State-dependent potentials **130**
4.1 Measuring magic wavelengths 130
4.2 Measuring the ground-state tune-out wavelength 135
4.3 Measuring the clock-state tune-out wavelength 141
4.4 Quantum simulation and computation with tune-out potentials 150

Conclusions and outlook **153**

Appendices **156**
A Transition properties for the empirical polarizability model 156
B Finite-element simulation and optical design of the main breadboard 157

References **159**

Introduction

Quantum mechanical descriptions of microscopic properties and dynamics have fundamentally shaped our understanding of atomic, optical, or solid state systems. The contrast to classically intuitive behavior does not only challenge our perception of quantum phenomena, but also complicates theoretical calculations of complex systems such as strongly correlated or disordered many-body states on classical computers due to the exponentially growing Hilbert space size [1–3]. This motivates the utilization of quantum particles to study such systems, leading to the concept of analog quantum simulators [4]. Immense progress has been achieved towards realizing such machines within the last decades, with more and more experiments reaching the boundaries of classically accessible simulations [5–8], entailing the necessity of benchmarking the simulated results [9, 10]. Similarly, the development of large-scale, programmable quantum computers to solve classically hard problems [11, 12] has advanced remarkably despite limitations on the state preparation, read-out, and gate fidelities [13], and first hints of a quantum advantage for specific problems were given [14, 15].

In both regards, ultracold atoms have emerged as a powerful platform, where early seminal discoveries, such as the observation of a quantum phase transition from a superfluid to a Mott insulator [16] or the condensation of pairs of fermionic atoms [17–19], were followed by the realization of non-trivial topological phases in artificial magnetic fields [20, 21] and many-body localized states [22, 23]. In the last few years, these developments have progressed to reports of spin-charge deconfinement in fermionic atom chains [24], fractional quantum Hall states [25], toric-code-type topological spin liquids in Kagome arrays [26], and continuous symmetry breaking in the dipolar XY model in square Rydberg tweezer arrays [27]. Simultaneously, neutral-atom systems have emerged as a leading contender in the race for the highest fidelities of single- and two-qubit gates [28, 29] and demonstrated the scalability to several thousands of physical qubits [30, 31].

A main reason for the success of ultracold atom experiments is the enormous amount of controllability and the vast number of tuning knobs quantum gas systems provide [5, 7]. Here, the degrees of freedom strongly depend on the chosen trap platform. Optical lattices do not only offer regular, defect-free potential landscapes, but also allow for adjusting the kinetic and potential energy of trapped particles by varying the lattice power or magnetic fields [6]. Here, the underlying optical potential can be shaped to provide the desired dimensionality or lattice structure, also enabling triagonal, hexagonal, or even octagonal order and, thus, the study of spin-frustrated systems, topological edge modes, or quasi-crystalline order [32–34]. The advent of quantum gas microscopes has further enabled the precise determination of atomic positions and spin states in optical lattices [35–39]. In addition, the interaction strength and range can be adjusted via Feshbach resonances [40] or Rydberg interactions [41, 42]. Depending on the chosen element and transitions, one can further cover a broad range of sensitivity to external or internal fields, which is of major relevance for highly accurate atomic clocks [43] or the search for new particles and changes in fundamental constants [44–46].

To be able to conduct quantum simulation experiments of the models of interest, it is often necessary to achieve an initial state with very low entropy and near-unity ground-state fractions [6]. This is particularly true for Hubbard(-like) models, where especially the fermionic model has gained considerable attention due to its capability to describe relevant aspects in the behavior of strongly correlated electrons in a crystal [47]. The standard approach to reach the absolute ground state and high filling fractions in an optical lattice for the last 20 years has been based on evaporative cooling in a dipole trap to reach a Bose-Einstein condensate or a quantum degenerate gas at sufficiently low temperature, which is then adiabatically transferred into the optical lattice to perform the experiment of interest [5]. While this cooling method has brought record-breaking temperatures as low as 450(80) pK for bosons [48], reaching very low temperatures below one tenth of the Fermi temperature is fundamentally more complicated in fermionic systems [49], limiting the exploration of the Fermi-Hubbard phase diagram [47, 50–53] and its implications on our understanding of, e.g., superconductivity [54]. Furthermore, despite progress towards accelerated evaporation and fast Bose-Einstein condensation of Er atoms in less than a second [55], the vast majority of quantum simulators suffers from low cycle times of 15 s or more, owing to the slow thermalization rates [56].

Arrays of tightly focused tweezer beams, on the other hand, provide the possibility to form arbitrary trap geometries with variable depths of the individual traps and to dynamically rearrange atoms, such that the initially large entropy of laser-cooled atoms can be removed and similarly homogeneous filling fractions as in a Mott insulator are possible [57–59]. This has also opened up the opportunity for a much faster preparation of atoms in the ground state, achieved by sideband [60–63], polarization gradient [26, 30], or Sisyphus cooling [64, 65]. The utilization of excitations to Rydberg states further enables sufficiently long-ranged dipole-dipole interactions to bridge the larger gaps between atoms in tweezers compared to optical lattices [57], which has been used to demonstrate highly entangled states [10, 66]. This in combination with large repetition rates and a reasonable potential for scalability [30, 31] renders tweezer arrays highly suitable for quantum processing applications. There has also been significant development towards tweezer-based atomic clocks recently, with reports of sub-wavelength movements [67] and spin squeezing [68, 69] to enhance the metrological precision.

Remarkable novel avenues have emerged with the demonstration of multi-species arrays in optical tweezers, where Rb and Cs atoms [70] as well as ^{171}Yb–^{174}Yb mixtures [71] have been simultaneously loaded and arranged to enable cross-talk-free control and read-out of data and ancilla qubits, which are essential for quantum error correction and otherwise require imperfect shelving or transport operations [59, 72]. A second promising hybrid approach unites optical lattices and tweezers to implant atoms on desired lattice sites, where they can controllably tunnel to adjacent sites. This can then be used to perform spatial search and boson sampling algorithms [73, 74]. A second application of this tweezer-lattice combination is the continuous loading and recycling of atoms to form large-scale arrays of atoms [75, 76].

A vital precondition for many of the aforementioned experiments is the knowledge of the dynamical polarizability of the relevant states at the trapping wavelengths. While large absolute values are beneficial as they enable deep, power-efficient traps, in particular the differential polarizability can be of great significance as it determines the effect of trap depth inhomogeneities on the observed transition linewidth [77]. Therefore, the operation at magic wavelengths, where this effect is fully canceled, has been of major importance for optical lattice clocks [43, 78], but has also been found useful for cooling and high-fidelity addressing purposes [62, 72, 79–83]. In contrast, for certain applications like improved cooling schemes [84, 85] or state preparation protocols [86–88], a non-zero light shift is required. First realizations of such state-dependent potentials have used spin-selective optical lattices to coherently delocalize atomic wavefunctions [89] and to arrange two atoms in adjacent double-well sites to study superexchange dynamics [90]. They have later been used to initialize a system with a single spin impurity [91, 92] and to observe anyonic statistics on a plaquette [93]. For elements with an orbital degree of freedom like ytterbium, these internal states can be interpreted as independent species, such that state-dependent lattices act on their relative mobilities and can cause an effective mass imbalance [94, 95]. Furthermore, state-dependent potentials lie at the heart of several quantum computing protocols [96–98], where in particular the concept of local, targeted detuning of individual atoms has gained considerable attention [91, 99, 100].

This thesis

The main subject of this thesis is the development of a hybrid tweezer-lattice quantum simulator with ytterbium atoms, employing state-dependent potentials and optical sub-Doppler cooling on the clock transition. The described experimental apparatus hereby bridges the gap between traditional lattice-based quantum simulators and dynamical tweezer systems in multiple ways, facilitating sideband cooling sequences to reach the motional ground state of an optical lattice significantly faster than with the traditional evaporation method and paving the way for the deterministic preparation of arbitrary initial states. To this end, we demonstrate enhanced loading and quasi-magic fluorescence imaging of bosonic ytterbium atoms in a tweezer array and extend the imaging facility to a deep three-dimensional clock-magic lattice, which we tune to state-insensitivity by means of a magic magnetic field angle with respect to the lattice polarization. Further, this thesis reports on new magic wavelengths for the clock transitions, which are detected via high-precision spectroscopic measurements, and wavelengths of maximal state selectivity (“tune-out”) for both the ground and the clock state, determined by heating-induced atom loss and thermometry measurements. We embed these results in a theoretical model for the dynamical polarizability of the ground and two lowest excited states and find very good agreement with experimentally quantified values. In light of the currently ongoing developments in our experiment towards 3D motional ground-state cooling and the implementation of tune-out tweezer arrays, a protocol for the controlled rearrangement of atoms in closely filled optical lattices as well as a pathway for the experimental simulation of two-dimensional lattice gauge theories is given.

Outline

This thesis is divided into five chapters, which are structured as follows:

Chapter 1 introduces the electronic structure and interaction properties of ytterbium atoms, with a particular focus on the dimorphism that is enabled by the transition to the metastable clock state. We then turn to a discussion of light-atom interactions and derive empirical models to provide accurate polarizability predictions of the three energetically lowest states. Furthermore, the main concepts of atomic traps are presented. We conclude the Chapter with an outline on the eventual purpose of the experiment as a quantum simulator for lattice gauge theories, and specifically consider the realization of the necessary state-dependent potential landscape.

In Chapter 2 the experimental apparatus is described, starting with the vacuum chamber, the magnetic coils, and the optical setups around the main chamber as well as the lasers. We then discuss and characterize the various stages to be able to trap atoms in a magneto-optical trap and to transfer them into optical lattices in various dimensions. As this allows us to address the clock transition, an overview of the manipulation methods of the clock state pair is given. This is followed by a description of the objective, which enables the generation of tweezer arrays and fluorescence imaging facilities, with a particular focus on the newly developed enhanced loading and molasses cooling capacity in our tweezer array.

Having established the experimental platform, Chapter 3 covers novel methods of molasses cooling during fluorescence imaging and reaching sub-Doppler-cooled temperatures in a magic lattice. While the former utilizes a newly discovered magic angle for the wider intercombination line, the latter is based on the ultranarrow clock transition. We demonstrate how cooling along a single direction in a one-dimensional lattice can reduce the temperature to a few μK, and introduce a swept sideband cooling technique to reach the motional ground state in a 2D lattice. Its extension to 3D as well as an outlook on an implementation of Raman sideband cooling in the clock-magic lattice is further outlined.

In Chapter 4 the first measurements of four distinctive state-dependent wavelengths in ytterbium are presented. We begin with the spectroscopic characterization of two new magic wavelengths for the optical qubit, followed by a description of tune-out wavelength measurements for the ground as well as the clock state based on a parametric heating scheme. Moreover, the implications of such maximally state-dependent wavelengths on relevant aspects of quantum computation and simulation are touched upon, with a particular focus on a dense atom resorting scheme.

The final Chapter completes this thesis with a brief summary of the central findings and provides a prospect of avenues to future work on this experiment.

Publications

The central results presented in this thesis have been published or are in preparation for publication in the following references:

- T. O. Höhn, E. Staub, G. Brochier, N. Darkwah Oppong, and M. Aidelsburger, *State-dependent potentials for the $^1S_0$ and $^3P_0$ clock states of neutral ytterbium atoms*, Phys. Rev. A **108**, 053325 (2023)

- T. O. Höhn, R. A. Villela, E. Zu, L. Bezzo, R. M. Kroeze, and M. Aidelsburger, *Determining the $^3P_0$ excited-state tune-out wavelength of ^{174}Yb in a triple-magic lattice*, 2024, arXiv:2412.14163

- R. M. Kroeze, T. O. Höhn, R. A. Villela, E. Zu, and M. Aidelsburger, *Clock sideband cooling of ytterbium to the 3D motional ground state*, in preparation

CHAPTER 1

An ytterbium quantum simulator

The selection of a specific element for a neutral atom quantum simulator is one of the most central decisions, as it determines the physical properties and, thus, the toolbox that can be used in experiments. In this Chapter, we delineate the relevant atomic properties of ytterbium and why it has been chosen for this experiment. We focus in particular on the far off-resonant atom-light coupling, where we develop an empirical model to accurately describe the light shift of the three most relevant states in Yb for potential trap wavelengths, before we move on to discussing some theoretical concepts on atom traps, i.e., magneto-optical traps (MOTs), optical lattices, and tweezers, that will be important in the context of this thesis. Furthermore, an outline on the quantum simulation protocol for lattice gauge theories (LGTs), which is the eventual goal of this experiment, and its implications on the specific experimental design is given.

1.1 The alkaline-earth-like atom ytterbium

The lanthanide rare-earth element Yb features a nuclear charge of $Z = 70$ and seven stable isotopes, among which five are bosonic with nucleon numbers of $A = 168, 170, 172, 174,$ and 176 with a nuclear spin of $I = 0$, joined by the two fermionic isotopes ^{171}Yb and ^{173}Yb [104]. While the latter two are anticipated to be mostly used in the future of the experiment, due to their non-vanishing nuclear spins of $I = 1/2$ and $I = 5/2$, respectively, the results in this thesis were mostly obtained with the most abundant ($\simeq$32% natural abundance) isotope, ^{174}Yb. The 70 electrons are arranged in the configuration $[\mathrm{Xe}]4f^{14}6s^2$ [105]. With two valence electrons in an outer s-shell and a set of complete inner shells, the electronic structure of Yb resembles the one of alkaline-earth metals like Ca or Sr, which is why it is referred to as an alkaline-earth-like (AEL) atom.

1.1.1 Level structure

The spins of the two valence electrons can align to form a spin singlet ($S = 0$) or triplet ($S = 1$), which consequentially determines the symmetry of the spatial wavefunction and manifests a He-like separation of energy levels into two manifolds. According to the selection rules, optical dipole transitions between the singlet and triplet manifolds are forbidden, owing to the necessary spin flip. This gives rise to metastable higher lying states, which can be used for extremely precise atomic clocks [78] and two-species quantum simulation [106, 107]. While the use of the spin-orbit (LS) coupling term notation $^{2S+1}\mathrm{L}_J$, indicating that the orbital angular momentum L, electronic spin S, and total electronic angular momentum J are good quantum numbers, is a reasonably good approximation, the large electron number entails a significant influence of j-j coupling [108, 109]. This further implicates that the dipole selection rules yield decent lowest-order estimates of the optical transition strengths, but electrostatic interactions as well as spin-orbit, Zeeman, and hyperfine coupling effects lead to finite admixtures of dipole-allowed states to enable weakly allowed intercombination lines, thus violating the selection rules. Since a detailed summary of these effects applied to the relevant energy levels in Yb can be found in [110], we will restrict this discussion to a mere description on the most important energy levels for this work, displayed in Fig. 1.1.

The $(6s^2)^1\mathrm{S}_0$ ground state is connected to the $(6s6p)^1\mathrm{P}_1$ state via the strong, dipole-allowed transition at 398.9 nm [111]. Owing to its large natural linewidth of $\Gamma_{399} = 2\pi \times 29.13\,\mathrm{MHz}$ [112], the substantial photon scattering rate, and only very weak leakage into the $(6s5d)^3\mathrm{D}_1$ state [113], this transition is perfectly suited for slowing, cooling, and imaging purposes. We also use it for initial absorption spectroscopy to test the atomic oven (Chapter 2.1.1), where the isotope shifts yield the characteristic multi-peak structure of Fig. 2.2.

The most prominent and practically advantageous case of state mixing is the $(6s6p)^3\mathrm{P}_1$ state in the triplet manifold, which inherits a finite linewidth of $\Gamma_{556} = 2\pi \times 183\,\mathrm{kHz}$ from the $^1\mathrm{P}_1$ state, to which it is spin-orbit-coupled in the intermediate coupling regime [110, 114]. Here, a marked difference to the generally very similar level structure in Sr arises, where this transition exhibits a linewidth of only $2\pi \times 7.4\,\mathrm{kHz}$ [115]. In Yb, the relatively short wavelength of 555.8 nm and its closed nature further contribute to its usefulness as the narrow-linewidth cooling transition in the MOT and in optical tweezers or lattices. In addition, the finite total electronic spin and the concurring Zeeman splitting allow for the precise calibration of magnetic fields for bosonic isotopes, while the emerging hyperfine structure for the fermionic isotopes additionally facilitates Raman sideband cooling and spin-selective imaging techniques (Chapter 3.3) [63], but also spin-state mixture initialization [94] and optical Stern-Gerlach separation measurements [116].

As the 578.4 nm $^1\mathrm{S}_0 \rightarrow {}^3\mathrm{P}_0$ transition does not only violate the spin selection rule $\Delta S = 0$, but also does not observe the necessary total electronic angular momentum change $\Delta J = \pm 1$ for $J = 0$, it is doubly forbidden. Therefore, the atom-light coupling vanishes for the bosonic isotopes. For the fermionic isotopes, the hyperfine interaction between states with different electronic angular momentum J but identical total atomic angular momentum F, caused by the non-zero nuclear spin and finite nuclear moment, leads to a small perturbation of the bare $^3\mathrm{P}_0$ eigenstate and thus to a small admixture of the $^1\mathrm{P}_1$ and $^3\mathrm{P}_1$ states [110, 116]. The engendered linewidths are minuscule with values of $\Gamma_{578} \simeq 2\pi \times 40\,\mathrm{mHz}$ for $^{173}\mathrm{Yb}$ [121] and $2\pi \times 53(6)\,\mathrm{mHz}$ in the case of $^{171}\mathrm{Yb}$ [120]. For the bosonic isotopes, the missing nuclear spin can be emulated by applying a strong external magnetic field [124, 125] and one can induce a finite transition matrix element — a technique that will be described in more detail in the next Section.

The dipole-allowed $^3\mathrm{P}_0 \rightarrow {}^3\mathrm{D}_1$ transition at 1388.7 nm [123] with a linewidth of $\Gamma_{1389} = 2\pi \times 309\,\mathrm{kHz}$ [122] has become a standard tool of Yb-based experiments to quickly repump atoms from the clock state. From the $^3\mathrm{D}_1$ state, the atoms predominantly decay back to the $^3\mathrm{P}_0$

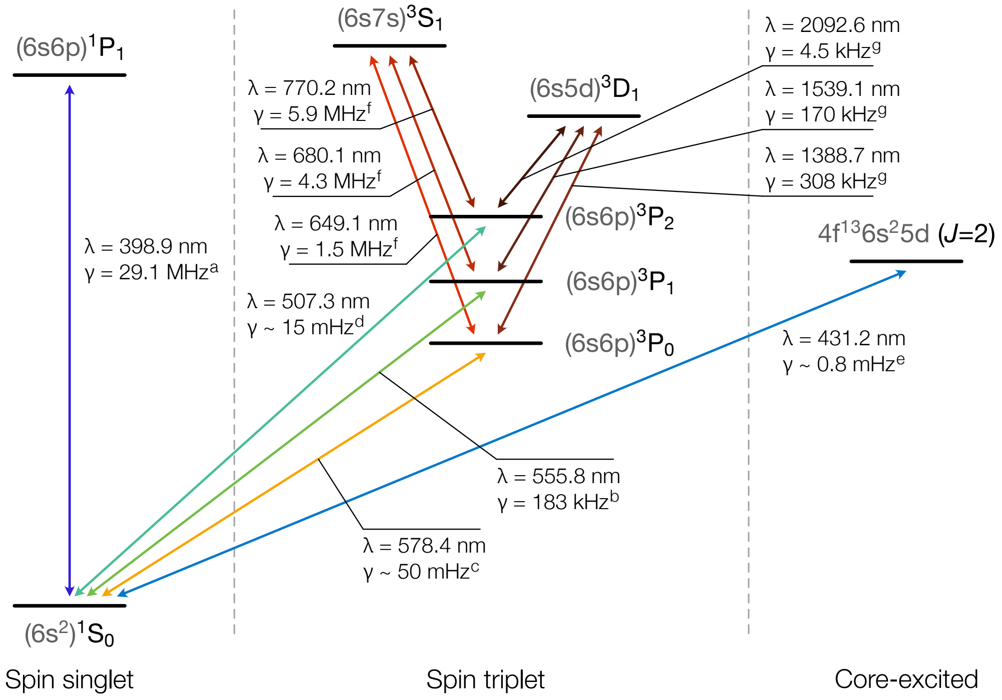

Figure 1.1 | Energy level diagram of ytterbium. Partial term diagram of the relevant low-lying electronic states in *LS* eigenstate notation for the states with a closed *f*-shell and in terms of the total angular momentum for the core-excited state ($J = 2$). Arrows indicate optical transitions that are mentioned in this work, labeled with their transition wavelengths λ and natural linewidths $\gamma = \Gamma/2\pi$. For the latter, we either display its measured or the inferred value from the *LS* coupling method discussed in the next Section. For the ultranarrow clock transitions we state the linewidths for ^{171}Yb. The $(6s^2)^1S_0$ and $(6s6p)^3P_0$ states will also be referred to as $|g\rangle$ and $|e\rangle$ throughout this thesis. Superscripts indicate the reference where the values for this transition were taken from: [a] [112], [b] [117, 118], [c] [119, 120], [d] [121], [e] [45], [f] [113], [g] [122, 123]

state with a branching ratio of 0.64, but 35% of the atoms end up in the $^3P_1$ state, from where they further decay to the ground state. Only a small fraction of 1% of the atoms are lost to the dark $^3P_2$ state in one repumping cycle. By driving this transition multiple times, we can repump more than 95% of the clock state atoms within less than ten cycles, allowing for reliable, independent imaging of the clock-state population and for the dissipative step of a resolved sideband cooling technique on the clock transition (Chapter 3). The maximally achievable repumping efficiency of 97.4% can be further enhanced by simultaneously repumping the atoms stuck in the $^3P_2$ state via the $^3S_1$ transition at 770.2 nm [126].

1.1.2 The clock transition

The existence of doubly forbidden and thus ultranarrow transitions with linewidths on the order of mHz [121] or even μHz [45, 127, 128] is one of the most outstanding properties of AEL atoms. This has made them very promising candidates for optical lattice clocks, which have been brought to fruition since with systematic uncertainties around or even below 10^{-18} in units of the clock frequency [129, 130]. This progress beyond the capabilities of microwave clock transitions has been fueled by the extraordinary Q-factors of $\simeq 10^{17}$, but also the very low sensitivity to external fields due to the vanishing total electronic angular momentum for both the $^1\mathrm{S}_0$ and $^3\mathrm{P}_0$ state. To this end, such transitions are denominated "clock" transitions, and we will interchangeably refer to the $^3\mathrm{P}_0$ state as the clock or e state for the remainder of this work. For quantum simulation purposes, the metastability of the clock state, entailed by its correspondingly large lifetime of $> 10\,\mathrm{s}$ is tremendously valuable, as it allows for an orbital degree of freedom. For the fermionic isotopes, this is further enriched by SU(N) symmetric interactions due to the decoupled electronic angular momentum from the nuclear spin [116].

The atom-light interaction of a stable laser close to the clock resonance, e.g., during spectroscopic measurements, is well described by the simple two-level-atom picture, taking only the ground state, denoted $|\mathrm{g}\rangle$, and the clock state $|e\rangle$ into account. In this case, and having applied the rotating-wave approximation, we can write the Hamiltonian as [77]

$$H_{\mathrm{TLA}} = \hbar \begin{pmatrix} 0 & \Omega_0/2 \\ \Omega_0/2 & -\Delta \end{pmatrix} \tag{1.1}$$

with the laser detuning $\Delta = \omega - \omega_0$ from the atomic resonance ω_0 and the resonant Rabi frequency

$$\Omega_0 = -\frac{\mathbf{d} \cdot \mathbf{E}}{\hbar} = -\langle \mathrm{g}|\, \hat{\varepsilon} \cdot \mathbf{d}\, |e\rangle \, \frac{E}{\hbar}. \tag{1.2}$$

Here, we treat the laser light classically, i.e., as an electric field

$$\mathbf{E}(t) = E_0 \cos(\omega t + \varphi) = \mathbf{E}^{(+)} e^{-i\omega t} + \mathrm{c.c.} \tag{1.3}$$

oscillating at an angular frequency of ω, and with $\mathbf{E}^{(\pm)} = \hat{\varepsilon} E_0 e^{\mp i\varphi}/2$ the positive-frequency electric field amplitude vector and the intensity defined as $I = 2c\epsilon_0 |E^{(+)}|^2 = c\epsilon_0 |E|^2/2$ [110, 131]. An in-depth derivation of the dipole matrix element $\langle \mathrm{g}|\, d\, |e\rangle$ is given in [110] and [77], and will be discussed further in Section 1.2. Using the generalized Rabi frequency $\Omega = \sqrt{\Omega_0^2 + \Delta^2}$ we obtain the eigenenergies

$$E_{\pm} = \frac{\hbar}{2}(-\Delta \pm \Omega) \tag{1.4}$$

to the dressed states

$$|+\rangle = \sin\theta\, |\mathrm{g}\rangle + \cos\theta\, |e\rangle\,, \tag{1.5}$$

$$|-\rangle = \cos\theta\, |\mathrm{g}\rangle - \sin\theta\, |e\rangle \tag{1.6}$$

with $\theta = \arctan(-\Omega/\Delta)/2$. Starting with all atoms in the ground state, irradiation with resonant light will therefore lead to the well-known Rabi oscillations,

$$|\psi(t)\rangle = |+\rangle\, e^{-i\Omega_0 t/2} + |-\rangle\, e^{i\Omega_0 t/2}, \tag{1.7}$$

and a π-pulse with $\Delta t_\pi = \pi/\Omega_0 = 1/2f_0$ will fully transfer the atoms into the excited state.

With the pulse duration fixed to this value while scanning the laser frequency across the resonance the clock state fraction will then follow a sinc^2 shape:

$$P_\mathrm{e}(\Delta) = \frac{\Omega_0^2}{\Omega_0^2 + \Delta^2} \sin^2\left(\frac{\pi}{2} \frac{\sqrt{\Omega_0^2 + \Delta^2}}{\Omega_0} \right). \tag{1.8}$$

Notably, one can thus change the observed linewidth by varying the Rabi frequency, e.g., by adapting the intensity of the laser beam. A different approach to a complete transfer from $|g\rangle$ to $|e\rangle$ is the adiabatic rapid passage (ARP), where we remain in the initial dressed state as we slowly ($\tau \ll 1/\Omega_0$) chirp the laser pulse from $\Delta \ll -\Omega$ across the resonance to $\Delta \gg \Omega$ or vice versa, which entails a population inversion. This protocol is more robust to inhomogeneities, e.g., due to trap light shifts, and can be further enhanced by a Gaussian intensity modulation [110].

In the presence of decoherence, be it the limited coherence time of the laser, temperature or interaction shifts, intensity inhomogeneities, or a short lifetime of the excited state, the ideal Rabi oscillations are damped and decay to a steady-state value of [77]

$$P_\mathrm{e} = \frac{s/2}{1+s}, \tag{1.9}$$

where we make use of the saturation parameter [110]

$$s = \frac{I/I_\mathrm{sat}}{1 + (2\Delta/\Gamma)^2}. \tag{1.10}$$

Here, we have introduced the saturation intensity $I_\mathrm{sat} = \pi h c \gamma / 3\lambda^3$ with $\gamma = \Gamma/2\pi$ the natural linewidth of the transition [77]. For the clock transition, the $|e\rangle$ lifetime exceeds the duration of most experimental sequences, but other sources of incoherence, in particular for a relatively hot atomic cloud, typically lead to dephasing after a few ms. For longer clock-pulse durations the lineshape therefore converges to a Lorentzian, with a maximum excitation fraction of 1/2.

In contrast to the hyperfine-interaction-induced finite linewidth of the clock transition for the fermionic isotopes, the nuclear spin of $I = 0$ for the bosonic isotopes inhibits light-atom coupling without the presence of external fields. A strong magnetic field, however, induces Zeeman coupling to the $^3\mathrm{P}_1$ state, $\hbar\Omega_\mathrm{Z}(B) = \langle {}^3\mathrm{P}_0 | \hat{\mu}\mathbf{B} | {}^3\mathrm{P}_1 \rangle$, with the magnetic dipole operator $\hat{\mu}$, and a B-field-dependent mixing angle $\xi = \Omega_\mathrm{Z}/\Delta({}^3\mathrm{P}_1 - {}^3\mathrm{P}_0)$ of the unperturbed eigenstates in first-order perturbation theory [124],

$$\left| {}^3\mathrm{P}_0{}' \right\rangle = \left| {}^3\mathrm{P}_0 \right\rangle + \xi \left| {}^3\mathrm{P}_1 \right\rangle, \tag{1.11}$$

ignoring the normalization prefactors for clarity. Thereby, quenching the transitions leads to a finite Rabi frequency of [110, 124]

$$\Omega(B) = \xi \Omega_{^3\mathrm{P}_1} = \Omega_{^3\mathrm{P}_1} \Omega_\mathrm{Z}(B)/\Delta({}^3\mathrm{P}_1 - {}^3\mathrm{P}_0) = \alpha B \sqrt{I} \cos(\theta) \tag{1.12}$$

for the angle θ between the magnetic field and the polarization of the clock light. The coefficient α, which includes the atomic parameters, has been measured to be $0.588\,\mathrm{Hz}/(\mathrm{G}\sqrt{\mathrm{mW/cm^2}})$

[125], which allows for reasonable Rabi frequencies of $\Omega_0 \simeq 200\,\mathrm{Hz}$ for an intensity of $10\,\mathrm{W/cm^2}$ and a magnetic field strength of $B = 100\,\mathrm{G}$. Notably, the Zeeman coupling is strong enough that it can also be used for the fermionic isotopes to adjust the Rabi frequency in an m_F-dependent way. As a different approach, a collinear excitation of the clock state in a three-photon process via the $^3\mathrm{P}_1$ and $^3\mathrm{S}_1$ states at moderate magnetic field strengths has been demonstrated for two bosonic isotopes in Sr [132, 133], which otherwise require similarly large magnetic fields to quench the transition [124, 134]. This technique could allow for very high clock Rabi frequencies of several hundreds of kHz also for ^{174}Yb.

While the linear differential Zeeman shift is a relevant effect for the other transitions we commonly use, with a shift of, e.g., $\Delta_\mathrm{Z} = -g_J \mu_\mathrm{B} B m_J = -1.449(7)\,\mathrm{MHz/G} \times B m_J$ for the $^1\mathrm{P}_1$ transition [135], where μ_B is the Bohr magneton, it is trivially zero for the bosonic and very small for the fermionic isotopes, where the latter is again induced by the hyperfine coupling. Nevertheless, it can play a significant role in the interorbital interactions [136, 137] and has been precisely determined for both isotopes [110], with an exemplary value of $\Delta_\mathrm{Z} = -191(7)\,\mathrm{Hz/G} \times B m_F$ for ^{171}Yb. In setups with a high spectroscopic precision, even at moderate magnetic fields also the quadratic shift from Zeeman coupling to the $^3\mathrm{P}_1$ state is significant. It was determined to be $\Delta_\mathrm{Z}^{(2)} = -0.0612(10)\,\mathrm{Hz/G^2}$ for ^{174}Yb [138] and $-0.0606(1)\,\mathrm{Hz/G^2}$ for ^{173}Yb [110][1], and is commonly used to calibrate the magnetic coils.

Contrary to the weak coupling of the clock transition to magnetic fields owing to the vanishing electronic angular momentum of both states, electric fields can strongly influence the transition. In particular, the cancellation or precise determination of differential ac Stark shifts is crucial for high-precision spectroscopy results and quantum simulation protocols that involve this orbital degree of freedom. We will thus discuss the wavelength-dependent light shift of both the $^1\mathrm{S}_0$ and $^3\mathrm{P}_0$ state in detail in Section 1.2. However, even for a perfectly cancelled differential ac Stark shift the clock light itself leads to a noticeable intensity-dependent shift, the so-called probe shift. It originates from the coupling to nearby transitions and is estimated to amount to $\Delta_\mathrm{S} \simeq 15\,\mathrm{Hz/(W/cm^2)}$ [44, 124].

1.1.3 Interactions

While atomic interactions will be particularly relevant for future quantum simulation experiments with the apparatus presented in this work (Chapter 4.4), they are also a crucial aspect in the context of lattice and tweezer loading, lifetimes, and certain cooling techniques. As detailed descriptions of the generally complex interatomic scattering processes can be found elsewhere [40, 116], we will focus on a short description of the properties relevant for this work.

Elastic collisions

Under the approxiation that the main interaction processes are binary elastic collisions with a spherically symmetric and sufficiently short-ranged inter-atomic interaction potential $V(\mathbf{r})$,

---

[1] Notably, one would expect a vanishingly small difference for the different isotopes [114].

and taking the low-energy limit, the scattering amplitude $f(\mathbf{k}, \mathbf{k}') = f(\theta)$ as defined in the scattered wavefunction

$$\psi(\mathbf{r}) \sim e^{i\mathbf{k}\cdot\mathbf{r}} + f(\mathbf{k}, \mathbf{k}')\frac{e^{ikr}}{r} \tag{1.13}$$

reduces to[2] [116, 139]

$$f = -\frac{1}{a^{-1} + ik}. \tag{1.14}$$

Here, $\mathbf{r}$ denotes the relative position and $\mathbf{k}$ and $\mathbf{k}'$ the wave vectors of the incoming and outgoing waves with a relative angle of θ. Typically, these approximations are reasonably good for the dilute and cold atomic clouds that are prepared in quantum gas experiments. Remarkably, the low-energy scattering behavior can thus be understood solely by knowledge of the s-wave scattering length a, where a positive (negative) value indicates repulsive (attractive) interactions. This parameter is determined empirically in most cases, since theoretical *ab initio* calculations require an exact treatment of the generally highly non-trivial interaction potential. While the scattering length is uniquely defined for the collisions of two ground-state atoms of a single isotope, they may vary significantly not only between isotopes, but also between different electronic states and for interorbital interactions, i.e., for collisions of an $|e\rangle$-$|g\rangle$ pair. For the latter, in the case of the fermionic isotopes the antisymmetric wavefunction under particle exchange further produces two distinct interaction states — an orbital triplet state, $|eg^+\rangle$, and the singlet states, $|eg^-\rangle$, with correspondingly symmetrized spin wavefunctions [116, 140].[3] An overview of the experimentally determined s-wave scattering lengths for the relevant isotopes and scattering channels is given in Table 1.1. We note that almost all scattering lengths are positive and sizeable, apart from the ground-state scattering length of ^{171}Yb, which stands out with an almost vanishingly small value. This is expected to influence the effectiveness of the lattice loading process, as this depends on the atomic thermalization via scattering; however, this did not present itself as a major issue in our setup (Chapter 2.6.1).

The full decoupling of electronic angular momentum from the nuclear spin further leads to the absence of spin-changing collisions and the emergence of an SU(N) interaction symmetry for the fermionic isotopes, with $N \leq 2I + 1$ [106, 116]. For ^{171}Yb, this corresponds to the standard SU(2) group, while the preparation of subsets of m_F states for ^{173}Yb flexibly allows for the study of larger N up to SU(6). This has been used to study the properties of a 1D Fermi liquid [146] and the equation of state of the 2D and 3D SU(N) Fermi-Hubbard model [147–149]. In the context of our experiment, this will be particularly relevant for the realization of non-Abelian lattice gauge theories (Chapter 1.4).

---

[2] Here, we have neglected the effective range term $-r_{\mathrm{eff}}k^2/2$, which is the first-order correction to introduce a finite energy dependence.

[3] This holds for atoms with different spins. For two atoms in the same spin state, only the anti-symmetric channel allows for collisions.

Isotope	^{174}Yb	^{173}Yb	^{171}Yb
$a_{gg}(a_0)$	$104.9(1.5)^{a}$	$199.4(2.1)^{a}$	$-2.8(3.6)^{a}$
$a_{eg}^{(+)}(a_0)$	$94.7(1.6)^{b}$	$1878(37)^{c}$	$240(4)^{d}$
$a_{eg}^{-}(a_0)$	n/a	$219.7(2.2)^{c}$	$389(4)^{d}$
$a_{ee}(a_0)$	$126.7(2.3)^{b}$	$306(10)^{e}$	$104(7)^{d}$
$\beta_{eg}^{(-)}(\mathrm{cm}^3\mathrm{s}^{-1})$	$\ll 10^{-14}{}^{f}$	$<3 \times 10^{-15}{}^{e}$	$\leq 2.6(3) \times 10^{-16}{}^{d}$
$\beta_{ee}(\mathrm{cm}^3\mathrm{s}^{-1})$	$2.0(1.4) \times 10^{-11}{}^{g}$	$2.2(6) \times 10^{-11}{}^{e}$	$4.8(2.1) \times 10^{-12}{}^{d}$

Table 1.1 | Scattering lengths and two-body loss coefficients of ^{174}Yb, ^{173}Yb, and ^{171}Yb. The s-wave scattering lengths a are in units of the Bohr radius a_0. The inter-orbital scattering length a_{eg} for ^{174}Yb and the one for the triplet scattering channel a_{eg}^{+} for the fermionic isotopes are displayed in the same row, as well as the two-body loss rates β_{eg} and β_{eg}^{-}. The values are taken from [a] [141], [b] [142] in agreement with [143], [c] [136], [d] [144], [e] [145], [f] [143], [g] taking the mean value of reported results in [142, 143].

Inelastic scattering

In addition to elastic collisions, we also have to consider inelastic scattering interactions if the particles are not strongly separated and once the electronic state enables relaxation processes. This applies to collisions of clock-state atoms with an atom in the ground state, but even more so to e-e scattering events. In these cases, the atoms can form a molecule, whose bound state is significantly lower in energy than the wavefunction for the separated atoms. Therefore, this process can release large amounts of energy, which can be converted to kinetic energy, allowing the colliding pair to escape from the trap [106, 140]. We can describe this loss process by the differential equation

$$\frac{\mathrm{d}n(t)}{\mathrm{d}t} = -\beta n^2(t), \tag{1.15}$$

with the two-body loss coefficient β, which is solved by

$$n(t) = \frac{1}{1/n_0 + \beta t} \tag{1.16}$$

with the initial atomic density n_0. In the presence of additional single-body loss channels of strength γ, e.g., due to collisions with vacuum background atoms or off-resonant scattering, this differential equation expands to

$$\frac{\mathrm{d}n(t)}{\mathrm{d}t} = -\beta n^2(t) - \gamma n(t) \tag{1.17}$$

and we obtain a resulting time-dependent population of

$$n(t) = \frac{n_0 \gamma}{e^{\gamma t}(n_0 \beta + \gamma) - n_0 \beta}. \tag{1.18}$$

We note that the *e-e* loss rate coefficients for all three main isotopes (Table 1.1), while still linked with uncertainty, are considerably large and can pose a severe limitation to the clock-state lifetime, as discussed in Chapter 4.3.

A loss process that is also affecting pure ground-state samples are three-body collisions, or recombinations, in which part of the binding energy of a weakly bound molecule is transferred onto a third involved atom [150]. Again, we can determine the solution to the corresponding differential equation $\mathrm{d}n(t)/\mathrm{d}t = -\kappa n^3(t)$ as

$$n(t) = \frac{n_0}{\sqrt{1 + 2\kappa t}}. \tag{1.19}$$

Due to the strong density dependence this effect only plays a role in relatively dense clouds, which can be the case for atoms transferred from a MOT into a deep 3D lattice (Chapter 2.6).

1.2 AC polarizability

Expanding on the (near-)resonant atom-light interaction delineated in Section 1.1.2, we now turn to a description of the far-detuned coupling of Yb atoms to light, which is essential for the understanding of optical lattices or tweezers and for the concept of state-dependent potentials. After a brief derivation of the theory behind the ac polarizability tensor, we outline the polarizability landscape for the three lowest-lying electronic states, the $^1\mathrm{S}_0$, $^3\mathrm{P}_0$, and $^3\mathrm{P}_1$ states, and its implications on the choice of wavelengths for optical traps and other techniques to adjust the differential light shift. Here, the empirical polarizability model, which was first presented in [101], is discussed and expanded to include the tune-out wavelength for the $^3\mathrm{P}_0$ state, but also to present an improved model for the $^3\mathrm{P}_1$ polarizability, which is of particular relevance for cooling and imaging purposes [63, 83, 151].

1.2.1 Far-detuned atom-light coupling

As the theoretical description of the atom-light interaction in [77] and its application on ytterbium atoms in [110] is highly elaborate and extensive, the following treatment closely follows their discussion and notation. Returning to the dipole interaction

$$V_{\mathrm{ac}}(t) = -\mathbf{d}(t) \cdot \mathbf{E}(t)/2, \tag{1.20}$$

with a classical electric field as in Eq. (1.3) and an induced oscillating atomic dipole moment $\mathbf{d}(t) = \mathbf{d}^{(+)} e^{-i\omega t} + \text{c.c.}$, we note that the role of the dipole moment has changed compared to Eq. (1.2) as we now consider the case of far-detuned light, i.e., $\Delta \gg \Gamma$. In this regime, the ac Stark or light shift as a second-order perturbation theory effect governs the interactions, and the induced atomic polarization and, consequently, the dipole moment depends on the external electric field, mediated by the dynamical polarizability $\alpha(\omega)$, which itself is a function of the detuning from the respective transition. Dropping the terms oscillating with 2ω as we are only interested in the time-averaged light shift $V_{\mathrm{ac}} = \langle V_{\mathrm{ac}}(t)\rangle$, this yields [110]

$$V_{\mathrm{ac}} = -\mathrm{Re}(\alpha(\omega))|E^{(+)}|^2 = -\frac{1}{2c\epsilon_0}\mathrm{Re}(\alpha(\omega))I. \tag{1.21}$$

We can use this expression to determine the dipole force [116]

$$\mathbf{F}(\mathbf{r}) = -\nabla V_{\mathrm{ac}}(\mathbf{r}) = \frac{1}{2c\epsilon_0}\mathrm{Re}(\alpha(\omega))\nabla I(\mathrm{r}), \tag{1.22}$$

which is the working principle of optical lattices and tweezers, where strong intensity gradients exert a restoring force on the atoms.

The potential experienced by an atom in a state $|\beta\rangle$ in an optical trap thus depends on the real part of the ac polarizability of this state, which is given by [77, 116]

$$\mathrm{Re}(\alpha_\beta(\omega)) = \sum_{\beta'\neq\beta} \frac{2\omega_{\beta'\beta}}{\hbar(\omega_{\beta'\beta}^2 - \omega^2)} \left|\langle\beta|\hat{\varepsilon}\cdot\mathbf{d}|\beta'\rangle\right|^2. \tag{1.23}$$

Here, we have to sum over the individual contributions from all relevant transitions to states $|\beta'\rangle$ if there is no single dominant transition close to the laser frequency ω. This is the case for most of the commonly used trapping laser wavelengths in Yb and will be particularly necessary for a correct determination of the polarizability landscapes in the next Section. The dipole matrix element $\left|\langle\beta|\hat{\varepsilon}\cdot\mathbf{d}|\beta'\rangle\right|^2$ is related to the transition linewidth $\Gamma_{\beta'\beta}$ by the expression [77]

$$\Gamma_{\beta'\beta} = \frac{\omega_{\beta'\beta}^3}{3\pi\epsilon_0\hbar c^3} \left|\langle\beta|\hat{\varepsilon}\cdot\mathbf{d}|\beta'\rangle\right|^2, \tag{1.24}$$

such that we can write the ac Stark shift as

$$V_{\mathrm{ac}}(\omega) = -\sum_{\beta'\neq\beta} \frac{3\pi c^2}{2\omega_{\beta'\beta}^3}\left(\frac{\Gamma_{\beta'\beta}}{\Delta_{\beta'\beta}} + \frac{\Gamma_{\beta'\beta}}{\omega_{\beta'\beta}+\omega}\right)I. \tag{1.25}$$

If we apply the rotating-wave approximation to the aforementioned case of an effective two-level system, this expression reads $V_{\mathrm{ac}}(\omega) = 3\pi c^2\Gamma I/2\omega_0^3\Delta$, which is negative and thus trapping for the energetically lower-lying state for $\Delta < 0$, while the higher-lying state experiences an anti-trapping potential and atoms in this state will therefore be pushed towards the intensity minima. This behavior is inverted for blue-detuned light, i.e., $\Delta > 0$. Notably, this antithetical shift of ground and excited state would be highly undesired in a multiorbital quantum gas experiment, as this would not allow for simultaneous trapping of all involved states. Instead, the existence of multiple relevant transitions in real atomic systems demands for a generalization of this intuition of red- and blue-detuned frequencies, as different contributing transitions can amplify or cancel each other, giving rise to non-trivial differential polarizabilities.

The specific case of a perfectly canceled polarizability is denoted as a *tune-out wavelength* and is particularly relevant for the quantum simulation scheme devised for this experiment, as laser beams at this wavelength do not couple to atoms in this state up to first order, while any other state generally exhibits a finite polarizability and thus can be addressed. Similarly important are *magic* wavelengths where the polarizabilities of two states of interest are identical, which suppresses the differential Stark shift on the corresponding transition to allow for trap-independent manipulation.

While this treatment is sufficient for the case of the ground and clock state in ^{174}Yb due to their vanishing angular momenta, the hyperfine structure in the fermionic isotopes requires the introduction of the polarizability tensor $\alpha_{\mu\nu}(\omega)$, which describes the anisotropic polarization response of the atom in a given projection m_F of the total atomic angular momentum F to the light field as [110]

$$d_\mu^{(+)} = \alpha_{\mu\nu}(\omega) E_\nu^{(+)}. \tag{1.26}$$

The corresponding ac Stark shift is then defined as [77]

$$V_{\mathrm{ac}} = -d_\mu^{(+)} E_\mu^{(-)}/2 - d_\mu^{(-)} E_\mu^{(+)}/2 = -\mathrm{Re}(\alpha_{\mu\nu}) E_\mu^{(-)} E_\nu^{(+)}, \tag{1.27}$$

where the real part of the polarizability tensor is given by[4]

$$\mathrm{Re}(\alpha_{\mu\nu}(\omega)) = \sum_{F',m_F'} \frac{2\omega_{F'F}}{\hbar(\omega_{F'F}^2 - \omega^2)} \langle F\, m_F |\, d_\nu \left| F'\, m_F' \right\rangle \left\langle F'\, m_F' \right| d_\mu \, | F\, m_F \rangle . \tag{1.28}$$

Decomposing the polarizability tensor into its irreducible scalar, vector, and tensor components, we obtain [77]

$$\begin{aligned}
\alpha^{(0)}(F;\omega) &= \sum_{F'} \frac{2\omega_{F'F}}{3\hbar(\omega_{F'F}^2 - \omega^2)} |\langle F \| \mathbf{d} \| F' \rangle|^2 \\
\alpha^{(1)}(F;\omega) &= \sum_{F'} (-1)^{F'+F+1} \sqrt{\frac{6F(2F+1)}{F+1}} \begin{Bmatrix} 1 & 1 & 1 \\ F & F & F' \end{Bmatrix} \frac{\omega_{F'F}}{\hbar(\omega_{F'F}^2 - \omega^2)} |\langle F \| \mathbf{d} \| F' \rangle|^2 \\
\alpha^{(2)}(F;\omega) &= \sum_{F'} (-1)^{F'+F} \sqrt{\frac{40F(2F+1)(2F-1)}{3(F+1)(2F+3)}} \begin{Bmatrix} 1 & 1 & 2 \\ F & F & F' \end{Bmatrix} \frac{\omega_{F'F}}{\hbar(\omega_{F'F}^2 - \omega^2)} |\langle F \| \mathbf{d} \| F' \rangle|^2
\end{aligned} \tag{1.29}$$

with the reduced matrix elements $\langle F \| \mathbf{d} \| F' \rangle$, which allows us to write the light shift as

$$\begin{aligned}
V_{\mathrm{ac}}(F, m_F; \omega) = &- \alpha^{(0)}(F;\omega) |E^{(+)}|^2 \\
&- \alpha^{(1)}(F;\omega) (i\mathbf{E}^{(-)} \times \mathbf{E}^{(+)})_z \frac{m_F}{F} \\
&- \alpha^{(2)}(F;\omega) \frac{3|E_z^{(+)}|^2 - |E^{(+)}|^2}{2} \frac{3m_F^2 - F(F+1)}{F(2F-1)} .
\end{aligned} \tag{1.30}$$

This expression can be simplified by introducing the degree of circular polarization q, which

---

[4] This only holds for linearly polarized light; for circularly polarized light the $\omega_{F'F}$ term in the nominator is replaced by ω.

is 0 for linearly polarized and +1 (−1) for right-hand (left-hand) circularly polarized light, such that [110]

$$\begin{aligned}V_{\mathrm{ac}}(F, m_F; \omega) = -\frac{I}{2c\epsilon_0}\Big[\alpha^{(0)}(F;\omega) \\ +\alpha^{(1)}(F;\omega) q(\hat{k}\cdot\hat{z})\frac{m_F}{F} \\ +\alpha^{(2)}(F;\omega)\frac{3|\hat{\varepsilon}_z|^2-1}{2}\frac{3m_F^2-F(F+1)}{F(2F-1)}\Big]\end{aligned} \tag{1.31}$$

for laser light with a unit wave vector $\hat{k}$ and polarization vector ε. The scalar shift only depends on the total angular momentum, while the vector and tensor shift further contain a dependence on the projection m_F. The linear relationship for the vector light shift acts as an effective linear Zeeman shift, but only occurs for light with a circular polarization projection on the quantization axis. This is contrary to the tensor shift, which is maximal for linearly polarized light along the quantization axis, but also non-zero for circularly polarized light. Given its dependence on the absolute value of m_F, the shift is analogous to a linear Stark shift [110].

The *LS* coupling approximation

While these formulae are powerful tools, they require knowledge of the reduced dipole matrix element $|\langle F\|\mathbf{d}\|F'\rangle|$, whose precise computation is generally a hard task. Complex numerical methods such as configuration interaction (CI) and relativistic many-body perturbation theory (MBPT) models have been applied to determine them for the relevant transitions for the Yb ground and several clock states, which allowed for an extrapolation of their respective polarizabilities [44, 152–154]. While these calculations are quite precise and offer decent predictions for the search of, e.g., new magic wavelengths, they disagree in parts, and the theoretical uncertainty of certain distinctive wavelengths like the clock-state tune-out wavelength can amount to tens of nm. In particular, the treatment of core-excited states, where an electron from the outer $4f$-subshell is excited, causes significant problems as these states lie outside the computational subspace of the employed techniques. We instead utilize a simpler method, closely following the calculations in [110], by approximating the involved states as eigenstates of the electronic spin and angular momentum operators, $\hat{S}$, $\hat{L}$, and $\hat{J}$. This strongly simplifies the hyperfine reduced matrix element computation, as we can now write it in terms of the finestructure matrix element [77]:

$$\langle F\|\mathbf{d}\|F'\rangle = \langle J\|\mathbf{d}\|J'\rangle(-1)^{F'+J+I+1}\sqrt{(2J+1)(2F'+1)}\begin{Bmatrix} J & J' & 1 \\ F' & F & I\end{Bmatrix} \tag{1.32}$$

Expressing the reduced matrix element of a fine-structure transition $J \rightarrow J'$ in terms of its linewidth in analogy to Eq. (1.24) [77],

$$|\langle J\|\mathbf{d}\|J'\rangle|^2 = \frac{3\pi\hbar\epsilon_0 c^3}{\omega_{J'J}^3}\frac{2J'+1}{2J+1}\Gamma_{J'J}, \tag{1.33}$$

allows for the usage of measured quantities to obtain the polarizability in the LS coupling approximation. While the transition frequencies $\omega_{J'J}$ are well known from various spectroscopic measurements [155], the actual linewidth of the very transition we are interested in is unkown for most transitions to higher-lying states that do not find application in typical experiments. Instead, only the radiative lifetimes τ of the excited states are known. Therefore, we again apply the LS coupling approach to also determine the dipole matrix elements for transitions to the remaining lower-lying states, which gives us an estimate of the branching ratios that can then be used to compute the transition linewidths of interest [110], $\Gamma = \beta/\tau$. To this end, we further decompose the fine-structure reduced matrix element into its spin and angular momentum components as [77]

$$\langle J\|\mathbf{d}\|J'\rangle = \langle L\|\mathbf{d}\|L'\rangle(-1)^{J'+L+S+1}\sqrt{(2L+1)(2J'+1)}\begin{Bmatrix} L & L' & 1 \\ J' & J & S \end{Bmatrix}\delta(S'-S)(1-\delta(\Pi_{l_1,l_2}-\Pi_{l'_1,l'_2})), \tag{1.34}$$

where $\Pi_{l_1,l_2} = (-1)^{l_1+l_2}$ is the parity operator and l_1 and l_2 are the individual electronic orbital quantum numbers of the two valence electrons, ensuring that all selection rules are respected. This at hand, we can compute the branching ratio

$$\beta(J',J) = \frac{\omega^3_{J'J}|\langle J'\|\mathbf{d}\|J\rangle|^2}{\sum_{J''}\omega^3_{J'J''}|\langle J'\|\mathbf{d}\|J''\rangle|^2} \tag{1.35}$$

where we sum over all states $|J''\rangle$ that are energetically below $|J'\rangle$. We note that the orbital reduced matrix elements in Eq. (1.34) are canceled in Eq. (1.35) for most of the states that are relevant for our model due to the selection rule $L = L' \pm 1$. The resulting polarizability curves for the $^1\mathrm{S}_0$, $^3\mathrm{P}_0$, and $^3\mathrm{P}_1$ states are depicted in [110].

However, the reduced complexity comes at the price of lower accuracy where configuration mixing and higher-order perturbation theory effects become crucial. In addition, this method does not take the whole static electric dipole polarizability $\alpha(\omega = 0)$ into account, which is relevant to describe core excitations and presents itself as a finite overall offset. This largely accounts for the deviation in the $^1\mathrm{S}_0$ polarizability between the CI+MBPT results from [152] and simple LS coupling estimate in [110]. In the next Section, we therefore enrich this simple model with empirically determined parameters by fitting to measured tune-out and magic wavelengths, which provides a very accurate description of the polarizability landscape of the clock state pair in the visible wavelength range.

Off-resonant scattering

Before, we however briefly turn to the imaginary part of the polarizability, causing off-resonant scattering. Intuitively, this can be understood as the action of dipole oscillations that are out of phase with the incident wave, leading to a dissipated power of [156]

$$P_{\mathrm{ac}} = \langle \dot{\mathbf{d}}(t) \cdot \mathbf{E}(t)\rangle = \frac{\omega}{c\epsilon_0}\mathrm{Im}(\alpha(\omega))I \tag{1.36}$$

and a consequential scattering rate of

$$\Gamma_{\mathrm{ac}} = \frac{P_{\mathrm{ac}}}{\hbar\omega} = \frac{1}{\hbar c \epsilon_0} \mathrm{Im}(\alpha(\omega)) I \tag{1.37}$$

with which atoms are absorbed and spontaneously reemitted. In the case of far-detuned traps, this process is undesired as it causes heating due to net momentum gain from the random emission direction after the directed absorption recoil. Expressing the imaginary part of the polarizability in a similar way as the real part in Eq. (1.23) and inserting it into Eq. (1.37), we obtain the scattering rate [77]

$$\Gamma_{\mathrm{ac}} = \frac{3\pi c^2}{2\hbar\omega_{\beta'\beta}^3} \left(\frac{\Gamma_{\beta'\beta}}{\Delta_{\beta'\beta}} + \frac{\Gamma_{\beta'\beta}}{\omega_{\beta'\beta} + \omega} \right)^2 I. \tag{1.38}$$

For cases in which we can apply the rotating wave approximation, this equation simplifies to a term proportional to $\Gamma^2_{\beta'\beta}/\Delta^2_{\beta'\beta}$, and we can compare the trapping potential to the scattering rate, yielding

$$\frac{V_{\mathrm{ac}}}{\Gamma_{\mathrm{ac}}} = \hbar \frac{\Delta}{\Gamma}. \tag{1.39}$$

Therefore, in this simple picture it is preferential to choose a trapping wavelength that is far detuned from any strong transition. Contrary to the light shift, however, it is highly non-trivial to generalize this to more complex multi-level systems, as interference effects between various transitions can enhance or suppress scattering at certain wavelengths. As this concludes the discussion of the scattering, we will now use the term polarizability equivalently to its real part for the remainder of this work.

1.2.2 An empirical model for ytterbium light shifts

To elucidate the total and differential light shifts for the two main transitions $^1\mathrm{S}_0 \rightarrow {}^3\mathrm{P}_0$ and $^1\mathrm{S}_0 \rightarrow {}^3\mathrm{P}_1$ in Yb over the range of wavelengths that are typically used in quantum gas experiments, we utilize the expression Eq. (1.31) in combination with experimental data on relevant transitions and distinctive wavelengths like magic or tune-out wavelengths.

The $^1\mathrm{S}_0$ state

Since the $^1\mathrm{P}_1$ state is the energetically lowest one that is connected to the ground state via a strong, dipole-allowed transition, it dominates the scalar polarizability α_0 for all wavelengths above 399 nm, apart from a small region around the intercombination line to the $^3\mathrm{P}_1$ state at 556 nm (Fig. 1.3). This renders light at almost all wavelengths in the visible and infrared range red-detuned and thus enables trapping of atoms in the ground-state, which conveniently allows for the use of powerful lasers emitting light at 1064 nm for, e.g., dipole traps and 532 nm for optical lattices or tweezers. The $^3\mathrm{P}_1$ transition in turn provides a zero-crossing of the polarizability at an accessible wavelength and at sufficient distance to the transition itself such that off-resonant scattering at this tune-out wavelength was expected to not be limiting,

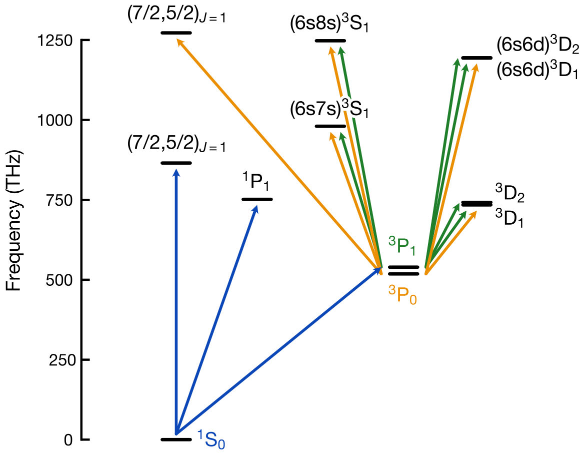

Figure 1.2 | Relevant energy levels and transitions for the empirical polarizability models. The transitions from the ground state are depicted as blue arrows, while the transitions from the ^{3}P$_0$ and ^{3}P$_1$ states are indicated in orange and green, respectively. The various states are ordered by their spin and orbital quantum number, apart from the core-excited states, which are listed in the ^{1}S column for visibility reasons. Notably, the ^{1}S$_0$ ↔ ^{3}P$_1$ transition is relevant for the polarizabilities of both involved states, but only marked as blue. Transitions to high-lying states that are accounted for by the fit parameters are neglected in this Figure.

which is confirmed by the experimental results (Chapter 4.2). Further transitions to the triplet manifold, which would violate the selection rules, can be safely neglected owing to the resulting marginal linewidths. Instead, we can focus on transitions to singlet states with odd parity. About 110 THz above the ^{1}P$_1$ state resides the core-excited state [Xe]$4f^{13}5d6s^2(7/2,5/2)_{J=1}$, where an electron from the $4f$-shell is excited to the $5d$ orbital [117]. Here, not only the Russell-Saunders notation breaks down, but also the standard numerical treatment of the polarizability, as it requires two valence electrons above closed shells [152]. As this state shares the total angular momentum $J = 1$ and the odd parity with the ^{1}P$_1$ state, the Coulomb interaction is expected to significantly mix these states, in which case also the LS coupling approach would fail. Naively ignoring this effect, we treat this state as sufficiently described by its linewidth of $\Gamma = 2\pi \times 11.1(6)$ MHz and the transition wavelength of 346.5 nm [117].

At even smaller wavelengths below 250 nm further ^{1}P$_1$ transitions with increasing lifetimes emerge, which however become less and less significant for the exact shape of the polarizability curve in the wavelength regime we are interested in due to the $\sim \omega_{J'J}^{-4}$ dependence. Instead, they mostly lead to a small positive[5] and almost constant overall shift. Moreover, for these states the branching ratio calculation is more complicated, since from there a decay to the ^{1}D$_2$ states is possible and the orbital reduced matrix elements in Eq. (1.35) do not cancel. We therefore neglect these transitions and instead absorb their action in a global offset as an empirical parameter. This parameter can be determined by fitting the bare scalar polarizability to the ground-state tune-out wavelength at 553.3 nm, whose measurement will be discussed in Chapter 4.2. We find that the small resulting offset of $-0.8\,h\,\mathrm{Hz}/\mathrm{Wcm}^{-2}$ leads to a precise

---

[5] A positive polarizability results in a negative potential, which is why the shift is negative in the context of Fig. 1.3.

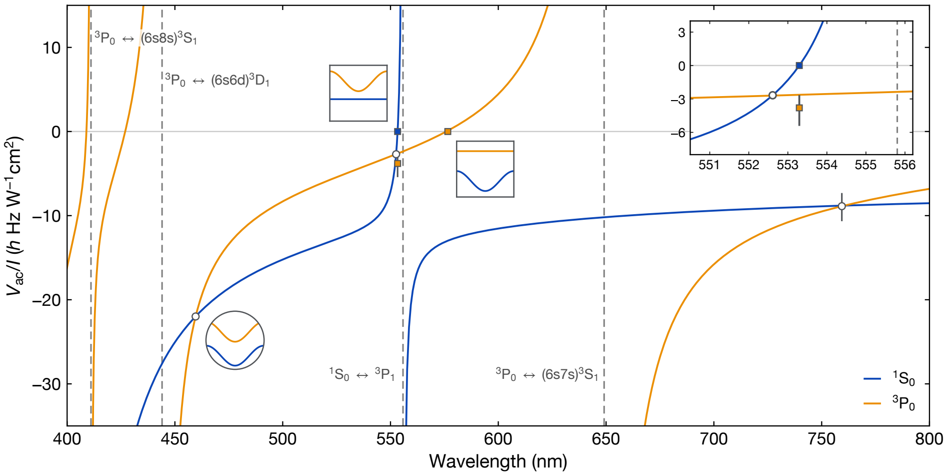

Figure 1.3 | Empirical model for the scalar ground- and clock-state light shift. We add a global offset to the *g* light shift (blue) obtained from the *LS* coupling model to exactly fit the tune-out wavelength at 553.3 nm (blue square). Similarly, we introduce an effective transition for the *e* light shift (orange) to fit to the measured *e* tune-out and magic wavelengths (circles) to obtain an improved estimate of the polarizability landscape. The schematics in squares illustrate the vanishing polarizability of a given state at its tune-out wavelength, while the encircled schematic indicates the identical potential of a magic trap. Notably, the total light shift at the 459.6 nm and 552.6 nm magic wavelengths has not been determined, so that the vertical position of the corresponding markers is only determined by the polarizability crossing. Measured absolute polarizabilities for the 759.3 nm magic and the *g* tune-out wavelength are denoted by grey errorbars. Inset: Zoom-in on the light shift close to the $^1S_0 \rightarrow {}^3P_1$ transition.

match of the static polarizability of our model to the value of $\alpha(0) = -6.61(28)\, h\,\mathrm{Hz/Wcm^{-2}}$ that was determined numerically [152, 153], indicating the validity of our approach. We note that here we use the notation in terms of the experimentally more intuitive intensity-normalized scalar potential $V_{\mathrm{ac},0}/I$, which is identical to the total potential for the bosonic isotopes and can be related to the scalar polarizability via the prefactors $-2c\epsilon_0$ as defined in Eq. (1.21). Remarkably, due to the precise knowledge of the dominant $^1P_1$ and $^3P_1$ transition linewidths [112, 117, 122] and the large frequency gap to higher-lying states that would require a more complex treatment, even the bare *LS* coupling estimate from [110] for the *g* tune-out wavelength is correct within 0.05 nm.

The $^3P_0$ state

Being part of the triplet manifold, the $^3P_0$ state couples to a completely different set of transitions than the $^1S_0$ state, which entails strongly diverging polarizabilities — a prerequisite for far-detuned state-dependent potentials. The dipole selection rules again constrain the set of transitions that need to be taken into account almost fully to ones that connect $|e\rangle$ to the $^3S_1$ and $^3D_1$ states. Consequently, the five lowest of these states largely determine the $^3P_0$ polarizability in the visible and infrared regime: the $(6s5d)^3D_1$ repump transition at 1388.7 nm, the $2\pi\times1.5(2)$ MHz wide $(6s7s)^3S_1$ transition at 649.1 nm, the $(6s6d)^3D_1$ transition at 444.0 nm with a linewidth of $2\pi\times4.1(1)$ MHz, the quite narrow $(6s8s)^3S_1$ transition at 411.1 nm with $\Gamma = 2\pi\times0.6(1)$ MHz, and the $2\pi\times2.4(1)$ MHz broad $(6s7d)^3D_1$ transition at 370.1 nm [110, 157]. The determination of the linewidths is performed analogous to Eq. (1.35) and an overview of the relevant transitions is given in Appendix A. A transition to a $^3\mathrm{P}_1$ state is further allowed if its parity is even, such as for the transition to the $(6p^2)^3\mathrm{P}_1$ state at 377.1 nm [155]. Here, we struggle again to ascertain the correct branching ratio as we would have to assume that the reduced dipole matrix elements for the transition to the $^3\mathrm{P}_0$ clock state are identical to the ones to the ^{3}D and the ^{3}S states, which is certainly not correct. With a short lifetime of just 15 ns [157], its impact on the polarizability in the blue spectral region is not negligible, and we estimate a linewidth of $\Gamma \simeq 2\pi \times 4\,\mathrm{MHz}$ by assuming a similar contribution from all matrix elements. We furthermore take the transition to the $4f^{13}5d6s6p(7/2,5/2)_{J=1}$ core-excited state at 397.6 nm into account [158, 159]. This state is peculiar despite its small linewidth of $2\pi \times 194(2)\,\mathrm{kHz}$, as it gives rise to a repulsive magic wavelength 16 GHz above the transition [130]. While its effect on the clock-state polarizability is overshadowed by the adjacent transitions, it provides a benchmark of our model at this lower end of the wavelength range we wish to consider.

Unfortunately, while their energies are well known [155], information about the lifetime of higher-lying $^3\mathrm{S}_1$ and $^3\mathrm{D}_1$ states is scarce. To still be able to accurately capture the measured magic and tune-out wavelengths, we introduce an additional, empirical transition, whose frequency and linewidth are free fit parameters. This effective transition is meant to compensate for the simplifications in our linewidth computations as well as for the limited transition dataset. We assume the ground-state polarizability to be sufficiently described by the offset model mentioned above, such that we can fit the $|e\rangle$ polarizabilities to the values for $|g\rangle$ at the experimentally determined magic wavelengths at 459.6 nm, 552.6 nm, and 759.3 nm. In addition, we can include the e tune-out wavelength at 576.6 nm to our fitting dataset, and we obtain a fitted transition at 376.65 nm with a linewidth of $2\pi \times 16.4\,\mathrm{MHz}$. Notably, this puts it in the direct vicinity of the two highest-frequency transitions, which indicates that our branching ratio calculations underestimate the actual linewidths here. We can also include a global offset in our fitting function, which would incorporate the effects of very high-lying states. However, this degree of freedom does not visibly change the polarizability trend above 400 nm and seems to rather counteract the fitted resonance as the fitted offset is small but positive, using the notation in terms of the induced potential V_{ac}/I. Consequently, the effective transition is shifted towards lower wavelengths and features an increased linewidth. This behavior cannot be motivated physically, since we would expect an attractive effect of the neglected higher-lying transitions, and we therefore refrain from using this offset in our model.

In an effort to reduce the sensitivity to the imperfect branching ratio calculation of transitions with unknown linewidths, we truncate the transition dataset and study its effect on the polarizability curve and the fitted resonance. Starting with the transitions at the highest frequencies, we observe the expected behavior: The fitted resonance first shifts towards lower wavelengths as the missing transitions at 370 nm and 377 nm need to be compensated, then upwards due to the now-gone 397 nm transition (Fig. 1.4). Simultaneously, the effective transition simply absorbs the linewidths of the neglected transitions. As the resulting changes in the polarizability at visible wavelengths are marginal, we can safely use the reduced transition dataset, which yields the fit parameters $\lambda_{\mathrm{eff}} = 374.7\,\mathrm{nm}$ and $\Gamma_{\mathrm{eff}} = 2\pi \times 23.6\,\mathrm{MHz}$. The resulting polarizability curve is displayed in Fig. 1.3.

In a direct comparison to the model that was in presented in [101], which does not contain

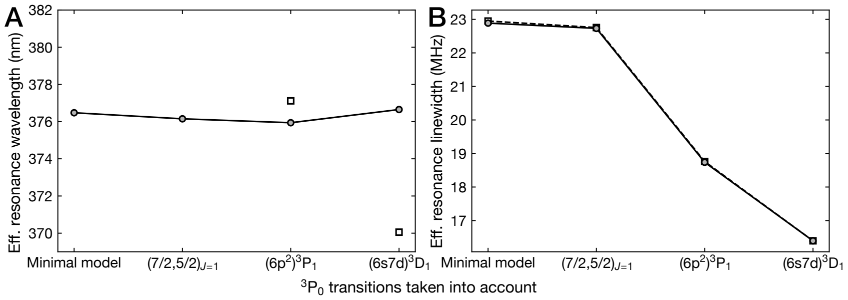

Figure 1.4 | Effect of fitting a reduced transition dataset for the clock-state polarizability model. A The empirical transition that we employ to fit the distinctive wavelengths is located right in between the $(6s7d)^3\mathrm{D}_1$ and $(6p^2)^3\mathrm{P}_1$ states (transition wavelengths depicted as white circles). Therefore, the position of the fitted effective resonance moves only slightly as these transitions are included in the model. Similarly, the $4f^{13}5d6s6p(7/2,5/2)_{J=1}$ core-excited state couples too weakly to the $^3\mathrm{P}_0$ state to induce a visible effect. **B** As the number of transitions that we take into account changes, the linewidth of the effective transition grows or shrinks correspondingly, as can be seen from the overlap with the summed individual transition linewidths (squares interpolated with a dotted line), using the full transition dataset as a common reference point.

the clock-state tune-out wavelength, we observe a small change of $\Delta\lambda_{\mathrm{eff}} = -1.4\,\mathrm{nm}$ and $\Delta\Gamma_{\mathrm{eff}} = 2\pi \times 0.7\,\mathrm{MHz}$ for our updated parameters, which however does not translate into a visible change of the overall polarizability landscape. This reflects the considerable accuracy of the old model already, which predicts the e tune-out wavelength to be at 575.52 nm, with a deviation of only $0.18\,h\,\mathrm{Hz/Wcm^{-2}}$ at the measured wavelength of 576.6 nm, and despite significant measurement uncertainties of the individual lifetimes of the most relevant states, i.e., in particular the $(6s7s)^3\mathrm{S}_1$ state. This is in stark contrast to the pure LS coupling model that expects a tune-out wavelength at $\simeq 540\,\mathrm{nm}$ [110]. On the contrary, the congruence with the computed $^3\mathrm{P}_0$ polarizability values from [152] is remarkable, and also the extracted static polarizability is found to be reasonably close. Hence, the prediction of the clock-state tune-out wavelength based on the numerical data from [152] is also very precise, as is the case for the ground-state tune-out wavelength at 553.3 nm. Later unpublished updates to this numerical model, which contained a rescaling of the correlation potential and led to significant shifts of the predicted distinctive wavelengths of interest, have worsened this accuracy [154].

Upon performing the same comparison of our model to the numerical data for the $^1\mathrm{S}_0$ state, we notice a highly concordant behavior in the low-frequency regime, which is consistent with the congruent static polarizabilities, but for wavelengths below the $^3\mathrm{P}_1$ transition the numerical simulation computes a weaker trend towards the $^1\mathrm{S}_0$ transition. This widening gap has also been observed in [110]. The discrepancy is particularly apparent at the blue magic wavelength, which was measured at 459.6 nm. While the *ab initio* calculations provide a predicted value of 459.3 nm, the corrections to the $^1\mathrm{S}_0$ polarizability to achieve a better fit to the red magic wavelength at 759.3 nm shift the prediction to 465.4 nm, in agreement with the first-principles computation in [153]. As our empirical model is able to capture the measured magic wavelengths, but also exhibits a large overlap with the numerical $^3\mathrm{P}_0$ data, which was not corrected in [152], we assume that this correction causes an overcompensation at lower wavelengths, as it is based on a fit of the matrix element of the $4f^{13}5d^26s_{J=1}$ transition at 267 nm. A second potential reason for this discrepancy is the treatment of the $4f^{13}5d6s^2(7/2,5/2)_{J=1}$ core-excited state. While it is not unlikely that the LS coupling approximation underestimates the effect of state mixing with the $^1\mathrm{P}_1$ state, the simplification of a negligible energy difference between these two states in the mixing calculation in [152] could be an overestimate. To elucidate this, we turn to the blue-detuned magic wavelength measured in [159]. Given the proximity to the $^3\mathrm{P}_0 \rightarrow 4f^{13}5d6s6p(7/2,5/2)_{J=1}$ transition, the position of the magic wavelength is almost independent of other $^3\mathrm{P}_0$ transitions and should thus offer a good indication of the accuracy of our model for the $^1\mathrm{S}_0$ polarizability around the $^1\mathrm{P}_1$ transition. We therefore re-include the core-excited transition for this purpose and find the expected magic wavelength at 753.9405 THz, i.e., within the measurement uncertainty, and at a polarizability of 726 $h\,\mathrm{Hz/Wcm^{-2}}$ compared to a measured value of 728 $h\,\mathrm{Hz/Wcm^{-2}}$ [159]. We therefore do not find evidence for a significantly underestimated state mixing in our model.

As a further check of the validity of our model in a different part of the spectrum we can use the clock-state polarizability at the ground-state tune-out wavelength. Unfortunately, the determination of an absolute, non-zero polarizability requires a precise gauge of the intensity, which is generally a very hard task. This is reflected in relatively large error bars, and the expectation value from our empirical model is right at the 1σ threshold, which is likely rather an indication of the limited accuracy with which we were able to determine the light shift (Chapter 4.2). In addition, we can utilize the polarizability ratios of 3.3(2) at 670 nm, 3.06(4) at 671.509 nm, and 1.97(5) at 690.1 nm reported in [95, 110] as benchmarks, and we obtain the values 3.26, 3.08, and 1.95.

We therefore believe to have the most precise model for the scalar $^1\mathrm{S}_0$ and $^3\mathrm{P}_0$ state polarizabilities in the visible and near-infrared wavelength range, with the largest systematic errors stemming from uncertainties in the measured $(6s7s)^3\mathrm{S}_1$ and $(6s6d)^3\mathrm{D}_1$ lifetimes. This can help to deliver expected polarizability ratios for new state-dependent lattices analogously to [95] or at useful non-magic trap wavelengths like 532 nm, where so far only theoretical estimates have been performed [80, 152, 153], but can also yield more accurate predictions of further distinct wavelengths, like the magic wavelength at 411.41 nm, the second e tune-out wavelength at 1022.3 nm, or the anti-magic wavelengths at 617.1 nm and 1134.2 nm, where the ground- and clock-state light shifts are equal in amplitude, but have opposite signs.

For the fermionic isotope ^{173}Yb we must also consider contributions from the vector and tensor shift. While it is common practice to minimize the vector shift by choosing linearly polarized light for lattice beams, the strongly focused beam in optical tweezers can lead to distortions of the polarizability, such that even for a purely linearly polarized input beam vector shifts can play a role [160]. However, due to the vanishing total electronic angular momentum in the ground and clock state, these contributions are generally orders of magnitude smaller than the scalar light shift. This is not the case at the scalar tune-out wavelengths, where contributions from the vector and tensor polarizability will remain finite. While for most of the applications this will most likely not be limiting as the sensitivity to the residual light shift in typical quantum simulation setups is too small, for applications where this effect does matter a small trap wavelength shift will allow for a $|m_F|$-dependent combined tune-out condition, similar to the cancellation of the tensor shift in lattice clocks [161]. While it would be favorable to translate the results of the empirical model for the $^1\mathrm{S}_0$ scalar polarizability to the vector and tensor components, it is *a priori* not evident how this can be realized for the empirical parameters determined for the scalar light shifts. As the overall effect of the tensor shift is about six orders of magnitude weaker than the scalar contributions, the simple *LS* coupling results from [110] are likely sufficient for most conceivable purposes.

The $^3\mathrm{P}_1$ state

Due to the growing importance of the $^3\mathrm{P}_1$ transition for efficient cooling and high-fidelity imaging purposes, it has also become more relevant to understand its differential polarizability. The quest for magic conditions to allow for homogeneous, trap-independent addressing of this transition has led to the discovery of several magic wavelengths [76, 83, 162] and magic angles [63, 72, 80]. Notably, these magic conditions strongly rely on the chosen isotope, in the above mentioned cases ^{171}Yb and ^{174}Yb, as well as on the hyperfine transition and the final m_F state of the $^3\mathrm{P}_1$ transition. This is a result of the finite total electronic angular momentum, which not only gives rise to hyperfine structure but also renders the vector and tensor shifts comparable in size to the scalar contribution. Hence, this state requires a markedly more complex treatment as we attempt an empirical model for its total polarizability. We again start with the *LS* coupling approximation as given by [110] to obtain the basis of our polarizability estimate. The $^3\mathrm{P}_1$ state shares the relevant transitions of the $^3\mathrm{P}_0$ state — apart from the $(6p^2)^3\mathrm{P}_1$ transition, which is dipole-forbidden for the $(6s^2)^3\mathrm{P}_1$ state —, but the resonance frequencies are shifted by -21 THz. This as well as the different Clebsch-Gordan coefficients further entail differing branching ratios and, thus, linewidths, as in particular the $^3\mathrm{P}_1 \rightarrow {}^3\mathrm{S}_1$ transitions are broader than for the clock state, while the $^3\mathrm{D}_1$ transitions are weaker (Appendix A). In addition, we have to take transitions to the $^3\mathrm{D}_2$ states as well as the intercombination line to the ground state into account. Close to the latter, the light shift exhibits the opposite sign compared to the one for the $^1\mathrm{S}_0$ state, in agreement with our intuition for a two-level system. According to the bare *LS* coupling model, this causes the scalar $^3\mathrm{P}_1$ light shift to be positive in between the 556 nm transition and the one to the $(6s7s)^3\mathrm{S}_1$ state at 680.1 nm, and also close to zero around 550 nm. The consideration of the tensor shift for linearly polarized light leads to a reduced total polarizability, but in particular for the $m_{F'} = 0$ state the total shift is still significantly smaller than for the $^1\mathrm{S}_0$ state. This however contradicts the detection of a near-magic condition for ^{174}Yb at 532 nm [80, 151] and a magic wavelength at 486.78 nm for the $F' = 3/2$, $m_{F'} = 1/2$ transition in ^{171}Yb [83]. This discrepancy is further supported by CI and MPBT calculations for the scalar polarizability that suggest a similar offset of the $^3\mathrm{P}_1$ *LS* coupling estimate as for the $^3\mathrm{P}_0$ state [44, 163, 164], motivating the usage of a similar empirical approach with an effective transition. *A priori*, the corresponding wavelength and linewidth can be chosen as free parameters that are determined by fitting to the experimentally known distinctive wavelengths. However, the similarity of the sets of states that the $^3\mathrm{P}_0$ and $^3\mathrm{P}_1$ states couple to invites to constrain $\lambda_{\mathrm{eff},^3\mathrm{P}_1}$ to $\simeq 385$ nm, with the 10 nm difference to λ_{eff} due to the states' energy gap and in the vicinity of the $(6s7d)^3\mathrm{D}_1$ and $^3\mathrm{D}_2$ states. In contrast, the linewidth can be quite different as the number of transitions that are absorbed in the effective transition as well as their strengths deviate significantly from the case of $^3\mathrm{P}_0$. We further have to incorporate this effective transition also into the vector and tensor shift, where the total

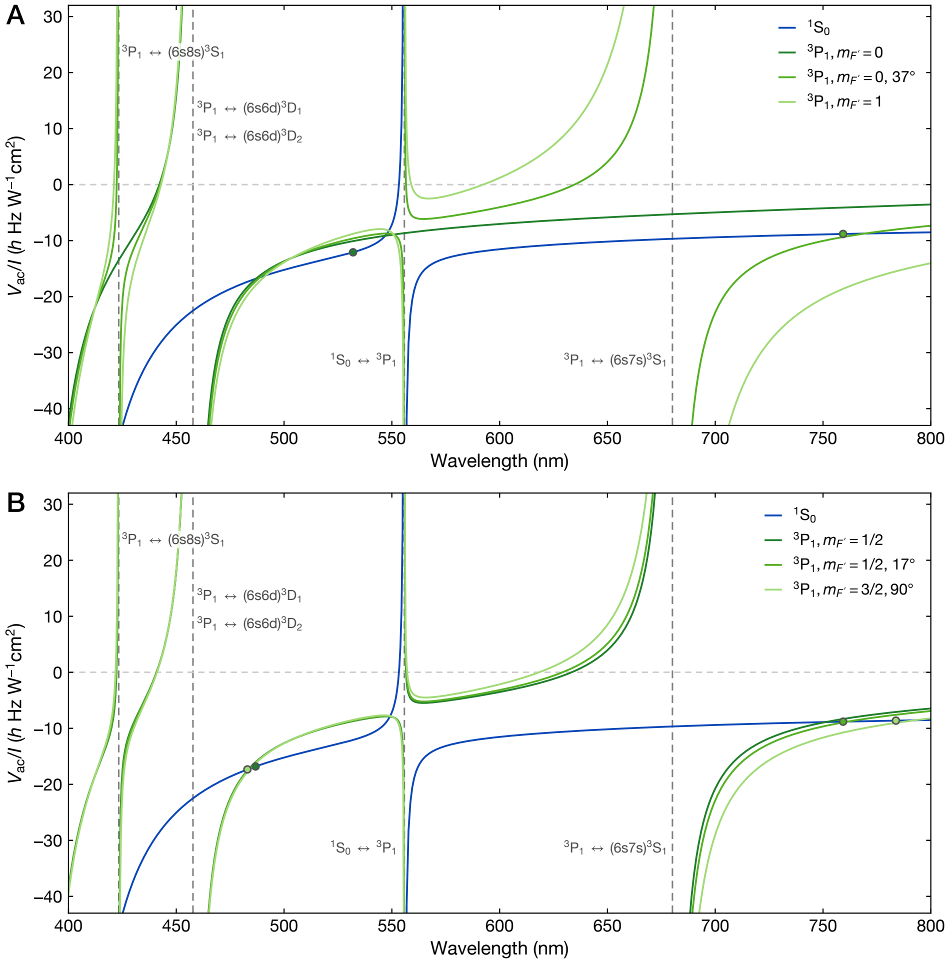

Figure 1.5 | Empirical model for the ^{3}P$_1$ light shift. A Total shift for selected transitions and magnetic field angles for ^{174}Yb. Using the *LS* coupling model as in [110] in combination with a effective resonance at the same frequency as for the ^{3}P$_0$ model and adjusted branching ratios for the $(6s6d)^3$D$_0$ transitions we find decent agreement with the measured near-magic condition at ≃532 nm [80, 151] and the magic angle at 759 nm (Chapter 3.1.1). Unless indicated otherwise, the polarization is chosen to be parallel to the quantization axis ($\vartheta = 0°$). **B** For the $F' = 3/2, m_{F'} = \pm 1/2$ and $m_{F'} = \pm 3/2$ transitions in ^{171}Yb, the overlap between predicted and measured magic wavelengths at ≃485 nm is very reasonable. The magic angles at 759 nm for $F' = 3/2, m_{F'} = \pm 1/2$ and at 783.8 nm for $F' = 3/2, m_{F'} = \pm 3/2$ are captured similarly well.

electronic angular momentum of the empirical excited state appears as a third free parameter. In order to maintain a minimal number of degrees of freedom, we therefore divide the transition into two parts, with one transition to an effective $J = 1$ and $J = 2$ state, respectively. We adopt the relative linewidths from the nearby $(6s7d)^3$D$_1$ and ^{3}D$_2$ transitions and assume identical energies, motivated by the negligibly small frequency difference between the $(6s7d)^3$D states, to enable the usage of a single effective wavelength and linewidth. This yields a similarly constrained model as for the ^{3}P$_0$ state, based on a minimal set of necessary assumptions. We utilize the magic angles of $\theta = 17°$ for the $F' = 3/2, m_{F'} = -1/2$ state in ^{171}Yb [72] and 37(1)° for the $m_{F'} = 0$ state in ^{174}Yb as discussed in Chapter 3.1.1 at 759 nm as a reference for our model, where θ is the angle between the quantization-axis-defining magnetic field and the polarization of the lattice beams. Furthermore, the magic wavelengths at 486.78 nm for the ^{171}Yb $F' = 3/2, |m_{F'}| = 1/2$ states [83] as well as the ones at $\simeq$483 nm and 783.8 nm for $m_{F'} = 3/2$ states [76, 162] provide a helpful testbed to find the linewidth of the empirical transitions as the single free parameter. This yields a value of $\Gamma_{\text{eff}} = 2\pi \times 59$ MHz, where we find the best agreement. This way, our model can plausibly reproduce the magic conditions for $m_{F'} = 0$ in ^{174}Yb at an angle of $\simeq$36° at 759 nm as well as the magic angles that have been determined for the fermionic isotopes. The near-magic condition at 532 nm for ^{174}Yb, however, does not appear to be captured very well, although an exact quantification of the discrepancy is non-trivial. This deviation is underlined by predicted scalar and tensor light shifts at 532 nm that differ by a factor of $\simeq$2 and $\simeq$1/2 from the measured values of $V^0_{\text{ac}} = -5.60(5)\, h\, \text{Hz/Wcm}^{-2}$ and $V^2_{\text{ac}}(m_F = \pm 1, \theta = 0) = 0.95\, h\, \text{Hz/Wcm}^{-2}$ [80]. It is not obvious where this disagreement stems from, given the largely consistent magic conditions at the remaining wavelengths, which render strong inaccuracies from the *LS* approximation and branching ratio simplifications unlikely, albeit possible. Therefore, a measurement of a magic wavelength at $\simeq$ 548 nm would help to elucidate potential shortcomings of the presented polarizability model for the $^3\text{P}_1$ state.

1.3 Trapping atoms

Having established the principles of resonant and off-resonant atom-light interaction, we now turn to a discussion of the slowing and cooling steps that are required to reach a cloud of cold atoms, followed by the theory behind optical lattices and tweezers. Since these concepts have been illuminated in great detail elsewhere [116, 165], we will restrict the scope of this Section to the main features.

The first stage in the typical cascade of cooling efforts for AEL atoms is the Zeeman slower (ZS), which uses a judiciously configured magnetic field gradient to maintain the resonance condition $\Delta + \Delta_{\text{D}} + \Delta_{\text{B}} = 0$ as the atoms get slowed down by scattering photons while they propagate through the magnetic field [165]. Here, the laser detuning from the atomic resonance Δ is negative to account for the positive Doppler shift $\Delta_{\text{D}} = kv$ and the spatially varied Zeeman shift $\Delta_{\text{B}} = (g_{F'} m_{F'} - g_F m_F)\mu_{\text{B}} B/\hbar$, with $k = 2\pi/\lambda$ the wavevector of the ZS light. For AEL atoms such as Yb, the stretched $^1\text{S}_0(F, m_F) \rightarrow {}^1\text{P}_1(F' = F + 1, m_{F'} = m_F \pm 1)$ transition offers the desired large scattering rate and isotope-agnostic slowing performance, but also requires a powerful ZS beam ($I \sim 100$ mW) to saturate the transition, given the saturation intensity of $I_{\text{sat}} = 60\,\text{mW/cm}^2$ [116]. Here, the scattering rate can be expressed in the context of Eq. (1.9) as

$$R_{\text{sc}} = \Gamma P_{\text{e}} = \frac{\Gamma}{2} \frac{I/I_{\text{sat}}}{1 + 4\Delta^2/\Gamma^2 + I/I_{\text{sat}}}, \tag{1.40}$$

with a maximum scattering rate of $\Gamma/2$ at $I \gg I_{\text{sat}}$.

With a similar working principle the magneto-optical trap (MOT) captures atoms in its center with the help of a magnetic field gradient A. This gradient leads to a linearly varying Zeeman shift, whose sign depends on the $m_{F'}$ state of a stretched transition. Correspondingly circularly polarized light is therefore tuned into resonance of a stretched transition if an atom is leaving the MOT center[6] such that the atom experiences a scattering force, slowing it down and pushing it back. The MOT resonance condition is thus given by [116]

$$kv + \frac{g_{F'} m_{F'} \mu_B}{\hbar} A x + \Delta = 0. \tag{1.41}$$

However, this condition can only be fulfilled if an incoming, initially untrapped atom is slow enough such that continuous scattering in strongly intensity-saturating MOT beams can halt it right at the MOT edge, i.e., after a propagation of $2\,w_{\mathrm{MOT}}$, where w_{MOT} is the MOT beam waist. This leads to the definition of the maximum capture velocity

$$v_c = \sqrt{\frac{2\hbar k \Gamma}{m} w_{\mathrm{MOT}}} \approx \sqrt{w_{\mathrm{MOT}}} \times 69\,\mathrm{m/s}. \tag{1.42}$$

Notably, for typical narrow-line 3D MOT configurations, the transition is massively power-broadened to $\Gamma' = \Gamma\sqrt{1 + I/I_{\mathrm{sat}}} \sim 10\,\Gamma$, which increases the capture velocity accordingly [116].

1.3.1 Optical lattices

Once the atoms are captured and cooled down to a temperature $T \sim T_D$, where $T_D = \hbar\Gamma/(2k_B) = 4.4\,\mu\mathrm{K}$ is the Doppler temperature limit of the ${}^3\mathrm{P}_1$ transition, they can be transferred into an optical lattice, generated by interfering laser beams. The simplest geometry is constituted by a retro-reflected beam, forming a standing wave with lattice spacing $a = \lambda/2$

$$I(\mathbf{r}) = 4 I_0(\mathbf{r}) \cos^2\!\left(\frac{2\pi}{\lambda} x\right) \tag{1.43}$$

with the intensity profile

$$I_0(\mathbf{r}) = \frac{2P}{\pi w_0}\, e^{-\frac{2r^2}{w_0^2}}, \tag{1.44}$$

and $r = \sqrt{y^2 + z^2}$. Note that we neglected the longitudinal expansion of the Gaussian beam around the waist w_0, as the Rayleigh range $z_R = \pi w_0^2/\lambda$ is typically much larger than the region of interest. The corresponding potential V at the lattice wavelength can then be inferred from the polarizability and we can approximate the potential at a single site as [166]

$$V(r, x) \simeq V_0 \left(-1 + k^2 x^2 - \frac{k^4}{3} x^4 + \frac{2}{w_0^2} r^2 - 2\frac{k^2}{w_0^2} r^2 x^2 \right), \tag{1.45}$$

using $k = 2\pi/\lambda$. Here, we have expanded the longitudinal sinusoidal potential as well as the radial Gaussian confinement by harmonic oscillators, also including a quartic distortion from the cosine. In addition, in the last term we take the lowest-order coupling into account. The two harmonic terms can be used to obtain the corresponding trap frequencies, with

$$f_l = \sqrt{\frac{2V_0 k^2}{m}} = \frac{2}{h}\sqrt{V_0 E_{\mathrm{rec}}} \tag{1.46}$$

---

[6] Or if a fast atom is entering the MOT region.

the lattice trap frequency along the strongly confined longitudinal axis, and

$$f_\mathrm{r} = \sqrt{\frac{V_0}{m\pi^2 w_0^2}} \tag{1.47}$$

the radial trap frequency. Here, we have introduced the recoil energy $E_\mathrm{rec} = \hbar^2 k^2/2m$, which is a common unit to express the lattice depth and amounts to $h \times 2\,\mathrm{kHz}$ for photons at the 759 nm magic wavelength. The energy spectrum in first-order perturbation theory is further given by [166]

$$E_n = \hbar\omega_\mathrm{x}\left(n_\mathrm{x}+\frac{1}{2}\right) + \hbar\omega_\mathrm{r}(n_\mathrm{y}+n_\mathrm{z}+1) - \frac{E_\mathrm{rec}}{2}\left(n_\mathrm{x}^2+n_\mathrm{x}+\frac{1}{2}\right) - E_\mathrm{rec}\frac{f_\mathrm{l}}{f_\mathrm{r}}(n_\mathrm{y}+n_\mathrm{z}+1)\left(n_\mathrm{x}+\frac{1}{2}\right), \tag{1.48}$$

which shows the deviation of the longitudinal band gap[7] from the equidistant harmonic oscillator levels as

$$\Delta E_\mathrm{n} = -E_\mathrm{rec}(n_\mathrm{x}+1) - E_\mathrm{rec}\frac{f_\mathrm{l}}{f_\mathrm{r}}(n_\mathrm{y}+n_\mathrm{z}+1). \tag{1.49}$$

Hence, in a 1D lattice we can spectroscopically observe a first sideband with a maximal excursion at $f_\mathrm{l} - E_\mathrm{rec}/h$ and a long tail towards the carrier for relatively large radial temperatures (Chapter 2.6.1). Notably, for the standard lattice depths used in spectroscopy sequences, where the calculation above holds, the band gap is considerably larger than the recoil energy the atom would receive upon the absorption of a probe photon, which is $E_\mathrm{rec} = 3.4\,\mathrm{kHz}$ for the clock transition. This ratio is quantified in the Lamb-Dicke parameter $\eta = \sqrt{E_\mathrm{rec}/hf_\mathrm{l}}$. We can therefore probe the clock state excitation as well as repump the atoms back into the ground state without adding momentum from the absorption recoil to the atoms if $\eta \ll 1$, i.e., the reception of the recoil kick is suppressed due to the discrete band structure, and the projection of the beams is mostly along the strongly confined lattice axis. This is equivalent to the suppression of Doppler shifts.

In the case of a shallow-angle lattice such as our vertical lattice (Chapter 2.6.3), we have to take the harmonic confinement along all three dimensions into account, and we can approximate the potential as[8]

$$V_\mathrm{z} = V_{0,\mathrm{z}}\, e^{-\frac{m}{2}(\omega_\mathrm{x}^2 x^2 + \omega_\mathrm{y}^2 y^2 + \omega_\mathrm{z}^2 z^2)} \cos^2\!\left(\frac{\pi}{a_\mathrm{z}} z\right) \tag{1.50}$$

with the harmonic trapping frequencies [56]

$$\begin{aligned} \omega_\mathrm{x}^2 &= \frac{8V_{0,\mathrm{z}}}{m}\left(\frac{2}{w_{0,\mathrm{v}}^2}\sin^2\theta + \frac{1}{2}\left(\frac{1}{z_{\mathrm{R,v}}^2}+\frac{1}{z_{\mathrm{R,h}}^2}\right)\cos^2\theta\right) \approx \frac{16V_{0,\mathrm{z}}}{m w_{0,\mathrm{v}}^2}\sin^2\theta \\ \omega_\mathrm{y}^2 &= \frac{16V_{0,\mathrm{z}}}{m w_{0,\mathrm{h}}^2} \end{aligned} \tag{1.51}$$

---

[7] For a detailed justification of this term we refer to [5, 110].

[8] The exact solution is quite involved, which is why we will use the second-order expansion in analogy to [56].

$$\omega_z^2 = \frac{8V_{0,z}}{m}\left(\frac{2}{w_{0,v}^2}\cos^2\theta + \frac{1}{2}\left(\frac{1}{z_{R,v}^2}+\frac{1}{z_{R,h}^2}\right)\sin^2\theta\right) \approx \frac{16V_{0,z}}{mw_{0,v}^2}\cos^2\theta$$

and the opening angle 2θ between the two beams. Here, we have allowed for elliptical lattice beams, i.e., the horizontal and vertical waists $w_{0,h}$ and $w_{0,v}$ and corresponding Rayleigh lengths $z_{R,h}$ and $z_{R,v}$ can differ, but we assume that both beams have equal sizes and are perfectly overlapped. However, for typically feasible beam sizes the Rayleigh lengths are much larger than the waists, which is why we can neglect these terms.

For a higher-dimensional lattice, where the beams are either orthogonally polarized or detuned from each other by more than the laser's spectral width, the individual potential contributions sum up to the total lattice potential, which can be approximately expressed as [110]

$$V_{\text{lat}}(x,y,z) = \sum_{i=\text{x,y,z}} V_i \approx \sum_{i=\text{x,y,z}}\left(V_{0,i}\cos^2(k_i r_i) + \frac{1}{2}\omega_i^2 r_i^2\right). \tag{1.52}$$

Here, r_i denotes the three directions x, y, and z, and the harmonic confinement frequencies consist of the root of the squared horizontal contributions $\omega = \sqrt{4V_{0,i}/mw_{0,i}^2}$ from the orthogonal horizontal beams and the vertical contributions defined in Eq. (1.51).

In optical lattices with at least moderate depths, the harmonic potential significantly alters the motion of cold and non-interacting atoms, and one can consider the system to be described by the tight-binding Hamiltonian, expressed in second quantization [116]

$$\hat{H}_0 = \int d^3r\hat{\psi}^\dagger(\mathbf{r})\left(-\frac{\hbar^2}{2m}\nabla^2 + V_{\text{lat}}(\mathbf{r})\right)\hat{\psi}(\mathbf{r}) = -J\sum_{\langle i,j\rangle}\hat{c}_i^\dagger\hat{c}_j, \tag{1.53}$$

where

$$\hat{\psi}(\mathbf{r}) = \sum_j w_j(\mathbf{r})\hat{c}_j \tag{1.54}$$

is the field annihilation operator defined in terms of the lowest-band Wannier function $w_j(\mathbf{r})$ and the annihilation operator $\hat{c}_j$ for an atom at the lattice site j. In this model, only nearest-neighbor hopping is allowed, supported by the negligible overlap of the Wannier function on non-neighboring sites for lattices deeper than $V_0 \simeq 5\,E_{\text{rec}}$. The tunneling amplitude J_n of an atom in the n-th Bloch band to an adjacent site can then be computed via the discrete Fourier transform of the band energy $E_n(\mathbf{q})$, where $\mathbf{q}$ is the quasimomentum of the Bloch wave eigenstates, such that [5]

$$J_n(\mathbf{r}) = \sum_{\mathbf{q}} e^{-i\mathbf{q}\cdot\mathbf{r}}E_n(\mathbf{q}). \tag{1.55}$$

For deep lattices one can approximate the tunneling rate for atoms in the lowest band as [5]

$$J \simeq \frac{4}{\sqrt{\pi}}E_{\text{rec}}\left(\frac{V_0}{E_{\text{rec}}}\right)^{3/4} e^{-2(V_0/E_{\text{rec}})^{3/2}}, \tag{1.56}$$

i.e., the tunneling rate depends approximately exponentially on the lattice depth. In the case of deep lattices we can further find that the Wannier functions are localized exponentially on the lattice site around $x = 0$, [167]

$$w_j(x) \sim e^{-(-E_n)^{1/2}x}. \tag{1.57}$$

For the general case of arbitrary lattice parameters and band occupations, the Wannier functions as well as the tunneling rates are computed numerically.

1.3.2 Optical tweezers

In contrast to optical lattices that use interference effects to generate arrays of tightly confined sites, optical tweezers take advantage of the strong focusing power of objectives with a high numerical aperture ($NA = n \sin\theta$). For a well-aligned tweezer, the intensity field that provides the trapping force approaches the shape of an Airy disk [168],

$$I(r) = I_0 \left(\frac{2J_1(1.22\pi r/\xi)}{1.22\pi r/\xi} \right)^2, \tag{1.58}$$

where $\xi = 1.22\lambda/2NA$ is the radial diffraction limit and J_1 is the Bessel function of the first kind of order one. The minimal size of an optical tweezer is thus given by its wavelength and the aperture of the objective. The exact shape of the mapping of a point source onto a finite extent is denoted as the point spread function (PSF) and is subject to the wavefront quality and intensity profile of the input beam. In particular, for a Gaussian envelope of the tweezer beam at the entrance pupil the point spread function also attains a Gaussian component. A detailed description of typical optical aberrations and their effect on the PSF can be found in [169]. Notably, this also affects the longitudinal intensity distribution, which can be expressed for a perfectly flat wavefront in a similar way as the radial one,

$$I(z) = I_0 \left(\frac{\sin\left(\frac{\pi z NA^2}{2\lambda}\right)}{\frac{\pi z NA^2}{2\lambda}} \right)^2, \tag{1.59}$$

which consequently motivates the definition of the longitudinal diffraction limit $\zeta = 2\lambda/NA^2$, also referred to as the depth of field in the object plane [170]. To evaluate the quality of a point spread function, multiple figures of merit exist. A typical choice is the radial distance ξ' from the peak to the first intensity minimum. However, this might obfuscate the true signal as certain aberrations, in particular spherical ones, can lead to a reduced width of the main peak at the expense of an increase in the power in the lobes, which overall worsens the imaging performance. In contrast, the Strehl ratio is a direct measure of a point spread function's proximity to the ideal Airy disk and thus of the wavefront error. For a detected PSF with peak intensity I_0, the Strehl ratio $SR = I_0/J_0$ quantifies its quality as it compares I_0 to the ideal peak intensity J_0. While this generally only necessitates the total power as additional information, technical factors like a finite pixel size can demand for additional corrections to obtain reliable results, as discussed in [169].

In a similar fashion to the formulation of trap frequencies in an optical lattice one can also approximate the tweezer potential as a harmonic oscillator, which yields the radial and longitudinal trap frequencies analogously to Eq. (1.47) with ξ and ζ as the relevant quantities of extent.

1.4 Quantum simulation of lattice gauge theories

In this last Section of the Chapter we will focus on the eventual purpose of the experiment as a quantum simulator to study lattice gauge theories (LGTs), which governs major design decisions. While several experiments have demonstrated building blocks on the path to such a quantum simulator [171, 172], only few actual realizations of dynamical gauge theories have been reported [26, 173–178]. This is mainly based on the intricate realization of the local gauge invariance, which is a fundamental part of any gauge theory, but is not natively realized in typical experimental apparatus. Instead, it has to be engineered via complex lattice geometries and state initialization techniques to provide the appropriate Hilbert space contraints. In particular, the simulation of basic features of a 1D U(1) quantum field theory in [175] requires an initial state with single atoms residing on all shallow sites of a tilted 1D superlattice and an interaction potential tuned to only allow for collective hopping of two particles onto their neighboring deep superlattice well, thus encoding the information on the matter and field states in the occupation of deep and shallow lattice sites.

The approach we are following promises a more intrinsic manifestation of local gauge invariance by precisely defining the potential landscape of the ground and clock state in Yb via state-dependent potentials within the lowest-energy manifold, which gives us accurate control over the possible tunneling processes. The realization of a U(1) Abelian LGT with fermionic matter has been theoretically outlined in [179], which is why we will discuss only the main ideas presented therein, and then move on to the practical subtleties. We will close the Section with an outlook to an extension of this protocol to the simulation of non-Abelian theories.

In 1D, the Hamiltonian of a spin-1/2 representation of discretized quantum electrodynamics is given by [179]

$$\hat{H} = -J\sum_j \left(\hat{\psi}_j^\dagger \hat{U}_{j,j+1}\hat{\psi}_{j+1} + h.c.\right) + m\sum_j (-1)^j \hat{\psi}_j^\dagger \hat{\psi}_j + \tau \sum_j \hat{E}_{j,j+1}, \tag{1.60}$$

where $\hat{\psi}_j^\dagger$ is the creation operator for a fermion of mass m on lattice site j, $\hat{U}_{j,j+1}$ is the parallel transport operator, rendering nearest-neighbor tunnelling gauge invariant, $\hat{E}_{j,j+1}$ the electric field operator, and τ the background electric field energy. Here, we use the common choice of a staggered mass, i.e., in an alternating fashion the charge at a matter site is thought of as positive or negative, corresponding to the notion of positrons and electrons, whose interactions are mediated by field sites [180, 181]. This allows us to define the gauge symmetry operator

$$G_j = E_{j,j+1} - E_{j-1,j} - q_j \tag{1.61}$$

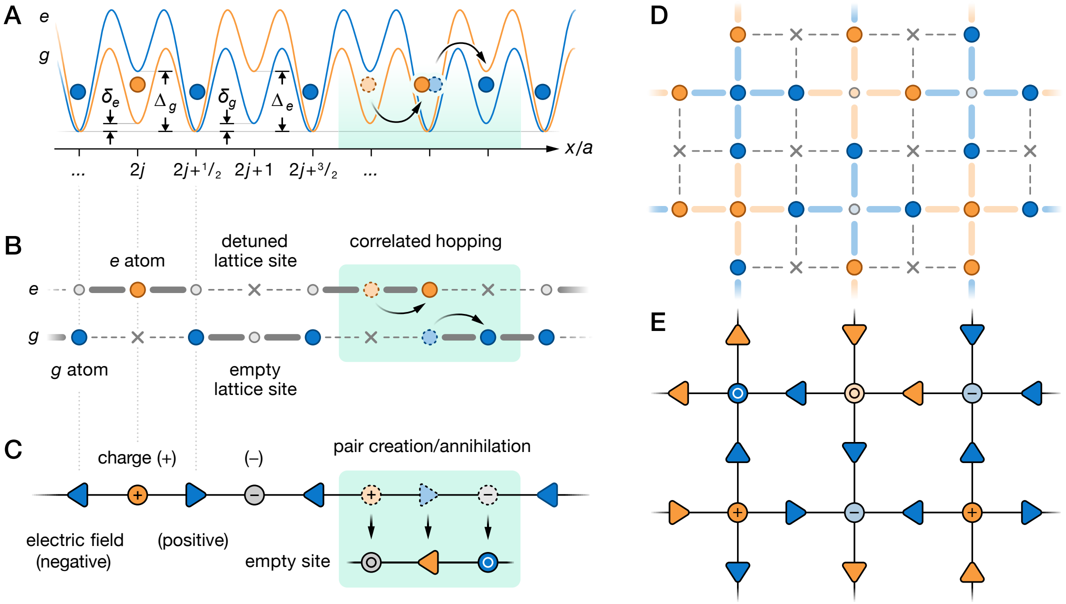

Figure 1.6 | Quantum simulation of lattice gauge theories with AEL atoms. **A** In a state-dependent staggered triple-well potential atoms in the ground (blue) and clock state (orange) are only free to move in a correlated manner (depicted in green shaded area) as single particle hopping is tuned out of resonance by selecting an appropriate depth of the center wells. **B** Abstracted potential geometry for the two states. Solid grey lines indicate that correlated hopping is possible, while the lattice sites indicated with a cross are far detuned to prevent tunneling (dashed line). **C** Mapping onto a U(1) quantum link model. Atoms on the center well correspond to matter with positive charge (*e*) or vacua (*g*) while the absence implies a vacuum in the former and an electron in the latter case. The lattice sites in between represent electric fields, whose directions depend on the orbital state as well as the position within the four-site unit cell, ensuring local gauge invariance. Correlated hopping of an *e*-*g* pair thus simulates the pair creation or annihilation dynamics. **D** This model can also be extended to 2D, where an atom in a given state can access five different sites arranged in cross shape, indicated by light blue and orange bars denoting the hopping bonds. Again, the potentials for *e* and *g* are shifted by two sites. Tunneling from link sides is only allowed in exactly two directions, such that the ninth lattice site per cluster is detuned for both states (grey cross). **E** The corresponding representation in the quantum link model is analogous to the 1D case. To enhance the visibility empty matter sites are also faintly color-coded. The figure is adapted with permission from [179].

with the charge $q_j = \psi_j^\dagger \psi_j - (1-(-1)^j)/2$ and $E_{j,j+1}\,|\psi\rangle = \pm 1/2$, which is equivalent to Gauss's law for $G_j\,|\psi\rangle = 0$. Hence, this relation needs to be fulfilled throughout the whole chain. It can be shown that this Hamiltonian can be realized by a Hubbard-like model for spin-polarized fermionic atoms in two different orbital states acting as different species in a state-dependent superlattice with an effective triple-well geometry for each state, which is shifted by two lattice sites for the $|e\rangle$ atoms with respect to $|g\rangle$ [179]. This mapping is schematically depicted in Fig. 1.6 A-C. We note that small energy offsets δ_{g} and δ_{e} suppress resonant single-particle hopping, and a large energy penalty Δ on every fourth site restricts the motion of a single atom to the triple-well system. The lattice sites available to both states then correspond to field sites, while the matter sites for electrons and positrons are available to only ground- and clock-state atoms, respectively. An atom in $|e\rangle$ on its matter site can then be thought of as a positive charge, and $|g\rangle$ atoms on the adjacent field sites can be mapped onto a negative (left) and positive (right) electric field pointing away from the positron. An empty lattice site at the center well for the ground state then corresponds to a negative charge, such that the positive electric field is terminated. Since all lower-order tunnelling processes are detuned, the fermionic statistics prevent the double occupation of sites with identical atoms, and an e-g double occupancy is penalized by the on-site interaction, the dominant dynamics in this model are correlated hopping events, where adjacent atoms in $|g\rangle$ and $|e\rangle$ tunnel in the same direction to their neighboring sites. This process can be understood as the creation or annihilation of electron-positron pairs and is the simplest example of a time evolution in such a gauge theory. From a technical perspective, this model can be implemented in various ways, but they resemble each other in that a superposition of a clock-magic lattice and state-dependent optical tweezers is necessary. One potential realization makes use of a retro-reflected lattice, where every second lattice site is strongly detuned for one of the two states by means of a tweezer close to, but not right at a tune-out wavelength for the other state. A second implementation is based on a superlattice with a vanishing relative phase between the short and the long sublattice, providing the staggered potential, while the tweezers are utilized to alternatingly deepen the shallow sites for g and e atoms. While superlattices have become a common tool in quantum gas experiments [38, 90, 182, 183], their combination with tweezers would be unique. We further note that all schemes require single-site resolution to read out the final occupation in the lattice.

A great advantage of this scheme is the ability to generalize it to (2+1)D. The simplest extension to two dimensions demands for an underlying lattice structure consisting of large plaquettes with four lattice sites per unit cell to realize matter vortices connected by field links, which hence resembles a Lieb lattice. This can be formed by the superposition of two orthogonal superlattices [184], or by overlapping a square lattice with additional tunable potentials [185]. However, in the case that the Lieb lattice potential needs to be state-insensitive, all involved wavelengths are required to be magic. In the former case, this would entail the usage of two monochromatic superlattices formed by retro-reflected short-wavelength lattices in combination with two additional beams that interfere at an angle of $2\theta = 60°$ to form a long-wavelength lattice with a spacing of λ. In total, this would involve twelve horizontal lattice beams spaced by 30° (Fig. 1.7 A). The latter would require a third tweezer potential, where both 759 nm and 459 nm light could be used. The experimental apparatus is designed such that both options are feasible, which necessitated amongst others a large-aperture design of the glass cell and the magnetic coils. A simpler but far more easily realizable approach is the usage of a *quasi*-Lieb lattice structure, which exhibits an additional lattice site in the center of the large cell, whose occupation however is strongly suppressed by the application of a tweezer (Fig 1.7 D). Such a lattice structure can be formed by a partial four-fold interference, with a diagonal lattice beam polarization that causes a superposition of the simple cubic lattice with a lattice constant $a = \lambda/2$ with the diagonal lattice with $a = \lambda/\sqrt{2}$ [186], as depicted in Fig. 1.7 B-C. This also adds to the range of tunable lattices geometries that can be realized with a bipartite lattice as described in [185].

However, for the 2D extension of the LGT ansatz denoted in [179] we require state-independent lattice wells at the link sites around the matter vertices, which in turn are supposed to be state-selective (Fig. 1.6 B). In the case of repulsive tune-out wavelengths, one can thus tune

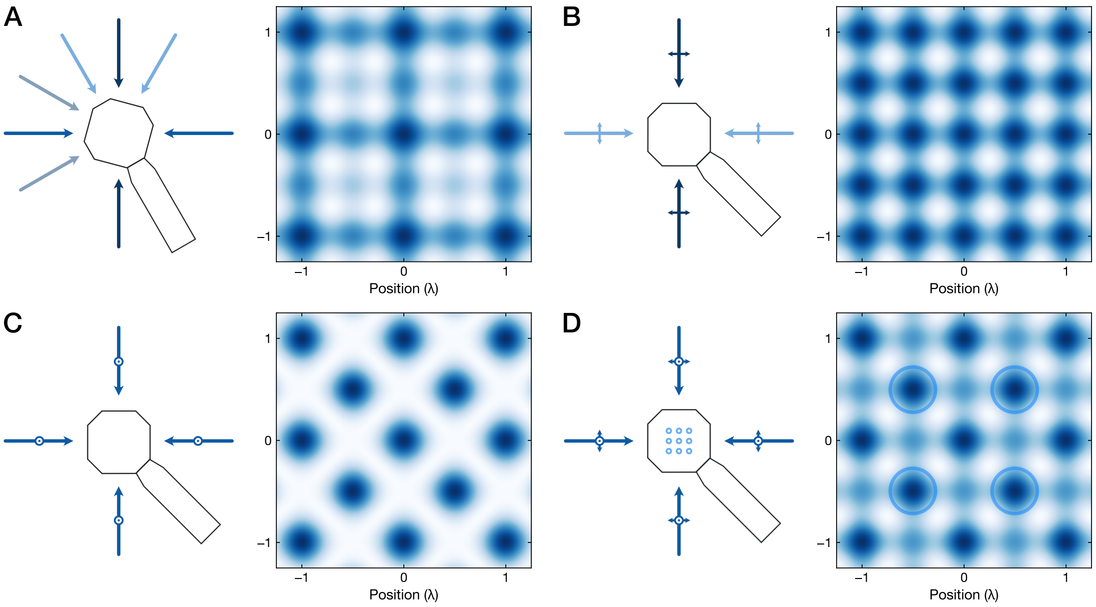

Figure 1.7 | **Realization of a magic Lieb lattice**. **A** A monochromatic Lieb lattice can be generated by the superposition of four different sublattices, two of which are retro-reflected and two are interfering under a steep angle of $2\vartheta = 60°$. Beams of the same color exhibit the same frequency and polarization and thus interfere. Dark blue colors represent a deep lattice potential, whereas a vanishing potential is depicted as white. **B** In contrast, two individual retro-reflected, mutually non-interfering beams generate a simple cubic lattice. This can either be realized by offsetting their frequency or by selecting their polarization to horizontal (depicted as small arrows). **C** Once the four beams are made to interfere, which requires their polarization to be vertical, the lattice geometry shifts to a diagonal shape with a $\sin^4$ profile, such that the new lattice constant is larger by a factor of $\sqrt{2}$ compared to the simple cubic case. **D** Choosing a polarization angle in between leads to a superposition of the lattices in **B** and **C**. This can be used to generate a Lieb-lattice-like structure if additional tweezers (depicted as light blue circles) offset the lattice well in the center of each plaquette to prevent tunnelling to this site. For the potential illustrated here we admix 1/4 of the diagonal lattice, corresponding to a polarization angle of 30°.

the deep vertex sites into resonance for the desired state by applying a correspondingly strong tune-out tweezer. Since the suitable tune-out wavelenths in Yb are attractive, a significantly larger number of tweezers would be required to realize the necessary potential. Therefore, the Lieb lattice structure is not the ideal geometry for our underlying magic lattice, and instead the combination of the simple cubic and diagonal lattice appears to be more suitable (Fig. 1.8 A). While the relative depths of deep and shallow wells can be tuned by adjusting the polarization ϑ of the lattice beams, the desired state-dependent potentials at the matter sites are realized by a pattern of g and e tune-out tweezers at every eighth lattice site, respectively. This relatively low density of tweezers ensures a sufficiently large spacing of $d = \sqrt{2} \times 759\,\mathrm{nm} = 1074\,\mathrm{nm}$ to prevent the typical loss effects related to beating of adjacent tweezers with a spacing well below $\simeq 1\,\mu\mathrm{m}$ [74]. We note that the lattice can be generated in two different ways: In a setup analogous to the 2D lattice described in Chapter 2.6.2 one can use two phase-locked beams at the same frequency and retro-reflect them at individual mirrors. The four beams

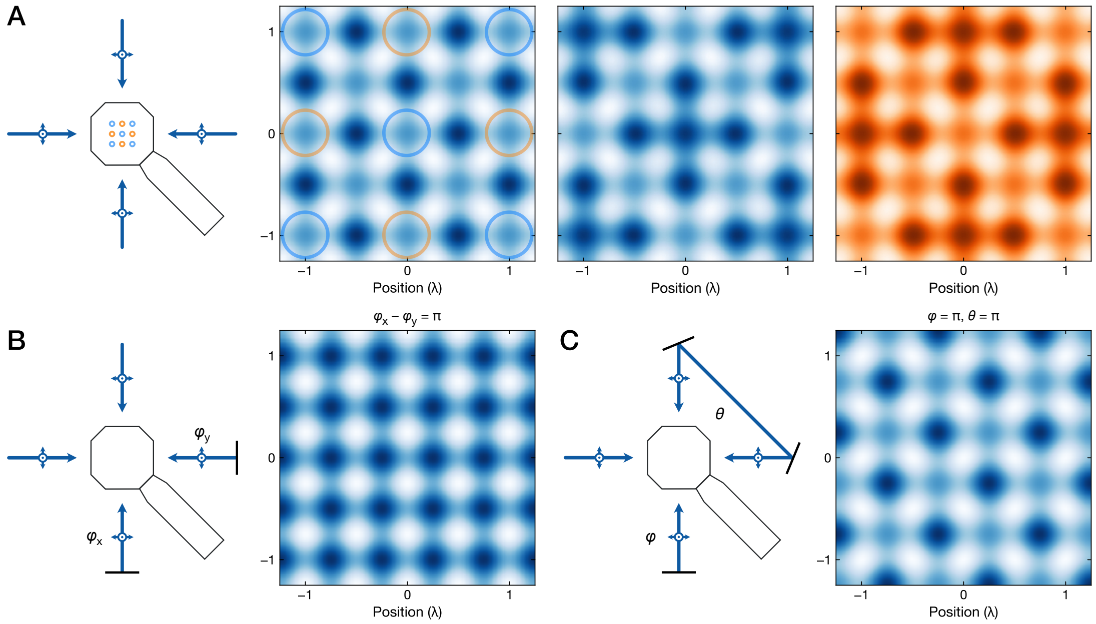

Figure 1.8 | Potentials for a 2D LGT simulation. **A** Using the lattice geometry with a partial four-fold interference, we can realize the necessary potential geometry for the 2D simulation as in Fig. 1.6 D-E by adding tune-out-wavelength tweezers at the vertices (blue: *g* tune-out, orange: *e* tune-out). The resulting lattice structures for the ground (blue) and clock state (orange) are depicted on the right, assuming diffraction-limited tune-out tweezers at the corresponding wavelengths 577 nm for the *g* and 553 nm for the *e* potential. The accessible landscape for each state takes the form of a four-legged cross with a small adjustable detuning δ_g between the vertex and the links. The detuned adjacent vertices are only accessible for atoms in the clock state. **B** While the bipartite lattice can be generated also with two retro-reflected beams, the relative phase $\varphi_x - \varphi_y$ between the two lattice arms is not intrinsically stable and can drift, such that the lattice is deformed. For a relative phase difference of π this leads to a simple cubic lattice instead. **C** With a bow-tie geometry, the two sublattices are topologically stable and only translate upon phase changes.

propagating with wavevectors of $\mathbf{k}_x$, $-\mathbf{k}_x$, $\mathbf{k}_y$, and $-\mathbf{k}_y$, respectively, where $\mathbf{k}_{x,y} = 2\pi/\lambda \hat{e}_{x,y}$, then lead to an intensity profile given by

$$\begin{aligned} I(x,y) = {} & \left(|E_1 e^{ik_x x} + E_2 e^{-ik_x x + i\varphi_x}|^2 + |E_3 e^{ik_y y} + E_4 e^{-ik_y y + i\varphi_y}|^2\right) \cos^2\vartheta \\ & + |E_1 e^{ik_x x} + E_2 e^{-ik_x x + i\varphi_x} + E_3 e^{ik_y y} + E_4 e^{-ik_y y + i\varphi_y}|^2 \sin^2\vartheta, \end{aligned} \tag{1.62}$$

where the relative phases along x and y are determined by the distance $d_{x,y}$ to their retro-reflecting mirrors, $\varphi_{x,y} = 2 d_{x,y} k_{x,y}$. Since these two phases are not coupled, their difference is *a priori* variable and therefore subject to drifts if not actively stabilized. For a relative phase of $\varphi_x - \varphi_y = 0$, this generates exactly the desired lattice. However, for any other phase difference the four-fold-interference sublattice generated by the vertical polarization component is deformed while the cubic lattice experiences a mere shift of its position, such that the total lattice geometry changes up to the extreme case of $\varphi_x - \varphi_y = \pi$, where we instead obtain a simple cubic lattice (Fig. 1.8 B). This is contrasted by the case of a bow-tie lattice, where the relevant phases are the distance from the center to the sole retro-reflecting mirror and back, $\varphi = 2dk$, and the phase from the diagonal propagation $\tilde{d}$, $\theta = \tilde{d}k$ (Fig. 1.8 C). The resulting intensity pattern is therefore

$$\begin{aligned} I(x,y) = \big(&|E_1 e^{ik_\mathrm{x}x} + E_2 e^{-ik_\mathrm{x}x+i\varphi+2i\theta}|^2 + |E_3 e^{ik_\mathrm{y}y+i\theta} + E_4 e^{-ik_\mathrm{y}y+i\varphi+i\theta}|^2\big)\cos^2\vartheta \\ &+ |E_1 e^{ik_\mathrm{x}x} + E_2 e^{-ik_\mathrm{x}x+i\varphi+2i\theta} + E_3 e^{ik_\mathrm{y}y+i\theta} + E_4 e^{-ik_\mathrm{y}y+i\varphi+i\theta}|^2 \sin^2\vartheta, \end{aligned} \tag{1.63}$$

and we notice that the relative phases of the diagonal sublattice along the diagonal axes $(\hat{e}_\mathrm{x} \pm \hat{e}_\mathrm{y})/\sqrt{2}$ are $\theta/2$ and $\theta/2 + \varphi/2$. Hence, the shape of both lattice components is topologically preserved and instead only the global position is changed upon variations in φ and θ [185–187]. Notably, this phase-change-induced translation will in general be independent of tweezer array shifts, which are mainly governed by the mechanical motion of the objective. To provide a stable superposition of the tweezer arrays onto the lattice potential, it is therefore imperative to achieve a highly passively stable system with relative drifts of $\ll a$ on timescales of several minutes to hours to prevent permanent mismatches [65, 82].

Eventually, this model is also extendable to simulate non-Abelian gauge theories such as quantum chromodynamics [188, 189]. Here, one can make use of the SU(N)-symmetric interactions in ^{171}Yb and in particular in ^{173}Yb that allow for a synthetic spin dimension that can simulate different spins in a spin-1/2 system, corresponding to U(1) × SU(2), or colors (U(1) × SU(3)) [106, 116]. To this end, we have to generalize the notion of Gauss's law to a conservation of particles on a link, also denoted as rishons [190]. We further have to impose a total spin singlet condition for all particles surrounding a vertex, corresponding to the triple wells in the 1D case. This is trivially satisfied for the SU(1) model described above using spin-polarized spins, but requires states of the kind $|\uparrow\downarrow\rangle - |\downarrow\uparrow\rangle$ or $|\mathrm{rgb}\rangle - |\mathrm{grb}\rangle + |\mathrm{gbr}\rangle + \ldots$ for SU(2)- and SU(3)-symmetric simulations. Thus, it is crucial to suppress spin-changing collisions between $|\mathrm{g}\rangle$ and $|e\rangle$ as they would violate the gauge invariance. Suppressing this exchange interaction is likely possible by applying a magnetic field that splits the m_F states differently for the two orbital states (Chapter 1.1.2), which detunes this interaction channel out of resonance. An indispensable precondition in this case is the ability to image the atoms in a spin-resolved fashion, which is discussed in Chapter 3. One can further allow for multiple particles per site in 2- or 3-rishon models, which would however suffer from prohibitively fast inelastic e-e losses without any further precautions. Instead, the usage of Rydberg dressing could lead to the desired interactions within multiple rishons [189, 191]. With such a setup, obvious goals are the studies of confinement in 2D and thermalization dynamics, but even the controlled breaking of gauge invariance by, e.g., the removal of atoms on matter sites, equaling the loss of a quark in a baryon, might entail very interesting insights into quantum chromodynamics and its limitations.

CHAPTER 2

Experimental design

At the initiation of the laboratory, several experiments had already demonstrated cooling of ytterbium atoms down to quantum degeneracy [145, 192–197] and shown the possiblity of single-site resolution in optical lattices [80, 198] and tweezers [151]. Therefore, this experiment leverages the experiences and developments of these preceding machines in many ways. At the same time, the combination of optical lattices and tweezers is still comparably unique, with just three other experiments that have demonstrated this conjunction so far [62, 65, 76]. This technique simultaneously allows for and necessitates some deviations from the classical experimental design on the levels of the vacuum chamber, the experimental setup, and the steps within the sequence to reach a cold atomic cloud inside a trap. In this Chapter, we describe the details of these considerations and designs, starting with the vacuum chamber and the magnetic coils. We then introduce the laser and main experimental setups, followed by a discussion of the experimental sequences and designs for loading the 3D MOT, optical lattices, or tweezers.

2.1 Vacuum chamber

An inevitable necessity for ultracold atom experiments is the isolation from the room-temperature environment and a low background gas scattering rate. Both are achieved by reaching a very high vacuum with pressures $\simeq 3 \times 10^{-11}$ mbar in the glass cell where the experiments are conducted. At these pressures, the vacuum lifetime typically exceeds a minute and the system is decoupled from the environment up to interactions with electromagnetic fields like the Earth's magnetic field, whose compensation is discussed in Chapter 2.2.3, or black-body radiation effects[1]. Furthermore, it is beneficial to ensure that the atomic flux is terminated once the MOT loading step is completed, since otherwise the directed atom beam will scatter off the trapped atoms and decrease their lifetime [116].

In our experiment, the vacuum chamber is separated into three main parts: The atom source, which provides a collimated atomic beam, the science chamber containing large

---

[1] To this end, a first generation of experiments is testing cryogenic systems to decrease the background scattering rate, which can extend the vacuum lifetime to even tens of minutes [199], and to reduce the sizeable contribution to the current systematic error in lattice clock experiments from the black-body shift. However, heat-shield coating with hydrogen seems to limit the cooling effect to last only a few days in some setups [31].

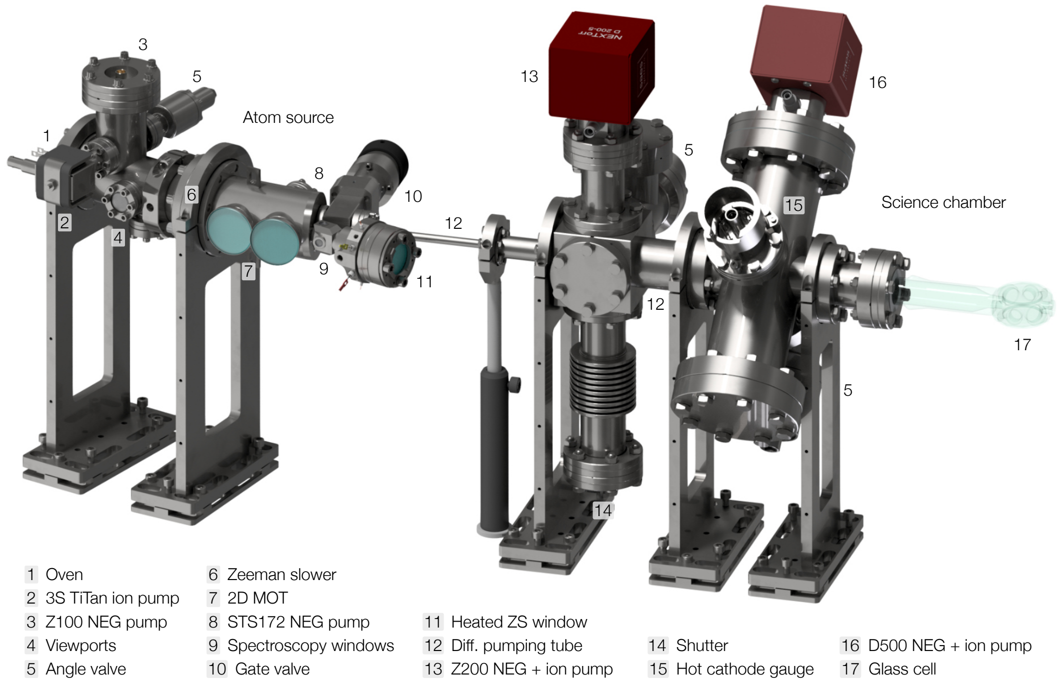

Figure 2.1 | CAD render of the vacuum chamber. While the separation of the atom source from the UHV main chamber via the differential pumping tube is clearly visible, the second tube is hidden in the part between the cube and the cross. Both NEG and ion pumps yield sufficient pumping rates for the respective gases in each section, and angle valves – placed on the far side in the orientation of this image – allow for effective diffusion to the turbo-molecular pump during the bake-out. The contiguous hot cathode gauge provides an approximate measure of the pressure inside the glass cell. As a strain relief, a short bellow is placed between the tube from the atom source and the cube, here depicted as a simple tube. The shutter is displayed in its closed position, while it typically remains open in the experiment, held in position by a bistable pneumatic actuator.

vacuum pumps and pressure gauges, and the glass cell (Fig. 2.1). Each of these sections will be discussed in the following.

2.1.1 Atom source

To eject atoms from a reservoir, either ovens or dispensers have been applied in quantum gas experiments. For Yb, the best combination to provide a pre-cooled atomic beam found so far is an oven followed by a Zeeman slower section. In the oven, typically a few grams of solid ytterbium are heated up to temperatures of $\gtrsim 380$ ℃ where atoms start to effuse from the solid state. Compared to alkali-metal elements like Rb, Na, or Cs, this is a rather high temperature, owing to the low vapor pressure of $\simeq 10^{-3}$ mbar at 400 ℃ [200], but still easily achievable with standard heating wires and temperature controllers. However, this results in a velocity distribution peaked at $\simeq 300\,\mathrm{m/s}$ for a typical operating temperature of 420 ℃ and thus necessicates slowing sections to efficiently load atoms into a MOT.

In our experimental apparatus, the oven as well as a Zeeman slower and a 2D MOT are realized within a commercial atomic beam source.[2] This system is designed to work as a compact, independent vacuum chamber, which only requires appropriately shaped and polarized beams for the Zeeman slower and the 2D MOT as well as a temperature control loop for the oven and a heated window once it is connected to the main science chamber. As the details of the mechanical design are proprietary, only a rough overview of the working principle can be outlined.

The atom source can be divided into four main sections: the oven, the Zeeman slower, the 2D MOT, and a differential pumping tube. In the oven section, the Yb reservoir is heated by a thermal resistor, whose current and hence its temperature is controlled via a PID feedback loop. Adjacent to the oven, an array of 13 mm long capillaries with a diameter of 210 μm serves the purpose of selecting and collimating atoms that are leaving the oven to provide a roughly collinear flow of atoms. At an operating temperature of 420 ℃, the manufacturer measured an initial flux of $\Phi \simeq 6 \times 10^{12}$ atoms/s after the capillaries. Unfortunately, this component exhibited major design flaws, which is why the oven had to be swapped twice within less than 30 months of operation. In the original oven that was part of the delivered atom source as well as in the second oven, a material was used for the capillaries that can react with Yb, which led to clogging of the nozzle in both cases after a few months of operation, leading to a strongly reduced flux.[3] In the first oven, the Yb reservoir further contained a significant amount of hydrogen which was at first believed to be responsible for the clogging as Yb and H_2 quickly react to YbH_2 above 400 ℃ and could therefore form growing compounds on the capillary walls. Hence, the two latest ovens that were used for the majority of the 3D lattice work described in Chapter 3.2 have undergone a degassing procedure to deplete the Yb reservoir from H_2. However, as the second oven also suffered from clogging, in the most recently installed oven the nozzles are made out of the same material that was used for the reservoir, which did not show signs of degradation or reaction with Yb in any oven model so far.

The capillaries are followed by heat shields and the Zeeman slower section, with a few centimeters of free flight in between which can be used for initial absorption spectroscopy measurements through adjacent viewports to determine the oven flux. Due to direct line of sight to the nozzle, these viewports end up being coated with Yb after a few weeks of normal operation and typically do not allow for further spectroscopy measurements anymore. Furthermore, a small 3 L/s ion pump,[4] a 100 L/s non-evaporable getter (NEG) pump,[5] and an angle valve are installed in promixity to the oven. The magnetic field for the Zeeman slower is generated by permanent magnets, which allows this section to extend over a distance of just a few centimeters. Once the atoms are slowed down, they reach the 2D MOT. This section contains a 5 L/s NEG pump[6] and two identical but slightly angled arrays of mirrors and waveplates. These arrays use a single beam each to achieve a reduction of the transverse temperature close to the Doppler temperature of $T = 3\,\mathrm{mK} \simeq 4\, T_\mathrm{D}$ as well as a deflection of the atomic beam by a total of 20° (Fig. 2.5). To this end, the 2D MOT not only produces a collimated atomic beam but also serves as an optical shutter, since only with activated 2D MOT

---

[2] *AOSense Beam-RevC-Yb*

[3] In a diagnosis by the manufacturer, the defective oven nozzles were described to "crumble apart" despite reports that it should be inert to Yb.

[4] *Gamma Vacuum 3S TiTan*

[5] *SAES NEXTorr Z100*

[6] *SAES STS172*

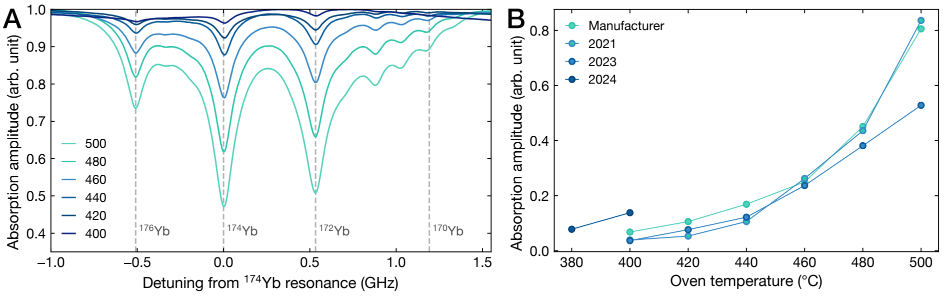

Figure 2.2 | Absorption spectroscopy of the commercial oven. **A** Absorption spectra on the $^1P_1$ transition for various temperatures, after the first oven swap in 2023. We use an intensity of $I \simeq 0.05\, I_{\mathrm{sat}}$ to not saturate the transitions. While the four most abundant bosonic isotopes are clearly visible, the fermionic transitions are suppressed and obfuscated for the chosen polarization. **B** Absorption amplitude of the ^{174}Yb transition dip as a function of temperature for all three ovens after the respective bake-outs. While the first two ovens show the onset of absorption only past 400 ℃, in agreement with measurements performed at the manufacturer before shipping, the latest oven exhibits an increase of flux by a factor of $\simeq 4$, which now allows us to run the oven at 380 ℃ instead of 420 ℃ as before. For fear of shortening the oven lifetime the oven flux was tested only up to 400 ℃ for this newest oven.

beams the atoms can reach the main chamber. Undeflected atoms, however, travel towards the Zeeman slower window. To prevent this window from getting coated with a reflective ytterbium layer, a heated, anti-reflection-coated sapphire window is placed in front of the viewport itself. The temperature of this hot window is chosen such that the effusion rate exceeds the atomic beam flux at least by a factor of 10, which corresponds to temperatures of 330 ℃ for oven temperatures of 420 ℃. Atoms that are impinging on the Sapphire window therefore do not adhere to it, ensuring a lasting operation of the Zeeman slower. Before they reach the heated window, undeflected atoms fly past three orthogonal, $\simeq 4$ mm large windows which are meant to be used for continuous absorption spectroscopy measurements. The corresponding signal can then be utilized to, e.g., lock the laser at 398.9 nm onto the atomic resonance, or to monitor the oven flux. Unfortunately, when the first oven started clogging, these windows became highly reflective, likely due to coating with Yb. According to the manufacturer, the spectroscopy windows are designed to have no direct line of sight either with the oven or the heated Zeeman slower window and therefore should not get coated under any circumstance. In other experiments, however, it has been observed that clogged capillaries can lead to erratic trajectories [201], although the exact process remains unclear as the distance between oven and spectroscopy windows is substantial.

In case the atoms get deflected by the 2D MOT beams, they first pass a gate valve, followed by a 108 mm long and 6 mm wide differential pumping tube. The gate valve is essential for the purpose of keeping the ultrahigh vacuum in the main chamber while the oven is swapped, such that only the atom source needs to be baked afterwards. The differential pumping tube, on the other hand, provides a pressure gradient between the science chamber and the atom source. This is crucial as the pressure measured by the ion pump next to the oven usually exceeds 1×10^{-9} mbar when the oven is running.

2.1.2 Science chamber

The atom source is attached to the ultra-high vacuum (UHV) chamber via a short con-flat (CF) 16 bellow to prevent stress on the atom source's tube flange. The main science chamber itself consists of two segments, a CF40 cube and a CF40/CF63 cross, separated by another 6 mm wide and 53 mm long differential pumping tube. This ensures a consistently low pressure in the glass cell, as we observe only minimal pressure changes of $\delta p \simeq 0.5 \times 10^{-11}$ mbar in the second segment despite pressure increases by two orders of magnitude in the atom source. The pressure is measured by a hot cathode pressure gauge, which is positioned next to a 500 L/s NEG and ion combination pump[7] and an angle valve. To provide high pumping rates during baking, a second angle valve is installed in the first segment, together with a 200 L/s NEG-ion combination pump.[8] Furthermore, a mechanical shutter, consisting of a long strut mounted at the bottom of a long flexible bellow, is attached to the cube. The shutter can be actuated pneumatically and was designed to serve as an additional atomic beam block in case the deactivated 2D MOT would not provide a sufficient suppression of the atomic beam flux. However, the vacuum-limited lifetime of $\tau = 250(30)$ s measured in the 3D lattice discussed in Chapter 2.6.4 indicates that this does not pose a problem and thus the shutter is constantly held in the opened position. Notably, this lifetime is on par with other quantum gas experiments reporting pressures of 1×10^{-11} mbar [116, 202–204], which indicates that the pressure of $p \simeq 3 \times 10^{-11}$ mbar measured by the hot cathode gauge is overestimated. In the long-term pressure graph, an overall clearly visible trend towards lower pressures can be observed, only interrupted by the pressure increases due to the oven swaps and modulated by the oven temperature. For a more in-depth discussion of the pressure limitations in our setup and details on the bake-out procedure we refer to [205].

2.1.3 Glass cell

Optical access is a valuable asset in quantum gas microscopes and optical tweezer experiments. To reach large numerical apertures, microscope objectives have to feature a large meniscus lens and typically need to be placed very close to the vacuum window, thus obstructing a large solid angle for beams that cannot be sent through the objective. Likewise, the optics necessary to generate deep optical lattices are preferably placed close to the atoms for various reasons, most relevantly to enhance the passive mechanical stability and to minimize the effect of inevitable local temperature variations, as discussed in detail in Chapter 2.6.4. Simultaneously, while the 3D MOT optics can be placed far from the atoms, the capture velocity and thus the trap's efficacy depends on the beam sizes as outlined in Chapter 2.5. Less stringent requirements have to be met in general for the remaining beams which are used for cooling or addressing of specific transitions. However, implementing this multitude of beams poses a major challenge. A more traditional approach to circumvent the concomitance of 3D MOT and optical traps is to spatially separate the two stages and transport the atoms from the MOT chamber to the glass cell [202, 206, 207]. This, however, greatly adds to the overall complexity of the experiment, reduces the efficiency due to imperfect transport, and increases the cycle time.

---

[7] *SAES NEXTorr D500-5*

[8] *SAES NEXTorr Z200*

In order to keep the experimental apparatus as simple and compact as possible and to enable cycle times of 100 ms, the glass cell's optical access is optimized to allow for a single-chamber design, entailing that no atom transport is required as the MOT is overlapped with the lattices and tweezers. This is achieved with an octagonal cross section and two alternating edge lengths with a relative ratio of 5:3. The glass cell frame offers eight horizontal bores with sizes of 16.1 mm and 11 mm, corresponding to opening angles of 24° and 32°, and 35 mm large vertical bores. Onto these bores UV-grade fused-silica windows[9] with a nano-textured broadband anti-reflectivity (AR) coating are fused.[10] The horizontal windows exhibit diameters of 19.5 mm and 14.5 mm at a thickness of 3.2 mm, while the top and bottom windows are stepped with an inner (outer) diameter of 34 mm (44 mm), a thickness of 3 mm of the protruding ring, and an overall thickness of 6 mm. This step is key to a minimal overall height of the glass cell of 26 mm, rendering a moderate objective working distance of 14 mm possible, while retaining a sufficient thickness to prevent bending due to the pressure difference of 1 bar. This cambering effect was simulated by means of a finite-element analysis for different window sizes and proportions, yielding an optimal compromise for the values mentioned above. While the calculated bending radii of 320 m and 400 m for the outer and inner surface, respectively, are not negligible, this effect is expected to be radially symmetric and therefore only appears as a small spherical aberration in the overall imaging performance, which can be compensated well. In contrast, if the specified window flatness of $< 1/10\,\lambda$ and parallelism of < 5 arcsec were not met, this would visibly compromise the imaging quality, as discussed in Chapter 2.7.

One of the goals during the conception of the glass cell design was to allow for twelve beams spaced by 30°, which is necessary to create a 2D monochromatic superlattice. This could have also been achieved with a rectangular cell, likely the most common type of glass cell used in recent ultracold atom experiments. However, owing to the complex contacting process for such cells, the choice of AR coatings is limited, and in most cases no AR coating is used at all, which can lead to very strong reflections, in particular for shallow-angled beams. Contacting windows with treated surfaces onto a glass frame, on the other hand, is viable, which thus facilitates a significantly more power-efficient setup. The nano-structure AR coating we chose uses a randomly etched moth-eye-like structure to provide very low reflectivities over a large range of wavelengths – the two-surface reflectivity was measured by the manufacturer to be $< 0.7\%$ for light at $400 - 1100$ nm and $< 0.5\%$ at 1389 nm for the horizontal windows[11] and $< 0.12\%$ from 400 to 850 nm for the stepped vertical ones,[12] measured at 0° angle of incidence (AOI). At selected wavelengths we were able to reproduce this performance, and even for non-zero AOIs the reflectivity appears to remain very low. The measured loss of $\simeq 2\%$ at 553 nm after four surfaces as part of determining the clock-state polarizability at the ground-state tune-out wavelength (Chapter 4.2) is therefore attributed to absorption in the fused silica bulk.

Upon attaching the glass cell to the vacuum chamber, great care was taken in ensuring a parallel alignment of the glass cell to the surface of the optical table. Two beams, one from the top and one from the front, were used to send the weak glass cell reflection back

---

[9] *Laser Components PP1724UV-S, PP0612UV, PP0712UV, custom design*

[10] *Precision Glassblowing, custom design*

[11] *TelAztec RAR-L2*

[12] *TelAztec RAR-L*

to itself, with a beam path long enough to provide a resolution of $\lesssim 1\,\mathrm{mrad}$. Despite this careful alignment, a later reproduction of this measurement after more than a year yielded a deviation of $2\,\mathrm{mrad}$ along the tubing direction, which could stem from a slow relaxation or set of the flange connection.

2.2 Magnetic coils

Controllable magnetic fields constitute the second essential ingredient for a cold atom experiment. In particular, they are required for generating a quadrupole field for the 3D MOT, for nulling out the Earth's magnetic field and other stray fields, and for producing Helmholtz fields to lift the degeneracy of states with different magnetic quantum numbers or to tune the interaction strength using magnetic Feshbach resonances [40, 136, 137]. In the case of most Alkali-metal atoms one can further use magnetic fields to trap or separate the atoms depending on their m_F state [38, 39], which in general is not possible in Yb due to its heavy weight and the low magnetic moment.

To this end, there are six pairs of coils built into the experiment: The main coils, three perpendicular sets of weak shim coils, additional compensation coils along the vertical direction, and a pair of strong coils along one horizontal direction, referred to as transverse coils.

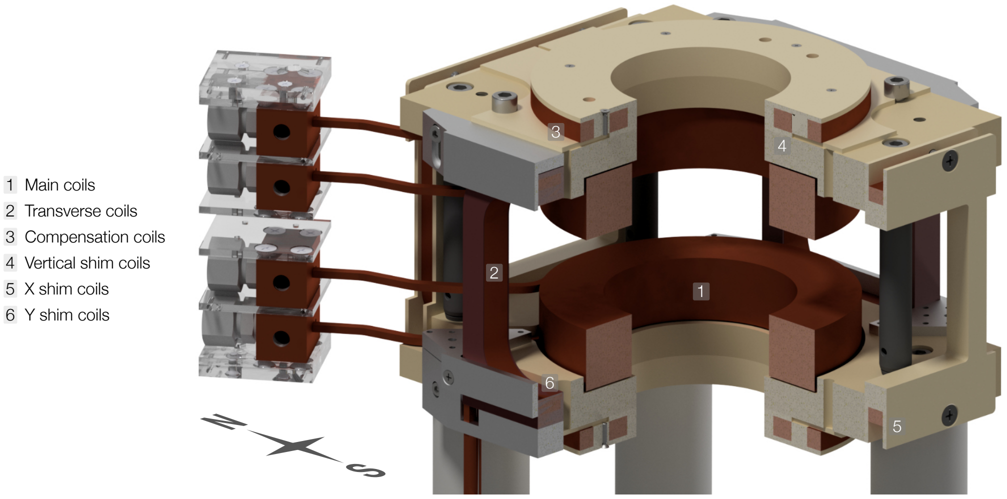

Figure 2.3 | CAD render of the coil mount. The two glass-fiber-enforced plastic plates hold the glued main coils in place and serve as a platform to which the independent mounts for the compensation coils, the vertical and horizontal shim coils, and the transverse coils are attached. The aluminium mounts to hold the latter also contain the independent set of anti-parallel shim coils along this direction. The power and water connections for the hollow-core wires are routed horizontally and almost parallel to the glass cell flange (leaving the coil cage towards the top left of the image, not depicted in this render for clarity) in the case of the main coils, and downwards to the optical table surface for the transverse coils.

2.2.1 Main coils

The main coils' purpose is twofold: First, to provide a strong quadrupole field during the MOT loading and compression, and second, to apply a large, homogeneous B field for clock spectroscopy in ^{174}Yb or separating the m_F states during Raman cooling in ^{171}Yb. The coils are oriented along the vertical direction to allow for maximal optical access in the horizontal plane and are placed as close to the glass cell as possible to maximize the B field that can be achieved. Simultaneously, the distance between the center of the coils of 62.2 mm is only slightly larger than the effective coil radius of 50.4 mm[13] to ensure maximal field strength and uniformity of the field in the Helmholtz configuration. Further, their inner diameter is chosen to allow for the insertion of the high-NA objectives. Ideally, one would also like to send laser beams under a steep angle through the gap between objective and coils. This is mostly relevant for the vertical MOT beams, but could also be used for vertical lattice and cooling beams. Due to the significant diameter of the objective's meniscus lens, the minimum possible incidence angle of such beams would require the coils to be either very thin or have a very large radius, though, and thus prohibit the use of such beams. Instead, the vertical MOT beams pass through the objective, as described in Chapter 2.3.

Another feature to strive for is reaching the orbital Feshbach resonance in ^{171}Yb at 1300 G [144]. This would require coils made out of flat-band wires which are glued onto a water-cooled heatsink as they can be compactly wound [208]. However, in this case, one has to ensure a surface flatness of typically $\lesssim 10\,\mu\mathrm{m}$ to allow for sufficient heat transport to the heatsink and to hereby prevent overheating the coils at large currents. Reaching this by emerizing the respective surfaces of custom commercial coils as initially planned proved to produce shorts as the insulation was partially chipped off, connecting several wires. Instead, the final coils consist of an almost identical pair of hollow-core copper wires with 48 windings, allowing for a brief[14] application of up to 500 G in parallel configuration or a vertical field gradient of up to 130 G/ cm in the anti-Helmholtz configuration where the magnetic field is zero in the center and increases linearly with distance. To generate these fields, currents of up to 70 A must be applied, requiring water cooling through the hollow cores with a hole diameter of 1.6 mm. The coils are glued to a nonmagnetic, high-tensile glass-fiber-enforced plastic mount,[15] connected by nonmagnetic, black anodized aluminium posts. The temperatures are monitored by several thermocouples glued to the coils. Their signals are also fed into the interlock to turn off the coil power supply to prevent overheating.

Switching between anti-Helmholtz and Helmholtz configurations is made possible by MOSFETs in combination with an H bridge. With this circuit we can also shunt the current, ramping down the magnetic field from several hundred to a few G within $\simeq 8$ ms as measured by spectroscopy on the $^1\mathrm{P}_1$ transition. However, due to the finite inductance and eddy currents

---

[13] Taking the arithmetic mean of the inner and outer coil diameter of 37 mm and 63.8 mm as well as the mean of the maximal and minimal distances of the coil surfaces of 87.6 mm and 36.8 mm and treating the coils as infinitely thin provides a sufficiently good approximation of the actual magnetic field. Taking the actual dimensions into account in more complex calculations yields corrections only on the percent level and is thus comparable to manufacturing uncertainties.

[14] For duty cycle times of $\simeq$ 50% at large B fields the required cooling power is significant, and the steady-state temperature passes the threshold of 20 ℃, which gets close to the interlock safety threshold of $\simeq$20.7 ℃.

[15] *EP GC 201*, manufactured by *Erhard Hippe KG*.

in adjacent components it takes $\simeq 50\,\mathrm{ms}$ until the field has completely decayed to below the $^3\mathrm{P}_1$ spectroscopy detection limit. (Fig. 2.4 F). To calibrate the coils, i.e., to determine which field strength is applied at the atom's position at a given current, we employ two different schemes. The first relies on the quadratic Zeeman shift on the $^3\mathrm{P}_0$ transition as discussed in Chapter 1.1.2 which can be spectroscopically interrogated with great precision and yields a calibration factor of 7.595(50) G/A (Fig. 2.4 A). In the second scheme we spectroscopically track the linear Zeeman splitting for the σ^+ and σ^- transitions on the $^3\mathrm{P}_1$ transition, which was determined to be 2.089429(70) MHz/ G [135]. For this purpose, we use a horizontal MOT beam that provides finite projections on the π as well as the $\sigma^\pm$ transitions to simultaneously resolve all three resonances. Since these measurements were performed with $^{174}\mathrm{Yb}$ and in the clock-magic lattice at 759.354 nm, care has to be taken to minimize systematic errors from the differential Stark shift for this transition as well as from state mixing due to a lattice-induced electric field as in Fig. 2.4 B, which was performed in a deep 3D lattice. Therefore, the spectroscopy pulse is applied right after the lattice is fully turned off for 1 ms, after which it is ramped back up again to image the atoms (Fig. 2.4 C). With this method we achieve a comparable calibration factor of 7.41(8) G/A, which is also in agreement with the calculated value of 7.23 G/A and the value of 7.74 G/A obtained with a Hall probe upon testing the coils.

2.2.2 Transverse coils

A second pair of hollow-core wire coils is attached to the side of the coil mount to allow for a versatile application of B fields also in the horizontal direction. This is necessary to be able to, e.g., drive the clock transition with a vertical beam or to apply a strong quantization axis along the magic angles for the $^3\mathrm{P}_1$ transition in $^{171}\mathrm{Yb}$ and $^{174}\mathrm{Yb}$. The coils consist of 9 windings and are rectangular with outer (inner) dimensions of 105.5 mm × 84.5 mm (79.9 mm × 59.8 mm), where the thickness and sizes are chosen such that they do not restrict the optical access. Instead, the coils are placed in the projection of the glass cell frame at a relative distance of 164 mm, i.e., a factor of 366% from the ideal Helmholtz configuration of $d = 0.5445\,a$, where a is the mean edge length of the rectangular coils. However, on the typical experimental length scales of $\lesssim 100\,\mu\mathrm{m}$ the resulting magnetic inhomogeneity is expected to be negligibly small. Water cooling allows for the application of up to 10 A in the horizontal direction, allowing for a maximal magnetic field of $B \simeq 25\,\mathrm{G}$. Again employing the linear Zeeman splitting method on the $^3\mathrm{P}_1$ transition, we obtain a calibration factor of 2.99(11) G/A. Notably, this was measured at moderate fields of up to 2 G without water cooling. This pair of coils is further used to compensate for stray magnetic fields in the east-west direction of the lab; here we found a field of 0.146(10) G to minimize the magnetic field at the atom position by measuring the crossing of the $^3\mathrm{P}_1$ σ^+ and σ^- transitions (Fig. 2.4 D). Interestingly, this direction is the only one that significantly deviates from the expected respective geomagnetic field component of 15 mG, but aligns with the direction of the adjacent optical tables and labs.

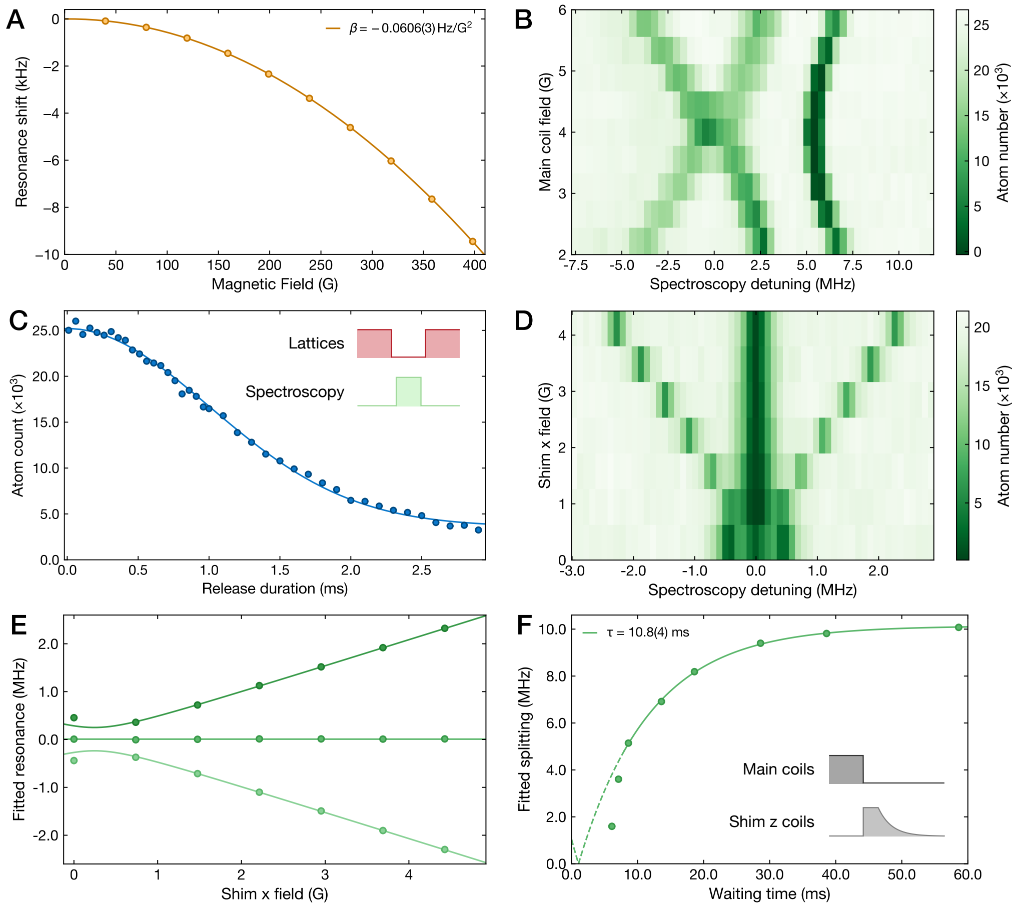

Figure 2.4 | Calibration methods for the magnetic coils. **A** Quadratic Zeeman shift on the $^3\mathrm{P}_0$ transition after calibration of the main coils. **B** Spectroscopy on the $^3\mathrm{P}_1$ transition in a $\simeq 4000\,E_{\mathrm{rec}}$ deep 2D lattice at 759 nm. By applying a 4 G offset field with the vertical shim coils we can scan across the inversion point. Despite a reasonable stray field compensation on the ~100 mG level, the individual resonances do not cross, which is an effect of the significant vertical electromagnetic field induced by the lattice, which mixes the m_J states for small external magnetic fields. **C** We thus perform $^3\mathrm{P}_1$ spectroscopy during a time of flight where the lattice is off, which is selected to be 1 ms. The atom loss during this time is still acceptable to provide spectroscopy signals with a large signal-to-noise ratio. The Gaussian fit serves as a guide to the eye. **D** Lattice-free spectroscopy with horizontal circularly polarized light to resolve the $\pi-$ and both σ-transitions. **E** Fitted resonance positions for the three transitions, using the fit function $\delta(m_{F'}) = m_{F'}\mu\sqrt{B_\perp^2 + (B_\parallel - B_0)^2}$. From the splitting behavior we can extract the calibration factor for the vertical shim field and both longitudinal and transverse residual offset fields. **F** Lingering magnetic field after turning off the main coils, detected via $^3\mathrm{P}_1$ offset spectroscopy. After a fast initial decay within $\simeq 8$ ms a much slower decay sets in, which we compensate by applying a counteracting exponential ramp with the vertical shim coils to suppress the total magnetic field 20 ms after the main coils have been turned off. The solid green line shows an exponential fit after 10 ms waiting time, and its deviation from the experimental data for shorter times is indicated by the dashed line.

2.2.3 Compensation coils

To null out the Earth's vertical magnetic field component and other potential stray fields we use a dedicated, additional pair of coils which is mounted on top of the main coils. Using 50 windings of 1 mm thick copper wire with a mean diameter of 125 mm we can generate 2.92 G/A as again determined via lattice-free $^3P_1$ spectroscopy, and we find the minimal distance between the σ^+ and σ^- transitions to occur at $I_0 = 143(1)\,\mathrm{mA}$ or $B_0 = 0.418(3)\,\mathrm{G}$. This value is in reasonable agreement with the vertical geomagnetic field strength of $B_{\mathrm{geo}} \simeq 0.440\,\mathrm{G}$.

2.2.4 Shim coils

A set of three weak coil pairs are attached to the six sides of the coil mount to be able to steer the position of the compressed MOT – in our case primarily to optimize the transfer of atoms from the MOT into the lattices or tweezers. They can further be used to stray field compensation or to apply a quantization axis in an arbitrary direction. However, the maximum field strength attainable with the horizontal shim coils is limited to $B \simeq 1.3\,\mathrm{G}$, owing to the 1 mm copper wires which are only passively cooled and therefore permit currents up to 2 A until the temperatures strongly increase. In addition, the relative spacing between the coils is 164.4 mm for the pair connected to the transverse coils and 192 mm to the orthogonal one which is significantly larger than the optimal Helmholtz configuration distance for dimensions of 82 mm × 62 mm and 102 mm × 93 mm, respectively. This as well as a restriction of the coils' height to 8 mm, allowing for 23 windings, is necessary to prevent loss of optical access. The vertical shim coil pair is mounted inside the compensation coils with a mean diameter of 90 mm and 35 windings. Calibrating the coils via spectroscopy on the $^3P_1$ transition in time of flight yields 2.46(4) G/A for the vertical shim coils, 0.66(1) G/A for the coils parallel to the transverse coils, and 0.67(1) G/A for the orthogonal horizontal pair. Since there is only one pair of coils along the north-south direction and the lattices and tweezers are located slightly north of the center of the coils, which requires the compressed MOT to be pushed in that direction, it is not possible to compensate for a measured residual field of $B_0 = 0.190(3)\,\mathrm{G}$ in northern direction, in agreement with the corresponding Earth's magnetic field component of $B_{\mathrm{geo}} \simeq 0.210\,\mathrm{G}$. While a later upgrade to the experiment to add a weak compensation coil pair with opposite polarity is feasible, the overall insensitivity of Yb to external magnetic fields does not render this particularly necessary.

2.3 Optical setup

The final main constituent of the experiment is the optical setup around the vacuum chamber, responsible for shaping and directing the various laser beams onto the atoms. Owing to the multitude of beams and wavelengths, almost all lasers and the corresponding laser setups are located on two adjacent optical tables. This does not only provide more space but also isolates the main experimental table from unavoidable mechanical, electric, or magnetic noise from shutters, acousto-optical modulators (AOMs), or Faraday isolators. The main experiment's optical setup is described in the following, whereas the individual laser setups are described in Chapter 2.4.

For the optics around the vacuum chamber two independent breadboards were chosen: a rather compact one for the Zeeman slowing and 2D MOT optics on one side of the atom

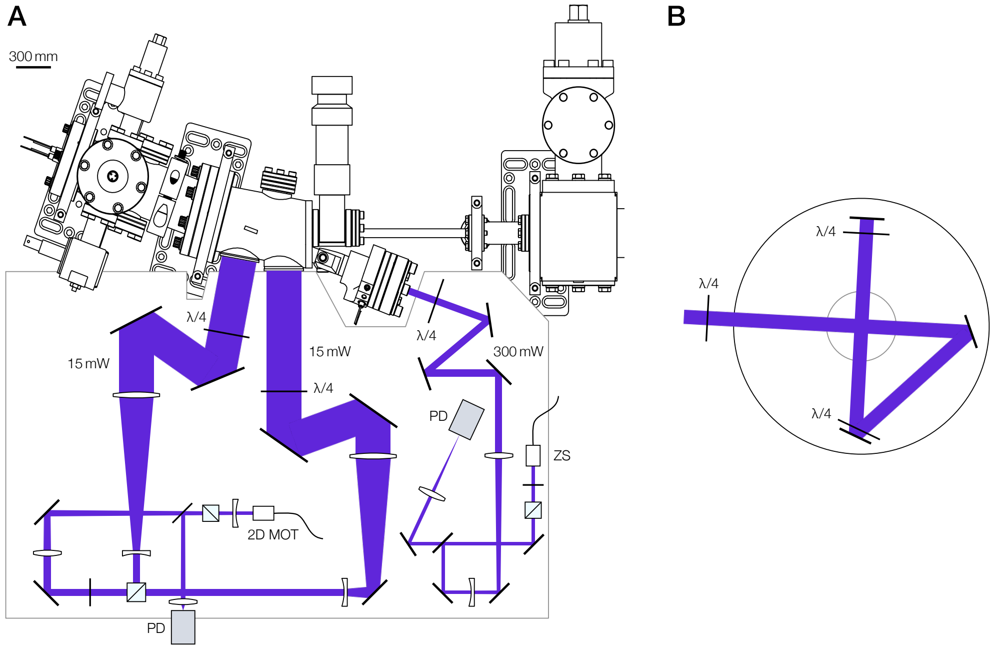

Figure 2.5 | Schematic of the atom source setup. A Illustration of the 2D MOT and ZS beam paths around the atom source chamber. The respective sizes and angles are to scale. **B** Working principle of the 2D MOT. Circularly polarized light enters the chamber and interacts with the atoms for the first time. It is deflected upwards by two mirrors and passes twice through a QWP in front of the first mirror to maintain the correct polarization. Upon retro-reflection, the light is rotated to the orthogonal circular polarization to complete the 2D MOT. Depicted is the rotated orientation of the 2D MOT system by $\simeq 3°$.

source, and one large, monolithic breadboard surrounding the glass cell. An off-the-shelf breadboard[16] with a cut-out for the coil mount which was used as the initial main breadboard to allow for the first experimental results was later replaced by a custom large-size breadboard,[17] designed for maximal space and stability. The experimental results discussed in Chapters 4.1 and 4.2 were performed with the initial setup, whereas the 3D lattice and the tweezers were implemented as part of the final, hybrid setup.

2.3.1 Atom source setup

To be able to run the atom source in the most efficient condition and to achieve the best atomic flux in the glass cell, we designed the corresponding setup to allow for a $6{\times}30$ mm elliptical beam for the 2D MOT and a 6 mm circular beam for the Zeeman slower.

For the 2D MOT beams, the light coming out of a single-mode polarization-maintaining (PM) fiber[18] and collimated by a fiber collimator[19] is expanded to 6 mm via a 3:1 telescope (Fig. 2.5). Given the large final size of the 2D MOT beams, for each of the two beams an individual 5:1 cylindrical telescope follows a 1" beamsplitter cube[20], and a strongly folded

---

[16] *Thorlabs MB6090/M*

[17] *Base Lab Tools, Inc., SABCUST836, custom design*

[18] *Fibercore HB450-SC, customized by Coastal Connections*

[19] *Schäfter+Kirchhoff GmbH, 60FC-4-M8-33*

[20] *Altechna UAB, M0078016, custom design*

configuration was chosen for 75×50 mm rectangular mirrors.[21] Each beam then passes through a 2″ multi-order quarter-wave plate[22] to obtain a right-hand circularly polarized beam in the point of view of receiver definition. Initially, we aligned both beams to impinge on the windows in the center, both vertically and horizontally, i.e., at a beam height of 50 mm. Indeed, at this height, the weak fluorescence of atoms passing through the 2D MOT windows and scattering photons were visible. However, we noticed that at this height and horizontal direction no backreflection from the retroreflecting mirror inside the atom source could be identified. Instead, a significant downwards tilt of $\simeq 3°$ had to be implemented to achieve a good overlap with the backreflection. This requires the beam height at the last incoupling mirror to be $\simeq 59$ mm, almost exceeding the tilt adjustment range of the mirror mount[23], which makes the vertical alignment of the beams relatively sensitive to misalignment. An equal relative power balancing and a total laser power of $\simeq$ 30 mW was found to yield optimal performance.

The Zeeman slowing beam uses the same collimator and a similar telescope combination as the 2D MOT. Note that, according to the manufacturer, the beam should mildly converge as it enters the heated window. We achieve this by placing the −75 mm and 300 mm telescope lenses at a relative distance of $\simeq 240$ mm from each other and thus 15 mm further apart than necessary for a collimated beam, thereby ensuring that the focus is at a distance of $\simeq 5$ m from the Zeeman slower. Due to space constraints, only one tunable mirror mount was used for the incoupling mirror. Therefore, a careful initial positioning and alignment is required. To this end, we use scattered light from the 2D MOT optics and coils as a reference, since good coupling is achieved when the Zeeman slower beam is roughly centered and does not scatter brightly at the orifices. Using the Zeeman slower window as a reference, i.e., making sure that the beam is centered with respect to the heating elements, or backreflection off the window were found to be misleading and thus not helpful. This initial aligment reliably brought us very close to the optimum. Again, the vertical axis appears to be more sensitive than the horizontal one. To allow this mirror and the quarter-wave plate to be placed only a few centimeters from the heated window, an M3-threaded breadboard was cut to make it fit closely to the atom source. This leaves the maximal amount of space for the main breadboard. The optimal power for a detuning of −580 MHz from resonance was initially found to be $\simeq 250$ mW, with a strong power dependence past 200 mW. Later changes in the 3D MOT setup as described in section 2.3.3 decreased the optimal power to $\simeq 220$ mW. For lower detunings, in spite of calculations from AOSense indicating otherwise, the optimal power as well as the overall 3D MOT loading rate is reduced, whereas for a detuning of −590 MHz the optimal power was back at 250 mW, but only with a small improvement compared to the initial values, which is why the detuning was kept at −580 MHz.

2.3.2 Intermediate setup

Apart from few exceptions, the majority of the beams is sent through the glass cell's horizontal windows, as displayed in Fig. 2.6. To this end, most of the optics are placed on one large, main

---

[21] *LENS Optics GmbH, custom design*

[22] *Altechna UAB, M0077955, custom design*

[23] *Thorlabs KM200S*

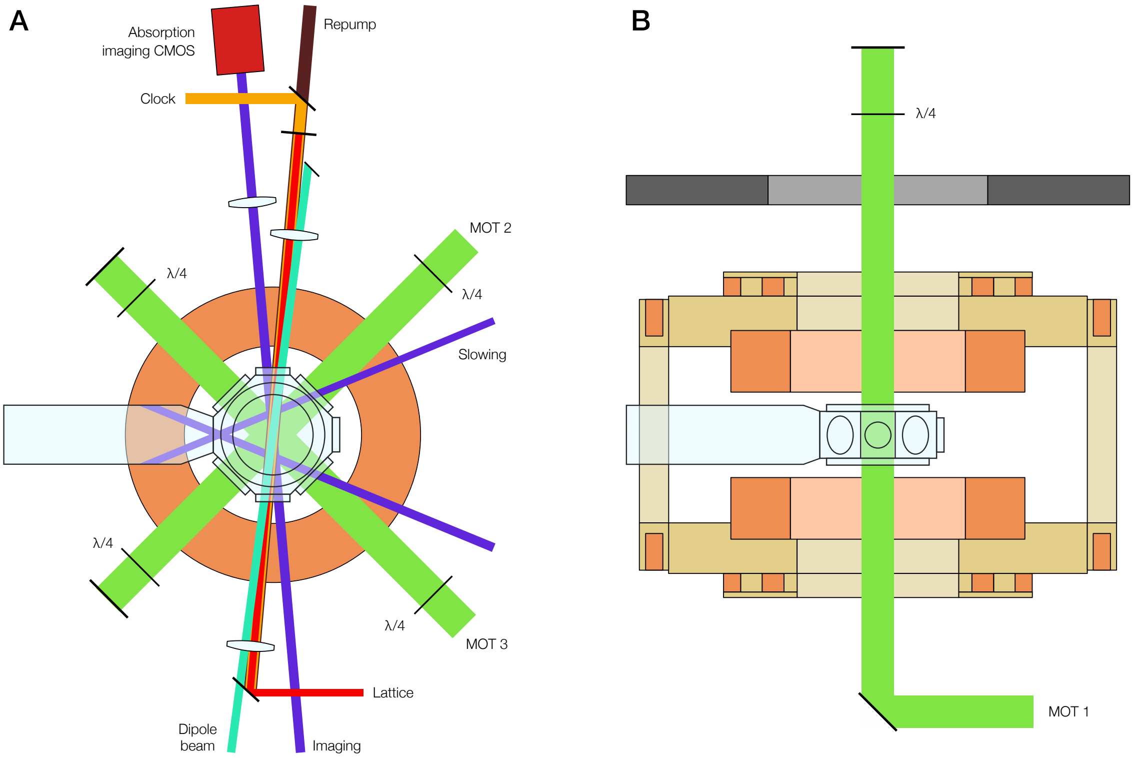

Figure 2.6 | Schematic of the intermediate setup. A Illustration of the beam paths on the mezzanine breadboard and **B** for the vertical MOT beam. The glass cell and coil components are to scale, while the beams are simplified and most optics are omitted for clarity. The relative angles of the various beams, however, represent the state of the experiment at that time, apart from a slightly exaggerated tilt of the magic dipole trap beam (turquoise).

breadboard, and the remaining beams are directed upwards from the optical table surface or downwards from an additional small breadboard mounted on top of the main one. As the design and manufacturing of the final "mezzanine" breadboard would have significantly delayed the progress, a preliminary setup was installed. Its main purpose was to test the crossed-slowing-beam-enhanced MOT loading (Chapter 2.5) as well as the clock spectroscopy in the 1D lattice (Chapter 2.6.1), and ended up also being used for the magic and ground-state tune-out wavelength measurements.

In this setup all three MOT beams at 556 nm are oriented perpendicular to each other and are retroreflected for maximal power efficiency and compactness – two beams are sent in within the horizontal plane, and one beam from the bottom (Fig. 2.6. The fiber collimators[24] with a focal length of 75 mm are chosen to provide beams with a large waist of 5.6 mm such that the aperture of the wider horizontal glass cell windows is used to full capacity. After the collimators, the polarization of each beam is cleaned from any unwanted components introduced by birefringence of the fiber or preceding optics via a combination of a half-wave plate (HWP) and a polarizing beam splitter cube (PBS). This is then followed by a beam sampler at an angle of 45°, reflecting ≃ 3% of the light onto a photodiode, whose signal is used to stabilize

---

[24] *Schäfter+Kirchhoff GmbH, 60FC-L-4-M75-01*

the intensity of the beam. This sequence of optics is used for all beams on the experimental table. In the case of the MOT beams, the polarization is further rotated by 1″ quarter-wave plates (QWPs)[25] before passing through the glass cell and in front of the retroreflecting mirror to ensure appropriate circular polarization for each of the beams.

The vertically polarized 399 nm slowing beams are sent in through the same horizontal glass cell windows as the horizontal 3D MOT beams, but under a steep half angle of 22.5° to create the crossing region $\simeq 18$ mm in front of the MOT center. This provides a short pathway to the MOT while preventing any significant overlap of the slowing beams with the MOT, which is vital due to the large scattering rate and recoil energy of the ${}^1\mathrm{P}_1$ transition. As the two beams are split up by means of a PBS, we further have to rotate the polarization of the horizontally polarized beam with a HWP to generate a net scattering force that counterpropagates to the atomic beam. The working principle and characterization of this slowing technique is further explained in Chapter 2.5.1.

The 759 nm lattice beam propagates horizontally, unlike most optical lattice clock experiments in which the effect of gravitational sag is typically reduced by aligning it with the strongly confined lattice axis [204, 209, 210]. However, this is not relevant for deep lattice potentials, and while the systematic uncertainties arising from such potentials matter for high-precision atomic clocks, they are exiguous in the magic wavelength measurements. To create such a deep lattice, up to 5 W of light is sent through a polarization-maintaining photonic crystal fiber (PCF)[26] with a large mode field diameter of 12.5 μm, minimizing the effect of Bragg scattering at very high intensities. The light is then outcoupled by a 20 mm fiber collimator[27] to produce a 1.6 mm-sized beam ($1/e^2$ diameter), focused down to a waist of 62 μm using a standard achromatic lens with a focal length of 200 mm[28], recollimated with an identical achromat on the other side, and retroreflected by a dichroic mirror[29] mounted inside a piezo-actuated mirror mount.[30] Optimal backreflection of the beam onto itself and thus a high-contrast standing wave are guaranteed by coupling the retroreflected beam back into the fiber and maximizing the power at the rejection port of the Faraday isolator. Back-coupling efficiencies of $\simeq 50\%$ were measured, taking the AOM's finite first-order diffraction efficiency into account. In this vein, we can reach lattice depths of up to $\simeq 50\,\mu\mathrm{K}$.

The retroreflecting mirror is chosen to be highly reflective ($> 99.5\%$) for 759 nm as well as the range $550 - 560$ nm while it is transmitting more than 95% of the light at 578 nm and 1389 nm. This is desirable as it allows for clock and repump beams co-propagating with the lattice beam, which is necessary to probe the clock excitation fraction in the Lamb-Dicke regime for the 1D lattice case. The clock beam is focused by the achromatic lens to a waist of $\simeq 110$ μm while the repump beam is kept large by means of a second lens. Both beams are superimposed with a long-pass dichroic.[31]

Absorption imaging is performed with a 6.6 mm wide 399 nm beam under a shallow angle

---

[25] *Altechna UAB, M0077959, custom design*

[26] *TraTech JMPR-2M-HP2.5FC MSL-LMA PM 15/230*

[27] *Schäfter+Kirchhoff GmbH, 60FC-L-4-M20-02*, adapted fiber receptacle to be compatible with FC/APC PCF

[28] *Thorlabs AC254-200-AB*

[29] *Optoman, PAN3901, custom design*

[30] *New Focus 8821*

[31] *Thorlabs DMLP650*

of 10.4° with respect to the lattice axis. The shadow on the blue beam cast by the atomic cloud is imaged onto a CMOS camera[32] with a 4:3 telescope consisting of a $f = 200\,\mathrm{mm}$ and $f = 150\,\mathrm{mm}$ achromatic lens pair. As the space on the breadboard is limited, the last lens as well as the camera are mounted in a vertical assembly, fully covered by a lens tube to minimize stray light exposure, and structurally stabilized by cage rods. We choose a long-pass dichroic mirror[33] to reflect the 399 nm beam up towards the absorption imaging camera such that 556 nm fluorescence light can be collected with a separate imaging setup.

In the final stage of this setup, the beam for the magic and g tune-out measurement was inserted. Depending on the type of measurement, the beam is either co-propagating with the magic lattice and thus retro-reflected by the same mirror to form a lattice (tune-out), or slightly tilted by $\simeq 1°$ (magic) to block the beam in front of the mirror, thereby preventing any backreflections as any formation of a standing wave would be detrimental. The beam is superimposed onto the lattice beam using a short-pass dichroic[34] and can be steered with a piezo-actuated mirror mount[35] to precisely optimize the overlap with the atomic cloud. The relative position of lattice and tune-out beam as well as the individual beam shapes at the atom position can further be monitored on a second identical CMOS camera by inserting a mirror on a flip mount. With the aid of a 1:1 telescope, the atomic plane is imaged onto the camera, using the small portion of light leaking through the retroreflection mirror.

2.3.3 Hybrid tweezer-lattice setup

The experiments we envision to conduct in the future entail a considerable technical complexity. In particular, coalescing a quantum gas microscope based on a 3D optical lattice with several tweezer arrays requires careful design both on the mechanical as well as on the optical level. In this Chapter the optical design of the upgraded experimental setup is discussed, comprising the magic 3D lattice and the 532 nm tweezer array, but also the setup for the e tune-out measurement.

Breadboard design

As for the fundamental distribution, the lattices and state manipulation optics are located on the main breadboard, whereas the microscope objective placed below the glass cell apportions the space on the optical table to the tweezer and fluorescence imaging path (Fig. 2.7). In this way, the large distances required to achieve a sufficient magnification for both the tweezer array spacing and the imaging (cp. Chapter 2.7) can be realized by folding the respective beam paths below the remaining optics on the mezzanine breadboard. Furthermore, placing the optics on the optical table yields a very stable reference and should therefore not excessively suffer from mechanical noise. Eventually, the breadboard above largely protects the beam paths from turbulent air flows which are known to pose a sizeable limit for highly stable imaging or tweezer beam paths as they can distort the wavefronts or erratically deflect the

---

[32] *Allied Vision Mako G-234B*

[33] *Thorlabs DMLP505*

[34] *Thorlabs DMSP650*

[35] *New Focus 8807*

beams [169]. While this aims at providing a high absolute stability of the tweezer array and imaging performance, relative stability between the lattices and the objective is of even greater importance for the purpose of future experiments in this setup. Following the discussion of the phase stability of lattices in Chapter 1.4, the passive stability of a lattice is mostly governed by the magnitude of fluctuations of the optical path length, rendering minimal distances of the retroreflecting mirror to the atomic plane preferable, while the objective determines the position of the tweezer arrays. To maintain a precise overlap of the tweezers with the desired lattice sites, the decisive lattice optics and the objective thus have to share a common reference. This is achieved by mounting the objective directly to the main breadboard and placing the lattice retroreflecting mirrors close to this mount and the glass cell. Both are fundamental for reaching common-mode mechanical vibrations and minimizing the effect of thermal expansion and contraction, i.e., changes of distances due to temperature fluctuations.

Moreover, selecting a material with a minimal coefficient of thermal expansion (CTE) as well as a low elasticity, usually expressed in Young's modulus, is expedient. Titanium alloys like grade-5 Ti combine an excellently low CTE of $8.6 \times 10^{-6}\,\mathrm{m/mK}$ with a high Young's modulus of up to 125 GPa, while still being machineable, and are both non-magnetic and relatively light with a moderate density of $\simeq 4.5\,\mathrm{g/cm^3}$ [211]. We therefore employ titanium for compact components such as the objective holders or screws around the glass cell. For larger components like the mezzanine breadboard, however, one typically has to rely on aluminium or stainless steel due to their superior machinability. Recently, also light-weight, highly stable and non-magnetic solutions based on carbon fiber reinforced polymers (CFRP) have been introduced. While they further benefit from the extremely low CTE of carbon fiber composites of $\simeq 1\text{-}2 \times 10^{-6}\,\mathrm{m/mK}$, which can be reduced even closer to zero by specifically designing the orientation of the fibers, large-scale CFRP breadboards with a custom cut-out for the coil mount become very costly [212]. Steel-based honeycomb breadboards also provide a high stiffness and can even dampen mechanical noise, but are very heavy and can be manufactured only in a limited number of forms. We therefore decided to choose a solid, monolithic aluminium breadboard with edge lengths of $1.0\,\mathrm{m} \times 1.2\,\mathrm{m}$ and a minimally sized cut-out to accomodate the coil mount and the vacuum chamber parts, trading in a mediocre elastic modulus of $\simeq 68$ GPa [213] and CTE of $23.4 \times 10^{-6}\,\mathrm{m/mK}$ [214] for compact and versatile mounting options for both the lattice optics and the objective mount. This allows the retroreflecting mirrors to be placed at a distance of 150 mm from the atomic plane, while the objective is mounted to the breadboard at a distance of $\simeq 110$ mm from its center. Taking standard daily peak-to-peak air temperature fluctuations on the optical table of 0.1 K as a reference, the lattice would drift by 0.1 lattice sites because of the change in air's refractive index and by 1.8 lattice sites due to the breadboard's thermal expansion [215].[36] This assumes that the temperature change of the breadboard is of the same magnitude and the breadboard expands around its center, the glass cell. Notably, sudden changes in the coil's duty cycle and thus its temperature can also locally influence the temperature of the surrounding breadboard and air around the glass cell even more significantly. To reduce this effect as far as possible, we placed the pillars that hold

---

[36] Changes in pressure and humidity similarly alter the refractive index, but the typical changes observed on the optical table of $\lesssim 5$ mbar in pressure and $\lesssim 1\%$ in relative humidity typically happen on slower timescales and translate to drifts by about one and 0.01 lattice sites, respectively.

the breadboard right below the most crucial optics. Assuming that the optical table surface is sufficiently far away from the coils and other heating sources, and taking into account the lower CTE of steel of $\simeq 16 \times 10^{-6}$ m/mK [214], one can approximate the pillars to define the local origin of thermal expansion. For later stages of the experiment, which potentially require maximally stringent constraints on drifts and instabilities, a specifically designed, compact second breadboard made from a low-expansion material such as Zerodur or CFRP can be placed on top of the main breadboard, which could also host a second generation of the objective mount, directly linking the two most crucial components. This would largely eliminate the detrimental effects of both mechanical as well as temperature fluctuations.

The positions of the pillars further determine the compliance and transmissibility of the main breadboard. It is usually advantageous to maximize the lowest vibrational eigenfrequencies, and to ensure that the most sensitive optics are placed where the amplitude of any low-frequency vibrational mode is minimal. We optimized this behavior with a finite-element analysis, assuming the pillar positions to be fully immobile and the pillar-breadboard connections to be perfectly rigid while neglecting the effect of the threaded holes. Naturally, larger distances between pillars allow for lower frequencies of vibrational modes to appear in between these points, so it is favorable to not exceed a maximum distance of 300 mm in our case to keep the resonance frequencies above 500 Hz. At the same time, the tweezer and imaging optics below the breadboard require sufficient space to allow for the necessary folded beam paths, so the maximum density is bounded from below to a minimal distance of $\simeq$200 mm. Further, in the model all pillars are assumed to have the exact same height and are ideally positioned, i.e., there is no additional stress from slightly differing pillar heights, varying breadboard thicknesses, or tilt. The real breadboard, however, suffers from these imperfections, although a careful placement and adjustment of the respective pillar heights on the level of 100 μm was performed prior to the insertion into the experiment. The results of the finite-element analysis are discussed in more detail in Appendix B. The pillars are made from aluminium and are filled with a mixture of lead balls and finely grained sand, which not only makes them heavier, providing better intrinsic stability than pure aluminium posts, but also dampens mechanical vibrations, similar to a mass damper.

3D lattice

The horizontal MOT and crossed slowing beam optics are aligned in almost the same way as on the temporary breadboard, as is the imaging beam (Fig. 2.7 A). The main differences pertain to the fiber collimators and following optics, which are placed further away from the glass cell, close to the edges of the larger breadboard, and the MOT beams, now being slightly tilted by $\simeq 2°$ with respect to the window's normal. The latter provides space for the two orthogonal horizontal lattice beams which are directed to the glass cell under a precise angle of $-5°$. To reach lattice depths of 1100 E_{rec} in each arm, the lattice beams are collimated to $1/e$ diameters of 3.1 mm by means of the 20 mm outcoupler from the previous setup, combined with a 2:1 telescope in the case of the first arm (L1), and a $f = 40$ mm outcoupler[37] for the second lattice beam (L2), until they are focused by achromatic, $f = 200$ mm lenses to a

---

[37] *Schäfter+Kirchhoff GmbH, 60FC-T-4-M40L-24*, adapted fiber receptacle to be compatible with FC/APC PCF

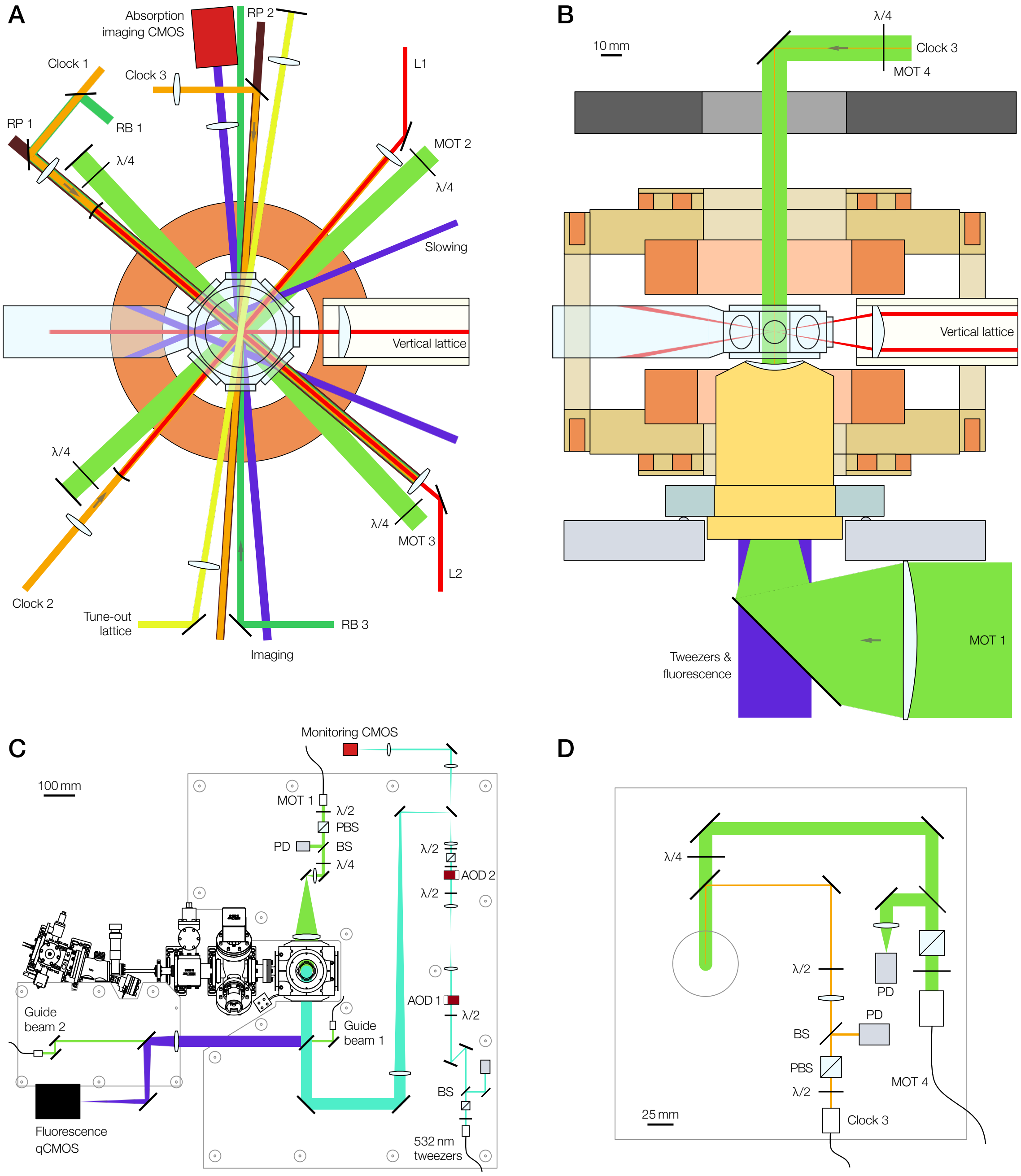

Figure 2.7 | Schematic of the final optical setup around the glass cell. **A** Illustration of the beam paths on the mezzanine breadboard. While all components, including beam sizes, are to scale in **B**-**D**, the positions of most optics and beam sizes in this panel are simplified for enhanced visibility. **B** A vertical semi-cut to illustrate the vertical beam propagation. For the purpose of clarity, the MOT and cooling beams are rotated into the plane of this Figure. The correct orientation is depicted in panels **C** and **D**. **C** Illustration of the optical layout below the main breadboard. While the optics for the 532 nm tweezers, the fluorescence light, and the guide beams are mounted on the optical table, the optics for the bottom MOT beam is attached to the lower surface of the main breadboard, i.e., at a different height to allow for future tweezer optics beneath. **D** Optical layout on the top breadboard.

calculated waist of $\simeq 32\,\mu$m at the atomic cloud. Instead of using a lens in combination with a planar mirror for retroreflection, in this setup the 0.5″ retroreflecting mirror, again coated with a dichroic coating,[38] is curved with a radius of curvature of 150 mm, minimizing the number of optical elements and the phase-stability-defining distance from the atom cloud to the mirror. The mirror is mounted in a compact piezo-actuated mirror mount[39] to allow for careful backcoupling of the retroreflected light into the fiber while blocking as little of the 3D MOT beam as possible. We rotate the horizontal polarization after the PBS used for polarization cleaning after the fiber to vertical by means of zero-order half-wave plates to realize a common polarization vector for both beams. As the lattice beams are generated from separate lasers, this leads to a usually unwanted four-beam interference with changed lattice spacings if the two laser frequencies are very similar, which is why we usually operate the lasers with a $\simeq 500$ MHz relative frequency spacing. Using the same fiber back-coupling technique to ensure optimal retroreflection, in this setup we exceed the efficiency measured in the temporary setup and reach values of $\simeq 60\%$ at the rejection port of the Faraday isolator on the laser setup. This is measured in relation to the power after the fiber on the experimental table, which is very close to the optimum one can expect under the assumption of a fiber coupling efficiency of 70% and losses of $2 \times 3\%$ at the beam sampling plates, neglecting further losses at mirrors, lenses, and waveplates.

The shallow-angle vertical lattice, which is discussed in more detail in Chapter 2.6.3, is aligned along the long axis of the vacuum chamber, such that the two beams enter the glass cell opposite the flange transition and in between the two slowing beams. The initial properties of the vertical lattice beam very much resemble the ones for the second horizontal lattice beam until it is beam-shaped by a cylindrical 3:1 telescope and sent through the Kösters prism where it is split up in two parallel beams. To generate the deepest lattice possible, the two beams are sent in under a maximally large angle of 20°, with the $f = 50$ mm aspheric focusing lens placed 20 mm in front of the glass cell window. This precludes using this window for any other beam unless it can be sent through the same lens. Notably, due to the geometry of the Kösters prism, the mirrors required to steer the beam under the optimal angle of 60° with respect to the horizontal plane also deflect the azimuthal angle of the elliptical beam. For our configuration, we find an optimal angle of the cylindrical lenses of 28° with respect to the vertical plane to align the azimuthal ellipticity angle with the lattice planes, maximally widening the beam horizontally to a waist of 27.1 mm while retaining a tightly focused vertical waist of 8.9 mm.

The clock state can be addressed with four different beams: One beam under an angle of 35° with respect to L2, i.e., with a projection on both horizontal lattice axes, which was mostly used to perform initial spectroscopy measurements in the 2D and 3D lattice, two beams that co-propagate with L1 and L2, respectively, using the curved dichroic retroreflecting mirror as a last leg of a telescope to focus the beams onto the atoms, and a fourth vertical beam overlapped with the top MOT beam using a short-pass dichroic. To reach high Rabi frequencies of $\Omega_0 \simeq 2\pi \times 8$ kHz even for ^{174}Yb at 400 G, the waist of the horizontal co-propagating clock beams is chosen to be 130 μm, which cannot be reached with a combination of a standard fiber collimator and just one lens in front of the curved dichroic mirror. Therefore, an additional

---

[38] *Optoman OPPN3136*

[39] *Newport 8807*

$f = 1000$ mm lens is inserted into the collimated beam with a diameter of 1.1 mm, which is then further focused by an achromat with a focal length of 250 mm placed $\simeq$80 mm before the curved dichroic. Notably, this clock beam size is expected to lead to an onset of observable spatial inhomogeneities in the intensity due to the Gaussian beam shape, with the outermost atoms in a 40 µm wide cloud experiencing a 10% lower Rabi frequency, although this effect has not had a measurable impact on the measured clock excitation fidelities. For each beam, the polarization is rotated to vertical to match the quantization axis defined by the strong main or transverse coils.

Similarly to the intermediate setup, two repumping beams are superimposed on the clock beams along L1 and in between L1 and L2 with long-pass dichroics. As only low intensities are required for a saturation of the repumping cycle, the beam size at the atom plane is chosen to be $\simeq$2 mm in diameter, which we reach by slightly defocusing the collimator[40] for the beam along L1 to reach an approximately collimated beam after the curved dichroic mirror. For the other repump beam, the collimated beam size after the $f = 8$ mm collimator is already sufficiently large and does not require further beam shaping.

For the measurements of the ${}^3\mathrm{P}_0$ tune-out wavelength, the corresponding lattice is formed at an angle of 40° with respect to L2 to provide significant overlap with both horizontal lattice arms. Crucially, this averts the complicated separation of the clock and tune-out beam, which are too close in frequency to allow for an efficient application of dichroic mirrors. Since the signal from the amplitude-modulated lattice is very small, the beam is strongly focused to 80 µm waist via an achromatic $f = 200$ mm lens, and re-collimated on the far side by a second achromat with a focal length of 250 mm, followed by a standard dielectric retroreflection mirror. This larger focal length for the second lens allows for an easier insertion of a beam block, which is necessary to prevent the formation of a lattice for initial alignment and the determination of the ground-state polarizability by means of Stark shift clock spectroscopy. Notably, this small waist leads to sizeable intensity inhomogeneities over the cloud size, similar to the effect described in Chapter 4.2 for the case of the g tune-out polarizability. As for the magic lattices, the generation of a standing wave is ascertained by coupling the retroreflected beam back into the fiber, which yields an approximate efficiency of $\simeq$50%, which in this case can only be indirectly estimated as the Faraday isolator rejection port happens to be at an unaccessible angle.

The most recent addition to the setup are four Raman beams operated near the ${}^3\mathrm{P}_1$ transition: two co-propagating with the clock beams along L1 and L2, one counter-propagating to the clock beam in between L1 and L2, and one vertical beam. All four beams are designed to have a waist of $\simeq$ 250 µm, which is sufficiently large to obviate inhomogeneity effects, but still small enough for fast Raman cycles even at large detunings. For the latter two beams, this is conveniently achieved with a single $f = 750$ mm lens placed shortly after the beam sampler. The other two beams are superimposed onto the 578 nm beams using a narrow-edge long-pass dichroic mirror,[41] where we employ its orthogonal, horizontal polarization to allow for a clean separation from the vertically polarized clock beams. As they also pass through the $f = 250$ mm achromat and the curved dichroic mirror, their beam diameter of 640 µm after the collimator and the distance to the lens is chosen to yield the desired waist at the atom cloud.

---

[40] *Schäfter+Kirchhoff 60FC-4-M5-08*

[41] *AHF F38-A567*

Tweezer array

The vertical dimension is used for fluorescence imaging and the generation of tweezer arrays, which is why the cross section (Fig. 2.7 B) is dominated by the microscope objective, owing to its large NA of 0.7022 and the aperture of 35 mm in diameter. To maintain optimal imaging performance, the optics surrounding the objective are selected to be correspondingly large and maximally flat. Therefore, mostly 3″ mirrors[42] are used to guide the imaging and tweezer beams, and a custom bandpass dichroic[43] of size 60 mm × 40 mm is employed to split the imaging light at 399 nm and 556 nm from the loading tweezer array at 532 nm (Fig. 2.7 C). The imaging light is focused onto a qCMOS camera[44] by achromats of different focal lengths, depending on the desired magnification. For this work, a focal length of 500 mm was chosen, resulting in a magnification of 20. To suppress stray light at other wavelengths apart from the fluorescence signal at 399 nm, a bandpass filter[45] transmitting light only at 400 ± 20 nm is mounted on a 50 mm long lens tube in front of the qCMOS camera. As the objective is not coated black on the inside, the loading tweezer array is a strong additional source of unwanted stray light, and an additional notch filter[46] to block light at 532 ± 15 nm is added.

The light for the crossed-AOD-generated 532 nm tweezer array is outcoupled from the PM PCF using an achromat with 60 mm focal length,[47] yielding a collimated beam size of 3.2 mm in diameter. After cleaning the polarization with a PBS, a HWP is employed to match the optimal polarization angle of the first AOD,[48] which is tilted by 40° to make the AOD pattern share the same principal axes as the 2D lattice. This in combination with a careful collimation and alignment of the AOD angle, mounted on a 5-axis stage,[49] enables us to reach up to 92% diffraction efficiency into the first order, when using a single frequency to drive the AOD. The orthogonal AOD is placed after a $4f$ telescope consisting of two achromats with 100 mm focal length. This images the 1D array generated by the first AOD onto the crystal of the second one, therefore minimizing potential mismatch in the conversion of the two series of RF frequency tones into a square array of optical tweezers. Furthermore, a second HWP again rotates the tweezer beam polarization to the optimal angle for the second AOD, which in turn diffracts up to 96% into the first order.[50] The AOD is followed by a combination of two HWPs and a PBS to both clean and arbitrarily adjust the polarization of the tweezer beams at the atom position, which is of importance for reaching magic-angle conditions [63]. In order to utilize the full high-efficiency bandwidth of 50 MHz, which is crucial to keep the beat frequency between adjacent tweezers as large as possible, it is mapped onto the objective's field of view (FOV) of 100 µm. Taking the AOD's measured total angular deflection range of 41 mrad and

---

[42] *Thorlabs BB3-E02*

[43] *Optoman OPPN2800*

[44] *Hamamatsu Orca-Quest C15550-20UP*

[45] *AHF F47-444*

[46] *AHF F40-534*

[47] *60FC-T-4-M60L-01*, adapted fiber receptacle to be compatible with FC/APC PCF

[48] *AA DTSX-400-532.556*

[49] *Thorlabs PY005/M*

[50] This value is the comparison between the power in the first order and the total beam power in front of the AOD, measured with a standard handheld powermeter at ≃ 1 mW input power. At this point, the zeroth order of the first AOD has been blocked.

the objective's effective focal length of 24.97 mm into account, a magnification of 10 serves this purpose. Since lenses with focal lengths of less than 100 mm tend to introduce observable spherical aberrations, the magnifying telescope comprises an achromatic $f = 100$ mm and $f = 1000$ mm lens pair. In the focus of the first telescope lens a backside-polished mirror is placed, whose leakage light is imaged via a 3:2 telescope on a CMOS camera[51] to perform intensity balancing and monitoring of the tweezer array.

Owing to the space restrictions introduced by the coils and the objective, the bottom MOT beam is required to be sent through the objective. However, to reach the desired wide, collimated beam, it has to be focused at the back focal plane of the objective. This strategy has been efficiently employed in several experiments [63, 216], where this plane was sufficiently close to the outermost lens to allow for a small mirror reflecting the converging MOT beams into the objective (Fig. 2.27). Owing to an unfavorable position of the back focal plane this is less straightforward with our objective. Instead, a large dichroic mirror, acting like a 80:20 non-polarizing beam splitter (NPBS) at 556 nm, is used to reflect the MOT light into the objective [62]. Placed very close to the dichroic, a 3″ plano-convex lens of $f = 150$ mm focal length provides the correct convergence angle of $\theta/2 = 14.6°$ to produce a collimated beam with a diameter of 12 mm in the glass cell. Since the required beam size at this point is close to the full clear aperture of 75 mm, the collimated beam after the 75 mm outcoupler is magnified by a telescope consisting of a $f = 30$ mm and a $f = 200$ mm lens after a QWP to make the polarization circular. The effect of the various optics, such as the dichroic and the objective on the polarization was found to be negligible in a test setup, which is why no additional HWP is implemented. Two steering mirrors are placed at a distance approximately equal to the focal length of the first telescope lens to allow for independent tuning of the position and pointing of the MOT beam at the atomic plane. Due to the position of the dichroic close to the objective, and to not obstruct the space on the optical table required for tweezer beam paths, the whole MOT beam path is attached to the bottom of the main breadboard, using a combination of lens tubes and cage mounts.

As the MOT beam possesses a highly non-Gaussian beam shape after passing through the objective (Fig. 2.27), it is not suited for retro-reflection. Instead, we use a separate MOT beam from the top, mounted on a compact breadboard above the coil cage and beam-shaped like the horizontal beams (Fig. 2.7 D). Onto this MOT beam we overlap the vertical Raman cooling via a PBS by selecting the orthogonal polarization. This has implications on the planned Raman cooling process, which will be discussed in Chapter 3.3. We can furthermore add a vertical clock cooling beam using a dichroic mirror. Notably, the aperture in the breadboard allows for angles of up to 17° with respect to the vertical axis, which is precisely the magic angle in ^{171}Yb for the ^{3}P$_1$ transition in the magic lattice at 759 nm. Thus, it is possible to perform the optical pumping step in a magic condition, which could allow for a more efficient cooling and lower temperatures. The projected beam path uses an angled mirror mount which directs the beam orthogonal to the MOT beam and ensures sufficient tunability.

---

[51] *Allied Vision Alvium 1800 U-240m*

Upgrades in the future

While the vertical cooling beams are crucial to reach single-site resolution, additional tweezer arrays at the tune-out wavelengths for the $^1S_0$ and the $^3P_0$ states and a more complex lattice setup are essential to implement the devised LGT schemes. The latter can be reached by creating a bow-tie lattice with adjustable polarization angles, realizing a tunable four-fold interference as described in Chapter 1.3.1. This requires the two retro-reflected horizontal lattice beams to be replaced by a single beam. The tune-out tweezer arrays are planned to be generated with crossed AODs, reproducing the 532 nm loading tweezer array. While overlapping the 577 nm tweezer beam onto the existing beams can be done with dielectrically coated dichroics, the wavelength separation for the 553 nm tweezer array to still allow for fluorescence imaging of 556 nm photons is more delicate. For moderate system size one can take advantage of judiciously chosen lattice potentials which then require only weak tweezer powers, such that losing a vast portion of the power at a NPBS is still sufficient. As an alternative, the tweezer beams can be separated from the imaging path, i.e., the tweezer beam paths would remain on the optical table, while the fluorescence detection would take place on the top breadboard. This solution requires the insertion of a second objective, which in turn demands for a similar NPBS solution for the top MOT and potential Raman beams. Furthermore, to avoid fluctuations of the imaged atoms one has to shield the imaging beam path from turbulences. A second objective would further allow for an increase of the effective NA, which however requires the technically challenging addition of two separate images.

2.4 Laser setups

Having discussed the laser beams required on the main experimental table, we now turn to the setups that provide the laser light at the correct frequency and power. Apart from the clock and the 577 nm tune-out setup, we uniformly use a system of self-designed compact optics mounts based on a dense M3 grid. This custom system has first been used in the now Tübingen-based potassium tweezer experiment [217] and has found widespread application in our group since [218, 219]. With two interleaved grids, each with a distance of 12.5 mm between the threaded holes, the breadboards allow for very compactly spaced optics. In addition, all bases are designed to guide the beam centered on the grid, which eases and accelerates the alignment while providing increased vibrational stability compared to standard M6-based setups as the default beam height is only 35 mm and the bases can be tightened to the breadboard directly instead of being clamped. In turn, this system suffers from lower stability in cases where the beam is not aligned to the row of threads and the components have to be clamped to the table. This is typically the case for AOMs and the optics thereafter.

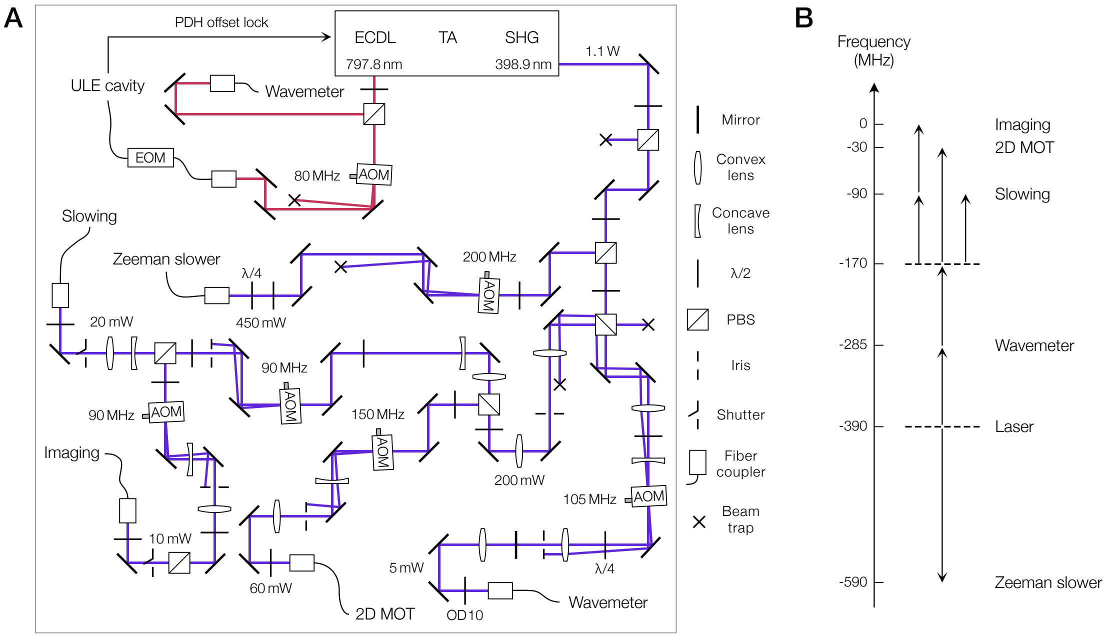

Figure 2.8 | Schematic of the blue laser setup. A Illustration of the optical beam paths. While the layout is close to the actual implementation on the breadboard, this image contains minor simplifications for clarity. Frequency-doubled light at 399 nm from the laser is split up into four branches, with three of them sharing an AOM double-pass to shift their frequencies. Light leaking through the retro-reflecting mirror is used for the wavemeter. The imaging beam passes two more AOMs to reach the resonance, while the slowing and 2D MOT AOMs are appropriately red-detuned. The independent high-power ZS beam is shifted down in frequency in a single-pass configuration. Fundamental leakage light at 798 nm is used for the offset cavity lock and for an auxiliary wavemeter beam. **B** Frequencies of the several branches and the relative frequency shifts induced in single passes (light grey) or in a double-pass configuration (dark grey).

2.4.1 Blue laser setup

The blue laser setup provides light to be used for the Zeeman slower, the 2D MOT, the slowing, and the imaging beam. The light is generated by an amplified and frequency-doubled ECDL[52] with an output power of $\simeq 1.1$ W at 398.9 nm. Since the ZS works most effectively at a detuning of -580 MHz, a large frequency gap to the resonant imaging light has to be bridged. Furthermore, the 2D MOT and slowing beams also require a significant detuning from the resonance, which is why a judiciously planned chain of AOMs is implemented to shift the frequencies of the respective beams. A sketch of the setup as well as the frequencies and detunings of each beam is displayed in Fig. 2.8. Given the proximity to the ultraviolet spectrum, we utilize fused-silica-based AOMs, which however suffer from a polarization-dependent diffraction efficiency. Therefore, most AOMs are installed in a single-pass configuration. As the ZS branch is the most power-demanding one, its light passes through just one AOM[53], which shifts the frequency down by -200 MHz, and is then polarization-matched and coupled into a single-mode PM

---

[52] *Toptica TA SHG pro*

[53] *IntraAction ASM-200B8*

fiber with core-less end caps.[54] The end caps allow for a larger beam size and thus lower intensity at the air-fiber interface, making it less prone to aging or power-induced damage, and we therefore employ them for all beams that can exceed 100 mW in the visible range. Thereby, over the duration of more than three years, the ZS fiber has only been exchanged once due to a damaged fiber end, despite a power of $\simeq$450 mW on the incoupling side. The remaining beams are guided through a double-pass AOM setup, detuning the light by $2 \times +105$ MHz. This allows for independent adjustments of the ZS detuning. The selected AOM[55] was tested to exhibit the best overall diffraction efficiency of $\simeq$53%. However, given a single-pass efficiency of 87%, one can gain in available laser power in the future by replacing the double pass. At the retro-reflecting mirror, the leakage light is fiber-coupled into a multi-mode fiber leading to the wavemeter.[56] After the double pass, the light is split up using a PBS, with one beam going through a 150 MHz AOM[57] to shift it to the net detuning of -30 MHz required for the 2D MOT. The other beam is sent through an AOM at 90 MHz,[55] followed by another PBS to separate the slowing beam from the imaging beam. The latter is shifted up by the remaining 90 MHz up via another AOM[55] to be resonant with the $^1\mathrm{P}_1$ transition. Both the slowing and the imaging beam further pass a home-built mechanical shutter before polarization matching and fiber coupling to fully suppress transfer of blue light onto the glass cell unless it is desired. As the imaging or removal of g atoms is separated in time from the loading, we can further adjust the frequency by tuning the offset lock frequency (discussed in detail in Chapter 2.4.8). The light required for this lock is taken from the laser port for the fundamental, i.e., at 798.8 nm. Part of the light is diffracted by an AOM[58] to allow for intensity stabilization, before it is coupled into the fiber of an electro-optical modulator (EOM) required for the offset lock. The remaining fundamental leakage light is directly fiber-coupled and can be used for monitoring the laser frequency on the wavemeter in cases where the second-harmonic generation (SHG) cavity fails to lock.

2.4.2 Green laser setups

For the purpose of providing light for the 3D MOT, molasses cooling, and Raman sideband cooling, we employ two separate laser setups operating at or near the $^3\mathrm{P}_1$ transition. This offers the required flexibility to choose the optimal Raman detuning or different hyperfine transitions for the MOT and optical pumping steps. To this end, the two setups are referred to as MOT and Raman setups, respectively.

MOT setup

Resonant light for the four MOT arms is produced in a fiber-coupled *Toptica TA SHG pro* system. Initially, the included *FiberMon* equipment was used to transport the light to the breadboard. However, after repeated failures of the fiber after the internal photodiode, which led to a slow degradation of the mode shape after the fiber, likely due to imperfect handling of

---

[54] *Coastal Connections, P-FaknsFAkns-3f/125/3-5*, using a *Fibercore HB450-SC* fiber.

[55] *Gooch&Housego I-M110*

[56] *HighFinesse WS8-2*

[57] *AA MQ150-A1,5*

[58] *Gooch&Housego AOMO 3080-122*

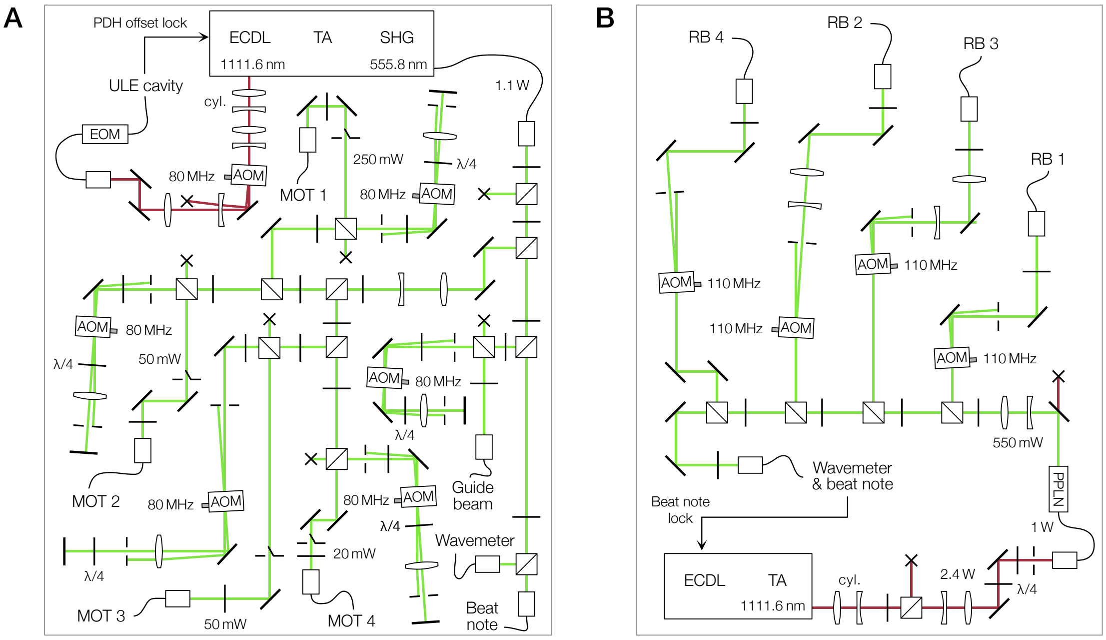

Figure 2.9 | Schematic of the green laser setups. A Illustration of the MOT laser beam paths, with a simplified layout for clarity. The fiber-coupled light at 556 nm is collimated and separated into a main high-power branch, which is then divided into the four MOT beams. Each beam can be tuned in frequency by a double-pass AOM configuration. Additional light is guided to the wavemeter and to the beatnote setup next to the Raman laser setup. Light at the fundamental wavelength is beam-shaped, frequency-shifted by an AOM and coupled to an EOM for the offset cavity lock. **B** Layout of the Raman laser beam paths. Light at 1112 nm is coupled into a waveguide PPLN frequency doubler after beam shaping and filtering of unwanted modes. The 556 nm light is separated from the fundamental using a dichroic mirror and then split up into four Raman beams, each of them passing through an AOM for fast switching and adjustments of relative detunings. An auxiliary fibercoupler is used for the wavemeter signal and for the beatnote lock.

the high power of $\simeq 1.2$ W in front of the fiber coupling, this was permanently replaced by a standard fiber of the same type,[59] causing no further issues since. The light from the fiber is collimated with an $f = 8$ mm achromat to a beam diameter of $\simeq 1.5$ mm and separated into two branches by a PBS. The transmitted beam is typically very weak and serves as a source for the wavemeter and the beatnote lock for the Raman laser. The strong, reflected beam is first demagnified to a size of $\simeq 0.5$ mm in diameter by means of a 3:1 telescope, and then split up into four separate double-pass AOM[60] setups. Each double pass is aligned in a cat-eye configuration to enable adjustments of the respective AOM frequency over several MHz around the center frequency of 80 MHz without losses in the fiber coupling efficiency. Shutters in front of the fiber couplers further avoid leakage of light onto the atoms. A fifth double pass was set up to serve as a guide beam for the objective and tweezer optics alignment, but can also be used as a green imaging or independent optical pumping beam.

---

[59] *Thorlabs P3-405PM-FC-2*

[60] *Gooch&Housego AOMO 3080-120*

Raman setup

The second laser[61] provides up to 2.4 W at 1112 nm. The second-harmonic generation is performed in a fiber-coupled waveguide PPLN crystal[62]. However, the fiber coupling efficiency of the infrared light into the fiber pigtail is limited to ≃ 40%. This is mostly due to a very irregular beam shape at the laser output that persists even after adjusting the cylindrical telescope after the tapered amplifier (TA). Inserting both a cylindrical and an intentionally defocused spherical telescope compensates for the most severe aberrations. To protect the fiber from damage, we block powerful higher-order modes with an iris in front of the fiber coupler. Despite this imperfect coupling, we can reach frequency-up-converted powers of 550 mW, corresponding to ≃ 1 W of incoupled fundamental light, for optimal quasi-phase and polarization matching conditions. The former is achieved by stabilizing the temperature of the waveguide to ≃ 0.01 ℃. After the waveguide, a dichroic[63] separates the 556 nm beam from the transmitted infrared light, which is then safely blocked. The green light is then split up into five separate beams, four of which are then frequency-shifted by +110 MHz by AOMs[64] and coupled into fibers, guiding the light onto the experimental table, while the fifth beam is directly coupled into a short fiber leading to the beatnote lock setup and a wavemeter port.

2.4.3 Clock laser setup

The clock laser setup is one of the two that are placed on a commercial M6 honeycomb breadboard.[65] The reduced transmissibility compared to the standard M3 breadboards, made from solid aluminium, helps in decoupling the laser linewidth from mechanical noise on the optical table, induced by, e.g., mechanical shutters on other setups or vibrations from water cooling lines. The setup is organized similarly to the MOT setup, with the main difference that the fiber-coupled laser,[52] capable of a power of up to 660 mW at 578 nm after the fiber, is mounted on the same breadboard as the optics. Furthermore, the three main beams pass through the AOMs[60] only once before they are fiber-coupled, since here the frequency scan ranges are typically significantly narrower than for the MOT beams. We employ commercial low-noise shutters[66] instead of home-built ones to minimize the mechanical noise on the laser light. Additional light is provided for the wavemeter and a beatnote setup, fed with clock light from the neighboring Yb lab via a 50 m long fiber. This greatly helped in initially finding the clock resonance and determining the zero crossing temperature of our ULE cavity.

2.4.4 Repump setup

The light for the laser setup for the 1388.8 nm $^3P_0 \rightarrow {}^3D_1$ repumping transition is provided by a fiber-coupled distributed-feedback (DFB) laser[67] on a temperature-controlled butterfly

---

[61] *Toptica TA pro*

[62] *NTT Electronics, WH-0556-000-A-B-C-M*

[63] *Thorlabs DMLP650T*

[64] *Gooch&Housego AOMO 3110-120*

[65] *Newport M-SG-23-2*

[66] *SRS SR475*

[67] *Acal BFi NLK1E5GAAA*

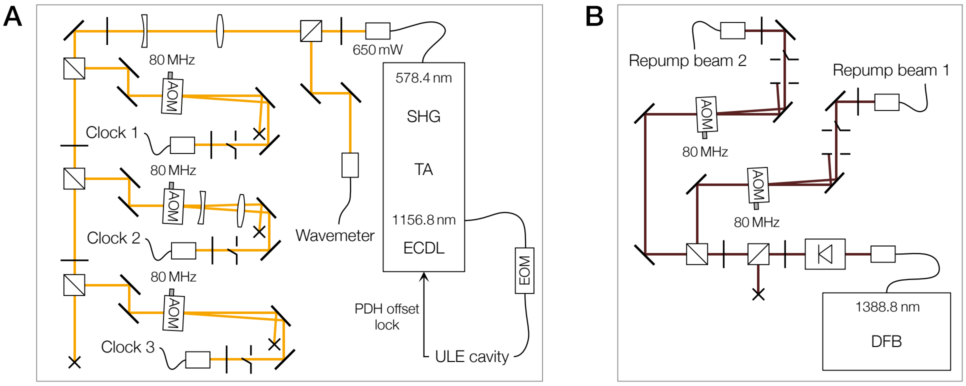

Figure 2.10 | Schematic of the clock and repumper laser setups. A The fiber-coupled output light of the 578 nm clock laser is collimated and split into five branches. Three beams pass through AOMs and low-noise shutters and are coupled into fibers to be transported to the main table. The fourth beam is used for wavemeter frequency monitoring, the fifth one can be used for beatnote measurements. For the frequency lock, fiber-coupled light at the fundamental frequency is modulated by a temperature-stabilized EOM and sent to the adjacent ULE cavity. **B** The collimated light from the fiber-coupled 1389 nm repumper laser is divided into two beams after passing through a Faraday isolator. In two identical AOM single-pass configurations we prepare the light for the fiber coupling. Two home-built shutters prevent unwanted resonant leakage light.

mount.[68] While the laser diode current control is based on a *Toptica DCC110* driver, the temperature stabilization for both the mount and the diode is performed by a digital home-built controller based on the *Thorlabs MTD415T* module, which requires minor adjustments to the laser mount. The output power of 28 mW is distributed between two branches after the optical isolator,[69] each of which consists of an AOM[70] followed by a shutter and an achromat coupling the light into a standard PM fiber.[71] As optical powers of $\lesssim 1$ mW are sufficient to saturate the transition by a factor of 10^5 for standard beam sizes, the intensity stabilization loop is optimized for a large photodiode gain and low-voltage setpoints. Given the large power-broadened linewidth of $\Gamma \simeq 100$ MHz and the insensitive nature of the repump process, the laser is not actively frequency-stabilized, and instead we only routinely re-optimize the laser frequency by scanning the diode temperature setpoint, which offers a relatively coarse but accurate enough tuning knob with a slope of -15.4 GHz/K. However, as the experimentally observed linewidth of $\Gamma \simeq 4$ GHz due to relatively strong short-term fluctuations of the free-running laser is significantly larger than the atomic linewidth, a frequency stabilization could improve the repumping duration to well below 100 µs, which would speed up the clock sideband cooling process (Chapter 3) significantly.

---

[68] *Newport LDM-4984T*

[69] *Thorlabs IO-4-1390-VLP*

[70] *Gooch&Housego AOMO 3080-197*

[71] *Thorlabs P3-1310PM-FC-10*

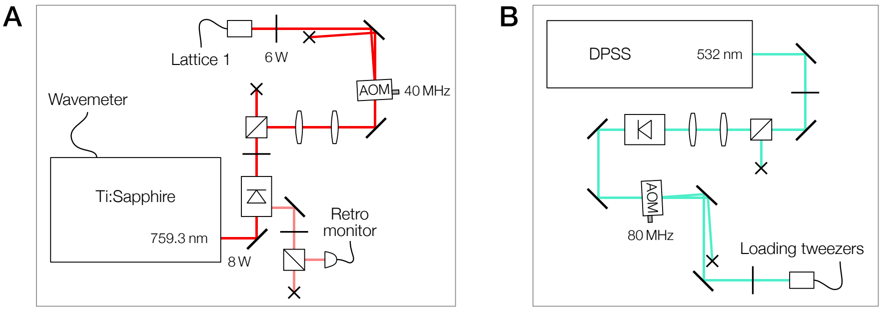

Figure 2.11 | Schematic of the lattice and the loading tweezer laser setups. A Simplified layout of the setup for the horizontal lattice arm 1, representative for all three lattice setups. Light from the Ti:Sapphire laser is sent through an optical isolator and an AOM until it is coupled into a PCF. For the horizontal lattices we monitor the retro-reflected power at the isolator rejection port (light red). **B** 532 nm tweezer setup. While overall very similar to the lattice setup, light from the laser is first beam-shaped to match the optimal size for the optical isolator, the AOM, and the fiber coupler.

2.4.5 Lattice laser setups

At the magic wavelength of 759 nm the most powerful available laser sources are Ti:Sapphire lasers. For our three lattice arms, we use three independent *Sirah Matisse CS* lasers, optically pumped with up to 25 W of 532 nm light by *Spectra-Physics Millennia eV* diode-pumped solid state (DPSS) lasers. The resulting output powers of up to 8 W in combination with a very Gaussian beam profile allow for as much as 4.6 W of lattice light after the fibers. About 10% of the power is lost at the Faraday isolator,[72] placed directly after the laser output and a periscope to direct the beam to a height of 35 mm. At the first rejection port of the isolators for the two horizontal lattice arms, we place a PBS, channeling the bulk of retro-reflected light into a high-power beam trap,[73] but also guiding a fraction onto a photodiode. This signal can be used for monitoring and optimization of the lattice alignment. In all three setups, the beam is then demagnified and diffracted by an AOM.[74] This AOM has been specifically selected due to its excellent thermal handling properties, as it exhibits negligible thermal pointing drifts even at a combined laser power of $\simeq 10$ W.[75] Separating the first order from the zeroth one by a D-shaped mirror and another high-power beam trap, we then couple the beam into the PCF using an aspheric lens.[76] As the two horizontal lattice arm setups are placed on the main optical table, the fibers are only 2 m long, while the setup for the vertical lattice is placed on the adjacent optical table such that a 4 m long fiber is sufficient to guide the beam at the desired position on the main breadboard.

---

[72] *Toptica SSR780*

[73] *Thorlabs BT600/M*

[74] *IntraAction AOM-402AF3*

[75] For this approximate result, we use $\simeq 3$ W of back-reflected power counter-propagating to the incident beam with a power of $\simeq 7$ W.

[76] *Thorlabs C397TMD-B*

2.4.6 Loading tweezer setup

As the laser source for the 532 nm loading tweezers we use a DPSS laser[77] with a power of up to 18 W. We again mount the laser on a honeycomb breadboard[78] to dampen mechanical noise from the water cooling. After the Faraday isolator[79] we use a cylindrical telescope to correct for the elliptical beam shape and diffract the light into the first order of an AOD.[80]. While the AOD requires an inconveniently large radio frequency (RF) power of 3 W at the center frequency of 80 MHz, the AOD provides a better high-power pointing stability than the modulators we tested at this wavelength. Given the very high optical power one requires for large arrays, this is an important prerequisite. The diffracted light is then coupled into a PCF,[52] transporting it onto the experimental table with an overall efficiency of ≃ 50% at a power of several W. We minimize the losses by placing the coupler as close as possible to the target fiber end position on the opposite optical table, allowing for a fiber length of 4 m. We plan to upgrade the setup in the future by switching the primary laser source to a 1064 nm, 55 W, very low-noise master oscillator power amplifier (MOPA),[81] which was originally planned to be used for a dipole trap. The light will then be single-pass frequency-doubled in a periodically poled Mg-doped stoichiometric lithium tantalate (PPMgSLT) SHG crystal [220, 221].

2.4.7 Tune-out laser setups

Since the uncertainties in the theoretical predictions for the tune-out wavelengths were considerable, we decided to use the less established but promising platform of vertical-external-cavity surface-emitting lasers (VECSELs), providing more than 10 nm of tuning range and output powers that exceed 1.5 W even at wavelengths that are almost unaccessible with, e.g., external-cavity diode lasers (ECDLs). In such a laser, a thin semiconductor gain chip is optically pumped by a strong laser at a lower wavelength; for our applications this is typically performed at 807 nm [222, 223]. The lasing cavity is then formed by the gain chip and a second, external mirror, such that the light is oscillating in free space. This space is used to place frequency-selective elements like etalon or birefringent filters (BRFs). For the tune-out wavelengths described in this thesis, one has to further double the frequency of the infrared fundamental light using a SHG crystal. In this case, typically V-shaped cavities are used, where the intermediate mirror is coated such that the frequency-doubled light is transmitted and outcoupled from the laser. While we also conceptualized and constructed a home-built VECSEL, which was tested to lase at ≃ 587 nm, we used commercial VECSELs[82] for the measurements due to their larger output power, better noise properties, and easier handling.

---

[77] *Coherent Verdi V18*

[78] *Thorlabs B6060A*

[79] *Thorlabs IO-5-532-VHP*

[80] *IntraAction ASD1002B47*

[81] *Coherent Mephisto MOPA*

[82] *Vexlum VALO SHG SF*

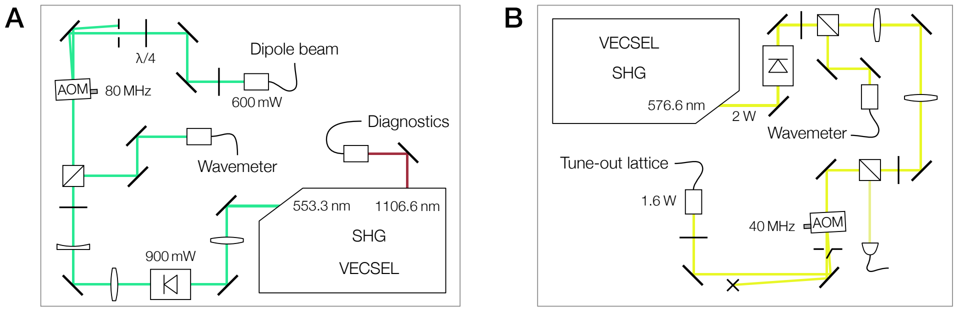

Figure 2.12 | Schematic of the green and yellow tune-out setups. A The 553 nm beam for the *g* tune-out wavelength is diverging as it exits the VECSEL, which is why we place a collimating lens close to the output. The beam then passes an optical isolator and telescope to resize the beam, until we couple the first order of a single-passed AOM into an end-capped fiber. **B** Similarly, the 577 nm light for the *e* tune-out lattice is collimated with a telescope and fiber-coupled after passing an AOM. To align the retro-reflected light back through the fiber, we pick up light at a cube in front of the AOM and place a temporary QWP in the beam path.

Green tune-out setup

The laser for the ground-state tune-out wavelength at 553.3 nm is mounted directly on the M3 breadboard. Owing to the laser design, the frequency-doubled Vexlum output beam is mildly divergent, necessitating an collimation lens after a periscope, but in front of the Faraday isolator[83] and a telescope. The laser beam is then split up into a branch that is coupled into a fiber leading to the wavemeter, and the main beam which passes through a standard 80 MHz AOM, which was recently replaced for a more power-stable 40 MHz AOM.[84] Up to $\simeq$900 mW of light are coupled into the fiber and guided to the optical table. However, the output power strongly depends on the precise temperature settings of the SHG crystal, the BRF, and the etalon and can change from mode to mode, which is why the maximum power used for the magic and g tune-out measurements is significantly lower. The laser can be locked to the wavemeter by feeding the error signal to a piezo-actuated mirror, thereby adjusting the cavity length to keep the frequency stable. As this laser constitutes a very early model of this type, it does not contain a second piezo like the newer yellow one, which would therefore require slightly more advanced solutions like a filtering cavity to allow for both fast and slow locks [224]. For the future application of this laser, which is mainly generating a potential offset for one state while leaving the other state unaffected, a wavemeter lock or even a free-running laser will most likely suffice as the induced potentials on the ground state for a detuning of a few GHz are still negligible (Chapter 4.2).

Yellow tune-out setup

Having noticed a distinct effect of the water cooling flowrate through the green Vexlum laser on its noise properties, we placed the laser for the 577 nm excited-state tune-out wavelength on

---

[83] *Thorlabs IO-5-560-HP*
[84] *IntraAction AOM-402AF1*

a damping honeycomb breadboard[85] to mitigate the vibrational motion from the chiller. We thus cannot use the custom M3-based optics mounts, which would commend a beam height of 35 mm, which we can exploit to omit the periscope. We therefore use the unorthodox height of $\simeq 43$ mm, corresponding to the laser output height. After the optical isolator[86] we pick up a beam for the wavemeter signal and collimate the main beam using a telescope. Due to the large output powers of up to 2.2 W and the corresponding thermalization issues we saw occurring with other AOMs, we utilize a very similar AOM[84] as for the lattices to allow for fast switching and intensity modulation. After a PBS that can be used for reflecting out the retro-reflected beam the light is coupled into a fiber with core-less end caps. Notably, because of the highly circular beam shape, we can achieve fiber coupling efficiencies of more than 75%. Furthermore, water absorption lines around the fundamental of the tune-out frequency strongly reduce the power output, necessitating a reduction in humidity to 11% by means of desiccant bags in the laser. Nonetheless, it is wise to avoid these frequency ranges during the tune-out measurement (Chapter 4.3).

2.4.8 Frequency locks

The lasers for the $^1\mathrm{P}_1$, $^3\mathrm{P}_1$, and $^3\mathrm{P}_0$ transitions are locked to an ultra-low-expansion (ULE) cavity – either directly via an offset Pound-Drever-Hall (PDH) lock or by means of a beatnote lock in the case of the Raman laser.

ULE PDH lock

The commercial reference cavity[87] that was purchased for this purpose consists of a single, 121 mm long ULE glass spacer[88] in a high-vacuum chamber onto which two high-reflectivity mirrors are optically contacted. The plano-concave cavity configuration with a radius of curvature of 1 m enables stable resonance conditions if the properties of the incoupled beams are matched to the cavity modes. The spacer rests on four pillars inside a vacuum chamber, pumped down to pressures of 10^{-9} mbar to thermally and acoustically isolate the cavity from the environment. A built-in Peltier element driven by a temperature controller[89] provides a thermally stable enviroment on the level of $\simeq 1$ mK, as measured by an out-of-loop thermistor. This, combined with an operation at the zero crossing of the CTE of the ULE spacer (Chapter 2.6.1), offers a stable frequency reference on the Hz level if the linear drift due to ageing is compensated by a feed-forward loop. As we lock lasers at three different wavelengths with increasing frequency stability requirements to the same cavity, the IBS coating is designed to yield a finesse of $> 10 \times 10^3$ for 798 nm and 1112 nm, and $> 150 \times 10^3$ for 1157 nm.

The ideal mounting direction of the breadboards around the cavity is vertical, connecting them directly to the vacuum chamber and deflecting the light by 90° through the horizontal cavity bore. With only limited breadboard space, we separate the blue from the yellow and

---

[85] *Newport*, custom design

[86] *Thorlabs IO-5-589-HP*

[87] *Menlo Systems ORC-Cylindric*

[88] *Corning, ULE 7973*

[89] *SRS PTC10*

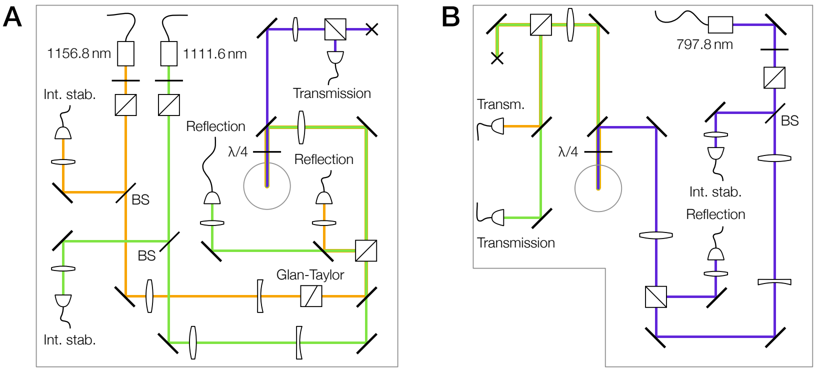

Figure 2.13 | Schematic of the optics around the reference cavity. A Layout of the green and yellow incoupling side. Light from the EOMs is collimated and sampled on a PD to allow for intensity stabilization. After a mode-shaping telescope the polarization of the 1157 nm beam is cleaned by a Glan-Taylor polarizer. The 1112 nm and the 1157 nm beams are superimposed on a dichroic mirror and focused onto the planar cavity mirror. Before passing through an achromatic QWP the transmitted 798 nm light is separated with a second dichroic. A mirror deflects the light onto the horizontal plane and into the cavity. The reflected light at each wavelength is monitored on separate PDs after a PBS and a dichroic mirror. To enhance the visibility, the color code of the respective frequency-doubled light has been used despite the infrared nature of all involved beams. **B** Layout of the blue incoupling side. Similar to the green and yellow breadboard, the 798 nm light passes a telescope, a PBS for reflection monitoring, a focusing lens, and an achromatic QWP until it is guided into the cavity. The transmitted 1112 nm and 1157 nm light is detected on PDs. At the position of the beam blocks one can place a camera to study the transverse cavity modes upon initial coupling into the cavity.

green optical paths, counterpropagating the respective beams in the cavity. The optical setups are displayed schematically in Fig. 2.13. To reach the optimal mode-matching conditions we shape the beam using a defocused telescope and a focusing lens. While the 798 nm light is coupled in from the planar side, the 1112 nm and 1157 nm light impinges on the concave mirror first, which is why here the refraction and propagation inside the spacer are taken into account to ensure the focus position at the planar mirror. For each beam, three photodiodes monitor the reflected and transmitted light as well as the total power after the fiber, allowing for intensity stabilization. After aligning the beams to the lowest transverse electromagnetic mode (TEM_{00}), we first verify the finesses by sweeping the laser frequency over the cavity resonance and observing the oscillatory behavior of the reflected light (Fig. 2.14 D). We can fit this ringdown feature caused by photons stored in the cavity with the solution of the differential equation [225]

$$\frac{dE}{dt} = -(1 - i\bar{\nu}t')E + i\eta, \tag{2.1}$$

where t' is the normalized field ringdown time, η is the drive rate containing the finesse $\mathcal{F}$ and the mirror transmission $\mathcal{T}$, and $\bar{\nu}$ is the parametrized frequency sweep rate, which also depends on the finesse. Numerically solving the result for the reflectivity and transmittivity, we obtain finesses of $26(2) \times 10^3$, $244(15) \times 10^3$, and $450(43) \times 10^3$ at 798 nm, 1112 nm, and 1157 nm, respectively, with the large uncertainty stemming from the multitude of fit parameters and, in the case of the clock light, a ringdown time exceeding the time over which the unlocked

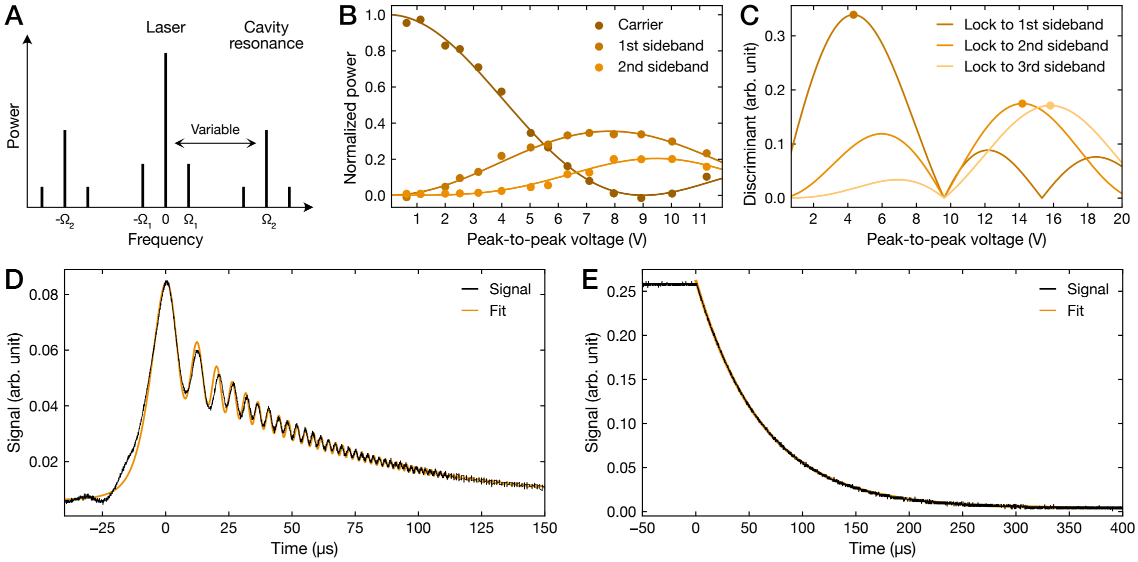

Figure 2.14 | Offset lock method, EOM characterization, and finesse measurements. A Light from the laser is phase-modulated to generate sidebands at Ω_1 and Ω_2. The sideband at Ω_2 is locked to the cavity resonance via the PDH sidebands at Ω_1, which allows for tuning of the fundamental laser frequency to match the atomic resonance. **B** Spectrally resolved power of the EOM for the clock laser as a function of the applied modulation depth. The solid line is a least-squares fit of the first three Bessel functions of the first kind, $J_{0,1,2}(V)$, to the data. **C** From this calibration one can determine the optimal voltage for a lock to the respective sideband. In this thesis, only locks to the first sideband are used. **D** Frequency sweep measurement of the cavity finesse at 1157.4 nm. The solid orange line is a fit to the data (black) and yields $\mathcal{F} = 450(43) \times 10^3$. **E** Photon storage ringdown measurement, which provides a more accurate value of the fitted finesse of $\mathcal{F} = 484.1(3) \times 10^3$.

laser is stable enough. Notably, this model takes losses at the mirrors from, e.g., absorption or scattering into account, thus using the expression

$$\mathcal{F} = \pi \frac{\sqrt{1 - \mathcal{T} - \mathcal{A}/2}}{\mathcal{T} + \mathcal{A}/2} \tag{2.2}$$

for the finesse, with the loss parameter $\mathcal{A}$ [226]. Despite the limitations, it is apparent that the finesses in particular for the MOT laser, but also for the clock greatly exceed the specifications and also surpass the values one can deduce from the calculated mirror reflectivities of 22×10^3, 178×10^3, and 339×10^3 for 798 nm, 1112 nm, and 1156 nm.

We lock the lasers to the cavity using a modified PDH technique, called offset or electronic sideband lock [116, 227, 228]. This allows us to tune the laser on the atomic resonance, to switch between isotopes, and to adjust this offset even during the measurement sequence. This method, which is illustrated in Fig. 2.14 A, relies on a lock to a modulation sideband with variable frequency Ω_1, which in turn is also phase-modulated at a lower frequency Ω_2 to generate a PDH error signal fed back to the laser. The resulting electric field is then given by [228]

$$E = E_0 e^{i(\omega_0 t + \beta_1 \sin(\Omega_1 t + \beta_2 \sin(\Omega_2 t)))}, \tag{2.3}$$

where ω_0 is the carrier frequency, and β_1 and β_2 are the modulation depths of the offset and the PDH sidebands, respectively. Expanding this expression up to second order in the modulation depths, this yields a power spectrum as in Fig. 2.14 B. Using this expansion, one can determine the frequency discriminant D, which describes the linear slope of the reflected power with respect to the detuning of the offset sideband from the cavity resonance for small detunings, to be

$$D = \frac{8\mathcal{F}P_0}{\Delta\nu_{\mathrm{FSR}}} J_1^2(\beta_1) J_0(\beta_2) J_1(\beta_2). \tag{2.4}$$

Here, $\Delta\nu_{\mathrm{FSR}} = c/2L = 1.236\,\mathrm{GHz}$ is the free spectral range (FSR) of the cavity, and $J_n(\beta)$ is the n-th order Bessel function of the first kind. From this relation one can read off the optimal modulation depths that maximize the discriminant to be $\beta_1 = 1.84$ and $\beta_2 = 1.03$, which can be transformed into RF powers by fitting the measured carrier and sideband powers after the EOMs[90] as a function of the applied voltage of the modulation signal (Fig. 2.14 C). To generate stable locks for each laser, we send the phase-modulated signal from the respective reflection photodetector through an amplifier and a mixer, which demodulates the PDH signal to provide the mixed-down linear response of the cavity. This is then low-pass filtered and turned into an actuation signal by a *Toptica FALC 110* module, which can be fed back to the laser by either controlling the diode current or the piezo voltage. In our case, the former is chosen. For the clock laser, we further clean the photodiode signal from any DC offset by placing a DC block in front of the low-noise amplifier, and we filter out high-frequency components from the other PDH locks as well as other noise. This is particularly necessary as the shared beam path and imperfect dichroics to separate the light at 1112 nm and 1157 nm can otherwise lead to strong cross talk between the two locks. With the laser referenced to the cavity, one can conduct a more precise measurement of the finesse at this wavelength by abruptly turning off the light with an AOM and studying the exponential decay of the transmitted light as the photons slowly leak out of the cavity (Fig. 2.14 E). This method yields a finesse of $\mathcal{F} = 269(1) \times 10^3$ for 1112 nm and $\mathcal{F} = 484.1(3) \times 10^3$ at 1157 nm.

In an effort to enhance the temperature stability of the cavity, the whole setup including the breadboards was encased in a plastic enclosure. To prevent the transfer of acoustic noise to the inside, the different segments are connected via a vibration-damping vinyl material. This enclosure reduces the amplitude of temperature fluctuations on the optical table by a factor of about 2 to $\Delta T \simeq 0.05\,\mathrm{mK}$.

Beatnote lock

Having a stable reference at hand, the Raman laser can be stabilized to the locked MOT laser at a variably detuning of up to several GHz by comparing the beatnote to a reference signal at the desired detuning. To this end, we superimpose the two beams at 556 nm on a separate breadboard using a NPBS. The light is then coupled into a single-mode PM fiber to avoid detrimental effects from imperfect wavefront or pointing overlap, and detected on a high-speed photodiode.[91] The frequency comparison and error signal generation is performed in

---

[90] *Jenoptik PM785* for 798 nm, *Jenoptik PM1064* for 1112 nm and 1157 nm

[91] *Thorlabs DET025AFC/M*

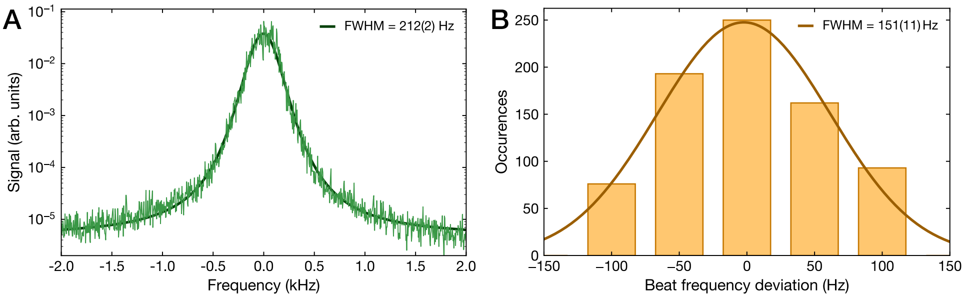

Figure 2.15 | Frequency stability of the cavity-locked 556 nm and 578 nm lasers, obtained by beatnote measurements. A Linewidth of the 3D MOT laser measured by beating its light with a similar laser locked to an identical cavity in an adjacent lab. The resulting linewidth is likely an overestimate as the long fiber between the labs presumably introduced a significant amount of additional noise. The full-width-half-maximum value refers to the 3 dB threshold. **B** Similarly, we detect the beatnote of our clock laser with the clock laser in a second neighboring lab [116]. We detect the frequency difference with a frequency counter and collect the deviation over a duration of 10 minutes.

a home-built lock box for detunings up to a few 100 MHz, while a modified RF evaluation board[92] allows for a phase-locked loop at larger detunings which would enable us to lock the Raman laser close to the $^3P_1$ $F' = 1/2$ transition, while the MOT laser has to remain at the $F' = 3/2$ transition [229].

2.5 MOT loading

Every experimental run starts by loading atoms into the 3D MOT, from where they can be transferred to a lattice or tweezer array. While the linewidth of the $^1S_0 \rightarrow {}^3P_1$ intercombination line offers a small Doppler temperature of $T_D = 4.4\,\mu K$, which benefits the handover of cold atoms to an optical trap, the maximum capture velocity of $v_c \simeq 7.2\,m/s$ (ignoring power broadening effects, cp. Chapter 1.3) for the beam sizes of $w_0 \simeq 5.5\,mm$ used to obtain the first MOT signal is markedly lower than the Zeeman-slowed mean longitudinal velocity of the atomic beam of $\langle v_x \rangle \simeq 40\,m/s$. To circumvent this discrepancy between ZS exit velocity and MOT capture range, in other experiments an additional 3D MOT stage using the broad $^1P_1$ transition has been employed [63, 162, 230, 231], as it is a standard procedure for Sr [64, 232–234], where this can also be combined with sawtooth-wave adiabatic passages (SWAP) [62, 235, 236] or frequency modulation [233] to artificially widen the effective linewidth of the $^3P_1$ transition. Similar modulation techniques have been employed in the first Yb experiments [194, 237] as well as modern tweezer setups [151] and have been predicted to work well for an AOSense system [238]. Inspired by the loading rate enhancement via crossed slowing beams at 399 nm prior to the 3D MOT in [239], however, we decided to investigate the feasibility of using a similar geometry in our setup.

---

[92] *Analog Devices EV-ADF4108EB1Z*

2.5.1 Slowing beams

In order to understand the necessity of the decelerating effect of the crossed slowing beams, we first study the properties of the Zeeman-slowed atomic beam as it propagates from the atom source to the glass cell. We assume a ballistic motion of the atoms as they emanate from the 2D MOT with the mean longitudinal velocity of $\langle v_\mathrm{x} \rangle = 40\,\mathrm{m/s}$ with the corresponding standard deviation of $\sigma_\mathrm{x} = 14.7\,\mathrm{m/s}$, as simulated by the manufacturer, and a transverse velocity distribution given by the radial temperature of $T_\mathrm{r} \simeq 4\,\mathrm{mK}$. By equating the kinetic and thermal energy we can identify the mean transverse velocity to be $\langle v_\mathrm{r} \rangle \simeq 0.6\,\mathrm{m/s}$. We further assume a uniform distribution of atom positions as they leave the first differential pumping tube and propagate the position and velocity vectors of a randomly chosen sample. This at hand, we can determine the portion and velocity of atoms that reach the MOT beam position in the center of the glass cell (Fig. 2.16 A). We further have to select for atoms that did not bounce off the walls of the second differential pumping tube, which poses a similarly stringent aperture limit given its small size. This yields a percentage of 3.1% of the initial flux that is accessible for our MOT. Crucially, owing to the relatively long flight distance of 645 mm to the MOT center, the longitudinal velocity distribution is markedly truncated at $v \lesssim 9\,\mathrm{m/s}$ as the slower atoms sag into the vacuum chamber before reaching the MOT. Hence, relying on the fraction of atoms with a velocity below the maximum MOT capture velocity consitutes an ineffective strategy, with maximally achievable loading rates of $2(1) \times 10^6\,\mathrm{s}^{-1}$ for ^{174}Yb at usual oven temperatures.

While an additional blue MOT, both in sequential or simultaneous shell configuration, allows for a significantly larger capture velocity range, it also greatly increases the complexity of the setup and the sequence and suffers from imperfect transfer efficiencies. Frequency-modulating the green MOT beams provides a relatively simple method of enhancing the capture rate, which is why this option was kept as a back-up. The easy-to-implement and yet effective slowing technique, however, allows us to directly address the atoms in the most prevalent velocity class while not disturbing the slower atoms that can be captured anyway. This is achieved by selecting a corresponding detuning of $\delta \simeq -90\,\mathrm{MHz}$ or $\simeq 3\Gamma$ to compensate for the Doppler shift at 40 m/s. The optimal combination of detuning and power is further governed by the distance of the crossing region to the MOT center, as the scattering of photons absorbed from the slowing beams lead to a redistribution of energy from the longitudinal into the radial dimension, which causes “blooming” of the atoms’ trajectories. This effect is minimized for short distances between the crossing region of the slowing beams and the MOT center, as realized in [239] where the slowing beams are guided parallel and close to the MOT beams. In our setup, this would limit the MOT beam size and, thus, the capture velocity, as they are designed to fill out the respective windows. Instead, we angle the slowing beams as described in Chapter 2.3.2 such that the beams will not intrude in any future beam path while keeping the crossing region close to the MOT. To quantify the expected increase in MOT loading rate, we simulate the slowing effect in two ways:

First, we perform a purely classical simulation, treating both the atomic motion and the light-atom interaction classically in a two-level picture. The latter is then described by the radiation force

$$\mathbf{F}_\mathrm{rad} = \hbar \mathbf{k} R_\mathrm{sc}, \tag{2.5}$$

where scattering rate R_{sc}, as defined in Eq. (1.40), depends on the local intensity $I(x, y, z)$ of the two slowing beams and the detuning $\delta' = \delta + \mathbf{k} \cdot \mathbf{v}$, accounting for the Doppler shift of the light with a wavevector $\mathbf{k}$ seen by an atom with velocity $\mathbf{v}$ (Chapter 1.3). This allows us to define an acceleration field generated by the two crossed slowing beams, each of them assumed to be Gaussian (Fig. 2.16 B, inset), and we can compute the atoms' dynamics by numerically solving the equation of motion, also taking the gravitational force into account. By evaluating the fraction of atoms within the capture velocity range, i.e., between 0 and 7.2 m/s, we can determine promising starting conditions for the tuning parameters power and detuning (Fig. 2.16 B). As anticipated, the largest capture rates are expected at a detuning of $\delta \simeq 90\,\text{MHz}$, and modest intensities of $I \simeq I_{\text{sat}} = 60\,\text{mW/cm}^2$ already suffice. Notably, this result overestimates the overall slowing efficiency as it assumes an idealized on-axis motion of the atoms through the crossing region. The calculation further neglects the discrete photon absorption and re-emission steps and the associated momentum kicks.

This diffusion effect in the transverse plane is taken care of in the second simulation, where we consider the interaction of the atom with the radiation field to be quantized. Choosing a Trotterization ansatz, we discretize the time propagation into steps of $\Delta t = 0.1 \times 1/\Gamma \simeq 3.4\,\text{ns}$, ensuring that the scattering probability per step is always much smaller than 1. Based on whether a randomly drawn number between 0 and 1 is below or above the scattering probability at the current atom position and velocity, we simulate a scattering event or perform a trivial propagation step. In the case of a scattering event, the change in momentum due to the absorption and re-emission into a randomly chosen direction is treated as a single process, and the atomic motion is computed according to the new velocity. In Fig. 2.16 C several sample traces are shown to illustrate the slowing as well as the "blooming" effect. For the simulation in Fig. 2.16 D-F, we stop each Monte Carlo run after ten million time steps or if the atom leaves the region of interest, which is given by the diameter of the glass cell tube of 11 mm in the radial and 2.5 mm behind the MOT center in the longitudinal direction, where the slowing beams cannot interact with the atoms any longer. To obtain reasonable initial phase space conditions, we randomly choose from two Gaussian distributions for the longitudinal and transverse velocities, respectively, and from a uniform distribution of positions at the first differential pumping tube end. We then perform the calculation of a ballistic motion again and reject the samples that would collide with the second differential pumping tube or the glass cell aperture. To decide if an atom counts as captured by the MOT after the Monte Carlo time propagation, we demand that its longitudinal position is close to or behind the MOT center and its velocity is below the maximum capture velocity. At each power and detuning combination we calculate the trajectory of 2000 atoms. From this we then obtain maximum MOT loading rates of $200 \times 10^6/\text{s}$ for a detuning of $-3\,\Gamma$ and a power of 12 mW, i.e., a colossal enhancement compared to the loading rate without the slowing beams. This result is supported by MOT loading measurements without slowing beams, which yield only marginal numbers of trapped atoms. However, we notice a strong dependence of the optimal slowing beam power on the atom source state and in particular on the ZS performance. While the best MOT loading rates were initially achieved at $P \simeq 4.5\,\text{mW}$, this later changed to 7.5 mW after we observed the onset of decay of the first oven. Fig. 2.16 H shows a typical MOT loading measurement as a function of the slowing beam power in the state of the experiment when this work was completed, i.e., with

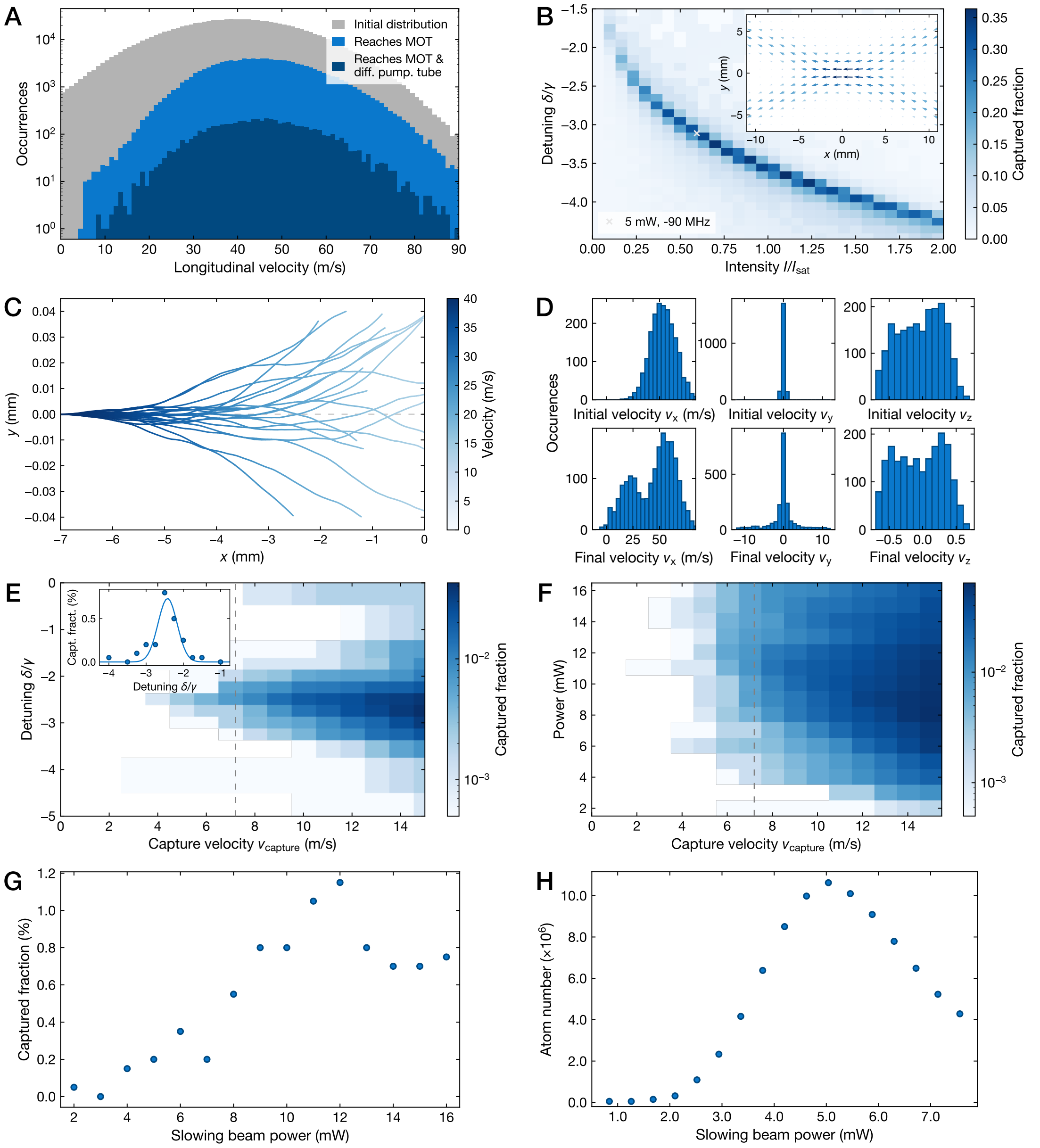

Figure 2.16 | Relevance and performance of the slowing beams. **A** Simulation of ballistic atomic motion out of the atom source tube. While 3% of the atoms pass through the second differential pumping tube and reach the MOT, the low-velocity tail of the longitudinal distribution is truncated. **B** Classical simulation of the slowing beam effect. We find the optimal parameter range at $\delta \simeq -3\,\Gamma$ and $I \simeq 0.6\, I_{\text{sat}}$. The position of the empirically optimized parameters $P \simeq 5\,\text{mW}$ and $\delta \simeq 90\,\text{MHz}$ is denoted by a cross. Inset: The radiation force field created by the crossed slowing beams in the horizontal plane. **C** Sample trajectories to illustrate the semiclassical simulation. Atoms starting with $v_x = 40\,\text{m/s}$ are slowed down as they absorb counter-propagating photons. Upon reemission, the random recoil kick broadens the horizontal velocity distribution, leading to a dispersed atomic beam. **D** Initial and final velocity distribution at $P \simeq 5\,\text{mW}$ and $\delta \simeq -90\,\text{MHz}$. **E** Fraction of captured atoms as a function of detuning and maximum capture velocity at $P \simeq 5\,\text{mW}$. Inset: Line cut at $v_c = 7.2\,\text{m/s}$ (grey dashed line). **F** Captured fraction for $\delta = -3\,\Gamma$. **G** Line cut at $v_c = 7.2\,\text{m/s}$. **H** Measured dependence of MOT loading rate on slowing beam power.

reduced MOT beam diameters. We attribute the discrepancy in the measured optimal power to the computed maximum to an imperfect alignment of the slowing beams. In particular, a larger distance to the MOT leads to a reduction of the optimal slowing power, as the transverse velocity distribution has to be narrower to allow the atoms to reach the MOT.

2.5.2 3D MOT

With active slowing beams and in the retro-reflecting three-beam setup, we were able to load 60×10^6 ^{174}Yb atoms within 1 s, with loading curves as in Fig. 2.17 B. To this end, we use a magnetic field gradient of $A_z = 4.9\,\mathrm{G/cm}$ along the vertical and $A_r = 2.4\,\mathrm{G/cm}$ in the horizontal directions, satisfying the trapping condition in the characteristic ellipsoidal shell region with a radius of $\hbar|\Delta|/\mu' A_r \simeq 2.2\,\mathrm{mm}$ and a thickness of $\hbar\Gamma\sqrt{1+I/I_{\mathrm{sat}}}/\mu' A_r \simeq 1.8\,\mathrm{mm}$ for a detuning of $\delta \simeq 36\,\Gamma$ and a power of $P = 60\,\mathrm{mW}$ in each beam, corresponding to an intensity of $I = 880\,I_{\mathrm{sat}}$. To reach dense atomic clouds as in Fig. 2.17 A, we compress the MOT by linearly increasing the gradient to $A_z = 15.6\,\mathrm{G/cm}$ within 100 ms and simultaneously ramping the detuning and the power down to $\delta \simeq 1\,\Gamma$ and $I \simeq 1\,I_{\mathrm{sat}}$, respectively. This does not only increase the density to $n \simeq 10^{11}\,\mathrm{atoms/cm^3}$, but also reduces the temperature to $T \simeq 35\,\mu\mathrm{K}$, as determined by time-of-flight absorption measurements (Fig. 2.17 D-E). Here, we utilize the dependence of momentum on temperature, $mv^2 = k_B T$, to fit the function

$$\sigma(t_{\mathrm{TOF}}) = \sqrt{\sigma_0^2 + \frac{k_B T}{m} t_{\mathrm{TOF}}^2} \tag{2.6}$$

to the extracted cloud sizes as a function of the time of flight t_{TOF}. Notably, while this temperature can be further reduced by choosing smaller final detunings and powers, this also quickly leads to increased atom loss. Whereas this trade-off is typically favorable in experiments that load a dipole trap or tweezer arrays, we find this comparably high temperature to provide the optimal signal for most of our lattice-based experiments, as it provides an efficient transfer into the lattice, which is turned on during the MOT compression ramp. After a hold time of 100 ms to allow the atoms to thermalize inside the lattice, the MOT beams are turned off and the magnetic field gradient is shunted.

In this setup, we simulated the situation with MOT beams created by two objectives by reducing the size of the vertical MOT beam with an iris. We observed that for equal detunings and unchanged power balancing the MOT performance remains almost steady up to a vertical beam size of $d \simeq 5\,\mathrm{mm}$, where an abrupt decay to zero at a beam diameter of 2 mm sets in, owing to the insufficient hold against gravity in large parts of the MOT. However, by tuning the relative intensities and reducing the detuning of the bottom beam one can counterbalance this deficit, which is the predominant reason for the mild reduction of MOT loading rate upon the insertion of the objective. Indeed, the majority of the $\simeq 35\%$ loss can be traced back to the lower MOT beam intensities of $I_r = 440\,I_{\mathrm{sat}}$ in the horizontal plane, $I_{\mathrm{bottom}} = 200\,I_{\mathrm{sat}}$ from the bottom, and $I_{\mathrm{top}} = 100\,I_{\mathrm{sat}}$ from the independent top beam.[93] This ratio in combination with a slightly larger gradient of $A_z = 5.5\,\mathrm{G/cm}$ and a detuning of $\delta_{\mathrm{bottom}} = 25\,\Gamma$ for the bottom beam

---

[93] Owing to its highly non-Gaussian, but rather flat-topped beam profile, the calculation of the MOT beam intensity after the objective assumes a uniform intensity across the beam.

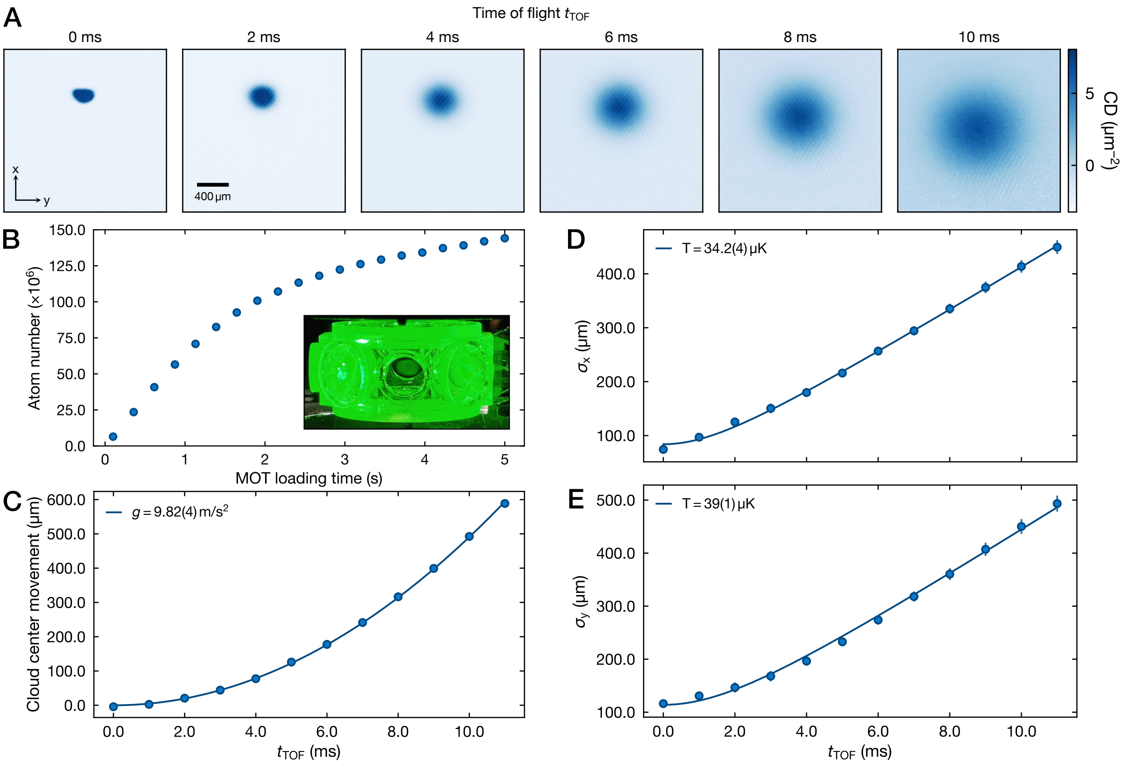

Figure 2.17 | Loading a 3D MOT. A Absorption images of the compressed MOT after varying the time of flight. Initially, the cloud is slightly deformed, but quickly becomes spherical as the atoms expand according to their initial momenta. Furthermore, they experience the gravitational pull along $-x$. **B** MOT loading rates of up to $\simeq 60 \times 10^6$/s could be achieved with maximal MOT beam sizes. The onset of saturation after 2 s is in part due to a too dense cloud which is not fully penetrated by the imaging light. Inset: Image of the uncompressed MOT of ^{174}Yb in the glass cell center, with its characteristic hollow-core shape due to the finite thickness over which the trapping condition is fulfilled. **C** By fitting the vertical cloud center position as the cloud drops after turning off the MOT we can calibrate the magnification of the absorption camera by ensuring that the fit yields the expected gravitational acceleration of $g = 9.81\,\mathrm{m/s^2}$. **D**, **E** Characterization of the MOT temperature by fitting Eq. (2.6) to the vertical and horizontal cloud sizes in A, respectively.

was found to be most optimal, but even an almost fully blocked top beam could be compensated for. This demonstrates the possibility of a five-beam MOT, which has been realized for Dy and Er [240] and was implemented in a recent Yb setup [241]. With the installation of the retro-reflecting mirrors for the horizontal lattice, the horizontal MOT beam sizes have also been compromised, leading to a reduction of the MOT loading rate by $\simeq 5\%$. In contrast to the loading parameters, which purely aim at maximal MOT atom numbers, in this final setup the compression powers and detunings are optimized for both atom number and temperature in the 3D lattice and the tweezers by maximizing the atom count in a shallow lattice or tweezer array. In this vein, we find a compression gradient of $A_z = 24.4\,\mathrm{G/cm}$ in combination with a detuning of $\delta_{\mathrm{bottom}} = 10\,\Gamma$ and $\delta_{\mathrm{r,top}} = 12\,\Gamma$ for the bottom and the remaining beams, respectively, at an intensity of $I \simeq 2\,I_{\mathrm{sat}}$ to work best. While the compressed MOT temperature of $T \simeq 30\,\mu\mathrm{K}$ is still significantly larger than the Doppler temperature, lower temperatures can only be achieved at the expense of atom loss. However, this temperature combined with the volume of $V \simeq 7 \times 10^{-5}\,\mathrm{cm}^3$ allows for a direct transfer into the 3D lattice or a tweezer array.

Notably, for large densities one has to ensure a sufficiently large power or small enough optical density, e.g., by choosing an extended time of flight. Thus, our standard MOT absorption images are taken with an imaging power of $P = 8\,\mathrm{mW}$, an imaging pulse duration of $50\,\mu\mathrm{s}$, and after a time of flight of 7.5 ms. Otherwise, the atom count is underestimated as the imaging light cannot fully penetrate the atomic cloud. We also take the non-linear dependence of the optical density on the imaging intensity in the modified Lambert-Beer law into account by experimentally calibrating the saturation count parameter, ensuring that the obtained atom count does not depend on the imaging power [242]. Hereby, we find an imaging-duration-dependent saturation count of $C_{\mathrm{sat}} = 169.367\,\mu\mathrm{s}^{-1}$.

2.6 Lattice loading

The eventual goal of our experiment, i.e., studying complex discrete systems based on Hubbard Hamiltonians, is facilitated by the use of judiciously engineered optical lattices (Chapter 1.4), but even for the steps en route lattices offer the trap depths, homogeneities, and versatility to serve as a pivot for most experiments. In contrast to the traditional approach, which uses time-consuming evaporative cooling in a dipole trap to then adiabatically load the BEC into the lattice, the direct loading from the MOT is fast, at the expense of a relatively high temperature of the atoms. While for early results like the magic wavelength measurements this did not impair the outcome, in-lattice cooling has become necessary for more advanced stages of the experiment and will be discussed in Chapter 3. In this Chapter we will discuss the setup and properties of the lattices used so far, but also delineate the standard manipulation and read-out processes we employ.

2.6.1 1D lattice

The main purpose of the one-dimensional lattice in the temporary setup was to set up the clock addressing infrastructure and to provide a reasonably deep trap for the tune-out modulation. To this end, the moderately focused lattice beams can create a standing wave with trap frequencies of up to $f_{\mathrm{l}} \simeq 90\,\mathrm{kHz}$ in the strongly confined dimension and $f_{\mathrm{r}} \simeq 280\,\mathrm{Hz}$ in the radial direction, as determined by parametric heating and lattice intensity quench experiments, respectively. The former technique utilizes modulation, in this case amplitude modulation, to observe a heating response at a multiple of the lattice trap frequency. Contrary to the tune-out modulation case, where only the atom count yields pronounced loss features around the resonance, modulating the lattice itself also leads to a fast, visible increase in the longitudinal temperature which we can detect by fitting the cloud size in the respective absorption images after a brief time of flight of $200\,\mu\mathrm{s}$ (Fig. 2.18 B). Notably, the width of the resonance feature strongly depends on the initial temperature of the sample as hotter atoms explore larger parts of the lattice site and therefore experience a weaker trap on average. For the lattice quench measurement to ascertain the trap frequencies along the weakly confined axes we abruptly increase the lattice

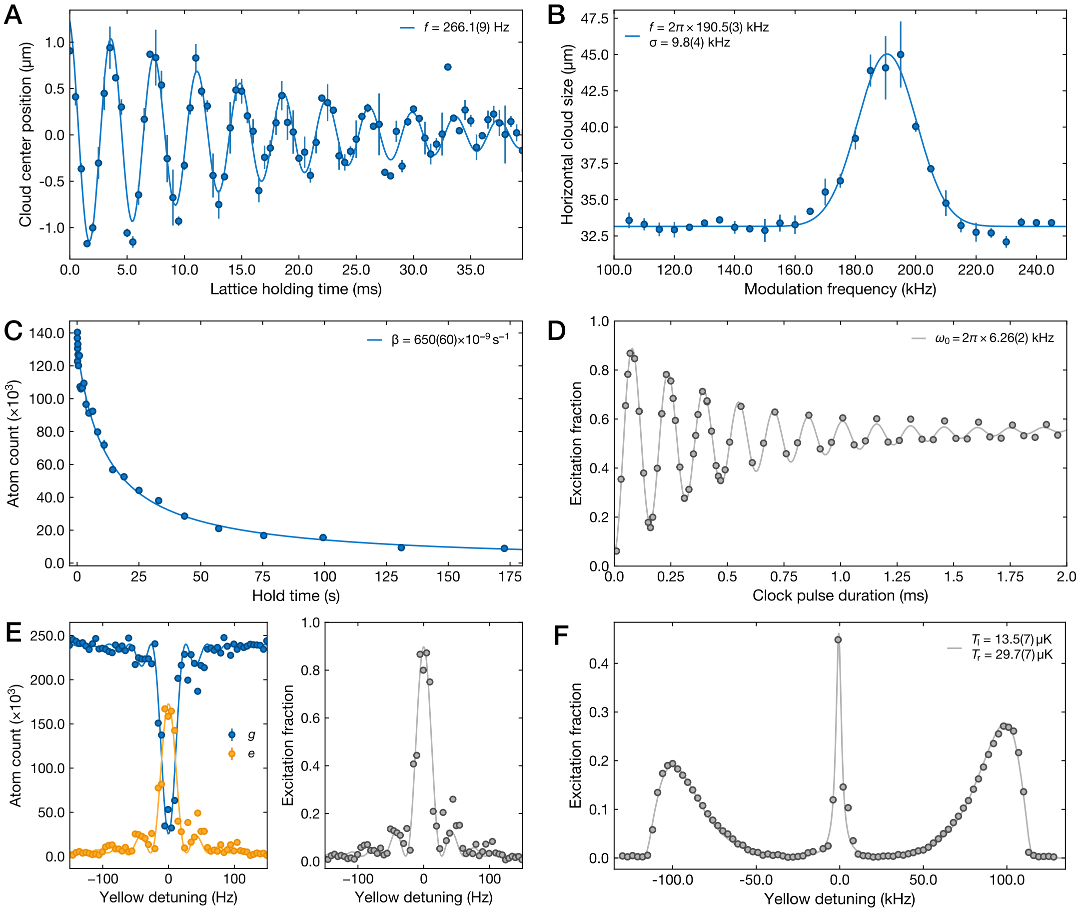

Figure 2.18 | 1D lattice characterization and clock spectroscopy. **A** Lattice quench measurement to ascertain the trap frequency along the weakly confined axes. A fast increase in the lattice depth induces a damped harmonic motion along the vertical direction as the total potential minimum including gravitational sag gets shifted upwards. This motion is detected by fitting a 2D Gaussian to the absorption images. **B** The trap frequency along the strongly confined axis determined by modulation spectroscopy. The parametric heating caused by amplitude modulation of the lattice is observed as a horizontally expanded cloud at twice the band gap. **C** Lifetime measurement in a deep 1D lattice. Scanning the hold time after turning off the MOT yields a decay that is well described by the two-body loss function Eq. (1.16) owing to collisions of relatively hot atoms at $T \simeq 20\,\mu\text{K}$. **D** Rabi oscillations on the clock transition at $B = 400\,\text{G}$ and with $P \simeq 300\,\text{mW}$ clock beam power. The fast visibility decay is a result of both temperature and collisional decoherence, which also limits the maximum excitation fraction into the clock state. **E** Coherent clock excitation spectrum after a π-pulse for a power of $P \simeq 500\,\mu\text{W}$ and $B = 30\,\text{G}$, yielding a Fourier-limited, fitted linewidth of $\Omega_0 = 15.8(4)\,\text{Hz}$. The significant difference between the g state depletion and the appearance of an e state peak on resonance is due to fast inelastic e-e collisions and lattice-induced losses from a Raman transition from the clock to the $(6s7s)^3\text{S}_1$ state, despite a massive detuning of 67 THz [72, 159], and an imperfect repumping efficiency. To obtain meaningful excitation fractions we thus correct for this calibrated discrepancy of $\simeq 25.3\%$ in 1D spectroscopy results. **F** Sideband spectroscopy of an uncooled cloud in a deep lattice. We can extract the axial trap frequency as well as the longitudinal and radial temperatures by fitting Eq. (2.9) to the data.

depth to the maximum after holding the atoms at a moderate depth. This sudden change in the harmonic trap frequency leads to a “sloshing” movement of the atomic cloud owing to gravitational sag, which can be observed as damped oscillations in the vertical cloud position at the trap frequency (Fig. 2.18 A).

These measurements can further help us elucidate the lattice waist and the polarizability of the $^1\mathrm{S}_1$ and $^3\mathrm{P}_1$ states at the magic wavelength. Equating the expressions for the radial and the longitudinal lattice trap frequencies, defined in Eq. (1.47) and Eq. (1.46), respectively, we can further estimate the lattice waist as

$$w = \frac{\sqrt{2}}{k_{\mathrm{lat}}} \frac{f_{\mathrm{l}}}{f_{\mathrm{r}}} = 61(3)\,\mu\mathrm{m}, \tag{2.7}$$

which however tends to underestimate the waist as the fit to the modulation spectroscopy result determines the mean trap frequency the atoms observe, which is less than the maximum trap frequency. By imaging the focus of the lattice beam we can obtain an independent gauge of the lattice waist of $w_0 = 67\left(^{+5}_{-1}\right)\,\mu\mathrm{m}$ in the atomic plane. These results can then be used to determine the intensity in combination with the calibrated photodiode voltage, corresponding to a power of $P_0 \simeq 3.9\,\mathrm{W}$. By calculating the lattice depth from the band gap between the lowest and the third lowest band we can convert the measured longitudinal trap frequency to the potential depth $V_0 \simeq 589\,E_{\mathrm{rec}}$, assuming a negligible fraction of atoms to be in higher harmonic levels that experience anharmonicities. From this we then get a polarizability of $10.6\,h\,\mathrm{Hz}/(\mathrm{Wcm}^{-1})$, which is in good agreement with values measured in the neighboring Yb lab [110, 243]. However, it deviates by 18% from the polarizability of $9\,h\,\mathrm{Hz}/(\mathrm{Wcm}^{-1})$ one can infer from [209]. Combined, we utilize these values to determine the uncertainty of the polarizability at the 759 nm magic wavelength to benchmark the empirical model in Chapter 1.2.

A second method of extracting the axial trap frequency f_{lat} is to perform sideband spectroscopy. While the $^3\mathrm{P}_1$ transition in Sr is narrow enough to allow for this technique in sufficiently deep traps, one has to resort to clock transitions for this purpose in the case of Yb. Despite the avoidance of trap-induced broadening effects in the magic lattice, it is still inherently challenging to obtain the first signal of the $^3\mathrm{P}_0$ transition. The standard procedure in this case is the detection of atom loss while the excitation frequency is swept across the resonance [116]. In our case, this was greatly aided by a beatnote measurement with the clock laser in the neighboring Yb lab (Fig. 2.15 B), helping us to precisely determine the cavity resonance position and, thus, the required offset lock frequency. This further allowed us to ascertain the zero-crossing temperature T_0, where the cavity length is extremal and the CTE vanishes up to first order. By measuring the beat frequency of both lasers while they are locked to their respective reference cavities and detecting the frequency shift for different cavity temperatures we find a parabolic behavior as expected, with an extremum at $T_0 = 25.435(4)$℃. Note that here the linear frequency shift of $\delta\dot{f} \simeq 58\,\mathrm{mHz/s}$, which was later determined via long-term spectroscopic measurements, initially obfuscated the signal, as the total duration of this measurement exceeded eight days. A second remarkable feature was observed in the transients. Following each temperature change, there is an almost immediate reaction of the cavity resonance, which was also observed in oscillations in the clock resonance position that were directly correlated to temperature oscillations of the laminar flow air curtain. A second, much slower, and crucially counterpropagating trend sets in on the timescale of several to tens of minutes. This initially caused significant confusion, as the transient behavior can seem very erratic, and only once the cavity has reached a thermal equilibrium again, which was typically found to be the case after $\simeq 1.5$ days, a meaningful frequency offset signal could be obtained.

Leveraging the stable frequency reference, we can trace the clock transition by detecting the loss of ground-state atoms as we scan the AOM frequency across the resonance. By employing the decay channel via the $^3\mathrm{D}_1$ repump transition (Chapter 1.1.2) we can also observe the simultaneous appearance of atoms in the $^3\mathrm{P}_0$ state [244].[94] Notably, in the bosonic isotopes such as ^{174}Yb one has to apply a considerable magnetic field to induce a finite transition matrix element. This can be utilized as an additional tuning knob to adjust the linewidth beyond power broadening. Therefore, in a standard spectroscopy sequence with ^{174}Yb the atoms in the lattice are exposed to clock light for a certain duration and at a given frequency while the Helmholtz field is on, followed by an absorption image of the atoms in the ground state after the coils are shunted. Since the atoms in the $^3\mathrm{P}_0$ state remain unaffected by the 399 nm light and the g atoms are entirely removed by a sufficiently long and powerful imaging pulse, a repump pulse can bring $\simeq 97.4\%$ of the e atoms back into the ground state, where they are imaged using a second absorption pulse. Subsequently, the lattice is turned off and the remaining reference and dark images are taken.

While in some measurements a fixed, long clock pulse duration is favorable, we mostly perform coherent clock spectroscopy, meaning that an exact π-pulse is applied when the laser is on resonance. This leads to a Fourier-limited lineshape as in Fig. 2.18 E, with the functional form of the fitting function given by Eq. (1.8). To identify the π-pulse time $T_\pi = \pi/\Omega_0$, we perform Rabi oscillations on resonance, which decay exponentially within a few oscillation periods unless sub-Doppler cooling is performed, as can be seen in Fig. 2.18 D. The corresponding dephasing is mostly induced by the occupation of multiple motional harmonic oscillator states and interaction shifts [142, 166].

For most of the time, such as for the magic wavelength spectroscopy runs in Chapter 4.1, we apply moderate magnetic fields of $B \simeq 100\,\mathrm{G}$ and clock powers of $P \simeq 10\,\mathrm{mW}$, which result in Rabi frequencies of $\Omega_0 \simeq 2\pi \times 50\,\mathrm{Hz}$. This allows for precision spectroscopy results with the ability to detect shifts on the order of a few Hz. For some measurements, however, it is desirable to achieve a fast transfer to the excited state, where Rabi frequencies of up to $\Omega_0 = 2\pi \times 2.8(1)\,\mathrm{kHz}$ at $B = 400\,\mathrm{G}$ and $P \simeq 300\,\mathrm{mW}$ can be used. This is particularly valuable in the case of sideband spectroscopy, as the Rabi frequency for driving a sideband transition is modified by the Lamb-Dicke parameter $\eta = \sqrt{E_\mathrm{rec}/hf_\mathrm{lat}}$, with E_rec the recoil energy of a clock transition photon. For a deep 1D lattice with $f_\mathrm{lat} \simeq 90\,\mathrm{kHz}$ this parameter is $\eta \lesssim 0.2$. Moreover, for a 3D ground-state fraction well below unity the sideband spectrum exhibits a distribution of resonances, which precludes a coherent excitation of all atoms at once. We therefore typically employ long, incoherent clock pulses with a duration of $> 10\,\mathrm{ms}$ to reach a dephased equilibrium, which allows us to obtain sideband spectra as in Fig. 2.18 F. From such spectra it is not only possible to extract the trap frequency along the clock beam, but also both

---

[94] While this is the most common method to bring the atoms back into the ground state, an adiabatic rapid passage as discussed in Chapter 1.1.2 can yield higher transfer efficiencies and does not require an additional laser [120, 245].

the longitudinal and radial temperature, T_l and T_r. While the former can be inferred from the ratio between the areas enclosed by the red and the blue sideband by inverting the relation

$$A_\mathrm{red}/A_\mathrm{blue} = \frac{\sum_{n_\mathrm{l}=1}^{\infty} e^{-n_\mathrm{l} h f_\mathrm{lat}/k_\mathrm{B} T_\mathrm{l}}}{\sum_{n_\mathrm{l}=0}^{\infty} e^{-n_\mathrm{l} h f_\mathrm{lat}/k_\mathrm{B} T_\mathrm{l}}} \tag{2.8}$$

which is derived from the respective Boltzmann distributions, the latter defines the shape and width of each sideband due the coupling term in the potential expansion Eq. (1.45). Intuitively, this can be understood as the effect of hotter atoms exploring larger parts of the pancake-shaped potential and therefore experiencing a weaker trapping force also along the longitudinal direction compared to very cold atoms in the radial motional ground state. Using Eq. (1.49) and assuming a thermal distribution of motional levels along the weakly confined axes we can approximate the blue and red sideband lineshape as [166]

$$P(\pm\delta)_\mathrm{b,r} = P_0 \sum_{n_\mathrm{l}=0,1}^{N_\mathrm{l}} e^{-\frac{E_{n_\mathrm{l}}}{k_\mathrm{B} T_\mathrm{l}}} \frac{h^4 f_\mathrm{l}^2}{E_\mathrm{rec}^2 k_\mathrm{B}^2 T_\mathrm{r}^2} (\gamma(n_\mathrm{l})_\mathrm{b,r} - \delta)\, e^{-\frac{h^2 f_\mathrm{l}}{E_\mathrm{rec} k_\mathrm{B} T_\mathrm{r}} (\gamma(n_\mathrm{l})_\mathrm{b,r} - \delta)} \Theta(\gamma(n_\mathrm{l})_\mathrm{b,r} - \delta) \tag{2.9}$$

with the negative sign of the detuning in the argument for the red sideband, the longitudinal energy gap $\gamma(n_\mathrm{l})_\mathrm{b} = f_\mathrm{l} - f_\mathrm{rec}(n_\mathrm{l} + 1)$ in the case of the blue and $\gamma(n_\mathrm{l})_\mathrm{r} = f_\mathrm{l} - f_\mathrm{rec} n_\mathrm{l}$ for the red sideband, the number of longitudinal harmonic oscillator levels $N_\mathrm{l} \simeq V_0/h f_\mathrm{l}$, and the Heaviside function Θ. We note that in this approximation only the linear dispersion of the harmonic oscillator states is considered, which is why this functional form is only valid for atomic clouds with sufficiently low temperatures with respect to the overall lattice depth, such that higher-order band structure corrections do not play a role. Applying this on the sideband spectrum in Fig. 2.18 F we obtain a longitudinal temperature of $T_\mathrm{l} = 13.5(7)\,\mu\mathrm{K}$ and a radial temperature of $T_\mathrm{r} = 29.7(7)\,\mu\mathrm{K}$, which also paradigmatically demonstrates the effect of a strong confinement on the Boltzmann distribution as well as the simple cooling technique of evaporating the hottest atoms that carry too much kinetic energy for the lattice, as both the longitudinal as well as the radial temperature is significantly lower than in the compressed MOT, but with a particularly sizeable difference for the former. This evaporation can be further enhanced by lowering the lattice depth even more, however at the expense of losing a significant amount of atoms. Holding the atoms in a $\simeq 700\,E_\mathrm{rec}$ deep lattice for variable hold times in turn leads to lifetime measurements as in Fig. 2.18 C, which are significantly affected by the large initial number of $\simeq 150$ atoms residing in a single lattice plane, where three-body collisions lead to a distinct deviation from an exponential decay. Instead a fit using Eq. (1.19) provides an excellent description of the loss curve. Therefore, we have to rely on much more sparsely filled 1D lattices or utilize the larger number of lattice sites in 2D and 3D lattices to obtain an estimate of the vacuum lifetime.

In a very similar fashion, we can also load ^{171}Yb atoms into the 1D lattice, despite the much lower scattering length (Chapter 1.1.3). Due to the non-zero nuclear spin, we can perform clock spectroscopy in significantly weaker magnetic fields and yet obtain faster Rabi frequencies of up to $\Omega_0 = 35(1)\,\mathrm{kHz}$, with the majority of the uncertainty stemming from a relatively slow response of the intensity controller for the first $\simeq 10\,\mu\mathrm{s}$. We further test optical pumping of both

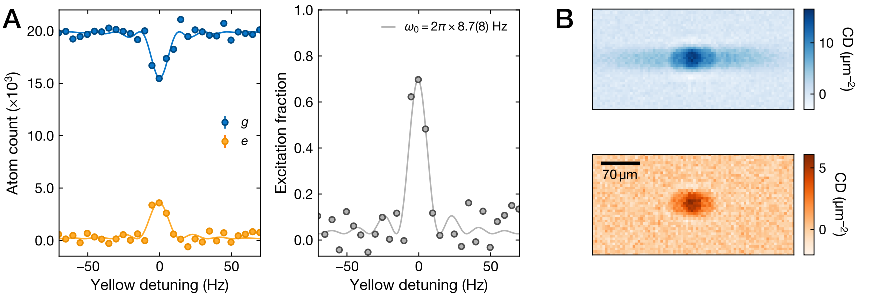

Figure 2.19 | Narrow spectroscopy in the 2D lattice. **A** Clock spectrum at $B = 50\,\mathrm{G}$ and $P \simeq 200\,\mu\mathrm{W}$. In comparison to Fig. 2.18 E the coherent clock excitation on the carrier is limited to the $N_{2D} \simeq 5 \times 10^3$ atoms in the 2D crossing region, while the majority of atoms in the 1D lattice wings observes a Doppler-broadened resonance. We therefore apply a correction factor of 3.7 to obtain the excitation fraction in the right panel. **B** Absorption images for g (top, blue) and e (bottom, red) state images. Clearly visible is the absence of atoms in the 1D lattice wings in the e image.

m_F states on the $^3\mathrm{P}_1$ transition, which will be of relevance for the initialization of spin-polarized samples and the dissipative step of the Raman sideband cooling process (Chapter 3.3).

2.6.2 2D lattice

As the horizontal 2D lattice consists of two independent retro-reflected 1D lattices, we combine them by iteratively moving one lattice axis until they appear at the same height in absorption images and cross at the desired position in the horizontal plane as determined via fluorescence imaging from below. Owing to the weak confinement along the vertical direction the signal from the latter is faint and one is restricted to very low imaging powers to not lose most atoms after very few scattering events. Therefore, an additional, however more coarse indicator of the 2D crossing region are the optimal x and y shim coil field strengths to efficiently load into each lattice arm. As in the 1D case, we can load the 2D lattice directly from the 3D MOT. Despite a moderate depth of $V_0 \simeq 350\, E_{\mathrm{rec}}$ in each arm, a significant number of atoms also populates the 1D lattice branches outside of the crossing region. A pure 2D lattice occupation can then be achieved by turning one lattice arm off at a time and handing the atoms over in between.

Performing an analysis of the individual lattice sizes by comparing the radial and longitudinal trap frequencies as in Eq. (2.7), we obtain waists of $w_0 = 44(2)\,\mu\mathrm{m}$, which is significantly larger than the $32\,\mu\mathrm{m}$ we would expect from Gaussian beam propagation computations. We attribute this deviation to aberrations induced by the focusing lens.

This step is not necessary in the case of clock spectroscopy with clock beam 3, which is not superimposed on any lattice axis. Hence, only atoms in the 2D lattice region can be addressed in the Lamb-Dicke regime and almost all atoms in the 1D lattice branches will be detuned due to their Doppler shift. In the clock-state absorption image after the repumping step we can thus identify the pure 2D crossing region. With a total number of tubes of $\simeq 25 \times 10^3$ and a typical atom number of $N \simeq 20 \times 10^3$ the maximum occupation on a single site is much smaller than in the 1D case, where the mean occupation number per layer in standard spectroscopy sequences was found to be 70(11). Remarkably, this allowed for very narrow spectroscopy results in a cloud cooled to $T \simeq 12\,\mu\mathrm{K}$ by aggressive spilling to $V_0 \simeq 220\,E_{\mathrm{rec}}$, with linewidths $\Gamma_{\mathrm{2D}} < 10\,\mathrm{Hz}$. This indicates that the minimum linewidths of $\Gamma_{\mathrm{1D}} \simeq 30\,\mathrm{Hz}$ obtained in the 1D lattice were actually interaction-limited. An exemplary signal is depicted in Fig. 2.19 A, at $B = 50\,\mathrm{G}$ and $P \simeq 200\,\mu\mathrm{W}$. At this point, the clock pulses reach durations of up to 100 ms, which leaves the atoms in a superposition with the ${}^3\mathrm{P}_0$ state for a significant period. However, due to the Raman scattering process via the $(6s7s)^3\mathrm{S}_1$ state (Chapter 4.3) and large inelastic collision coefficients [143] the $1/e$ lifetime of this state in a 2D lattice at this depth and at such moderate temperatures is limited to few 100 ms, which complicates further reductions of the linewidth in this configuration.

Similar to the 1D lattice case, we can also perform sideband spectroscopy in the 2D lattice. However, here the relatively simple result of Eq. (2.9) breaks down as the two radial axes can no longer be described by a single frequency and cold atoms do not necessarily occupy the trap center anymore. Instead, they might be trapped in a tube in a shallow part of the lattice arm along which we probe the sideband occupation. We therefore observe a wider distribution of sideband frequencies, which can be fitted by the model discussed in Chapter 3.

2.6.3 Vertical lattice

To reach the strong confinement in all three dimensions necessary for efficient fluorescence imaging we further equip our experiment with a vertical lattice. For this purpose, a wide array of design choices has been explored already, in particular in the context of quantum gas microscopy. This was mostly driven by the challenge to simultaneously achieve large trap frequencies, wide spacings to simplify loading into a single plane, and minimal instabilities. While a retro-reflected vertical lattice is power-efficient and can provide excellent phase stability, it requires a suitably high-reflectance-coated and shaped surface in front or within the objective, and the small resulting vertical lattice constant renders the removal of atoms in unwanted planes challenging. So far, "slicing" on such a compact scale has only been successfully performed in alkali metals by selectively detuning atoms on a magnetically sensitive transition via a magnetic field gradient [36, 246–248]. Using the ${}^3\mathrm{P}_2$ clock transition, one can circumvent the weakly susceptible nature of most transitions in Yb to magnetic fields as this ultra-narrow transition features a sufficiently large Zeeman splitting to allow for a resolution of individual planes in typical gradients. This was demonstrated to work in a vertical lattice generated by two beams intersecting at a shallow angle θ [80], which increases the lattice constant as

$$a_{\mathrm{v}} = \frac{\lambda}{2\sin(\theta)}. \tag{2.10}$$

This larger spacing has also been exploited for magnetically targeting a single remaining plane in alkali-based microscopes, where narrow hyperfine-structure transitions can be used to selectively remove or shelve atoms [35, 249–252]. In Yb, however, the necessity of a stabilized clock laser at the ${}^3\mathrm{P}_2$ transition at 507 nm renders this technique prohibitively complex if the generation of a single 2D plane is its sole purpose. In contrast, accordion lattices with variable intersection angles allow for very wide spacings initially to load just a single lattice plane from the previous trap, which can then contract to a tight lattice during imaging [37, 198, 253, 254].

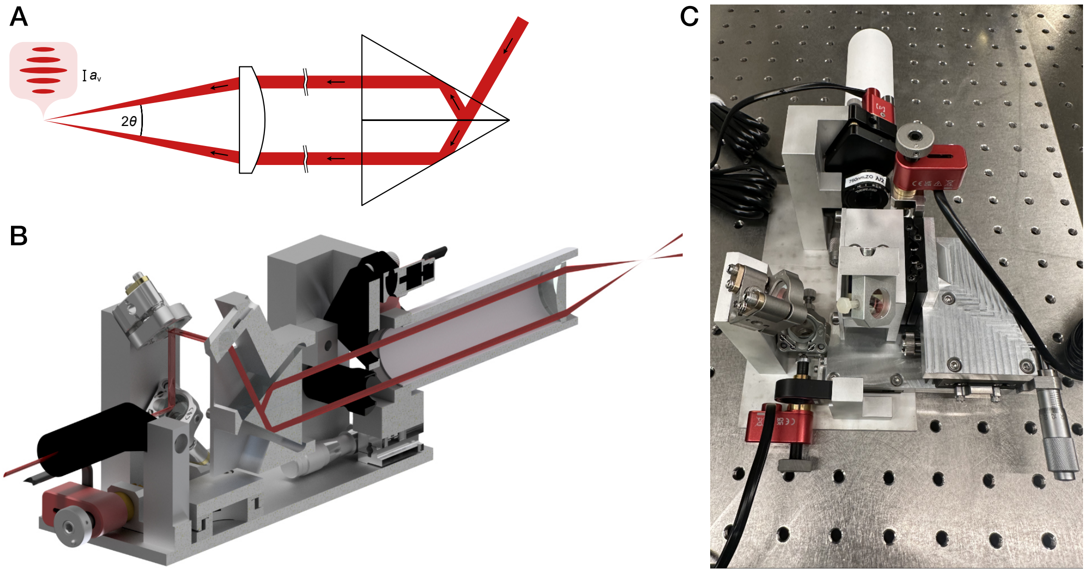

Figure 2.20 | Vertical lattice mount. **A** Schematic of the working principle. A Kösters prism generates two parallel beams, which are focused and brought to interference by a lens. **B** Cross section of the mount and relevant optics. The ingoing beam can be reproducibly aligned onto the mount using two irises in between a long lens tube. Two mirrors are used to steer the beam onto the fixed mirror mount, which guides the beam towards the prism. Before traversing a lens tube, which holds the aspheric focusing lens, each beam propagates through a window, which can be tilted for the upper beam. This allows for tuning of the interference phase. **C** Picture of the mount in a test setup without the irises installed. However, a waveplate was mounted in the upper beam, which was later removed as the prism does not measurably change the relative polarization.

This flexibility comes at the cost of reduced passive stability, in particular due to asymmetric beam paths or mechanical motion. A third approach utilizes a strongly focused light sheet in lieu of a lattice to provide additional vertical confinement [65, 255], which avoids the generation of multiple planes but limits the attainable trap frequencies in this dimension.

Choosing a maximally symmetric ansatz to generate a shallow-angle lattice, we aim at a highly stable system, combined with a moderate vertical lattice spacing of $a_\mathrm{v} = 2.2\,\mu\mathrm{m}$ and depths of up to $f_\mathrm{v} = 45\,\mathrm{kHz}$. The design follows the conception in [256], where a Kösters prism,[95] consisting of two symmetric, fused-silica halves glued together to form a non-polarizing, equilateral triangle, is used to split a single, collimated incoming beam into two parallel beams. In the optimally aligned case, an aspheric lens then recombines the beams at the focus, causing the desired interference fringes (Fig. 2.20 A). Therefore, the number of degrees of freedom upon alignment is limited owing to the inherent symmetry, and a worst-case difference in the beam path lengths of less than 400 µm can be deducted from simple geometric considerations, taking into account mechanical tolerances and a misaligned setup that generates a lattice with a potential equal to half the maximally possible depth. While designs with other prisms such as Wollaston prisms or PBS have also been brought to fruition [252, 257], they suffer from the drawback that they either require a focus inside the crystal to

---

[95] *B. Halle, IKP 040*

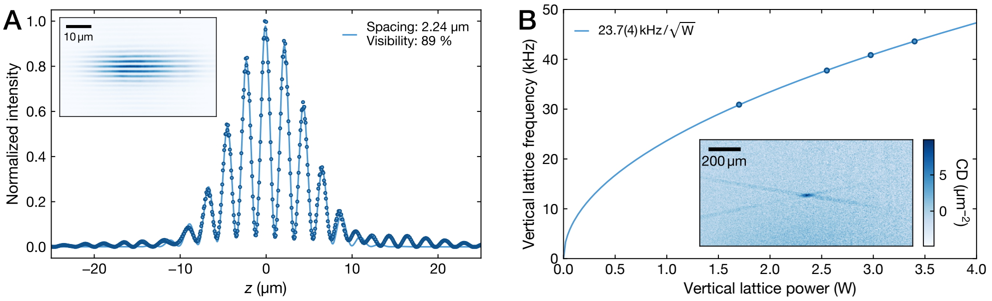

Figure 2.21 | Characterization of the vertical lattice. A Horizontally integrated intensity profile measured in the test setup. The solid line is a least-squares fit using Eq. (2.11), from which we obtain the visibility and lattice spacing. The *x*-axis is corrected for the magnification of 25. Inset: Image of the magnified vertical lattice. **B** Lattice depth calibration using modulation spectroscopy and fitting the peaks in the cloud size, similar to Fig. 2.18. The least-squares fit indicates a maximum trap frequency of $f_z = 48$ kHz at $P = 4$ W total power. Inset: Absorption image of atoms trapped in the vertical lattice as well as the dipole traps formed by the individual beams outside the crossing region.

image both crossing and focus onto the atoms with a telescope, which can quickly lead to dire spherical or coma aberrations, or a set of at least two independent mirrors, which opens the door to position and phase drifts of the lattice due to relative mechanical motion.

In the setup depicted in Fig. 2.20 the angle θ and, in conjunction, the lattice spacing a_v are determined by the distance between the parallel beams in front of the lens and its focal length. A strict upper bound of $2\theta_{\max} = 24°$ is further set by the size of the glass cell bore of 11 mm. Taking the finite beam size, the protrusions to retain the lens, and slight margins for alignment into account, we find an angle of $2\theta \simeq 20°$ to be optimal. This corresponds to a beam separation of $d \simeq 18$ mm for a focal length of $f = 50$ mm, which conveniently allows for the usage of an off-the-shelf asphere with a diameter of 25 mm.[96] Targeting a vertical extent below 20 μm to contain less than 10 planes, the vertical beam size in front of the lens is required to be $w_{0,z} = 1.5$ mm. With a cylindrical 3:1 telescope[97] we expand the horizontal beam size in the atomic plane to a waist of $w_{0,y} = 26.6(3)$ μm, approximately concurring with the Gaussian envelope of the horizontal lattice beams. In Fig. 2.21 A, inset, an image of the lattice at the focus is shown, taken in a test setup with a magnification of 25. Crucially, the fitted vertical dimension of $w_{0,z} = 8.7(1)$ μm is quite close to the theoretical expectation of 7.8 μm, indicating that the aspheric lens indeed images the beam with a close-to-diffraction-limited performance, despite the eccentric beam positions. Similarly important is a high contrast, which we consistently find to be $V \gtrsim 90\%$ by fitting the function

$$P(z) = A\, e^{-2z^2/w_{0,z}^2} \left(C \cos(\pi z/a_v)^2 + 1 - C\right) \tag{2.11}$$

to a vertical line cut of images taken in the test setup and extracting the visibility

$$V = \frac{I_{\max} - I_{\min}}{I_{\max} + I_{\min}} = \frac{C}{2 - C} \tag{2.12}$$

---

[96] *Asphericon ALL25-50-U-U*

[97] This telescope is mounted under an angle of $\vartheta \simeq 30°$ with respect to the vertical axis to account for the 60° deflection at the mirror in front of the prism

from the fitted baseline C. We attribute the finite baseline to imperfect power splitting at the prism and small aberration effects, while polarization mismatch seems to play a negligible role. Furthermore, we can extract the lattice constant $a_\text{v} = 2.23(1)\,\mu\text{m}$ from this fit. To obtain a more complete picture of the full 2D interference pattern, we integrate the signal over all columns. We then determine the image rotation angle that maximizes the spacing by analyzing the high-frequency column power of the Fourier-transformed image. This takes a potential tilt of the lattice plane with respect to the horizontal axis into account. As we would expect, this rotation is consistently found to be well below 1°. Fitting the resulting integrated intensity profile with Eq. (2.11) as displayed in Fig. 2.21 A yields very similar results aside from a slightly worse visibility of $V = 89(1)\%$, with the uncertainty determined from the results of several alignment iterations. To benchmark the fitted lattice constant a_v, we further detect the position of the high-frequency peak in the Fourier-transformed integrated line cut, which agrees with the fit result within error bars.

Aligning the vertical lattice is made possible by means of several high-precision motional stages. The longitudinal position can be adjusted by a translation stage,[98] onto which a 100 mm long lens tube is mounted, which in turn holds the asphere. This lens tube is made of the low-CTE ceramic *Macor* to reduce the effect of local temperature changes from the nearby main coils. The independent prism mount can be adjusted in pitch and yaw, which would ideally transform into purely translational changes in the horizontal and vertical direction, respectively, if the prism could be mounted at a distance equal to the focal plane of the lens. However, this ideal setup, which has been realized in [256], is not feasible in our case due to space constraints.[99] Therefore, any tip or tilt of the prism inevitably induces a collateral rotation of the lattice planes, which is inconsequential for a rotation around the vertical lattice axis. Any undesired rotation around the transverse horizontal axis, on the other hand, has to be compensated by a vertical translation of the prism (Fig. 2.22). To minimize the effect of any alignment step on the vertical lattice properties, in particular on the distance and parallelism of the two beams after the prism, the goniometer[100] and rotation stage[101] for pitch and yaw adjustments are mounted to cause a rotation around the center of the fixed incoupling mirror that is attached to the top of the prism mount. To ensure a reliable and reproducible alignment of the lattice beam on this mirror, in particular after the insertion into the experiment where no direct diagnostics is possible, we utilize a detachable set of two irises in front of the periscope mirrors, connected by a 170 mm long lens tube. Hence, a singular alignment of the periscope mirrors in a test setup is sufficient to achieve overlap of beam waists and crossing with the desired lattice constant. To maintain this initial alignment, the mirror mounts[102] are thermally compensated to withstand drifts caused by temperature changes. To counteract phase fluctuations and to ensure a stably centered position of the main lattice plane, a picomotor-driven mirror mount[103] can slightly

---

[98] *Newport M-SDS25*

[99] In contrast to the setup in [256], a $f = 100$ mm aspheric lens would lead to a beam separation of 36 µm and a vertical beam size of $w_0 = 3$ mm, which would exceed the size of the Kösters prism.

[100] *OptoSigma GOHT-40A40BMSR*

[101] *OptoSigma KSPT-406MH*, customized for picomotor compatibility

[102] *Newport Suprema ZeroDrift ST05-F2H*

[103] *Newport 8886*

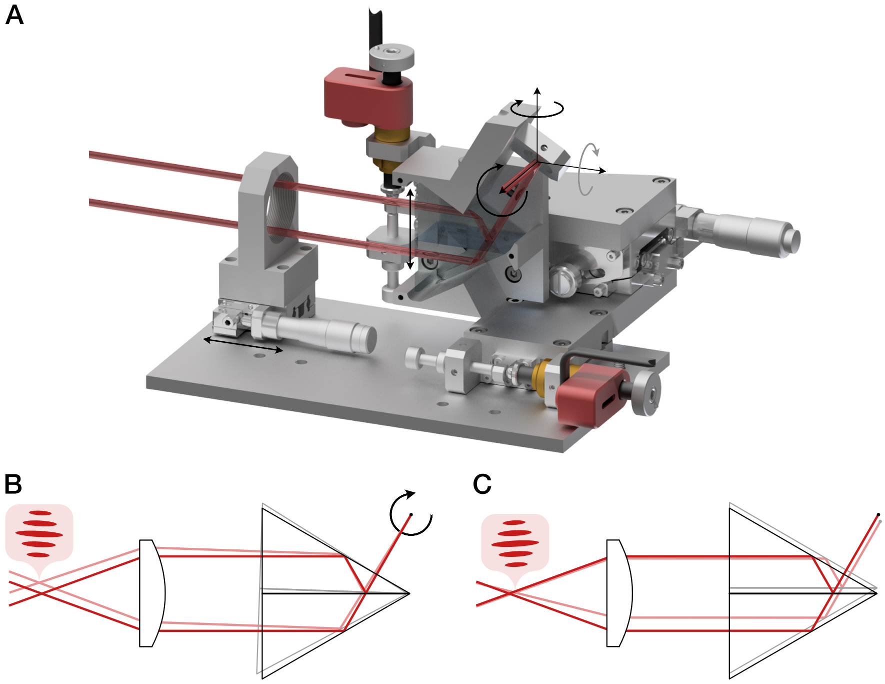

Figure 2.22 | Alignment of the vertical lattice. **A** Degrees of freedom of the vertical lattice mount. A translation stage controlling the position of the focusing lens allows for longitudinal alignment, while a picomotor-controlled rotation stage adjusts the transverse horizontal position of the lattice. The vertical position and tilt is defined by a goniometer and a translation-stage. Both rotation axes are chosen to pass through the incoupling mirror, which is firmly attached to the prism mount. This ensures that the beam impinges on the prism under the optimal angle of 60° with respect to the splitting plane, guaranteeing parallel beams after the prism. The roll degree of freedom is not adjustable as the corresponding lattice tilt was found to be negligible. **B** Exaggerated visualization of the effect on the lattice by adjusting the goniometer and **C** the vertical translation stage. As the distance from the splitting plane to the lens exceeds the focal length, a rotation of the prism does not only result in a vertical translation, but also in a small tilt of the lattice planes. This can be compensated by a prism translation. However, due to limited space the translation stage is not oriented parallel to the ingoing beam and therefore any adjustment will also lead to a changed beam separation and, hence, lattice spacing. Higher-order effects involve longitudinal shifts of the crossing point.

rotate a 3.2 mm thick, nano-textured window.[104] A tilt of $\delta\theta = 1.45°$ encompasses a relative phase change of 2π with respect to the second beam passing through the same window, but in a fixed mount. With an overall transmission of $T \simeq 96\%$ of the whole setup at the lattice wavelength a total power of $P_{\text{diss}} \simeq 50\,\text{mW}$ is dissipated at and within the optics at full power.

Before obtaining a first signal of the prealigned vertical lattice we first test the heating-induced pressure increase, as the lattice beams provoke local heating and thus diffusion and desorption of various gases from the glass cell tubing where their power is partially absorbed. To this end, we slowly ramp up the lattice power until we see a response on the hot cathode gauge, which initially happened at $P \simeq 2\,\text{W}$ total power after the fiber. From this point on, we incrementally increase the power and wait for the pressure to settle. Despite the gradualness the pressure had risen to 1.2×10^{-10} mbar after we reached the full power for the first time,

---

[104] *Newport 05Q20RAR.L*

but decreased back to the base level within the next hours. We perform this step whenever the vertical lattice has been realigned, although the pressure increase is typically not detectable if the lattice position is only marginally adjusted. Consequently, we trace the lattice beams by scanning the shim coil currents around the expected position until a signal of captured atoms is visible in absorption images. Crucially, the individual lattice beams provide a sufficiently confining potential to trap atoms not only in the interference region, but also in the dipole traps as can be seen in Fig. 2.21 B, inset, which eases the search for the initial signal significantly.

We probe the potential generated by the vertical lattice with modulation spectroscopy and find that we can approximately reach the calculated trap frequency of 46.0 kHz for a total power of $P = 4\,\mathrm{W}$ (Fig. 2.21 B), assuming perfect interference of two equally strong, unaberrated beams, which intersect at an angle of $2\theta = 20°$.

2.6.4 3D lattice

After initial alignment, the vertical lattice was displaced by a few mm from the 2D lattice, mostly due to an off-centered position of the 2D lattice. As more substantial translations are easier to accomplish by moving the horizontal lattices, we align them iteratively onto the vertical lattice position by taking sequential images of the individual lattice beams to create a 3D lattice with a maximum total depth of $V_{3\mathrm{D}} \simeq 6000\,E_{\mathrm{rec}}$. This does not only allow for fluorescence imaging, which will be discussed in detail in Chapter 2.7.5, but also leads to a remarkable lattice loading pattern (Fig. 2.23). The typical lattice loading regime used in the 1D lattice measurements is a $1000\,E_{\mathrm{rec}}$ deep trap, beyond which a reduction of the loading efficiency is observed. In a 2D lattice we find a very similar optimum of the total lattice depth, indicating that this phenomenon is rather related to the total trap depth or intensity instead of, e.g., the inhibition of thermalization of MOT-cooled atoms by a reduced atom density per lattice site. The vertical lattice then adds a third layer to study this effect, and fluorescence imaging allows to study the population only in the 3D region, where the molasses cooling is effective. Here we can detect a balancing effect where a shallower horizontal lattice can be compensated by a deeper vertical one, offering a local optimum at a combined horizontal lattice power of $\simeq 900\,E_{\mathrm{rec}}$ and at $\simeq 300\,E_{\mathrm{rec}}$ vertical lattice depth. We find a significantly stronger global maximum, however, in a very deep 3D lattice configuration at $\simeq 4000\,E_{\mathrm{rec}}$ horizontal and $\simeq 1000\,E_{\mathrm{rec}}$ vertical depth, allowing for loading rates of $\simeq 70 \times 10^3$ atoms within just 100 ms, which roughly corresponds to a 3D filling fraction of 0.5. We confirm via absorption imaging that in this deep loading regime only the 3D lattice region is populated, indeed, since the individual lattice arms remain in the intermediate depletion condition. Upon changing the MOT compression detuning and gradient parameters, we find weak trends towards an optimum at larger depths for larger detunings, while a MOT beam frequency closer to resonance appears to allow for weaker loading lattices. Notably, we cannot resolve any change in the optimal MOT compression detunings compared to the weaker loading regime. We hypothesize that in the intermediate, bad loading regime the lattice, being non-magic for the MOT transition, detunes the atoms out of the MOT resonance condition at the lattice wells, while for even deeper lattices the stronger Stark shift in combination with the very strong attractive potential allows for rethermalization into the lattice despite subpar MOT conditions. However, we note

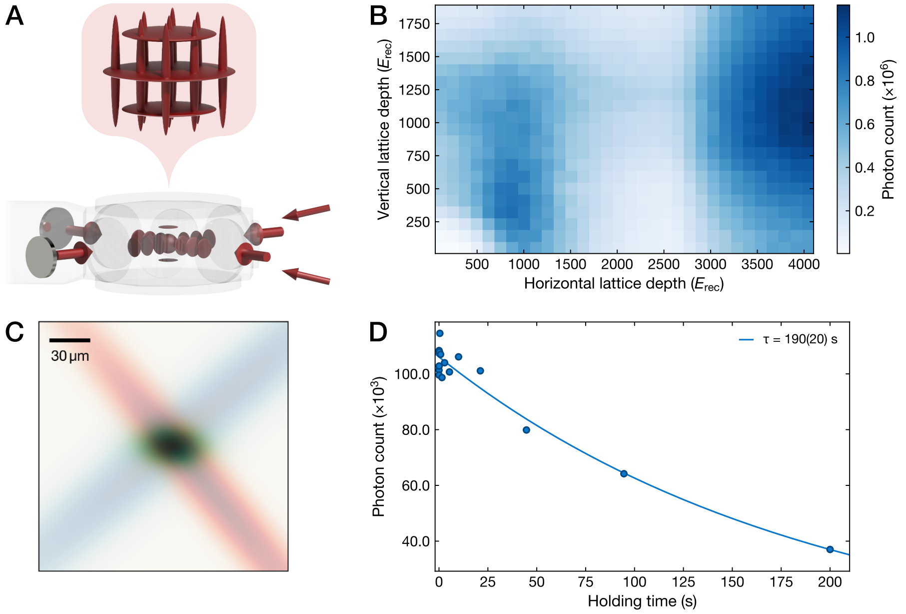

Figure 2.23 | Trapping atoms in a 3D lattice. A Simplified sketch of the 3D lattice geometry with two retroreflected horizontal lattice beams forming tubes in the crossing region, which are vertically sectioned by the pancake-shaped potentials generated by the shallow-angle vertical lattice. **B** The loading efficiency into the 3D lattice region, probed with molasses-cooled fluorescence imaging (Chapter 3.1.2), exhibits a strongly non-linear dependence on the lattice depth, with a first local maximum at a combined horizontal lattice depth of $\simeq 900\,E_{\mathrm{rec}}$ and a weak vertical lattice contribution of $\simeq 300\,E_{\mathrm{rec}}$, where we did not adjust the recoil energy for the larger lattice spacing in the vertical lattice. After an intermediate regime where loading into the 3D lattice is almost fully suppressed and only the weaker 1D lattice arms are populated, a stronger second maximum in very deep traps with depths of $\simeq 5000\,E_{\mathrm{rec}}$ is observed. **C** By imaging the three lattices individually, we can determine their relative positions and align them onto each other. While we use absorption imaging from the side to align the lattices vertically, fluorescence imaging enables us to find the optimal horizontal overlap, as depicted in this false-color plot, with lattice arm 1 shown in blue, lattice arm 2 in red, and the vertical lattice in green. **D** Lifetime of ground-state atoms in the 3D lattice, performed after rethermalized clock-sideband cooling in a 1D lattice and with fluorescence imaging.

that this effect demands for further study by, e.g., testing the loading efficiency in even deeper lattices to elucidate whether a second depletion regime exists, or by similar measurements in various lattice configurations for the fermionic isotopes, where the different spin structure changes the overall lattice light shift, which could confirm or falsify our hypothesis that this is the cause for the observed bimodal loading parameter pattern.

The additional vertical confinement also extends the ground-state lifetime in the lattice to more than 3 minutes (Fig. 2.23 D), which we assume to be mostly vacuum-limited. This lifetime can be directly extracted from a single exponential fit to a cooled cloud, or by taking the initial two-body losses into account. Despite the deep lattice potential and the low filling fraction of $\simeq 0.5$, collision-induced loss of atoms is significant at temperatures of $T \simeq 25\,\mu\mathrm{K}$, as the atoms can tunnel through the lattice with a rate of $J \simeq 20\,\mathrm{Hz}$ using Eq. (1.55). Once the atomic temperature is cooled $T < 10\,\mu\mathrm{K}$, corresponding to $\bar{n} \simeq 1$, thermal tunneling is

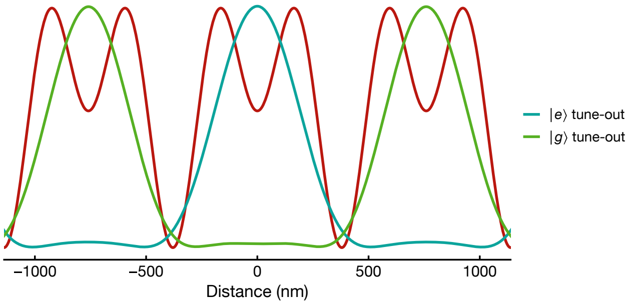

Figure 2.24 | Illustration of the lattice and tune-out tweezer potentials. To-scale sketch of the extent of optical tweezers at the ground- and clock-state tune-out wavelength at 553 nm (green) and 577 nm (blue) for a NA of 0.7 relative to a magic superlattice potential with a spacing of $a = 759/2$ nm (red). The computed overlap of the diffraction-limited tweezer potential with the adjacent lattice site is below 10%.

suppressed to $J \lesssim 1$ mHz and collisions cease to play a role. The cooling method used to obtain these temperatures is described in Chapter 3.

2.7 Microscope objective

The final essential ingredient for our experiment is the microscope objective,[105] responsible for the generation of optical tweezers and single-site resolution imaging in the lattice. To minimize the overlap of a diffraction-limited clock-state tune-out tweezer with the adjacent lattice sites to $<10\%$, we selected a NA of 0.7 (Fig. 2.24). To this end, we use Eq. (1.58) and integrate the intensity weighted with the lattice potential above $a/2$ for $a = 380$ nm and $\xi \simeq 502$ nm the diffraction limit at 577 nm for a NA of 0.7. Since the exact position of this tune-out wavelength was unknown at this point, and the theory predictions spanned 565 to 590 nm, depending on the model [44, 97, 110, 152–154], the objective is optimized for 399 nm and the range between 532 and 590 nm. Although the lenses are further AR-coated to reflect $\simeq 3\%$ of the light at these wavelengths in total, i.e., at all surfaces combined, the calculated transmission at 399 nm is only 73%, due to a strongly absorbing glass which is essential to optimally compensate for chromatic aberrations. In a test setup, the measured transmission was even lower at $T \simeq 65\%$. As this poses a decisive limitation of the imaging efficiency at 399 nm, we also discussed the option of a single blue-transmission-optimized objective for imaging, while the second objective would be used for the tweezers. However, the moderate transmission gain of 5% would have substantially impacted the FOV, which is why we did not further pursue this option.

Because of its position in the center of strong magnetic coils the objective housing has to be non-metallic. The stiff polyetherimide thermoplastic *Ultem* has emerged as the industry standard for such applications and has also been chosen for our objectives. The mechanical design was optimized for overall compactness and in particular for a very short excess length beyond the entrance and exit pupil, which is crucial for the objective MOT beam setup described in Chapter 2.7.2.

---

[105] *Special Optics, 54-35-25@399&532-590nm*, custom design

2.7.1 Objective mount

The large NA in combination with the sizeable working distance of 14 mm demands for large-diameter lens arrays inside the objective. This does not only pose technical challenges due to the correspondingly large overall objective diameter of 56 mm, but also compounds the complex task of accurate alignment, in particular the alignment onto the glass cell where a relative tilt of 0.25 mrad can already visibly distort the point spread function [169]. Therefore, the ability to carefully control the objective position in all three dimensions as well as tip and tilt and to execute minuscule adjustments is vital. We achieve this by constructing a custom 5-axis stage, controlled by picomotors.

In the first design, which was intended to be arranged around the flat-band-wire coil system, the objectives are inserted into relatively compact vertical piezo stages,[106] enabling fast and precise objective focus changes and especially refocusing even within the sequence. These piezo stages, also made from *Ultem* to prevent eddy currents, are mounted within titanium buckets, which are in turn referenced to an outer breadboard-like aluminium structure (Fig. 2.25). With an overall height of just 25 mm, the objective mounts do not overtop the objectives itself, which is of major importance for the objective MOT beam concept. Each inner mount is designed to rest on three main support points, the spheric tips of the vertical picomotors,[107] to provide a minimally constrained geometric plane. These three picomotors are equidistantly oriented on a circle of radius 97 mm around the optical axis and are responsible for arbitrary tilt or height adjustments. To ensure a firm connection to the surrounding outer mount for the top objective, four compression springs made from titanium are located next to the picomotors. Owing to the symmetry-breaking rectangular shape of the piezo stage we employ two springs at the short edge, symmetrically placed around the picomotor, and one spring close to each of the diagonal picomotors, on the conduit to the objective center to prevent any potential tipping. Their stiffnesses are chosen to be at $F \simeq 8\,\mathrm{N}$ around the centered position.[108] At a maximum extension of 2 mm the retention force combined with the gravitational pull amounts to 16 N, which is close to but does not exceed the maximum force of 22 N a picomotor can exert. The alignment in the horizontal plane is made possible by two orthogonal picomotors,[109] both acting on the center of the inner mount. Again, we utilize springs to make sure the picomotor tips remain the pivots, but here we select a combined stiffness that almost reaches the maximum picomotor force upon the maximum excursion of 4 mm. By placing the springs as far out as possible we reduce the crosstalk between the two horizontal axes. The design further includes three screws that can be pre-adjusted to a minimum height to prevent that accidental misalignment of the objective causes a collision with the glass cell.

While the initial design of the bottom objective mount became unrealizable because of the more compact hollow-core coil mount, the top mount was manufactured and later tested by a neighboring lab. It is also being used in two labs at MPQ, where one mount has been integrated with only minor changes[110] [258], whereas the mount for the second lab is a significantly

---

[106] *MCL Z100,* customized

[107] *Newport 8321*

[108] The individual strength of the springs at the short edge of the piezo stage are correspondingly halved.

[109] *Newport 8301NF*

[110] The picomotors were exchanged for screws and PEEK was used instead of titanium.

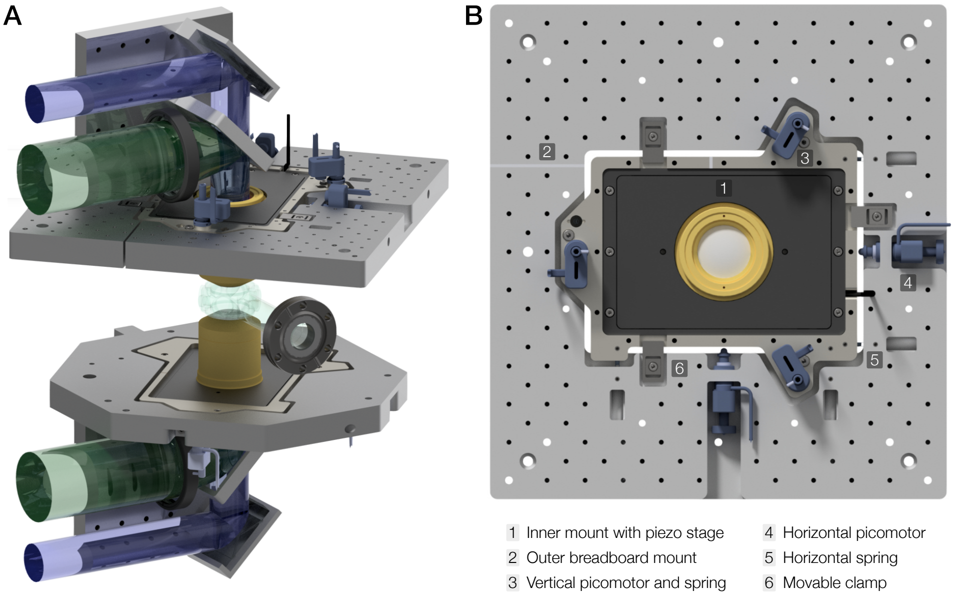

Figure 2.25 | Illustration of the initial objective mount design. **A** Arrangement of the two objectives with their respective mounts. Each objective rests in a piezo stage, mounted inside a titanium structure, which is referenced to the outer breadboards by means of picomotors and springs. Further displayed is the separation of the MOT beams (green) from the imaging and tweezer beams (blue) with a dichroic. **B** Top view of the upper objective mount. Almost all vertical springs are hidden beneath the picomotors (blue), while the horizontal springs, positioned far out to improve the sensitivity to yaw, are visible. Clamps allow us to lock the inner mount in place after the objective is aligned.

improved version, with fully decoupled translational degrees of freedom – decoupled from each other as well as the tip and tilt adjustment by including translation-stage-like guiding rails and using several independent shells for the inner mount [259].

Owing to the enormous tweezer beam path lengths it is highly non-trivial to achieve a stable setup for all three envisioned tweezer wavelengths with an objective from the top. We therefore redesigned the bottom objective mount to fit in between the coil mount pillars, however keeping the general idea of a picomotor-based 5-axis stage. Since the piezo stage itself was too large and the switch too sudden to develop a custom piezo solution, the only remaining knob to adjust the focus vertically is the simultaneous movement of all three vertical picomotors. To ensure that this movement is also uniform, i.e., the picomotors perform steps of identical sizes, we use a maximally symmetric design, consisting of a ring-shaped inner titanium mount which the objective is screwed into. The outer, fixed mounting structure consists of an aluminium bracket that is attached to the bottom of the mezzanine breadboard, close to the position of the retro-reflecting mirrors for the optical lattice. Just as for the top mount, the two parts are connected by a combination of picomotors and springs, where the latter are again judiciously chosen to provide a maximal force in the contemplated working windows while not overstraining the former. A planar indentation in the circular inner mount provides the contact points for the horizontal picomotors, slightly breaking the symmetry of the circular inner mount.

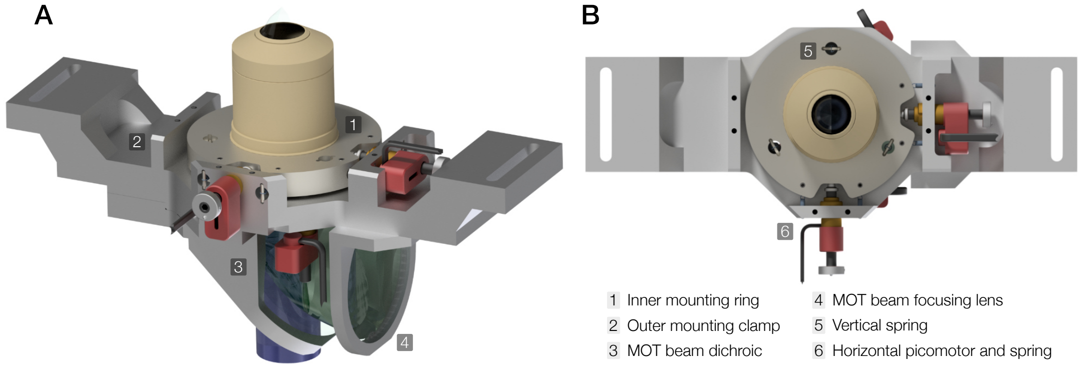

Figure 2.26 | Design of the second bottom objective mount. **A** Similarly to the first design, the objective is mounted inside a titanium-ring, which is held in place by picomotors to adjust its position and angle. Due to the limited space in between the coils, the outer mount is shaped in form of a bracket. The dichroic that separates the imaging and tweezer beams from the bottom MOT beam as well as the focusing lens are firmly attached to the mount. **B** Top view of the objective mount. The vertical picomotors and springs are aligned at equidistant angles, such that the symmetry is only broken by the horizontal picomotors.

2.7.2 The bottom MOT beam

The lower surface of the outer bracket exhibits a breadboard-like grid of threaded holes, which we utilize to mount the bottom MOT beam optics. We further provide for the usage of a mirror positioned in the center of the objective to project a focused MOT beam onto the back focal plane. If the size of this mirror is small compared to the objective aperture, the introduced aberrations are negligible, which can be intuitively understood as a low-frequency truncation of the Fourier transform, not affecting the resolution of details. Unfortunately, the back focal plane for the optimal objective lens design is 34 mm behind the outermost lens. A 10 mm wide collimated MOT beam at the atomic plane therefore implies a beam size of 14 mm at the entry facet, with a beam convergence half angle of 11.6°. Adapting the objective design to move the back focal plane further out or to reduce the convergence angle compromises the imaging properties and increases the effective focal length. Alternatively, one can deviate from a collimated configuration and select a focus in front of the back focal plane. Moving the focal spot 20 mm further out would entail a reduction of the MOT beam diameter of 6.4 mm at the entrance pupil, but also a significant inwards curvature of the wavefront, which does not necessarily harm the MOT efficiency. Placing the mirror as close as geometrically possible to the objective without clipping the MOT beam then requires a mirror size of 7 mm. Fig. 2.27 D shows the aberrations one would expect for such a mirror, and the effect of various mirror sizes on the Strehl ratio. Selecting a maximally acceptable size of 9 mm in turn allows for a $\simeq 8$ mm large MOT beam in the atomic plane. Upon testing the effect of reducing the vertical MOT beam size in the preliminary setup, we found a marginal decrease of the loading rates down to 8 mm in diameter, followed by a sharp decrease below 6 mm. Placing a 7 mm large mirror embedded in the imaging beam center therefore constitutes one viable option, but requires a suspension-based mounting structure close to the objective. The objective mount is designed to allow for such a solution, with a recess for a larger mirror to reflect the MOT beam onto the small mirror mounted on a base which can be held in place by three thin ropes. However,

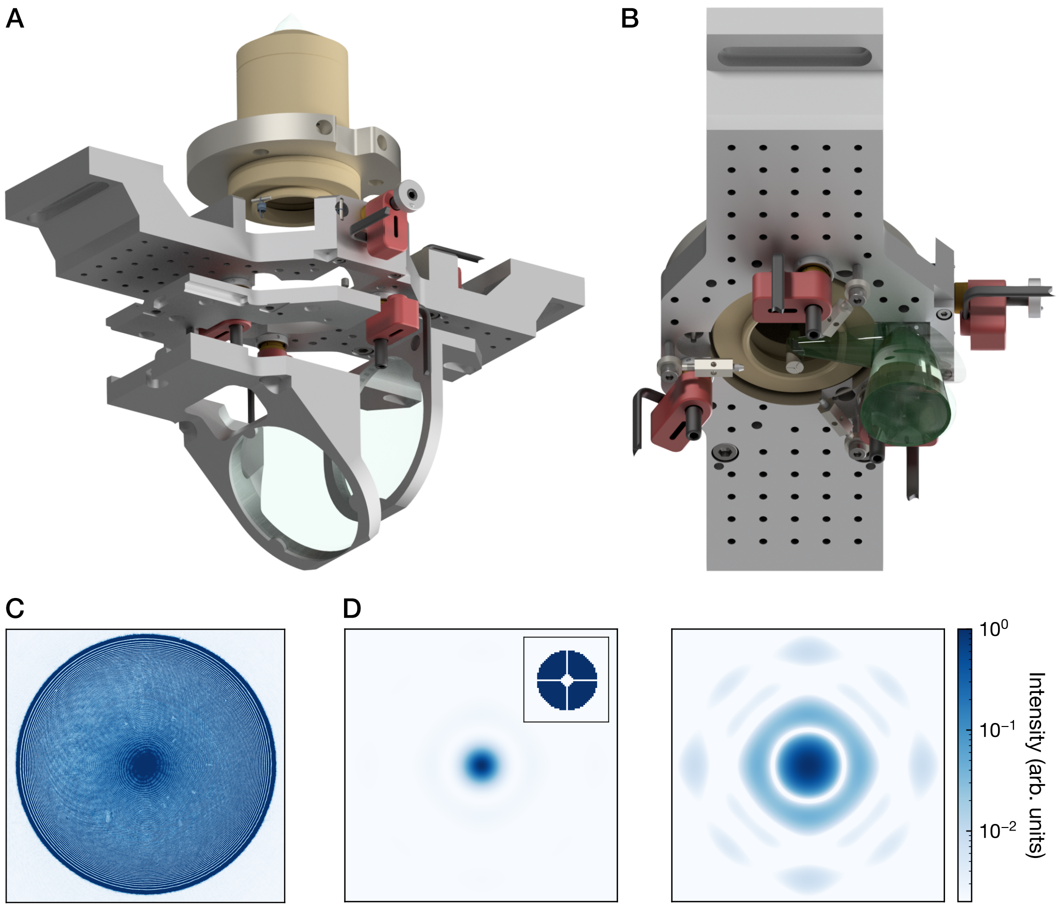

Figure 2.27 | Overlapping the bottom MOT beam with the imaging beam path. **A** Schematic of the "exploded" objective mount components including the MOT beam focusing lens and the dichroic mount, highlighting the functionality of the glider and its base plate. Rails and stop bolts ensure reproducible de- and attachment of the dichroic. **B** The alternative solution features a 7 mm large mirror in the center of the imaging beam, close to the objective's entrance aperture, which is held in place by adjustable titanium wires. A second mirror and a focusing lens provide a suitably shaped beam (green) further upstream. **C** Beam profile of the bottom MOT beam after the objective in a test setup, taken at a larger distance to the objective than the working distance to fit the whole beam on the camera. At this point, the beam width is 4.2 mm in diameter and the non-Gaussian, partially flat-top-like profile is clearly visible. The test setup did not include the dichroic, which further alters the beam shape. **D** Simulated impact of a 7 mm large mirror, attached to four wires (inset), on the imaging performance. While almost invisible in the linear scale (left), one can see the PSF deformation in the logarithmic scale (right), causing a square-like widening of the lobes while the PSF center is almost unaffected. For a three-wire geometry as visualized in **B** the aberrations analogously exhibit a mild trefoil pattern.

the mirror needs to be precisely cut into an elliptical shape without damaging the reflective surface, which turned out to be highly non-trivial.

We thus focused on a different approach that utilizes a dichroic mirror to superimpose the MOT beam onto the tweezer and imaging beams, similar to [62]. In this scenario, the MOT beam can be chosen to be up to 12 mm large and collimated at the atoms as the convergence angle is less severely limited. However, one has to accept significant power losses at the dichroic owing to the tune-out wavelength at 553.2 nm which is too close to the $^3P_1$ resonance to allow for a substantial separation with dielectric coatings. Furthermore, in order to offer the option of efficiently imaging green fluorescence, e.g., from a Raman cooling process, it is expedient to select a large transmission at 556 nm, which entails losing a considerable portion of the MOT light. We selected a dichroic mirror with 80% transmission at this wavelength and $> 95\%$ transmission at 399, 532, and 577 nm.[111] With this dichroic, the effective power per MOT beam is reduced to about one half of the value used in the preliminary setup. Notably, we underestimated the effect of the spread of angles of incidence due to the convergence, which leads to locally enhanced but also reduced reflectivities, causing some areas of the MOT beam after the objective to be significantly darker than the average. From a technical perspective, two main challenges arise. First, since the available overall height is limited to 205 mm by the mezzanine breadboard, and the minimum beam height of the tweezer beam path is 50 mm, the MOT beam with a collimated size of $d \simeq 75$ mm in front of the focusing lens needs to be guided right below the objective mount, which itself is designed to be as flat as possible without impairing the mechanical stability. Therefore, the focusing lens mount consists of a slender ring structure with small extrusions to provide an area of support for the glued 3″ lens and a base plate with a carved out center and slotted holes to allow for fine *in situ* adjustments of the focus position. In a similar fashion, the mount to which the dichroic is glued had to be carefully designed in order to offer sufficient space for the mirror that is mounted on the optical table and reflects the tweezer beams upwards. This task is further complicated by the second challenge, which is the necessary detachability of the dichroic mount. During the objective alignment process, the objective itself or add-on tools like irises or a mirrors need to be inserted or removed, which requires a temporary removal of the dichroic. However, upon reinsertion the exact position and angle needs to be recovered since otherwise the alignment progress would be vitiated. We thus devise a dual structure with one base firmly attached to the objective mount, featuring a set of rails on which the main dichroic mount can glide into place. A stop bolt prevents the glider from moving too far, and the mount can be screwed tight. In this vein, we do not observe any apparent displacement of the tweezer or the MOT beam during the alignment process.

2.7.3 Objective performance

Because of the optical complexity of the objectives and their vulnerability to imperfections or damages, it is a common practice to test and characterize the microscope objectives in a separate setup before inserting them into the experiment. This further helps to understand the precision requirements and informs on alignment techniques that reliably work in the final setup where the imaging performance can usually only be quantified indirectly by observations of the atomic signal. These tests and strategies for our objectives have been described in great detail in [169], which is why the following will be restricted on a brief overview of the main results.

The main figure of merit is the PSF, which can be obtained by imaging a point-like light source. We use a 250 nm large pinhole on a resolution test chart[112] and image the diffracted

---

[111] *UltraFast Innovations, BS2209*

[112] *Technologie Manufaktur, TC-RT01*

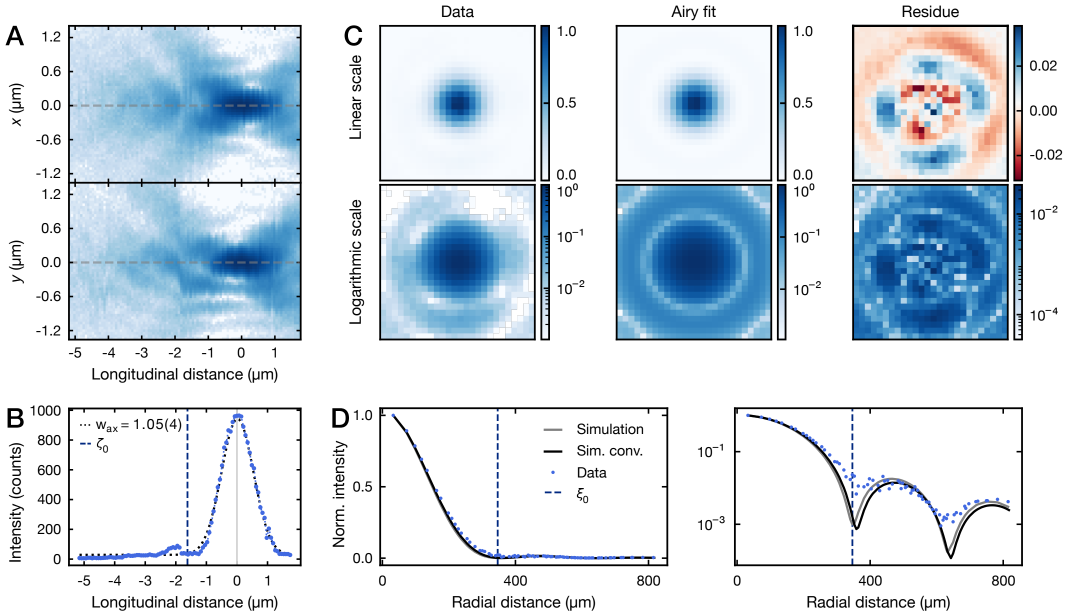

Figure 2.28 | Diffraction-limited performance of the objective in a test setup. A Shape of the point spread function in the horizontal and vertical plane for an axial scan across the focus in logarithmic scale, at 399 nm and with a 250 nm wide pinhole. The asymmetry between the two planes in the focus position and the divergence of the intensity maximum around it indicate astigmatic aberrations, while the asymmetry in the y-plane cut hints at coma. **B** Axial intensity distribution in the center of the point spread function. We fit to this with a Gaussian distribution (black dotted line) and we find that the fitted Gaussian waist is in good agreement with the expected value of $w_{\mathrm{ax}} = 1.11\,\mu\mathrm{m}$. The dark blue dashed line indicates the expected axial diffraction limit ψ_0. **C** PSF at the focus, in both linear and logarithmic scale. By comparing the data to the fitted Airy disk we can observe a cross-like pattern in the residue, which is a clear sign of astigmatism. **D** Despite the aberrations, the objective performance is still diffraction-limited as the aximuthal average of the PSF displays a minimum close to the expected Rayleigh limit ξ_0 (dark blue dotted line) and follows the simulated perfect Airy disk (grey solid line). The effect of the finite aperture size is small, as shown by the black solid line, where the ideal Airy disk is convolved with the aperture. The figures are adapted with permission from [169].

light with a $f = 1000$ mm achromatic lens onto a high-resolution camera.[113] The resulting magnification of 40.1(2) allows us to sample the PSF with an effective pixel size of 46 nm. By scanning the relative distance between objective and resolution chart we can then determine the focus position, at which the signal was found to be optimal using both Airy disk fits and a determination of the Strehl ratio. As both objectives fulfill the criterion for a diffraction-limited performance of a Strehl ratio > 0.8 at 399 nm as well as 532 nm, they exhibit only small but visible optical aberrations (Fig. 2.28 A). For the objective that is implemented in the experiment at this stage, the main aberrations are astigmatism and coma, while the second objective shows mostly trefoil contributions. From this analysis we can expect a resolution of $\xi = 364(5)$ nm at 399 nm and 465(11) nm at 532 nm in our experiment. We can also derive the axial extent, which is linked to the depth of field, from a Gaussian fit to the intensity in the center and obtain waists of $w = 1.05(4)\,\mu$m and 1.28(5) µm for 399 nm and 532 nm, respectively.

---

[113] *Allied Vision, Alvium 1200 U-1240m*

The subsequent test is a repetition of this procedure, but for an off-axis point within the FOV. Again, we observe a performance in accordance with the specification as the Strehl ratio drops below 0.8 only beyond a distance of 50 µm from the optical axis for 399 nm light, which greatly exceeds the 3D lattice area. For the tweezer light at 532 nm the diffraction limit is achieved even for distances as large as 100 µm, with a PSF that is only marginally deformed. This comfortably allows for 50×50 tweezer arrays with a spacing of 2.8 µm, which is also the estimated maximum number of tweezers we can achieve in our current setup.

2.7.4 Tweezer loading

With the objective capable of producing diffraction-limited tweezers, the goal for the preceding beam path is to provide a plane wave at the entrance pupil, i.e., we have to ensure that the remaining optics are correctly aligned and do not introduce severe additional aberrations. One limiting factor in this endeavor is the surface quality of the optics involved. In particular, we identify a general soft upper limit of $\lambda/10$ on the acceptable flatness of the reflecting optics in front of the objective before the imaging fidelity suffers from a disturbed wavefront, while the effect is typically less strong in transmission. We attribute this to the predominant surface imperfection, as determined by high-precision interferometric measurements, which is bending either along one axis or radially out- or inwards, thus causing astigmatism in the former and spherical aberrations in the latter case for a reflected beam. However, we observe that in most cases both surfaces are similarly bent, which then diminishes the effect on the wavefront of a transmitted beam. Notably, it is possible to correct for such introduced aberrations by using a similarly bent but orthogonally oriented mirror at a different position, but this is generally hard to realize accurately. Instead, we interferometrically scrutinize a large set of mirrors and select the ones that yield the best flatness results. While we find unsuitably curved surfaces for some off-the-shelf 3″ mirrors, most of them exceed our expectations with flatnesses $\lesssim \lambda/15$ even after glueing them into the mirror mounts[114] at three corners. Similarly, one of the dichroics to split the tweezer and imaging light offers a flatness of $\lambda/20$ when loosely held in place. However, as soon as we clamp or glue it into its custom mount at more than one point the rectangular dichroic starts to strongly bend along its long axis, independent of where the glue is applied and which glue is used. We ascribe this behavior to the relatively thin substrate with a thickness of just 7 mm. To circumvent this issue, we glue the dichroic at just one corner with a low-shrinkage UV curing adhesive,[115] which compounds the measured flatness only slightly. As the last optical element before the objective, the size of the bottom MOT dichroic is mostly governed by the required MOT beam size and we can afford a substrate thickness of 12.7 mm. Hence, the interferometric measurements do not indicate any bending after it was glued into its mount. Unfortunately, for such large diameters the overall intrinsic surface flatness tends to be subpar, and indeed we determine a value of $\simeq \lambda/6$ for the best mirror. Crucially, the unevenness of the two surfaces appears to be asymmetric, which will thus also cause non-trivial deformations of the transmitted tweezer beam wavefront.

---

[114] *Thorlabs Polaris-K3S4* for horizontal, custom mount for upwards reflection.

[115] *Thorlabs NOA61*

The best possible optics at hand, we take great care upon their alignment.[116] Especially the placement of the lenses demands for precision, as any tilt or displacement with respect to the optical axis will cause coma and astigmatism, while an imperfect longitudinal position gives rise to spherical aberrations. We use the thoroughly ascertained optimal relative distances between the lenses from the test setup as well as the de- and reflection of the guide beam at each lens to minimize these effects. This guide beam was previously aligned such that the backreflection of the lower glass cell window is overlapped with the ingoing beam close to the second AOD, at a distance of more than 2 m. In combination with a pointing sensitivity of $0.5 - 1$ mm using a pinhole card, this corresponds to an angular sensitivity of $0.25 - 0.5$ mrad. In this process, we also determine the angle mismatch between the two glass cell windows to be $\delta\theta \simeq 2$ mrad. Once the objective is inserted and aligned horizontally onto the guide beam position using an iris, we can leverage the guide beam and the detachable 10:1 telescope lenses to align the objective onto the glass cell. Here, we make use of the Newton rings created by the various curved surfaces inside the objective and move the vertical picomotors until the backreflected rings align concentrically on the ingoing beam.

To obtain the first tweezer signal, we utilize a single, very deep tweezer, which is turned on during the MOT compression stage and whose size is artificially widened to several μm by an iris, and observe the blue fluorescence signal of atoms as they quickly get ejected from the trap by the powerful imaging light at several tens of I_{sat}. This allows us to optimize the compressed MOT position to achieve good overlap with the position of the tweezers. In a tighter tweezer we can then observe a direct signal of trapped atoms with a weaker imaging beam. Notably, the light shift on the ${}^1\text{P}_1$ transition induced by the tweezer light is substantial for such a strong beam, which is why either the imaging detuning or the tweezer power has to be adapted at this step. Since the imaging-induced heating is not countervailed at this point, most atoms escape during the exposure time, which is why the histogram shows a broad distribution. To counteract this heating effect we perform molasses cooling on the ${}^3\text{P}_1, m_J = 0$ transition in a weak magnetic field and slightly blue-detuned from the free-space resonance by $\delta \simeq 1\Gamma$, similar to the method described in [151, 260] (Fig. 2.29 A). Using the light from the horizontal MOT beams at $I \simeq I_{\text{sat}}$ and a weak ($I \ll I_{\text{sat}}$) blue imaging beam, we can now clearly resolve two discrete peaks in the histogram (Fig. 2.30 C), delivering the binary information whether a single or no atom was present. This also demonstrates the concurrent effect of blue-shielded collisions induced by the cooling light, as even without any additional photoassociation (PA) pulses double occupancies are fully suppressed while the typical single-tweezer loading efficiency of $\simeq 65\%$ significantly exceeds 50%, which would be expected for a Poisson-distributed, parity-projected sample. This has so far only been demonstrated for Rb [261–263], K [264], and ^{171}Yb [63], but not for ^{174}Yb.[117] Remarkably, the optimal detuning for the first image appears to be red-shifted by $\simeq 100$ kHz to the peak we find for subsequent images after post-selecting for initially occupied tweezers, determined by fitting the empirical distribution

$$P(\delta) = \frac{A}{\beta}\, e^{-(z+e^{-z})} \tag{2.13}$$

---

[116] A more fine-grained description of the alignment procedure is given in [169].

[117] We note that the histogram in [260] appears to display a very similar behavior, but is not further mentioned in the text.

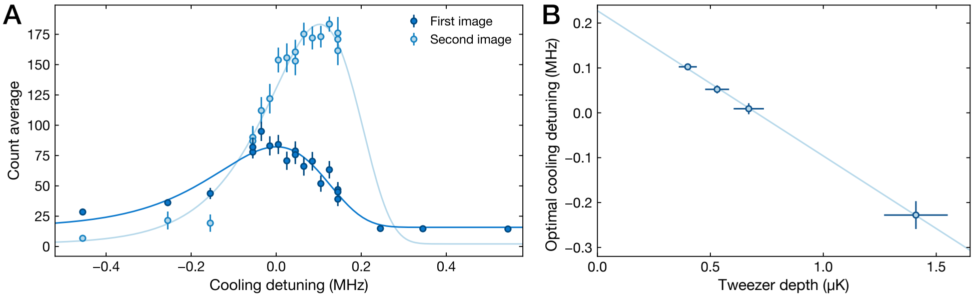

Figure 2.29 | Enhanced tweezer loading and molasses cooling. A Average number of detected photons for the first and second image as a function of the 556 nm molasses beam detuning. While a lower detuning seems preferable for the first image, a more blue-detuned beam leads to an enhanced collection of scattered photons due to the suppression of trap loss, with a baseline of $\simeq 20$ counts for effectively uncooled atoms at large detunings. An empirical fit using Eq. (2.13) is displayed as a solid line. **B** The optimal detuning shows a weak but noticeable negative correlation with the tweezer depth, which is likely caused by a tweezer-induced local shift of the magnetic field. Note that the y-axis values exhibit a systematic error of $\simeq 200$ kHz due to uncertainties in the π transition resonance determination.

with $z = (\delta - \mu)/\beta$ to the averaged photon counts. Furthermore, the maximum counts for the second image exceed the amplitude of the first-image peak by more than a factor of two. This indicates that a separate slighlty red-detuned shielding pulse could provide the energy for a weakly-bound molecule to expel one atom, while a more blue-detuned cooling beam helps to retain more atoms during imaging. The optimal detuning for the second image weakly depends on the tweezer power and exhibits a downwards slope (Fig. 2.29 B), in disagreement with the lightshift measured in [151]. This could be a result of the weak vertical external magnetic field of $B = 1$ G that could allow a deep tweezer to locally induce a comparable field, potentially causing a change in the tensor shift. We note that around the time of the measurement slow changes in the cavity expansion rate accumulated to a significant deviation from the feed-forwarded correction, which was only found and determined later. The position of the π resonance therefore had to be traced back, causing a significant systematic uncertainty $\simeq 200$ kHz on the y-axis intercept. Using just a single pulse, we find that the molasses cooling suppresses imaging-induced atom loss sufficiently well that we can image atoms for several tens or even hundreds of ms, which leads to a very clear separation of the single- and no-atom peak in the histogram. For typical tweezer sequences we choose an exposure time of $t_{\text{exp}} = 50$ ms, yielding a classification fidelity of 99(1)%, which is given by the overlap of Gaussian fits to the two peaks and limited by the atom loss during imaging. The latter is quantified by imaging the same atom multiple times, and we find a loss rate of 1(1)% per image. To achieve this, we find a reduction of the tweezer depth to $f_{\text{r}} \simeq 135$ kHz and $f_{\text{l}} \simeq 30$ kHz helpful as determined by modulation spectroscopy (Fig. 2.30 D), corresponding to a trap depth of $U_0 = h \times 11.7\,\text{MHz} = k_{\text{B}} \times 0.56\,\text{mK}$. At this lower depth, however, the averaged loading efficiency is slightly decreased from 58(2)% to 55(2)%, which could indicate that the blue shielding is indeed assisted by a change of the quantization axis from the tweezers itself. We note that this measurement was performed in a square tweezer array consisting of 5×5 tweezers at a distance of 10 μm to each other. We therefore attribute the larger loss rates in deeper tweezers mostly to imperfect homogenization

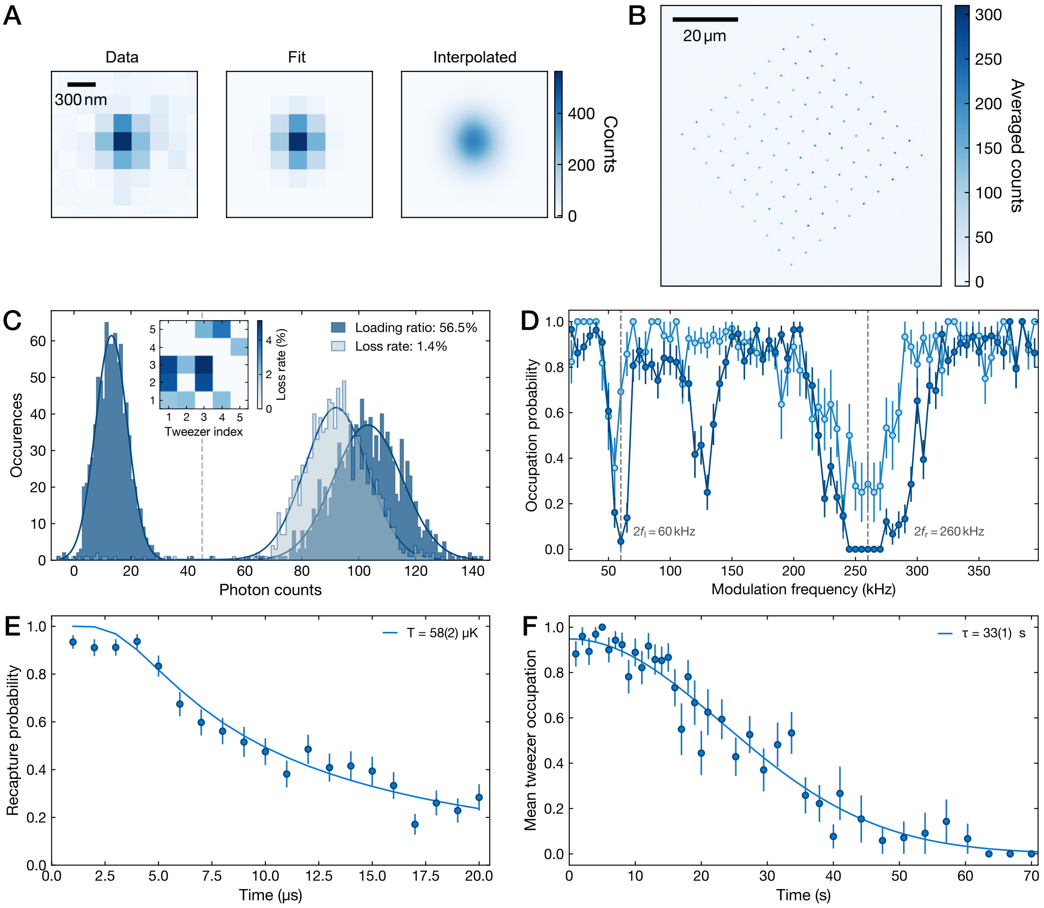

Figure 2.30 | Characterization of the 532 nm tweezer array. A Fluorescence image of a single tweezer, imaged with 399 nm light. A Gaussian fit to the raw data yields waists of $w_{0,x} = 348(11)$ nm and $w_{0,y} = 412(14)$ nm, showing astigmatism. The expected waist from a diffraction-limited beam is 339 nm. The panel on the right displays a bicubic interpolation of the fitted data. **B** Image of a 10×10 array, spaced by 5 μm. Despite averaging over 50 individual images one can see inhomogeneous brightnesses, owing to imperfectly balanced tweezer powers affecting both the loading and cooling fidelity. **C** Histogram of a typical $5{\times}5$ array after 50 ms exposure time and 80 averages. In the first image (dark blue), the single-atom peak is well-separated from the peak that indicates a vacant tweezer. From a double-Gaussian fit (dark solid line) we can estimate the imaging fidelity. The molasses cooling further allows to retain more than 50% of the atoms in the tweezers. The histogram of initially occupied tweezers is displayed in light blue, indicating a loss rate of $\simeq 1(1)\%$. Inset: The tweezer-resolved loss rates show that only few tweezers account for the majority of all losses. The relative shift of the peaks for the first and second image is due to background light impinging on the camera before the actual image is taken. **D** Trap frequency measurement in $\simeq 7$ mW deep tweezers using modulation spectroscopy. In the dark blue sequence the modulation parameters were chosen to clearly resolve the longitudinal resonance, which saturates the resonance at the radial trap frequency. In a separate measurement (light blue) the modulation is then adjusted to display the radial resonance well. The solid line is a linear interpolation. **E** Release-recapture measurement for a varied release time during which the tweezer is off. The probability of a recapture event depends on the atomic temperature. A Monte Carlo simulation fit (solid line) yields a temperature of 58(2) μK. **F** Lifetime of uncooled atoms in the tweezer array. The $1/e$ lifetime of 33(1) s is obtained by an empirical Gaussian fit (solid line) and agrees with the result of a single exponential fit within error bars.

of the tweezer arrays, which is also observed in a spatial map where some tweezers show multiple loss events while a majority exhibits vanishingly low rates.

The homogenization algorithm of the array is based on a reference camera image and uses a simple PID loop to adjust the RF power of the individual tones sent to the AODs, while the phases are chosen randomly and equidistantly. Typically, within $3-5$ iterations we reach an intensity distribution with a standard deviation of $\sigma \lesssim 5\%$ according to the camera image. Owing to the complex imaging process, this can translate into larger inhomogeneities in the actual tweezer depths, which is why one would perform a calibration of the camera image once maximally power-balanced tweezers are required [82].

Analogously to the lattice case, we can also perform lifetime measurements in the tweezers where we scan the hold time of the atoms in $P \simeq 18\,\mathrm{mW}$ deep tweezers. This measured lifetime of $\tau = 33(1)\,\mathrm{s}$ can likely be extended by intermittent molasses cooling cycles to balance heating from the tweezer itself [199]. Eventually, we can employ the release-recapture technique to determine the temperature of the atoms [265]. Here, we quench the tweezer light off for a variable amount of time and observe the number of atoms that are retained after the tweezer array is restored. Very cold atoms will not travel far horizontally in the short time of flight and can thus be recaptured even after longer wait times. Notably, a gravitational drop beyond the depth of field will always constitute a limit on the maximum achievable release time. As we did not cool the atoms for this measurement after they were imaged for the first time to determine which tweezers are occupied, this informs on the imaging-induced heating and its compensation by the molasses cooling. We quantify the temperature by performing a classical Monte Carlo-based fit to the data. The fit model samples a given number of atoms — in our case 10^6 — and stochastically assigns a position and velocity vector relative to the tweezer center according to a Boltzmann distribution [265],

$$\Delta \mathbf{r}_{\mathrm{x,z}} = \sqrt{\frac{k_{\mathrm{B}}T}{2\pi m f_{\mathrm{r,l}}}} \tag{2.14}$$

and

$$\Delta \mathbf{v} = \sqrt{\frac{k_{\mathrm{B}}T}{m}}, \tag{2.15}$$

with temperature as the fit parameter and the tweezer trap frequencies of $f_{\mathrm{r}} = 210\,\mathrm{kHz}$ and $f_{\mathrm{l}} = 47\,\mathrm{kHz}$ as fixed input parameters. We propagate the atoms' position and vertical velocity during the period of free time of flight with a simple ballistic equation of motion, and we can determine its final kinetic and potential energy at the time of the tweezer restoration. By comparing this quantity to the trap depth, we can decide whether the atom counts as recaptured or lost, and compare this outcome to the data. The fit then yields a temperature of $T = 58(2)\,\mu\mathrm{K}$, in good agreement with the uncooled temperature in a similar experiment with ^{174}Yb [260]. Notably, this is larger than the mean temperature of atoms in the compressed MOT, indicating that the atoms are quite hot after the exposure to imaging and cooling light, and further measurements with varying imaging powers and different trap depths can likely elucidate the onset of critical heating that leads to elevated losses during imaging and afterwards. Similarly, in the future we can test the minimal temperature we can achieve with molasses

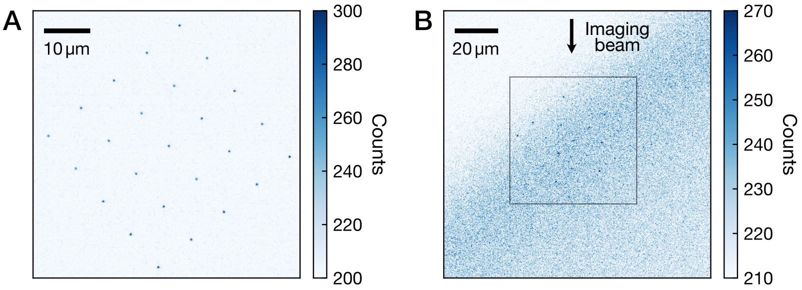

Figure 2.31 | Imaging atoms in a 5 × 5 **tweezer array overlapped with a 1D magic lattice. A** Image of the bare tweezer array, averaged over 50 iterations. **B** Single-shot image of atoms trapped in the 532 nm tweezers and in a 759 nm 1D lattice. While the tweezers operate in a quasi-magic condition for the $^3P_1$ cooling transition, the lattice potential is not cooling-magic and the atoms are quickly lost from the lattice after scattering blue photons. We can thus not only detect the diagonally oriented lattice itself, but also observe a large number of photon counts from escaping atoms on the lower right edge of the image, as the imaging beam is irradiating the traps from above. Grey square: Region of interest in **A**.

cooling by adding a cooling pulse before the release, which should reduce the temperature to $T \simeq 20\,\mu\mathrm{K}$ according to the results from [260].

2.7.5 Fluorescence imaging

Similar to fluorescence imaging in the tweezers, we can also collect photons scattered by atoms in a lattice. This modality can be used complementary to absorption imaging and is particularly useful in the context of single-site-resolved imaging. Without the necessary resolution or in the case of atoms occupying several vertical lattice planes, such that a high fraction of atoms will reside outside the depth of field, the retrieval of absolute atom counts from fluorescence images is highly non-trivial as the number of scattered photons per atom is only reliably gaugeable with separable histogram peaks. However, in contrast to absorption images it is possible to generate fluorescence snapshots with very large signal-to-noise ratios (SNR) by selecting long exposure times of a few 100 ms, in case an appropriate cooling technique is applied to suppress atom loss during imaging. Further, the high-NA objective and the very-low-noise qCMOS camera in combination with a precisely aligned tube lens aid the fluorescence image SNR. For the results in this thesis, we use the 399 nm imaging beam that is also used for absorption images to scatter blue photons. We note that it is also possible to use the 556 nm $^3P_1$ transition for imaging, and in particular collect the photons that are scattered during molasses or Raman cooling steps [63, 151]. This can increase the imaging efficiency as the lower recoil energy and transition linewidth reduces the susceptibility to atom loss, at the expense of a larger PSF. Notably, the proximity to the ground-state tune-out wavelength will strongly complicate the necessary optics once all planned tweezer arrays are installed, which is why we aim at continuing to use blue fluorescence light.

While it is possible to obtain a fluorescence signal of atoms trapped in a 1D lattice geometry, the two weakly confined axes cannot hold the atoms against the quickly accumulated recoil energy, and we can only observe a relatively weak signal. This was still found sufficient to overlap the horizontal lattice arms onto the tweezer array (Fig. 2.31). In this image, the molasses cooling detuning is chosen to be optimal for the 532 nm tweezers, which is not the ideal detuning for the 759 nm lattice owing to the unequal differential $^1S_0 - {}^3P_1$ polarizability and therefore the signal of atoms in the lattice is very faint. The polarizability difference in ^{174}Yb is not irreconcilably large, though, and we suspect that a quasi-magic condition exists where the polarizabilities are sufficiently small to allow for simultaneous cooling in both traps, which will then allow for *in situ* optimization of the tweezer array alignment onto the lattice. A similar quasi-magic condition is used for fluorescence imaging in the deep magic 3D lattice, where the strong confinement along all three dimensions provides an ideal basis to retain the atoms. This mechanism is described in the next Chapter.

CHAPTER 3

Ground-state cooling in a magic lattice

The existence of considerably large trap frequencies in optical traps with strongly confined axes opens up a suite of cooling techniques that leverages the discrete vibrational level structure. Among the oldest and most commonly used cooling schemes are polarization gradient and gray molasses cooling [30, 58, 262, 266, 267], which use a changing polarization of a harmonic trap to create a Sisyphus process, where the atoms are excited when they acquire a finite potential energy, but are repumped to the bottom of the potential, causing a net energy loss. Similarly, Λ-enhanced gray molasses and electromagnetically induced transparency (EIT) techniques transfer cooled atoms to dark states induced by two interfering lasers that couple multiple ground states to a common excited state [264, 268, 269]. Even lower temperatures have been reached with Raman sideband cooling schemes [60, 61, 250, 270–272], where two Raman beams drive a transition to the sideband of a second ground state via a far-detuned virtual excited state. Notably, all these cooling methods can be related to a Raman coupling process to a lower motional state, where for the former judiciously designed light shifts supersede the role of the two-photon detuning in Raman sideband cooling [273].

While these cooling schemes work well in spinful alkali atoms, they can only be partially applied to the case of fermionic AEL atoms and cannot be used at all for spin-less bosonic AEL isotopes such as ^{174}Yb. Compared to a single demonstration of EIT cooling in ^{171}Yb on the 556 nm transition [274], Raman sideband cooling has been shown to be versatile and work well in different trap wavelengths and configurations with this isotope [63, 72, 76, 275]. Spin-agnostic cooling techniques such as Sisyphus cooling in traps with differing potential depths for the ground and excited state have found widespread application in particular in Sr-based experiments [64, 65, 233], but has also been demonstrated in ^{171}Yb recently [276]. Resolved sideband cooling using a single-photon transition to the red sideband of the excited state has become similarly popular in AEL atoms, with very high ground-state fractions reached within just tens or few hundreds of ms [62, 82, 234, 277, 278]. Notably, these cooling techniques can be combined with a shelving trick of atoms in the motional ground state to convert the remaining atoms in higher vibrational states to vacancies in the so-called erasure cooling scheme [279].

In this Chapter, we will delineate the first demonstration of sideband cooling in ^{174}Yb, based on a combination of a clock-state sideband transition and a dissipative deexcitation after repumping to the $^3D_1$ state. This allows us to reach nK temperatures and axial ground state fractions in excess of 90% both in 1D and 2D optical lattice systems. Moreover, a pathway to an extension to 3D lattices and the applicability to fermionic isotopes is discussed, followed by a concept to realize spin-polarized ^{171}Yb atoms in the ground state via Raman sideband cooling in a 3D lattice. Before delving into these methods to reach the absolute motional ground state, we start with a discussion of a molasses cooling technique on the $^3P_1$ intercombination line that enables high-fidelity fluorescence imaging in a magic lattice. Here, the missing spectral resolution of the trap frequencies limits the minimal temperature to several μK, as cooled atoms are not dark to the cooling light, but it allows for the fast reduction of entropy to counteract heating induced by fluorescence imaging on the $^1P_1$ transition. The results presented in Sections 3.1 and 3.2 are in preparation for publication [103].

3.1 Molasses cooling

Collecting a vast number of fluorescence photons scattered by trapped atoms in a lattice is a decisive mechanism for quantum gas microscopes, but can also help to boost the signal-to-noise ratio for experiments without single-site resolution [36, 37, 120]. The pivotal prerequisite for a large photon count is the balancing of scattering-induced recoil heating to retain the atom at its original lattice site, which is why oftentimes the scattered photons of the cooling light itself, e.g., from near-resonant molasses or Raman beams, are used [35, 249, 250]. In cases where a transition is not suitable for cooling purposes because of its large linewidth, but favorable over other transitions owing to its short wavelength, as is the case for the $^1P_1$ transition in AEL atoms, simultaneous cooling on a different transition is required. To this end, Sisyphus cooling on the $^3P_1$ transition has been demonstrated to allow for single-site resolution imaging on the broad 461 nm transition in an optical lattice using ^{84}Sr [255]. In a similar vein, it has been shown for ^{174}Yb that molasses cooling on the 556 nm intercombination line can counteract the scattering of 399 nm photons in a 532 nm lattice [80], where the small lattice constant necessitates the usage of such short-wavelength imaging light. In contrast to the Sisyphus cooling method that is also commonly used in Sr tweezers [65], unresolved molasses cooling on the broader $^3P_1$ transition in Yb does not rely on but instead suffers from inhomogeneities in the trapping potential. Therefore, the near-magic condition for this transition at 532 nm was found to be a decisive ingredient for effective cooling during fluorescence imaging, as it allows for homogeneous cooling in the whole trap and for atoms in all bands.

For a clock-magic lattice at 759 nm, so far no realization of efficient fluorescence imaging has been reported, and the scalar polarizabilities of the $^1S_0$ and $^3P_1$ states are expected to vary significantly at this wavelength, rendering the lattice non-magic for the cooling transition. However, the magic angle that was found for ^{171}Yb in optical tweezers at this wavelength [72] as well as our polarizability model indicate the existence of a magic angle also at this wavelength. This would render the 759 nm lattice compatible with molasses cooling and allow for high-fidelity fluorescence imaging with single-site resolution.

3.1.1 Magic angle

Magic angles can generally be used for transitions that are less narrow than clock transitions, but narrow enough that light shifts at the trap wavelength play a crucial role, like the $^3\mathrm{P}_1$ state. Here, one can adjust the tensor shift contribution to cancel the finite scalar differential polarizability by selecting the appropriate direction of the magnetic field with respect to the trap beam polarization. For optical lattices consisting of multiple beams at relative angles to each other, the polarization is typically constrained, and the magnetic field vector needs to be adjusted. Due to the limited stability and calibration accuracy of magnetic fields along an arbitrary direction in most experimental apparatus, this method is more coarse than the usage of a carefully measured magic wavelength, whereas for single-beam traps like 1D lattices, optical dipole traps, or tweezers it can also be possible to rotate the polarization and keep the magnetic field fixed [280]. Hence, the magic angles reported for Yb have been determined with a precision on the level of $\sim 1°$ [72, 80]. This precision, however, entirely suffices for typical trap depths in ultracold Yb experiments, given the comparably broad linewidth of the $^3\mathrm{P}_1$ transition. Similarly, our determination of the absolute magic angle for ^{174}Yb in the clock-magic lattice is restricted by our magnetic coil calibration uncertainty on the order of a few percent, as discussed in Chapter 2.2.

Following the standard approach of near-magic spectroscopy, we observe the light shift of the three $^3\mathrm{P}_1$ resonances, corresponding to transitions to the $m_{F'} = 0, \pm 1$ states, increase or decrease at a given lattice wavelength and angle between the magnetic field and the lattice beam polarization as the lattice power is ramped up (Fig. 3.1 A, inset). Vitally, this requires a clearly defined, uniform polarization across the whole lattice, which is why we use a matching vertical polarization of the horizontal lattice beams, and we turn the horizontally polarized vertical lattice off during this spectroscopic measurement. Similarly, the magnetic field is chosen to be as strong as possible to reduce the lattice-induced tilt in the local quantization axis as observed in Fig. 2.4 B, where the uncooled transverse coils impose a limit of 4.8 G.[1] This restricts the magnetic field vector to rotations in the vertical plane orthogonal to the main chamber axis. Utilizing the time-of-flight method developed in Chapter 2.2.1 and a brief spectroscopy pulse, we can confirm the zero position of the π transition, determined by fits to the corresponding spectra with a Lorentz distribution (Fig. 3.1 A). As we ramp up the 2D lattice power during the spectroscopy pulse, we start to observe the characteristic resonance shifts, whose slope significantly varies for different polar magnetic field angles θ. In particular, for an angle of $\theta = 38°$ the light shift almost vanishes. However, as the total lattice power exceeds $P \simeq 3.5\,\mathrm{W}$, corresponding to a lattice depth of $V \simeq 1000\,E_{\mathrm{rec}}$, a systematic curvature towards lower frequencies appears. This curvature is found to be more severe for smaller θ, which agrees with our expectation that the vertical electric field generated by the lattice beams competes with the external magnetic field [281]. To model this behavior, we use a second order polynomial function without any constant term and fit the data, such that we obtain a linear and a quadratic light shift contribution. While the quadratic shift does not contain actual physical information and is an artifact of the weak external field, we can use the fitted

---

[1] While the transverse coils can be water-cooled, persistent technical difficulties with a chiller so far did not allow for the usage of higher currents in this coil pair.

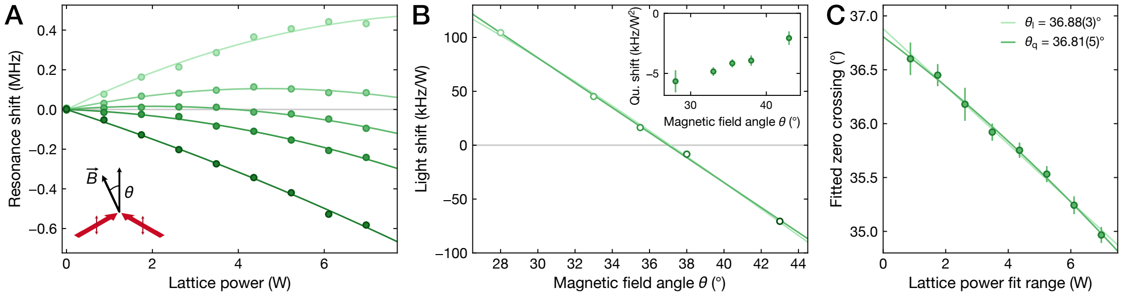

Figure 3.1 | Magic angle spectroscopy for a moderate magnetic field. A The shift of the π transition to the ${}^3\mathrm{P}_1$, $m_{F'} = 0$ state is probed for various lattice powers and magnetic field angles with respect to the vertical polarization of the two lattice beams (inset). While the resonance shift follows the anticipated linear dependence for low lattice powers, a quadratic trend sets in for lattice depths above $V \simeq 1000\,E_{\mathrm{rec}}$, corresponding to a combined lattice power of $P \simeq 3.5\,\mathrm{W}$. We thus fit the data for each angle with a quadratic function without offset (solid lines). **B** Using the fitted linear component (the color indicates the corresponding data in **A**), we observe a zero crossing of the differential Stark shift at $\vartheta = 37.0°$, obtained from a linear fit (dark green solid line). Over this range, the linear approximation deviates only slightly from the correct scaling $V_{\mathrm{ac}} \propto 3\sin^2\vartheta - 1$ (Eq (3.1), light green). Inset: The quadratic deviation from the purely linear light shift decreases for larger magnetic field angles, where the overlap with the lattice-induced magnetic field becomes larger. **C** To investigate the systematic uncertainty accompanied by this magnetic field tilt we fit a purely linear function without offset to subsets of the data in **A**. Starting with the lowest lattice power datapoints, we iteratively extend the fit range towards higher powers, which thus lead to a change in the fitted light shift and to a different zero-crossing. Extrapolating this trend to the y-axis intercept with a linear (ϑ_l) and quadratic (ϑ_q) function, we obtain a deviation of 0.2° compared to $\vartheta_{\mathrm{magic}}$.

linear component to extract the magic angle. We can use Eq. (1.31) to find the Stark shift dependence on θ for a fixed wavelength and obtain

$$\Delta V_{\mathrm{ac}}(m_{F'}) = -\frac{I}{2c\epsilon_0}\left(\Delta\alpha^{(0)} + \alpha^{(2)}\frac{3\cos^2\theta - 1}{2}(3m_{F'}^2 - 2)\right) + \mu B m_{F'}, \tag{3.1}$$

where we made use of the fact that the ground state does not exhibit any tensor shift and the vector shift is zero for a linearly polarized lattice. In addition, the Zeeman splitting of the $m_{F'} = \pm 1$ states is taken into account. For the π transition, this reduces to a $\cos^2\theta$ dependence, which we can use to extract a zero crossing at 37.1°. However, the narrow angular range of the data does not support this model well, owing to the expected minimal curvature at these angles. Therefore, one can approximate this dependence to be linear, which yields a magic angle of

$$\theta_{\mathrm{magic}} = 37.0(1.5)°. \tag{3.2}$$

While the statistical uncertainty of 0.09° is small, we have to take the more sizeable systematic uncertainty from the resonance shift curvature into account. To gauge this effect, we use a purely linear fit to the weak-lattice subset of the data and determine the zero crossing of the resulting light shifts. We can now increase the lattice power threshold up to which we fit the data and observe an ever decreasing extracted value for the root (Fig. 3.1 C). In this vein, we can extrapolate the trend to the hypothetical zero crossing at a vanishing lattice power

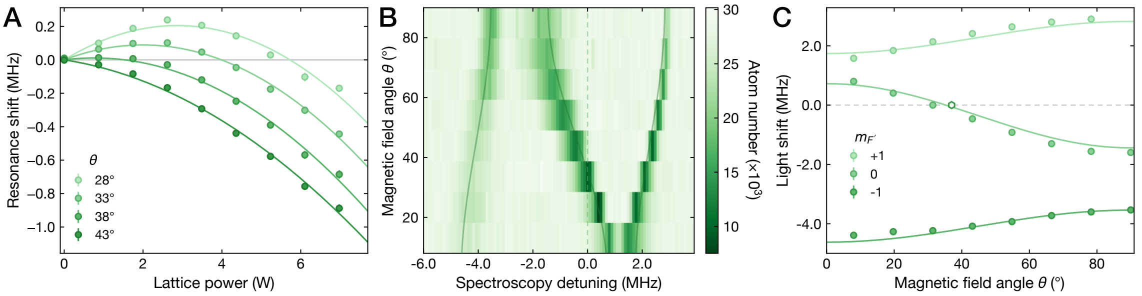

Figure 3.2 | Magic angle spectroscopy at low magnetic field amplitudes. A Bending of the $^3\mathrm{P}_1$ π transition for a magnetic field strength of $B = 1.5\,\mathrm{G}$ and various field angles ϑ relative to the vertical polarization of the lattice beams as the lattice power is increased, causing a tilt of the local quantization axis. At this B field amplitude the quadratic resonance shift overwhelms the linear component even at low lattice powers, preventing a meaningful extraction of the magic angle. **B** Resonance shifts of the three $m_{F'}$ transitions in a 1100 E_{rec} deep 2D lattice upon changing ϑ, probed with a circularly polarized spectroscopy beam with a minimal angle of $\simeq 45°$ to the magnetic field vector. We fit the resonances with three Lorentzian distributions and use Eq. (3.1) to extract the ratio of $\Delta\alpha^{(0)}$ and $\alpha^{(2)}$, assuming the coil calibrations to be precise such that the Zeeman splitting is not a free parameter. Displayed as solid lines are the corresponding fits. **C** The fitted resonance positions and the polarizability fit as a function of ϑ as determined in **B**. The magic angle of $\vartheta_{\mathrm{magic}} = 37°$ is indicated with a white hexagon, and its error bar does not contain the contribution from the coil calibrations, since the datapoints use the same calibration factors. The remaining error bars for this Figure are determined from the resonance fit uncertainty and are smaller than the datapoints.

and obtain a value of 36.88° for a linear extrapolation and 36.81° for a quadratic fit. Using the larger deviation from the latter, we receive a systematic uncertainty of 0.2°. This value, however, is overshadowed by the uncertainty stemming from the magnetic coil calibration, with relative uncertainties of 1.6% and 3.7% for the main and transverse coils, respectively. The resulting accuracy of the applied magnetic field angle around θ_{magic} is thus $\delta\theta = 1.1°$, taking the root mean square of the two individual uncertainty contributions. Almost negligibly small is the effect of the uncompensated geomagnetic field along the orthogonal direction, which amounts to 0.07°.

We note that this measurement result agrees with the expected value of 37.8° from the measured magic angle of $\theta_{\mathrm{magic}} \simeq 17°$ for the $F' = 3/2, m_{F'} = 1/2$ transition in ^{171}Yb [72] within the error bars. For this calculation we neglect the isotope shifts of the dominant transitions, which are typically on the order of a few GHz and thus insignificant at this wavelength.

To study the Stark shift of all three $m_{F'}$ transitions over the maximal accessible magnetic field range, we rotate the external magnetic field into the plane parallel to the main chamber axis, which we denote with the azimuthal angle $\phi = 0$. Along this direction, the field strength is even more limited to 1.5 G, which is why the light shift curvature for the π transition is prominent even for low lattice depths (Fig. 3.2 A). Conveniently, this magnetic field strength puts the $\sigma^{\pm}$ transitions in its direct proximity, and we can observe the light shifts evolve as expected from Eq. (3.1) in single spectroscopic measurements at a lattice depth of $V \simeq 1100\,E_{\mathrm{rec}}$ (Fig. 3.2 B-C). In particular, this confirms the measured magic angle within the measurement uncertainty.

3.1.2 Near-magic narrow-line cooling in a clock-magic 3D lattice

While the knowledge of the magic angle paves the way for magic molasses cooling during fluorescence imaging in a clock-magic trap, this is complicated in our 3D lattice setup by the horizontal polarization of the vertical lattice, which is chosen for optimal confinement strength. Thus, it is impossible to reach the magic angle for atoms on every lattice site as the local polarization axis will depend on the position within the lattice. However, as θ_{magic} is close to 45° and the $^3\text{P}_1$ transition is sufficiently broad, it is still possible to find a near-magic condition that enables long exposure times with controllable atom loss in a very deep 3D lattice. This leads to high signal-to-noise-ratio images with a four-fold increase in the detected photon count compared to molasses-free imaging after 200 ms exposure to a weak ($I \simeq 10^{-3} \times I_{\text{sat}}$) blue imaging beam and two horizontal, retro-reflected molasses beams at $I \simeq 0.8\, I_{\text{sat}}$ (Fig. 3.3 A). Here, the stark contrast in the relative intensities is governed by the almost two times larger recoil energy for 399 nm photons as well as the substantially larger scattering rate compared to the narrow 556 nm transition. We find this effective magic condition for an orientation of the magnetic field with a polar angle of $\theta \simeq 60°$ and and azimuthal angle of $\phi \simeq 60°$. Remarkably, this is in disagreement with our intuition, in particular given the worse cooling performance right at the measured magic angle (Fig. 3.3 B) and the trend to vanishing differential Stark shifts at smaller θ for deeper lattices. We attribute the discrepancy to the weak magnetic field strength of 1.5 G and the complex interplay of the orthogonally polarized horizontal and vertical lattice beams at a total lattice depth of $\simeq 4500\, E_{\text{rec}}$, as not only the polar angle leads to a strong shift of the relevant π transition, apparent in the varying molasses cooling resonance, but also the azimuthal angle ϕ (Fig. 3.3 C-D). In particular the latter decisively determines the width and thus the effectiveness of the cooling feature, where large angles are strongly preferred. This is congruent with the expectation that a magnetic field in the plane spanned by the two polarization vectors satisfies the near-magic condition best. Close to the optimal configuration, the molasses resonance right below the π transition can be identified as a sharp peak. At this frequency, the cooling light is sufficiently far red-detuned from the carrier transition to mostly drive the red sideband. Given the natural linewidth of $\gamma = 183\,\text{kHz} \simeq f_1$, atoms that are cooled to the ground state will still scatter photons, i.e., the cold atoms are not fully dark and will thus gain recoil kicks, and in particular the probability of sideband heating via blue sideband transitions is not negligible. This limits the minimal achievable temperature to several µK [80, 273]. Remarkably, we also notice a second, broader feature red-detuned from the σ^- transition, spanning almost 4 MHz in total. We identify this peak as the molasses cooling resonance next to the inhomogeneously broadened transition to the $m_{F'} = -1$ state, where we can keep a subset of the atoms at certain trap depths cold, such that they remain in the lattice longer and scatter more photons, while atoms on a different equipotential surface are detuned. We anticipate this feature to allow for the study of the trap depth homogeneity once our setup enables single-site imaging [282], which is currently hindered by the occupation of several vertical lattice planes. Atoms in off-center planes are out of focus and therefore contribute with a blurred PSF, obfuscating the signal of atoms in the in-focus layer. A potential method to reach the occupation of a single 2D plane within the 3D lattice is described in Section 3.2.3.

Furthermore, we note that we observe the molasses cooling effect also for horizontally

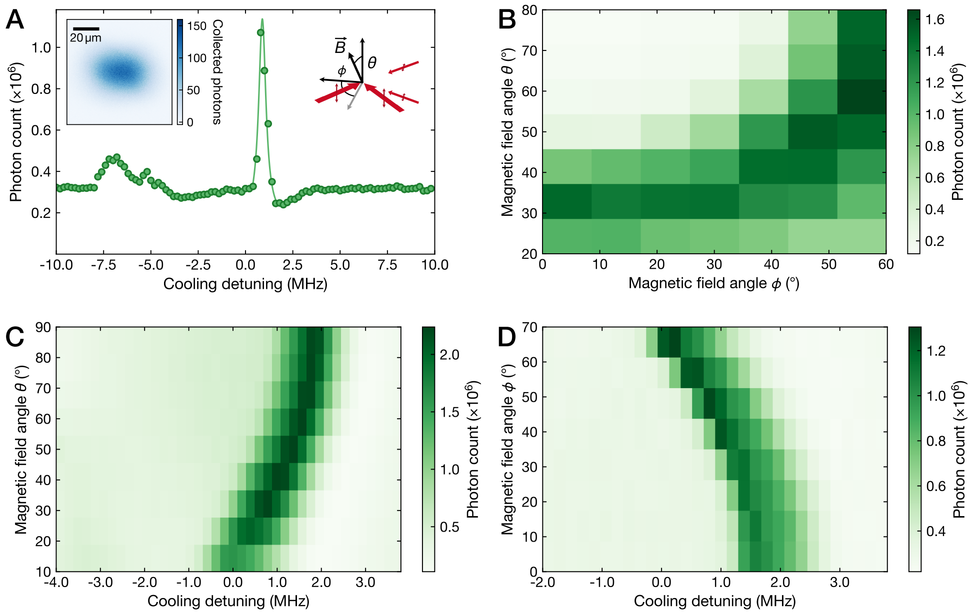

Figure 3.3 | Near-magic molasses cooling condition in a clock-magic 3D lattice. **A** The sharp molasses cooling resonance appears slightly red-detuned from the π transition, which however is shifted by the 3D lattice compared to the free-space resonance. The solid line is a Lorentzian fit serving as a guide to the eye. On resonance, due to a spectral filter in front of the camera the number of collected photons is slighly reduced compared to the far-detuned and thus uncooled background photon count. Notably, next to the σ^- transition a second, weaker and broader cooling resonance is visible, displaying the spatial inhomogeneity due to the non-magic condition. Since the vertical lattice beams are horizontally polarized (right inset), the polarization symmetry of the 2D lattice is broken and it is not possible to reach the magic angle for the whole lattice. Introducing the azimuthal angle φ relative to the vertical lattice wavevector allows us to find a near-magic condition sufficient to enable efficient cooling. Left inset: Fluorescence image with 399 nm imaging light of a molasses-cooled cloud. **B** Angular dependence of the near-magic magnetic field vector. For a polar angle close to ϑ_{magic} the horizontal lattices experience a satisfied magic condition, but the vertical lattice is non-magic if the magnetic field is aligned orthogonal to its polarization $\varphi = 0$. For larger azimuthal angles the vertical lattice starts to become magic and an optimal condition is found at $\vartheta \simeq \varphi \simeq 60°$. **C** For a fixed $\varphi \simeq 60°$, varying the polar angle does not lead to significant changes of the cooling efficiency. Instead, only a shift in the optimal cooling frequency is observed. **D** In contrast, the non-magic vertical lattice at $\vartheta = \vartheta_{\text{magic}}$ and for small φ also affects the number of scattered photons, in agreement with **B**.

polarized lattice beams at a similar polar angle, but with a reduced efficiency, such that the imaging beam intensity has to be reduced and less photons are scattered within the same exposure time. While a precise photon-atom count calibration without single-site resolution is complex and therefore still pending, we estimate a collection of $\simeq 25$ photons per trapped atom within 200 ms in this case, while we seem to detect up to $\simeq 50$ photons per atom in the case of vertically polarized horizontal beams.

In some cases it might be worthwhile to reduce the exposure time, e.g., in the case of state-selective imaging of g and e atoms. As discussed in more detail in Chapter 4.3, the clock-state atoms suffer from a fast loss process in the deep imaging lattice by means of a Raman transition to the $^3\text{P}_1$ and $^3\text{P}_2$ states via the $^3\text{S}_1$ state, where the former transfers the atom back to the ground state. Hence, the observed ratio of ground- and clock-state atoms from fluorescence images is skewed, and in particular the number of remaining clock-state atoms after long-exposure images of the ground-state fraction can be very low. Due to technical reasons it is not possible to controllably select a longer exposure time for the second image[2] and we therefore either use shorter exposure times of only 50 ms, or we independently detect g and e images in alternating shots by toggling a strong resonant "blow-away" pulse on the $^1\mathrm{P}_1$ transition, followed by a repumper pulse before the imaging starts. In the former case, we can afford a larger imaging pulse intensity, as a faster heating rate is outweighed by an increased scattering and photon collection rate. To ensure that we do not accidentally image ground-state atoms during the second exposure time, we stop the molasses cooling 30 ms before the end of the first imaging duration to gradually remove all ground-state atoms from the trap as they scatter 399 nm photons, akin to a blow-away pulse. However, for the results shown in this thesis we mostly rely on separate imaging of atoms in the ground and clock state due to the significantly larger signal-to-noise ratio we can achieve via the long exposure time.

Recently, very fast fluorescence imaging of Er atoms trapped in an optical lattice and tweezers on the 30 MHz wide 401 nm transition using two counter-propagating high-intensity beams has been demonstrated, based on earlier work in Li [283–285]. The scattering of tens of photons within just a few μs is made possible by free-space imaging and alternating brief pulses from opposing directions, only causing a moderate momentum spread from the diffusive random walk motion upon re-emission of a photon instead of fast acceleration in the propagation direction of a single imaging beam. While this momentum spread prevents a direct compatibility with single-site-resolved imaging in our magic lattice, we expect it to yield a similar signal in the homogeneously loaded 3D lattice with the benefit of a strongly reduced imaging duration. However, the counter-propagation of the second beam would not allow for the simultaneous usage of the current absorption imaging setup (Fig.2.7 A), which is why this fluorescence modality has not been tested yet.

3.2 Resolved sideband cooling on the clock transition

In contrast to the 7 kHz wide $^3\mathrm{P}_1$ transition in Sr, the 556 nm transition in Yb is not narrow enough to resolve the trap frequencies, the prerequisite for resolved sideband cooling, in any typical optical lattice or tweezer array. Instead, in order to target a sideband transition one has to resort to the much narrower clock transitions or perform two-photon Raman transitions as discussed in Section 3.3. For the former, the lack of spontaneous decay within viable experimental timescales demands for a different dissipative step to remove the entropy from the system. Choosing the $^1\mathrm{S}_0 \rightarrow {}^3\mathrm{P}_0$ transition, the $^3\mathrm{P}_0 \rightarrow {}^3\mathrm{D}_1$ repumping transition is an ideal candidate due to the reasonably large linewidth of $\Gamma = 2\pi \times 308\,\mathrm{kHz}$, which can be easily power-broadened to several tens of MHz, the favorable branching ratios with only marginal losses into the dark and untrapped $^3\mathrm{P}_2$ state, and the long wavelength of 1389 nm, entailing a

---

[2] Owing to the absence of a physical shutter, the camera records photon counts even before the trigger to start the exposure is sent. Therefore it would be possible to send a late trigger after some precursory exposure, but this is less controlled and can lead to systematic errors.

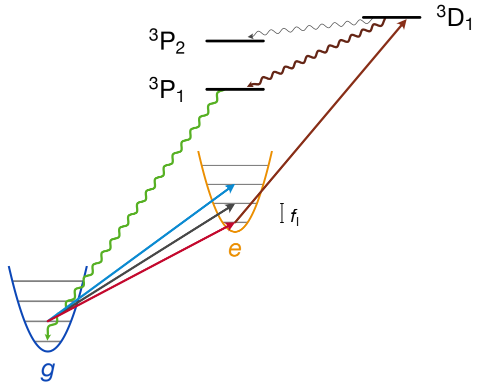

Figure 3.4 | Clock-transition sideband cooling in Yb. The very narrow linewidth of the ^{3}P$_0$ transition allows to resolve the individual sidebands even in comparably weak magic optical traps, such that we can selectively drive the red $|g, n\rangle \rightarrow |e, n-1\rangle$ or blue $|g, n\rangle \rightarrow |e, n+1\rangle$ sideband transitions, which are detuned from the carrier by the trap frequency along the clock beam wavevector, $\pm f_l$. For a transition to the red sideband, this step initiates the cooling process, which is followed by incoherently driving the repumping transition to the ^{3}D$_1$ state, until the *e* atom has either decayed back to the ground state or is stuck in the dark ^{3}P$_2$ state. Since this dissipative process is strongly agnostic of the motional state, the atom has lost the kinetic energy hf_l after a full cycle. Once the motional ground state has been reached, the red sideband cannot be driven, rendering the cold atoms dark to the cooling light.

low recoil energy of $h \times 595$ Hz. Tuning the frequency of a clock beam to the red sideband, one can then drive the $|g, n\rangle \rightarrow |e, n-1\rangle$ transition, and a subsequently or simultaneously applied repumper pulse will transfer the atoms in the clock state predominantly back to $|g, n-1\rangle$ via the ^{3}P$_1$ state, as the radiative decay preserves the motional state owing to the suppression of blue and red sideband transitions by a factor of $\eta^2(n+1)$ and $\eta^2 n$, respectively [273]. Repeating this process therefore iteratively reduces the axial harmonic oscillator level by one quantum. Atoms in the motional ground state, however, cannot be addressed by the clock beam anymore and are thus dark to the cooling beams. This enables one to reach considerable ground-state fractions along the cooled, strongly confined axis [278]. In particular, even temperatures below the recoil limit of $T = 410$ nK for the decay cascade can be achieved, as the collection of recoil momenta is impeded by the lattice band gap.

While this scheme works very well along the axial direction of a 1D lattice, cooling atoms also along the weakly confined axes requires more elaborate schemes involving counter-propagating clock beams to address specific velocity classes of the Doppler-broadened radial spectra [126], or lattices blue-detuned from the 1389 nm ^{3}P$_0$ → ^{3}D$_1$ transition to enable a Sisyphus cooling process driven by a clock excitation to the repump lattice potential minima [276]. However, both methods necessitate two orthogonal beam pairs, each consisting of two counter-propagating beams, along the weakly confined directions, which can be unfeasible due to limited optical access along these directions in certain experimental setups, especially in combination with high-NA objectives. We therefore introduce a simple extension of the basic 1D sideband cooling scheme with single longitudinal clock and repumping beams to show 3D cooling of ^{174}Yb atoms by means of lattice-quenched rethermalization in Section 3.2.1. In Section 3.2.2 we further delineate resolved sideband cooling in a higher-dimensional lattice, which has not been demonstrated for Yb so far. Section 3.2.3 then offers an outlook on reaching the 3D motional ground state by extending this method to the vertical direction. We further discuss the possibility to use this method to load a single vertical lattice plane via momentum refocusing, which would allow for the first demonstration of single-site resolved imaging of Yb in a magic lattice.

3.2.1 Rethermalized 1D sideband cooling

For ^{171}Yb, the finite clock transition matrix element allows for a relatively strong coupling, with carrier Rabi frequencies exceeding 10 kHz. Correspondingly, the red sideband, where the Rabi frequency is modified by a factor of $\eta\sqrt{n}$, can also be addressed with sub-ms pulses. The broad distribution of trap frequencies experienced by $T_\mathrm{l} \simeq 10\,\mu\mathrm{K}$ cold atoms in a 1D lattice during the sideband pulse leads to the well-known long tail towards the carrier [166], which leads to an incoherent sum of detunings for the sideband pulse, preventing coherent Rabi cycles on this sideband transition. Therefore, the simplest cooling strategy involves a continuous application of the clock and repump beams, where a moderate intensity of the latter ensures a controllable light shift on the clock transition. Since the excitation to the $^3\mathrm{D}_1$ state is typically still faster than the sideband Rabi frequency, this process is mostly limited by the sideband addressing rate and can quickly decrease the mean longitudinal temperature, such that a ground state occupation of $> 90\%$ can be reached within tens of ms [278]. As an alternative, one can use a sequence of interleaved clock and repump pulses, where each pulse duration is chosen to reach a near-saturated population transfer.

While the general scheme can be readily carried over to cool ^{174}Yb atoms, the clock Rabi frequencies are inherently limited by the applied magnetic field strength. With our experimental setup, where we can reach up to 400 G and 300 mW of optical power in the clock beam, this leads to a saturation of the sideband excitation after $\simeq 1$ ms at a detuning of -80 kHz from the carrier in a $\simeq 580\,E_\mathrm{rec}$ deep lattice with co-propagating clock and repump beams. However, even with a 0.5 ms long clock pulse, about 75% of the saturated sideband population can be addressed. For $\simeq 2$ mW of 1389 nm light, we are able to repump all atoms from the clock state within 0.5 ms, such that we can choose a duration of 1 ms for each cooling pulse pair, using the sequential cooling method and the most efficient clock pulse duration. As we repeat this cooling pulse sequence, we observe a marked reduction of the red sideband height, which is indicative of a lower longitudinal temperature. For a pulse train consisting of 30 clock and repumper pulses each, we reach temperatures of 3.1(2) µK and 15.4(3) µK along the longitudinal and radial directions, compared to initial temperatures of $T_{\mathrm{l},0} = 9.3(6)\,\mu\mathrm{K}$ and $T_{\mathrm{r},0} = 11.7(4)\,\mu\mathrm{K}$ (Fig. 3.6), where we have “pre-cooled” the cloud by spilling the hottest atoms after loading the lattice by reducing the lattice depth to $290\,E_\mathrm{rec}$ for 150 ms. Here, the temperatures are determined from a fit with the approximative Eq. (2.9) to both the full sideband spectrum as well as a zoom-in on the blue sideband. We can extract both T_l and T_r from each fit, but as the ratio of the areas below the red and blue sidebands is a precise gauge of the longitudinal temperature here we rely on the fit to the full spectrum. Similarly, the finely resolved blue sideband contains more accurate information about the radial temperature — with the exception of the uncooled dataset, where both radially and axially high temperatures

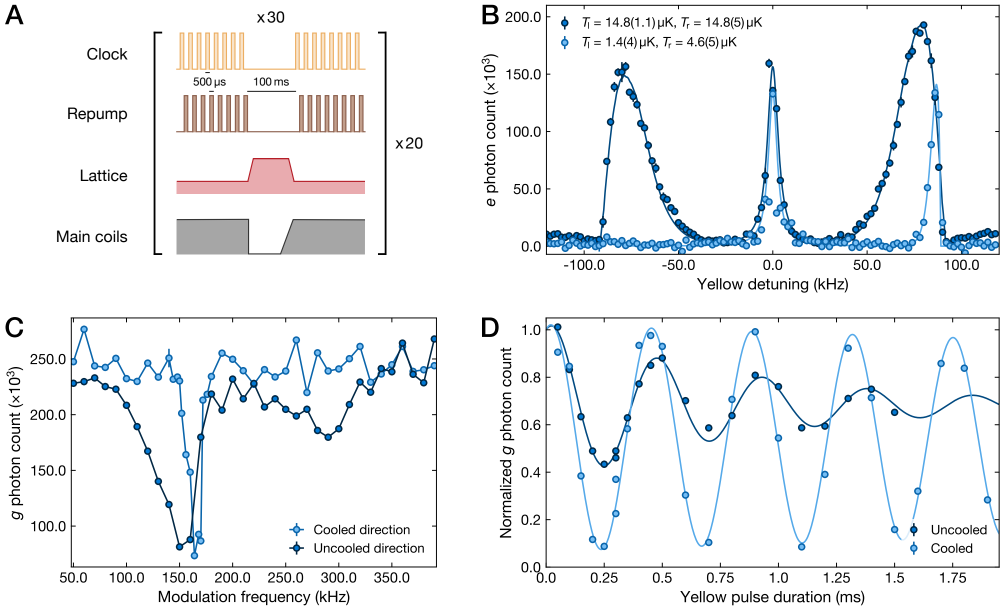

Figure 3.5 | Rethermalized clock sideband cooling in a 1D lattice. **A** Schematic of the experimental sequence. At a strong magnetic field of 400 G we address the red sideband on the clock transition with 0.5 ms short pulses, followed by equally short 1389 nm repumping pulses. After 30 repetitions the atoms are sufficiently close to the motional ground state and we wait for the atoms to redistribute the radial kinetic energy via elastic collisions. To enhance the collision rate the lattice depth is ramped up to $\simeq 1500\,E_{\mathrm{rec}}$. The coils are turned off during the wait time to minimize the heating from the high currents. This process can be repeated multiple times to reduce the radial temperature. **B** Sideband spectra of the atomic cloud before (dark blue) and after 20 cycles of rethermalized sideband cooling (light blue). The red sideband is virtually suppressed and the width of the blue sideband is strongly narrowed, indicative of the temperature reduction. The temperatures are determined by a fit with Eq. (2.9) (solid lines). **C** Modulation spectroscopy measurements of the cooled sample show narrow heating resonances in the 1D lattice used for sideband cooling (light blue). Upon switching to the second horizontal lattice after a hand-off in a 2D lattice we observe a significantly broader resonance (dark blue), demonstrating the heating caused by the change in the lattice dimensionality. The solid lines are a linear interpolation. **D** While the Rabi oscillations suffer from limited excitation ratios and fast motional dephasing in an uncooled cloud, clock pulses after sideband cooling yield almost full-contrast oscillations with significantly longer decoherence times of $\simeq 30$ Rabi cycles, as obtained from damped sinusoidal fits (solid lines).

lead to a partially ambiguous result with correspondingly large statistical uncertainties, which is why we rely on the well-resolved result from the full spectrum for $T_{\mathrm{r},0}$. At this point, we observe a slight change in the shape of the blue sideband, as the lower longitudinal mean vibrational state $\langle n_{\mathrm{l}} \rangle$ leads to a sharper high-frequency cut-off trend, while the low-frequency tail grows. We note that this observed increase in the radial temperature can be expected as an effect of recoil kicks along the weakly confined directions from the spontaneous decay cascade. Further increasing the number of cooling pulses to $\simeq 50$ leads to a fully suppressed red sideband, with longitudinal temperatures of $\lesssim 1\,\mu\mathrm{K}$.

Remarkably, we observe a reappearance of this sideband if we introduce a wait time of $\simeq$ 50 ms before the 20 ms long, incoherent sideband pulse, accompanied by a visible reduction of the blue sideband extent, which further manifests for longer wait times. This is an effect of the

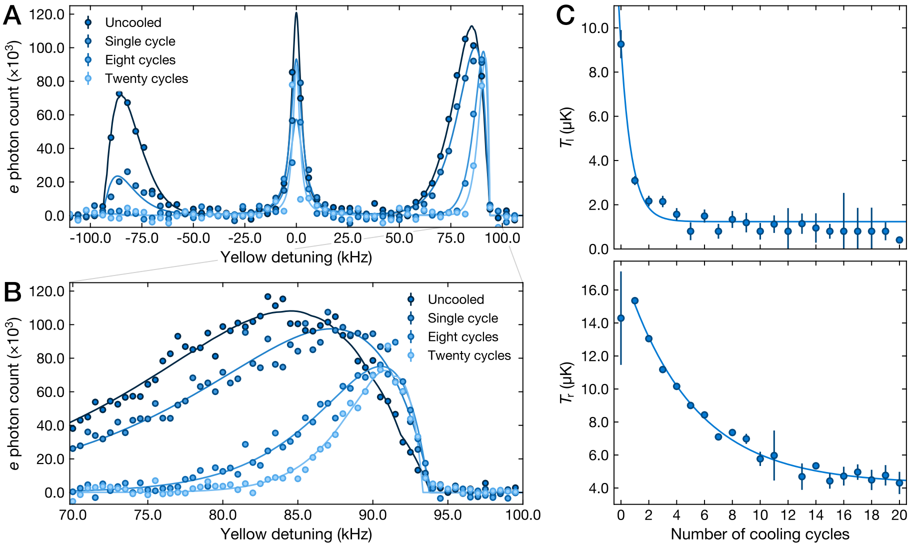

Figure 3.6 | Temperature evolution for different rethermalization cycle numbers. **A** Starting with a slightly colder cloud as in Fig. 3.5 B by spilling the hottest atoms, we see a marked reduction of the red sideband amplitude after the first sideband cooling pulse train. At this point, the blue sideband mostly reflects the different longitudinal temperature. However, as we apply more cooling cycles with interleaved rethermalization periods, not only does the red sideband fully vanish, but also the blue sideband is compressed. **B** Zooming in on the blue sideband, we can clearly observe the step-wise reduction of the radial temperature resulting in a narrowing sideband resonance. **C** By fitting the full sideband spectrum we extract the longitudinal temperature (top panel) as a function of the applied cooling cycles. The fast reduction to $T_l \simeq 3\,\mu\text{K}$ within a single cycle illustrates the effectiveness of the cooling method along the strongly confined axis. For very low T_l the fit becomes sensitive to the single-shot noise in **A**, limiting the accuracy of the fit. Bottom panel: From the finer resolution of the blue sideband in **B** we can obtain the radial temperatures, showing an exponentially decreasing trend converging towards a minimal temperature of $T_r = 4.2(2)\,\mu\text{K}$. For large axial temperatures, the fit to the blue sideband is insufficient to distinguish the radial and temperature longitudinal contributions, causing a large statistical uncertainty for the uncooled dataset. The fit to the full spectrum, in contrast, can utilize the red sideband height to obtain a radial temperature of $T_{r,0} = 11.7(4)\,\mu\text{K}$.

considerable mean atom occupation per lattice layer of $\simeq 230$, which leads to myriad collisions and thus rethermalization among the spatial dimensions. Notably, due to the longitudinally lower temperature the atoms initially propagate in an almost fully 2D plane, which enhances the collision rate to $\simeq$ 10 kHz. However, these elastic collisions mostly occur head-to-head, such that the rethermalization is generally much slower. To intensify the speed with which the radial kinetic energy is redistributed to the longitudinal direction, we find it useful to increase the lattice depth to $\simeq 1500\,E_{\text{rec}}$, where the rethermalization time is approximately halved to a $1/e$ time of $\simeq$ 40 ms. This can be explained by the lattice depth dependence of the localization of the Wannier functions around the potential minimum, since this lattice quench augments the overlap of the atomic wavefunctions along the strongly confined axis. We note that we observe a simultaneous rise of the longitudinal steady-state temperature by $0.6(3)\,\mu\text{K}$, but no indication of collision-induced atom loss.

Performing a second sequence of sideband pulses after a wait time of $\simeq$ 100 ms, where the rethermalization trend is found to have saturated, we can again cool the atoms close to the longitudinal motional ground state with a fitted temperature of $T_\mathrm{l} = 2.2(2)\,\mu\mathrm{K}$, but we simultaneously detect a reduced radial temperature of $T_\mathrm{r} = 13.1(3)\,\mu\mathrm{K}$. We turn the strong magnetic field off during the waiting period to minimize the effective duty cycle, since otherwise the coils cannot be sufficiently cooled. This process can be repeated, which leads to a continuous shrinkage of the width of the blue sideband. We quantify this reduction to entail an exponential reduction of the radial temperature, while the red sideband vanishes within four cooling cycles to below the detection limit we can achieve without multiple averages. We note that the extracted values for the longitudinal temperatures in Fig. 3.6 C are likely overestimates as we have to restrict the fitting range from below to ensure the convergence of the fits for most datasets with no distinguishable red sideband amplitude. After 20 cycles we then see an asymptotical radial temperature of $4.2(2)\,\mu\mathrm{K}$, indicating that at this temperature the collision rate has decreased to a value that is no longer sufficient to redistribute the kinetic energy within the chosen wait time.

Fig. 3.5 B demonstrates the difference in the sideband spectra between an uncooled cloud, where we did not apply any spilling of hot atoms, and a sideband-cooled sample. From the carrier peak height we can further deduce an upper bound on the incurred losses from the cooling, which we estimate to be $\simeq 15\%$, which agrees with the fraction of 2.6% of repumped atoms that decay to the dark $^3\mathrm{P}_2$ state for an initial longitudinal mean occupation number of 2.9 and four additional cooling cycles that are on average necessary due to the rethermalization from the radial directions. The mean radial occupation number at the final temperature is $\langle n_\mathrm{r} \rangle \simeq 230$, which is sufficiently low to also produce a very sharp parametric heating resonance dip in a modulation spectroscopy measurement (Fig. 3.5 C), reflecting the narrow blue sideband owing to the significantly reduced excursions of the cooled atoms along the weakly confined axis. However, this situation changes as we transfer the atoms to the power-balanced orthogonal horizontal lattice arm and perform the same measurement there, where we observe the typical widened resonance. This demonstrates the adversary effects of changing the dimensionality of the system for a substantial mean occupation number along this direction, which is then mapped onto a larger temperature as the strong confinement is ramped up.

The effectiveness of the longitudinal cooling also enables a strongly improved clock state addressing fidelity, as can be seen in Fig. 3.5 D. Motional dephasing of hot atoms in various harmonic oscillator levels leads to both reduced π-pulse contrast and fast decay of the Rabi oscillations, whereas in the cooled case up to 93% of the atoms can be coherently excited to the clock state and the oscillations remain coherent for a $1/e$ number of $\simeq 30$ cycles. While the missing fraction to full-contrast oscillations can be partially traced to the remnant non-zero harmonic oscillator level occupation, we estimate this to be the case for less than 2% of the atoms. Instead, we attribute this effect to the presence of interaction shifts in the 1D lattice planes as well as to original e atoms that are repumped back to the ground state via the $^3\mathrm{S}_1$ Raman channel during the imaging of ground-state atoms. In particular the latter can amount to $\simeq 8\%$ spurious counts (Chapter 4.3, [120]) despite a short exposure time closely following the clock pulse.[3] The clock-state photon count, however, is biased by the fast inelastic collisions of e-e atom pairs in the 1D lattice. To avoid this, several techniques including coherent

---

[3] The wait time until we start the imaging is limited by the slow ramp-down of the magnetic field, which we can compensate from 20 ms after the end of the clock pulse (Chapter 2.2.1).

delocalization in excited lattice bands and ratchet-like lattice loading methods from the MOT have been developed to reduce the atomic density while maintaining large atom numbers [120, 286]. We further notice that the dephasing time correlates with the inverse of the Rabi frequency, i.e., with the time that atoms spend in the clock state, which underlines the role of interactions in this process. Therefore, the clock excitation fidelity is aided by the spatial separation of cold atoms in higher-dimensional lattices.

An additional observation pertains to the cooling performance in a very deep lattice. We find that for trap frequencies and thus optimal cooling detunings of $f_\text{l} > 100\,\text{kHz}$ it is increasingly hard to reach very low mean occupation numbers, with minimal $\langle n_\text{l} \rangle$ of 0.5 for a $\simeq 2000\,E_\text{rec}$ deep lattice. This effect could stem from the departure of the $^3\text{D}_1$ state from a sufficiently near-magic condition. Although the large power-broadened linewidth of the repumper transition appears unlikely to be limiting, the light shift of this state at 759 nm is essentially unkown and could become significant in such deep lattices, which would cause a local dependence of the repumping efficiency. The potential reason of the necessary overall longer cooling time due to the smaller Lamb-Dicke factor can be excluded, as the cooling in the weaker lattice does not show a worse performance upon a reduction of the clock beam power by the same amount.

While the results presented in this Section for the first time illustrate the feasibility of fast resolved clock sideband cooling in ^{174}Yb, a crucial disadvantage of the rethermalization method to reduce the 3D temperature of the sample is its dependence on the slow energy redistribution process. This leads to total cooling sequence durations of up to 2.8 s, and the minimal achievable temperature along the weakly confined axes is limited to a few μK. Therefore, a straightforward extension of this technique involves direct sideband cooling along both horizontal lattices, which will be discussed in the next Section.

3.2.2 2D sideband cooling

While we now know that sideband cooling on the clock transition can quickly remove kinetic energy of atoms along the beam's direction at a given lattice frequency, the different energy landscape in the 2D lattice renders this method more challenging. When we probe the sideband spectrum along one lattice arm with uncooled atoms in a 2D lattice, we observe distinct differences compared to the 1D case. As the most evident difference, the tails towards the carrier extend significantly further and are not fitted well by Eq. (2.9) anymore. Also, the second sidebands are clearly visible and do not possess a clear cut-off at $2f_\text{l}$, but instead appear smeared out, reaching well into the first sidebands. This behavior can be traced back to the broken symmetry along the orthogonal horizontal direction, where the atoms cannot move freely any longer, but are trapped inside tubes, while the motion along the vertical direction is still only constrained by the weak Gaussian confinement. Therefore, in contrast to the one-dimensional lattice we cannot approximate all lattice sites to be identical, since atoms that are trapped in distant sites from the center experience a weaker maximum lattice potential even when they travel to the center of their tubes. For a 40 μm wide atomic cloud in a 2D lattice with horizontal beam diameters of 90 μm, we therefore obtain a substantially broadened distribution of the maximum trap frequencies the atoms can observe. Since the clock spectroscopy beam detects the projection of the local trap frequency onto its wavevector, i.e., it is only sensitive to the local contrast of the lattice arm parallel to the spectroscopy beam, this leads to an even wider spread, where atoms can reside on lattice sites that appear shallow since the local trapping potential is predominantly provided by the orthogonal lattice beam. Remarkably, this allows us to directly discern deep from weak lattice depth projections as the brightness of the fluorescence image spatially varies during the clock detuning sweep across the sidebands. The resolution of this phenomenon is slightly obfuscated, however, by the atomic motion along the vertical direction that adds the well-known radial-temperature-dependent tail feature to the individual spectrum of each tube.

This necessitates a more complex treatment of the sideband spectrum, which takes the initial size of the cloud with respect to the lattice beam waist along which the sideband is probed into account. We further have to adapt the calculations for the lineshape contribution of individual lattice sites to take the strong confinement along the second horizontal axis into account, finding that the term linear in $\gamma(n_l) - \delta$ in Eq. (2.9) vanishes as a result of the changed density of states along the now single weakly confined axis [103]. This compresses the size of the radial tail for each lattice site. Additionally, we can safely neglect the very weak dependence of the sideband distribution function on the temperature along the orthogonal horizontal direction and treat the two strongly confined axes as independent of each other. While this provides an analytical expression, the Gaussian lattice depth inhomogeneities in the horizontal plane cannot be captured in a simple functional form. Therefore, we sample over a grid of lattice sites of adjustable density to generate a discrete set of lattice depths, whose summed contributions to the overall sideband spectrum are weighted with a Gaussian population density. As this summation slows down the calculation severely, we typically constrain the grid size to arrays of at most 30×30 and discard the minuscule contributions from lattice sites at distances larger than 3σ from the center. As a side effect, this entails a peaky sub-structure on the modeled sideband spectrum shape from the individual summands. We smoothen the peaks by convolving over the fitted carrier linewidth to reduce the risk of fitting to data artifacts.

Crucially, this model requires independent knowledge of the cloud size with respect to the lattice waist, since the broadening effects of this ratio and the radial temperature are too similar to leave the former as a free fit parameter. We therefore use the extracted waist of $w_0 = 44(2)\,\mu\text{m}$ from Chapter 2.6.2 and employ fluorescence images to fit a 2D Gaussian distribution and extract an estimate of the cloud extent. For the lattice loading parameters we use for this type of measurements we consistently find a cloud size of $\sigma = 15(1)\,\mu\text{m}$, which however might be an overestimate due to the substantial spherical aberrations of atoms in vertical planes far out of the depth of field. Using this value for our sideband model nevertheless, we find a very good agreement with the data for the first sidebands (Fig. 3.7 D), whereas our theoretical description of the second sidebands consistently appears to overvalue the actual strength for high longitudinal temperatures. Since the second sidebands do not contain additional physically relevant information, we do not investigate this further at this point and instead restrict our evaluation to the first sidebands.

The inhomogeneous trap depths in the 2D lattice also demand for a more advanced approach as we turn to sideband cooling. We find it no longer sufficient to use a single cooling frequency, which only addresses a specific class of atoms in a certain spatial region of the lattice. A result of this naive single-detuning technique is depicted in Fig. 3.7 B, where we can observe dent-like

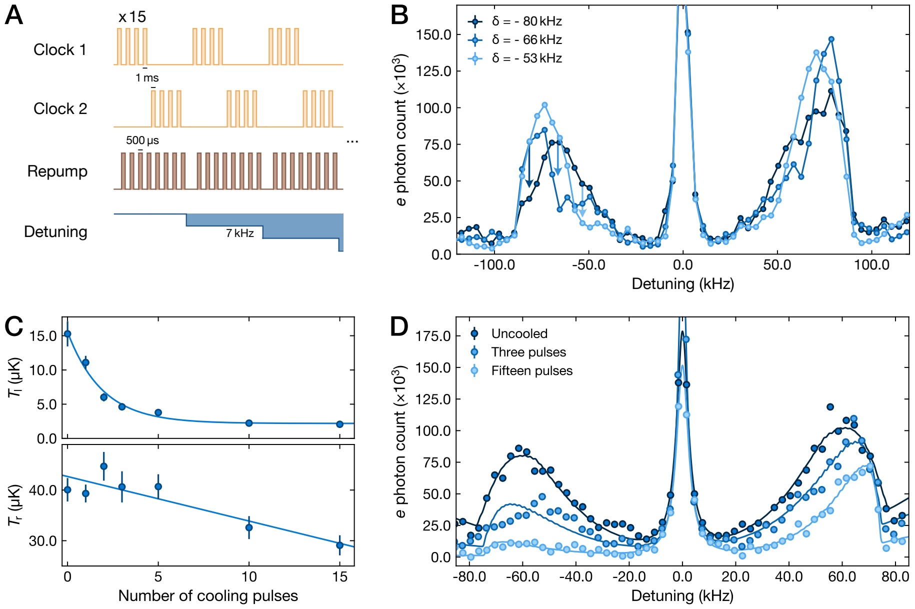

Figure 3.7 | Multi-tone sideband cooling in a 2D lattice. A In a simple extension of the 1D cooling scheme to a $\simeq 750\,E_{\text{rec}}$ deep 2D lattice we apply a pulse sequence of up to 15 1 ms long clock pulses along one arm, interleaved with repump pulses and followed by identical cooling steps along the orthogonal, intensity-balanced horizontal lattice arm. Due to the trap depth inhomogeneity in the 2D lattice, further repetitions of this cooling sequence at a different cooling detuning are necessary to address all atoms. Here, we find six discrete frequency steps by −7 kHz, starting at −30 kHz and ending at −72 kHz, to yield very high ground-state fractions. While the order with which the two horizontal directions are cooled does not show any effect on the final temperature along each arm, we observe a clearly worse cooling performance if the sign of the cooling detuning steps is changed. **B** Cooling at a single clock pulse frequency leads to a clear reduction of the red sideband amplitude at this frequency and slightly below, illustrating the effect of the lattice depth inhomogeneity on the total sideband spectrum. Here, the horizontal position of the arrows indicates the chosen cooling detuning δ. **C** Varying the number of pulses per detuning step leads to a fast initial temperature reduction along the cooling direction to $\simeq 5$ μK for three pulses, but we have to apply 15 pulses to reach a temperature close to the asymptotic value of $T_l \simeq 2$ μK at this lattice depth. The radial temperature decreases slowly but linearly with the number of pulses, which we attribute to thermalization as the total cooling duration increases. **D** From the corresponding sideband spectra we can further learn that the cooling efficiency is not spatially uniform, as the red sideband for three cooling pulses per cycle exhibits an irregular shape where the amplitude in the intermediate detuning regime is only slightly reduced compared to the uncooled case. Thus, the overall cooling duration can likely be reduced by adjusting the number of pulses for each detuning.

features in the red sideband below the cooling beam detuning, which highlights the limited responsiveness of the 2D-trapped atoms. This is in contrast to the 1D lattice case where atoms are free to move through the potential minimum even when they are radially hot, such that all atoms can be addressed by a single cooling beam detuning just above $-f_l$. Therefore, effective cooling of the whole sample in 2D requires pulses at variable detunings. A first attempt of cooling pulses at three different frequencies, spaced by 10 kHz to cover a range from $\simeq -70$ kHz to $\simeq -45$ kHz, leads to a significantly improved result of $\langle n_l \rangle \simeq 0.4$, where we hold the atoms in a $\simeq 680\,E_{\text{rec}}$ deep lattice with balanced horizontal lattice arms, such that the sideband spectra obtained from clock pulse interrogation with the two co-propagating spectroscopy beams yield

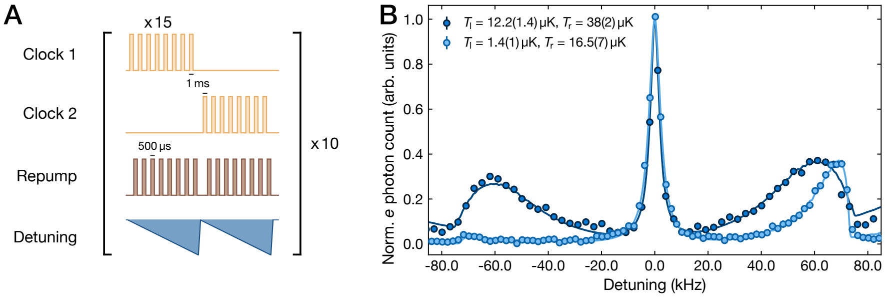

Figure 3.8 | Sweeping sideband cooling in a 2D lattice. **A** Instead of sending multiple cooling pulses at a constant detuning as for the multi-tone cooling scheme, we can also iteratively change the cooling frequency during each pulse train by performing a frequency sweep, starting with pulses at the onset of the sideband close to the carrier and ending with a detuning of $\delta \simeq f_l$. Afterwards, we switch to the orthogonal lattice arm and repeat this process. We find 15 pulses during each frequency sweeps to achieve the best cooling performance. While the experimental realization utilizes two independent signals from direct digital synthesizers (DDS) for the two clock beams, here we depict them as a single source for reasons of clarity. **B** After ten such cycles (light blue), the red sideband is barely visible and we detect a temperature reduction to $T_l \lesssim 1.5\,\mu$K along both horizontal lattice arms compared to initial temperatures of $\simeq 13\,\mu$K, which is determined by probing the sideband spectrum with both horizontal clock beams independently and fitting the 2D sideband model, where we sum over 30 different lattice depths within a cloud size of $\sigma \simeq 15\,\mu$m. The temperature along the weakly confined vertical direction is also substantially reduced, owing to weak but present rethermalization in multiply occupied sites. The fit result for the hotter sample however strongly depends on the cloud size, which is non-trivial to carefully assess with a considerable number of lattice planes out of the objective's focus.

the same trap frequency of $f_l = 74$ kHz. Here, we use a similar pulse sequence to the 1D case, however with a clock cooling pulse duration of 1 ms, owing to the clock power distribution among both horizontal beams, and with 20 pulses per cooling detuning. We note that we still require only the repumper beam along lattice arm 1, since this dispersive process is agnostic of any directionality. As expected, cooling along one lattice arm leaves the temperature along the orthogonal direction essentially unchanged, but we can interleave identical cooling pulse trains for both clock beams, i.e., apply a given number of clock pulses along the first arm before switching to arm two at the same detuning, then switch back to lattice arm one at the next detuning, until the sample is cooled down horizontally to a temperature of $T_h \simeq 2\,\mu$K. With this tri-tone method, we however still observe a remnant red sideband, which we ascribe to the imperfect addressing of atoms at even smaller detunings. We thus expand the range of cooling detunings to seven values from -30 kHz to -72 kHz, spaced by 7 kHz. As most atoms are addressed by more than one pulse sequence due to the long radial tail, we reach near-asymptotic longitudinal temperatures of $T_l \simeq 1.5\,\mu$K after 15 pulses, and even for a single clock pulse per frequency step along each axis we observe a significant reduction of the horizontal temperature (Fig. 3.7 C). We further detect a linearly decreasing radial temperature as the number of pulses grows, which is consistent with slow rethermalization during the longer overall cooling duration. This redistribution of energy is much weaker than for the 1D lattice as the occupation per 2D lattice site is substantially lower, such that a considerable fraction of atoms can only collide with other atoms after randomly tunneling to adjacent populated sites. Hence, we detect only minimally reappearing red sidebands if we introduce wait times of up to 2 s between the cooling sequence and the sideband spectroscopy pulse.

Assessing the magnitude of cooling-induced losses as a significant figure of merit for the applicability of this scheme is substantially complicated in the 2D lattice case by very fast inelastic *e*-*e* losses from doubly occupied tubes. After the horizontal cooling the atomic wavefunctions are strongly confined to the center of each lattice site, such that the atoms are bound to collide within few oscillation periods along the vertical direction, whereas the uncooled atoms are much less likely to scatter. Experimentally, we can quantify this effect by studying the combined $e + g$ signal as a function of the delay between the clock excitation and the repump pulse, which shows a rapid loss within $\simeq 5$ ms. Unfortunately, this timescale is too fast for pure clock-state imaging, since we require a comparably long blow-away pulse for residual g atoms in this case, such that this collisional loss effect strongly dominates the signal reduction for cold samples. We can inhibit these losses by adding a weak vertical lattice after the clock pulse to separate the atoms before they can collide, such that we can gauge the fraction of lost atoms to be slightly weaker than for the rethermalized 1D cooling. We expect these losses to be largely recoverable by adding a repump beam resonant with the $^3\mathrm{S}_1$ transition to regain the atoms trapped in the $^3\mathrm{P}_2$ state. In our case, the magnitude of the incurred losses does not justify the additional complexity from such a beam.

Upon permuting the order of horizontal cooling axes we cannot identify any difference in the sideband spectra with a given clock beam, which is in contrast to the markedly higher temperatures if we reverse the order of detuning steps. This can be explained by the effect that hotter atoms appear closer to the carrier and we thus increase the chances of addressing a single atom multiple times in subsequent detuning cycles until it has reached the motional ground state, while it is possible to accidentally disregard cooled atoms if the cooling beam detuning is moved closer to the carrier.

To avoid this effect, we also test a slightly different approach, where the cooling beam frequency is swept across the red sideband during a single pulse sequence, followed by an identical sweep along the second lattice arm (Fig. 3.8 A). We can again repeat this process multiple times until the ground state fraction is sufficiently large. While we mostly observe a dependence of the final temperature on the total number of pulses, we find that very few cooling pulses per sweep lead to a worse cooling performance as the frequency gap introduced by the finite repump pulse durations gets too large. With 15 pulses per sweep and ten repetitions we achieve longitudinal temperatures of $T_\mathrm{l} = 1.3(1)\,\mu\mathrm{K}$ in a $\simeq 720\,E_\mathrm{rec}$ deep lattice, and we observe an even stronger reduction of the radial temperature compared to the septa-tone cooling method. Notably, it does not appear straightforward to reach horizontal temperatures below $1\,\mu\mathrm{K}$, corresponding to an average harmonic oscillator state of $\langle n_\mathrm{l} \rangle \lesssim 0.1$, with this method alone. Reducing the lattice depth, however, allows us to reach nK temperatures, which is in line with our observations in the 1D lattice where the cooling limit is similarly defined by the lattice depth. This motivates a reduction of the lattice depth after the initial cooling sequences, which is only fully effective if also the radial temperature is sufficiently low to prevent spilling losses in the weaker lattice.

3.2.3 3D sideband cooling

Having demonstrated multi-directional clock sideband cooling, the addition of a third cooling direction in a 3D lattice appears natural. However, in our apparatus the magnetic field strength along the horizontal plane we can generate with the transverse coils is limited to $\simeq 25\,\mathrm{G}$. This does not only impede the vertical clock sideband cooling in ^{174}Yb, as the corresponding clock pulses are required to be 16 times longer compared to the horizontal pulses in a 400 G field, which can only be partially compensated by a larger optical power in the vertical beam, but also exacerbates the quest for an initial signal: Along the horizontal directions it is convenient to use the lattice beams as a guide to achieve a decent initial overlap with the atomic cloud, which typically yields a reasonable spectroscopic signal right away. For the vertical beam, we are lacking this means of assistance, which is why a broadened clock transition would be helpful. Therefore, it is expedient to switch to ^{171}Yb, where the magnetic field strength requirements are markedly less stringent and larger Rabi couplings can be achieved. Unfortunately, recurring technical issues with the water chiller for the main coils prevented us from exploring the clock coupling along the vertical axis. Therefore, this Section is restricted to a theoretical discussion of the expected sideband shape from the vertical lattice and its implications on vertical cooling avenues.

Besides the smaller Rabi frequency in ^{174}Yb, a major difference for cooling along the vertical lattice axis is the weaker longitudinal confinement, which also results in a larger Lamb-Dicke factor. While one would intuitively expect this to result in a poorer cooling efficiency, we anticipate this effect to be secondary as we still reside well in the resolved sideband regime. In addition, we conjecture from the reciprocally proportional lower temperature limit we observe in 1D and 2D that the smaller light shift in the dissipative steps, which we suspect as the reason for this limiting effect, may outweigh the increased chance of motional level-changing decay processes. A third challenge is imposed by the significant harmonic confinement along the vertical direction, which is in contrast to the negligible expansion of the horizontal lattice beams due to the much larger Rayleigh lengthscale. This will result in resolvable vertical lattice planes in the sideband spectrum for a sufficiently cold cloud, as displayed in [56]. In addition, the radial motion is now fully suppressed, such that the sideband shape is now purely defined by the discrete motional levels along each lattice axis as well as the further enhanced inhomogeneous projections of the local lattice depths. Therefore, the sidebands carry almost neglibly little information on the orthogonal temperatures, rendering 3D thermometry necessary to obtain the temperatures along each lattice axis. For an uncooled sample in a 3D lattice, this leads to a plateau-like sideband spectrum without any clear features apart from a cut-off at the horizontal lattice trap frequency f_1. In order to cool atoms in all vertical planes, this will likely necessitate even larger frequency sweep ranges than for the 2D case, interleaved or followed by a similar multi-frequency cooling sequence along the vertical direction, until we can resolve single sharp sideband peaks similar to the sideband spectra in optical tweezers [72]. At this point, the determination of the temperatures along each lattice axis can be performed by comparing the area under the red and blue sidebands as defined in Eq. (2.8).

Crucially, in future experiments we are only interested in the atoms in the center plane, which we can sharply image with our objective, and fluorescence signal contributions from atoms in residual planes are detrimental as they provide a blurred photon background. Therefore, a significant auxiliary goal of vertical cooling beyond reaching the 3D motional ground state is to achieve a single occupied vertical lattice plane. As outlined in Chapter 2.6.3, Yb provides only limited options to selectively remove atoms outside the desired plane with a resonant pulse. Instead, a viable pathway is provided by the release-and-retrap method [287, 288], where an initially widespread atomic cloud is contracted to the center of a harmonic trap by momentum refocusing after cooling in a lattice potential. Semiclassical calculations suggest that this method should provide a large refocused fraction of atoms in the central vertical lattice plane after an abrupt ramp-down of the vertical lattice, which is quenched back on after an evolution in the harmonic confinement of the 2D lattice for a duration of $T_\mathrm{r}/4$, if the vertical temperature is brought to $\lesssim 1.2\,\mu\mathrm{K}$, and almost complete wavefunction overlap for $T_\mathrm{r} < 600\,\mathrm{nK}$. From this point on, the probability of loading an atom into an adjacent plane as the vertical lattice is ramped back up is largely defined by the extent of the wavefunction in the harmonic trap, and thus the refocusing fidelity benefits from maximally deep 2D lattices. Remarkably, for our lattice parameters the simulated results are almost independent of the initial temperature, which is typically defined by the MOT loading temperature and determines the spatial extent of the could, indicating a negligible expected influence of anharmonicities in the lattice potential.

A second approach that should not require the presumably tortuous and inefficient overall cooling of the whole 3D cloud leverages the high spectral resolution of the clock transition to selectively cool atoms in the central vertical lattice layer. Here, we can utilize our knowledge of the 2D sideband spectra combined with the sideband peak of the deepest vertical lattice layer to apply cooling pulses that only address the atoms in this single plane, which strongly reduces the required detuning ranges, making the cooling sequence shorter and more efficient. As the cold atoms in the lattice sites of interest will barely move during a brief lattice quench while the uncooled atoms will quickly escape, a release-and-recapture step can help to strongly reduce the atomic density in unwanted vertical planes. A second, more deterministic avenue of removing hot atoms in these planes is provided by erasure cooling [279], where atoms are transferred to the $^3\mathrm{P}_0$ state on the carrier transition, but only atoms in non-zero motional levels are brought back to the ground state via a second clock pulse resonant with the corresponding blue sideband, driving the $|e, n\rangle \rightarrow |g, n-1\rangle$ transition. After or during this sideband pulse, resonant 399 nm light quickly heats the atoms out of the lattice, such that we retain only the shelved atoms in $|e, 0\rangle$. Since a small, but finite number of atoms also populates the lowest motional level in unwanted lattice planes and thus remain trapped, we can use the aforementioned momentum refocusing method to bring them to the central lattice layer. With this method, a significant fraction of atoms is discarded, which might not be desired. Therefore, by the extension of the initial cooling detunings to adjacent vertical lattice planes we can enhance the number of atoms that can be refocused after erasure cooling.

While the clock sideband cooling results discussed in this Chapter refer to ^{174}Yb, we expect the discussed methods to be directly transferable to the fermionic isotopes, since this cooling scheme has already been demonstrated for ^{171}Yb [278] and the more complex spin structure in ^{173}Yb should not lead to significant differences in moderate magnetic fields. Instead, the finite dipole matrix element eliminates the requirement of large magnetic fields and rather improves the cooling efficiency due to the significantly faster Rabi oscillations we can achieve with an otherwise identical setup, which accelerates the cooling in particular along the vertical axis. Notably, the final spin configuration after a clock sideband cooling cycle will be unpolarized, such that subsequent or simultaneous optical pumping on the $^3\mathrm{P}_1$ transition will be necessary to achieve a cold, spin-polarized sample.

3.3 Raman sideband cooling

An alternative cooling method for the fermionic isotopes that directly yields a spin-polarized atomic cloud is Raman sideband cooling on the $^3\mathrm{P}_1$ transition. This has been shown to work well for ^{171}Yb atoms in magic traps at 759 nm, with demonstrations of fast cooling to mean vibrational occupation numbers of $\langle n\rangle \simeq 0.05$ in optical tweezers [72] and $\langle n\rangle \simeq 0.23$ in a 2D lattice consisting of a cavity-enhanced lattice arm [275]. Here, the two ground-state spin levels are coherently coupled via a two-photon Raman transition detuned from the $m_{F'} = \pm 1/2$ levels of the $F' = 3/2$ state, where the Raman detunings $\Delta_{\mathrm{RB}} \gg \gamma$ and intensities allow for fast, resolved sideband transitions by selecting a correspondingly chosen relative detuning. This coherent step is then followed by a (near-)resonant optical pumping step to close the cooling cycle by spontaneous emission (Fig. 3.9 A). For the optical pumping step it is wise to choose a σ transition, as the atoms preferably decay back to the ground state upon emission of a π photon, given by the two times larger branching ratio from the excited state, which reduces the average number of scattered photons during the cooling cycle.

The optimal implementation depends on the experimental conditions and the trap geometry, as good control of the circular polarization for the σ Raman and pumping beams as well as appropriate Zeeman shifts of the $^3\mathrm{P}_1$ states are crucial to reach very low final temperatures. In our setup it is beneficial to use the top MOT beam, denoted as MOT beam 4 in Fig. 2.7, for optical pumping along the vertical direction in a magnetic field created by the main coils, and a perpendicularly polarized beam for the σ Raman leg, such that the two beams can be superimposed with a PBS. For the π Raman transition we then plan on using three different Raman beams, two of which are co-propagating with the horizontal lattice beams, to allow for cooling along each spatial direction, as sketched in Fig. 3.9 B. With high optical powers of up to $\simeq 100$ mW available in each beam and waists of $w_0 \simeq 250\,\mu$m, we can reach very fast two-photon Rabi frequencies Ω_{R} even for large detunings, where

$$\Omega_{\mathrm{R}} = \frac{\Omega_1\Omega_2}{2\Delta_{\mathrm{RB}}} \tag{3.3}$$

and $\Omega_{1,2}$ are the single-photon Rabi frequencies for the two Raman legs. Preliminary calculations suggest that Gaussian π pulses of a total duration of 20 µs (43 µs) are sufficient to provide a virtually complete population transfer to the red sideband of the opposite spin state along the horizontal (vertical) direction at a detuning of 2 GHz [229], which is the bandwidth limit of the beat lock photodiode. For the optical pumping step, one would ideally choose the $F' = 1/2$ submanifold, since there only the desired σ transition can be driven and the dark state cannot experience recoil kicks due to unwanted excitations. However, due to the isotope shift of $\simeq 6$ GHz to the $F' = 3/2$ states this would necessitate an independent laser or limit the

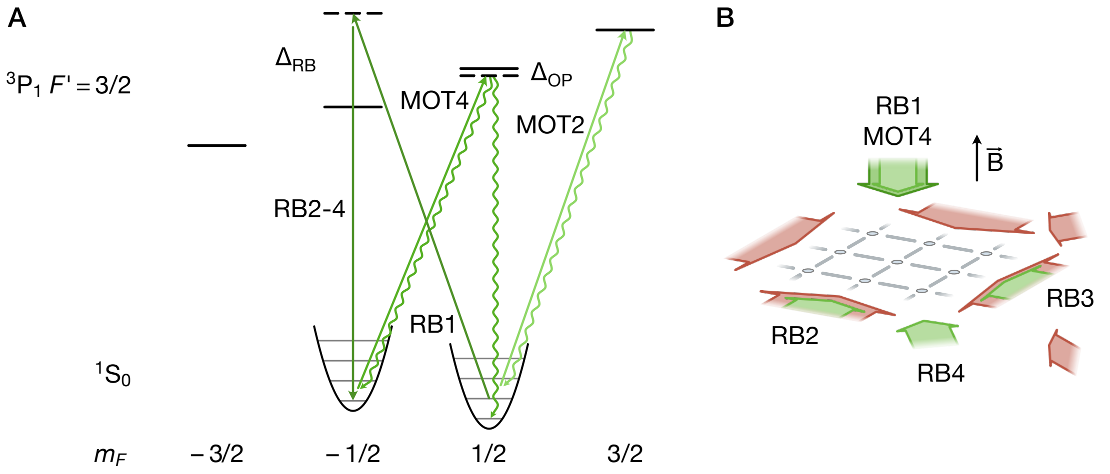

Figure 3.9 | Envisioned Raman sideband cooling scheme in ^{171}Yb. A We start the cooling cycle in a spin-polarized sample with a Raman sideband transition from $|m_F=1/2,n\rangle$ to $|m_F=-1/2,n-1\rangle$, where each Raman beam pair is detuned from the excited state by $\Delta_{RB}\simeq 2$ GHz (dark green). The dissipative step is initiated by an optical pumping transition to the $|F'=3/2,m_{F'}=1/2\rangle$ state, from where the atoms preferably decay back to $|m_F=1/2,n-1\rangle$, preserving the reduced vibrational state. To account for non-magic trapping conditions, the detuning Δ_{OP} for this step can be chosen empirically to yield the best pumping efficiency. Spin-selective imaging can be performed on a stretched transition to the $m_{F'}=\pm 3/2$ states using a horizontal MOT beam to allow for vertical scattering of light (light green). **B** Illustration of the optical layout, displaying the necessary beams for the Raman cooling scheme as well as the individual lattice beams. The circularly polarized beams for the σ Raman leg (RB1) and the optical pumping (MOT4) are vertically aligned and parallel to the magnetic field, while the horizontal Raman beams (RB2-4) are linearly polarized. RB2 and RB3 co-propagate with the lattice beams to achieve a maximal overlap of the total wavevector with the respective lattice arm, while RB4 allows for independent addressing of the vertical motional state.

maximum detuning for the Raman step, which would be given by a high-frequency AOM to detune the Raman beams from the $F'=1/2$ transitions. We will therefore attempt to detune the $m_{F'}=\pm 3/2$ states using a considerable Zeeman shift of $\gtrsim 10$ MHz in magnetic fields of $\simeq 10$ G to make off-resonant excitations of the dark state highly unlikely.

Since the optical pumping step requires light that is resonant or slightly red detuned to prevent sideband heating, we have to ensure a sufficiently near-magic operating condition to prevent that the inhomogeneous lattice depth shifts certain atoms into a blue-detuned regime, where the cooling is no longer efficient. One can counteract this effect by choosing a detuning Δ_{OP} such that all atoms experience sufficiently red-detuned pumping light [63]. However, this leads to a prolonged optical pumping pulse duration and causes local differences in the efficiency of this process, which likely limits the minimal temperature. Therefore, we can alternatively tilt the quantization axis with respect to the MOT beam by 17° to reach the magic condition for ^{171}Yb, which entails a corresponding tilt of the vertical Raman beam to allow for fast subsequent pulses without having to wait for the magnetic field to settle, and adjusted polarization vectors of the horizontal Raman beams.

For the envisioned quantum simulation protocols that allow for a spin degree of freedom also spin-resolved imaging techniques are essential. While it is possible to Zeeman-shift the $|g, m_F\rangle$ and $|e, m_{F'}\rangle$ states sufficiently far to allow for spin-selective shelving of atoms in one spin state to the $^3\mathrm{P}_0$ state, the lattice-induced losses in the deep imaging lattice prevent efficient subsequent imaging of both spin states. Instead, we can take advantage of the stretched transitions to the $m_{F'} = \pm 3/2$ states to let atoms in the bright state scatter fluorescence photons, while the unwanted coupling of the dark spin state is prevented by a large Zeeman shift. We note that this requires us to employ a horizontal MOT beam to allow for the emission of atoms into the direction of the objective, as this would be suppressed for the vertical MOT beam.

CHAPTER 4

State-dependent potentials

This Chapter presents the measurements of four distinct state-dependent wavelengths for the $^1S_0$ and $^3P_0$ clock state pair in ^{174}Yb: two magic wavelengths as well as the ground- and clock-state tune-out wavelength. The magic wavelengths are detected via clock spectroscopy by minimizing the differential ac Stark shift introduced by a dipole trap beam, while the tune-out wavelengths are measured by parametrically heating atoms with a modulated additional lattice. We further determine the non-zero polarizability of the corresponding clock-transition counterpart at the respective tune-out wavelengths. These results are then used to optimize and benchmark the empirical model for the $^1S_0$ and $^3P_0$ polarizabilities, as discussed in Chapter 1.2. The central findings of Chapters 4.1 and 4.2 have been published in [101], the results of Chapter 4.3 are in preparation for publication [102].

4.1 Measuring magic wavelengths

Optical traps generally induce a differential Stark shift on internal atomic states, leading to inhomogeneities and broadening when the transition that connects them is driven. Small or vanishing differential light shifts therefore ease the possibility of optical addressing of atoms. In alkali metals, most traps are already sufficiently close to magic for the relevant optical transitions due to their simple electronic structure, and magic conditions are mostly relevant for the elements Cs, which possesses a comparably large fine-structure splitting [79, 131]. For the narrow hyperfine transitions, on the other hand, magic conditions can only be found close to the transitions themselves, which entails substantial scattering rates [289]. In AEL atoms, the rich electronic structure and thus strongly differing polarizability landscapes for the states of interest lead to the existence of many experimentally accessible magic wavelengths, but also to wide spectral regions with strong polarizability deviations. This is particularly relevant for the narrow dipole-forbidden transitions. While for some applications this state selectivity can be useful as discussed in the following Sections, magic-wavelength traps for the clock state pair have become ubiquitous in the context of lattice or tweezer clock experiments [68, 82, 115, 130, 290–292], where the maximal state insensitivity necessary for high-precision spectroscopy requires the precise cancellation of scalar, vector, or tensor shift components. They have also found widespread applications in quantum computation and simulation experiments, as they enable high-fidelity qubit gates and read-out schemes [72, 83, 293], or in atomtronics [294]. Especially in the context of Rydberg physics, moreover the existence of triple-magic wavelengths for the ground, excited, and Rydberg state has been theoretically explored [295, 296].

Magic wavelengths are commonly measured spectroscopically by scanning the laser around the supposed position and recording the light shift on the transition in dependence of the wavelength. Furthermore, to reduce the sensitivity to systematic errors, in most measurements the power is varied at each wavelength [151, 209]. To ascertain two previously undetermined magic wavelengths for the clock transition in ^{174}Yb we also utilize this exact scheme. However, while it is typically the trap itself whose wavelength and power is scanned, we leverage the well-known magic wavelength at 759.3 nm to provide a 730 E_{rec} deep, state-independent lattice potential in which we can probe the clock transition with small linewidths of few tens of Hz as outlined in Chapter 2.6.1. Light at around the new magic wavelengths to probe the Stark shift is then delivered via an almost collinear, focused dipole beam with a waist of $w_0 \simeq 125\,\mu\mathrm{m}$. This waist is chosen to provide a high intensity in the atomic plane, but is not small enough to lead to a significant inhomogeneity across the atomic cloud, given the lattice waist of $\simeq 65\,\mu\mathrm{m}$ and typical radial cloud sizes of $\sigma \simeq 16\,\mu\mathrm{m}$. We further prevent the formation of a lattice, which would lead to locally differing Stark shifts and thus broadening of the transition, by blocking the dipole beam after is has passed through the glass cell, which is why a small relative angle of $\simeq 1°$ to the lattice beam is necessary. We ensure optimal overlap with the atomic cloud by maximizing the light shift at a significant detuning from the magic wavelength with a picomotor-driven mirror mount and record the resulting beam position relative to the lattice beam on a camera that approximately images the atomic plane.

For the 459 nm magic wavelength we use an optical parametric oscillator (OPO),[1] which can provide up to 80 mW at longer wavelengths and on average 60 mW of blue light on the experimental table. Each measurement consists of three coherent clock frequency scans around the expected resonance with and without the dipole beam, at a magnetic field of $B = 100\,\mathrm{G}$ and a clock beam power of $P \simeq 5\,\mathrm{mW}$, such that we obtain a linewidth of $\Omega_0 \simeq 60\,\mathrm{Hz}$ from a Rabi lineshape fit. We repeat this measurement for in total ten different dipole beam power values, such that we can fit a linear function to the data and extract the differential light shift V_{ac}/P at this dipole beam frequency. Here, we randomly choose the order of powers and detunings and digitally lock the OPO as well as the lattice laser to the wavemeter to suppress the influence of potential drifts in alignment or frequency. Producing these fitted light shifts at various frequencies over a range of almost 4 THz leads to an approximately linear scaling with frequency (Fig. 4.1 D). However, a slight negative curvature is overt. This can be reproduced by a comparison with the expected differential light shift from the empirical model in Chapter 1.2. In order to prevent self-referencing loops, given that the empirical model is fed by the extracted magic wavelength, we therefore restrict the datapoints that we take into account to a detuning of ± 1 THz around the magic wavelength, where this curvature effect is less severe, and fit the remaining dataset with a linear function, whose zero crossing is the magic wavelength. To quantify the systematic uncertainty stemming from the residual curvature, we return to the empirical model and compare the corresponding deviation to a linear fit in a mostly result-

---

[1] *Hübner Photonics C-WAVE VIS+IR Low Power*

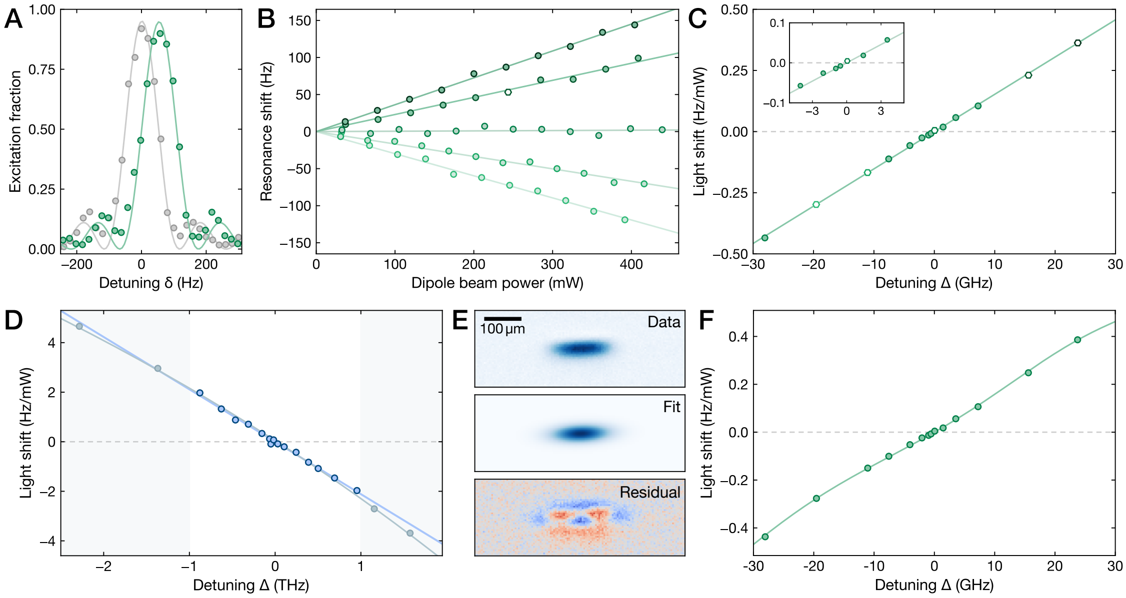

Figure 4.1 | Measurement of the blue and green magic wavelengths in ^{174}Yb. A For a dipole beam frequency close to, but not right at the magic frequency the clock resonance is shifted (green) compared to the bare resonance (grey). We quantify the shift by fitting a Rabi lineshape (solid lines). The corresponding datapoint is shown as a white hexagon in **B**. **B** The extracted resonance shifts increase linearly with the applied dipole beam power and change sign as the green magic frequency is crossed. We obtain the light shifts from the slopes of linear fits (solid lines), with the respective data points shown as white hexagons in **C**. **C** Close to the magic frequency we can approximate the light shift to be linear in the detuning, such that we can determine f_{green} with a linear fit to the data. The error bars correspond to the standard deviation (**B**) and 1σ-fit uncertainty (**C**) and are smaller than the data points. Inset: Zoom-in on the datapoints close to f_{green}. **D** With the same technique we also obtain the light shifts close to the blue magic wavelength. However, due to less available laser power and a smaller differential polarizability slope a larger frequency range has to be probed, over which the polarizability curvatures are no longer negligible, as illustrated with data from the empirical polarizability model (grey solid line). We therefore restrict the dataset to detunings of $\pm$1 THz and assess the resulting systematic uncertainty introduced by the linear fit (blue solid line) by means of a comparison to the more complex polarizability model. **E** In order to determine the influence of pointing drifts we fit to the absorption images of the atomic cloud in the lattice with a rotated 3D Gaussian distribution. This enables us to estimate the dipole beam intensity averaged over the whole cloud, which is also relevant for the calculation of the clock-state polarizability at the ground-state tune-out wavelength as discussed in the next Section. **F** Light shift data for f_{green} without compensation for the photodiode filter etaloning effect. Instead, the fit function includes the calibrated sinusoidal correction, yielding an almost identical root.

agnostic way. More specifically, we calculate the values for the light shift at the laser frequencies where the data was taken, such that we obtain a discrete set of light shift values from our model. This dataset is fitted with the same linear function as the measured data, and we subtract the extracted zero crossing from the actual magic wavelength that the empirical model predicts and arrive at a value of $\delta f_{\text{sys}} = +11$ GHz. This way, we cancel the mismatch of 30 GHz between the predicted and measured wavelength without the introduction of further fitted offsets. We note that this assumes an adequate description of the curvature by our effective model, which we believe to be valid. Further potential systematic errors from, e.g., misalignment during the measurements are found to be negligible. In total, we thus attain a magic frequency of

$$f_{\text{blue}} = 652281 \pm 10_{\text{stat}} \binom{+11}{-0}_{\text{sys}} \text{ GHz.} \tag{4.1}$$

Here as well as for the results to follow in this Chapter, the statistical uncertainty is given by the 1σ-error of the fit.

Later, in a measurement with a tweezer array at this magic wavelength our result was confirmed within the error bars [162]. In particular, the reported result of $f_{\text{blue}} = 652295.6(7)$ GHz underlines the validity of our estimate for the systematic error. We note that the significantly smaller uncertainty of this measurement is a result of the strongly focused light in a tweezer array, leading to a three to four orders of magnitude larger intensity at moderate individual tweezer depths. As any deviation from the magic wavelength will lead to inhomogeneneous broadening from imperfectly balanced tweezers as well as from the finite extent of the wavefunction in the traps, in this case a spin-echo type measurement has to be performed to retain the optimal frequency resolution.

In a similar vein, the measurement of the green magic wavelength is aided by laser powers of up to 500 mW after the fiber, but also by a steeper slope of the differential polarizability, which translates into a significantly smaller frequency range of $\simeq 50$ GHz over which we can probe the light shift response to achieve similar resonance shifts. This renders the consideration of polarizability curvature effects superfluous and we can safely fit a linear function to the light shift data to receive a value of

$$f_{\text{green}} = 542502.05 \pm 0.08_{\text{stat}} \binom{+0.01}{-0.11}_{\text{sys}} \text{ GHz.} \tag{4.2}$$

For this measurement we find two other sources of systematic uncertainty relevant. From the recorded beam position of the dipole beam we first note a drift of 25 µm with respect to the lattice, which is not negligible as this corresponds to a 10% reduction of the peak intensity in the cloud center, assuming perfect initial alignment. This however is an overestimate of the intensity reduction observed by the whole atomic cloud, which is why we fit a rotated 3D Gaussian distribution to a representative set of recorded absorption images of the atomic cloud in the lattice. This yields an axial and transverse size of $\sigma_{\text{l}} = 288(18)$ µm and $\sigma_{\text{r}} = 16.52(4)$ µm, where the error bar includes the fit uncertainty as well as the propagated uncertainty from the relative angle between the imaging and the lattice beam of 10.4(5)°. Taking the measured waist of 125(15) µm and the relative angle between lattice and dipole trap of 0.75(12)° into account and integrating the Gaussian dipole beam intensity over the atomic density distribution, we obtain weighted mean intensities of 3.8(8) kW/cm^2 for an optimal overlap and 3.5(8) kW/cm^2 for the translated case, which corresponds to a reduction to 92.6% of the initial intensity. Assuming a linear evolution of the beam displacement, we can then correct the recorded light shifts at each dipole beam frequency for the intensity reduction and compute the resulting zero crossing, which is offset by −110 MHz from f_{green}. Notably, this treatment assumes an accurate image of the atomic plane onto the reference camera, which is a conservative approximation and likely overestimates the actual pointing drift and its effect on the measurement. The second significant contribution to the systematic uncertainty originates in a relatively severe etaloning behavior introduced by a spectral filter in front of the photodetector that is used to stabilize the intensity of the dipole beam. This filter blocks stray light in particular from the lattice beam to prevent crosstalk. While the photodiode calibration was also checked at five different, randomly chosen dipole beam frequencies during the measurement, the results seemed consistent with the photodetector uncertainty apart from one outlier. In order to verify this calibration, we carefully measure the photodiode voltage at a constant laser power, determined with a low-noise integrating sphere,[2] for various laser frequencies, and we observe a clear sinusoidal behavior with a relative amplitude of $\simeq 20\%$ and a periodicity of 58.7(4) GHz, in agreement with the filter thickness of 5 mm. We further rule out a power dependence and calibrate the etaloning curve on two successive days to ensure that this behavior is static. This at hand, we can apply the newly gained calibration factors to rescale the fitted light shifts, such that we obtain the data in Fig. 4.1. To quantify the corresponding systematic uncertainty, we linearly propagate the fit errors of the four fitted parameters — frequency, phase, amplitude, and background for the sine —, which amounts to a value of 10 MHz. We can further benchmark the validity and accuracy of this rescaling method by including the etaloning correction into the magic-wavelength fitting function and use the constant photodiode calibration factor for the light shift data instead, which reproduces f_{green} well within the statistical uncertainty associated to the fit. The result is displayed in Fig. 4.1.

It is to be expected that the blue magic wavelength will be of great relevance for tweezer-based experiments as the shorter wavelength entails substantially smaller tweezers and thus tighter traps at the same power. In addition, the ground- and clock-state polarizability is expected to be more than twice as large compared to the magic wavelength at 759 nm, such that a tweezer array at this wavelength can provide seven times deeper tweezers with the same input power, which roughly compensates for the higher available laser power at 759 nm. The smaller diffraction-limited size further allows for a reduced spacing of the tweezer, assuming that here the overlap of side lobes with adjacent tweezers is the limitation in a given experimental apparatus. However, it has to be noted that the trap wavelength is short enough to allow for two-photon ionization processes to occur if an atom is in the clock state, which could limit the lifetime of e atoms in 459 nm tweezers. In stark contrast, it is unlikely that the green magic wavelength finds significant applications as a trapping wavelength owing to the much smaller polarizability compared to both the blue and red magic wavelength. A second seemingly deterrent feature is the proximity to the intercombination line, as one could expect noticeable off-resonant scattering. However, in a simple calculation that takes only single transitions into account, we find that the scattering rate induced by the $^1\mathrm{P}_1$ transition is of very similar magnitude, such that interference or optical pumping effects are not negligible. To test this and to be able to compare to the scattering rate at the nearby tune-out wavelength, we therefore perform a lifetime measurement by holding the atoms in the 730 E_{rec} deep lattice, identical to the procedure for the g tune-out measurement described in detail in the next Section, while the dipole beam is kept at a constant power of $P \simeq 230$ mW. However, we only notice an insignificant lifetime difference of 0.1(8) mHz to the measurement without the dipole beam at

---

[2] *Thorlabs S140C*

an overall single-exponential decay rate of 46(1) mHz, indicating that the the scattering rate at this frequency does not pose a large limitation.

4.2 Measuring the ground-state tune-out wavelength

In alkali elements, tune-out wavelengths of the ground state occur in direct proximity to electronic transitions, and in particular the lowest wavelength can only be found in between the D1 and D2 fine-structure transitions. Measurements of such tune-out wavelengths can therefore help to determine the relative transition matrix elements, as has been done for Li, K, Rb and Cs [297–302]. They further allow to constrain the theory polarizability curves around optical transitions [297–299, 303, 304], which is particularly relevant for more complex atoms such as Dy [305] or even molecules [306], and can yield oscillator strengths and state lifetimes [298, 300]. These measurements can also provide a benchmark for quantum electrodynamic calculations since high-precision measurements of tune-out wavelengths in He can resolve discrepancies to predictions by fundamental atomic structure theory [303, 307], and can be used to enhance the determination of the black-body radiation shift in optical clocks [298]. Eventually, optical Feshbach resonance beams at tune-out wavelengths prevent the additional parasitic dipole force from deforming the optical trap [308].

Since the measurement of a tune-out wavelength involves the determination of an absolute and not a differential light shift measurement, one can typically not resort to spectroscopy. Instead, the vanishing atom-light coupling is leveraged. This can be performed, e.g., by matter-wave-enhanced Kapitza-Dirac diffraction after sending sequences of standing waves, i.e., optical lattice pulses, through a BEC, such that the atoms undergo stimulated two-photon scattering events. Quenching off the lattice then enables the observation of atoms in several diffraction orders spaced by $2\hbar k$ after a time of flight [298, 302, 304, 305, 309]. Tune-out wavelengths have further been measured interferometrically by observing a vanishing phase shift $\phi = -\int V_{\mathrm{ac}} dt/\hbar$ in a Mach-Zehnder interferometer with fast atoms [297, 301, 310], in combination with a multi-pass cavity [300], or in a BEC using Bragg scattering [299]. Additionally, a tune-out wavelength has been measured in a pump-probe measurement in a hot, high-density vapor cell via the vanishing dispersion at the tune-out wavelength, where the probe beam is not refracted [311]. Furthermore, static changes in the center-of-mass position by a displaced, circularly polarized dipole beam close to a vector-shifted tune-out wavelength in a BEC of Cs atoms [308] and deviations in the total trap frequency recorded by the momentum of an oscillating He BEC [307] have been employed. Another method to observe the vanishing coupling to light at the tune-out wavelength is periodic modulation of a beam close to the tune-out wavelength to either induce dynamical changes in the atomic density, which was performed in He [303], or parametric heating, as measured in Sr and ^{23}Na^{40}K molecules, where also the shift in the stimulated rapid adiabatic passage (STIRAP) two-photon resonance allows one to determine the polarizability [204, 306].

For our measurement of the ground-state tune-out wavelength we utilize the heating-induced atom loss method by resonant modulation as first demonstrated in [204] since it does not require a BEC or an interferometric setup. Here, atoms in the deep 1D lattice are perturbed by an additional lattice close to the tune-out wavelength, which is modulated at a multiple of the trap frequency f_z. This excites the atoms to higher vibrational bands until they can escape from the trap, such that an enhanced loss rate can be measured unless the lattice is at the tune-out frequency and thus cannot induce heating. To this end, we superimpose the 553 nm beam onto the magic lattice, such that a combined lattice is formed, and spectroscopically maximize its overlap using the introduced light shift on the clock state as a probe. Owing to the incommensurate wavelengths, amplitude modulation of the tune-out lattice will then lead to a mixture of phase and amplitude modulation observed by the atoms, depending on the lattice site they populate. This leads to two well-resolved resonances at both the axial trap frequency and its first multiple upon scanning the modulation frequency as displayed in Fig. 4.2 B, corresponding to excitations by one or two harmonic oscillator quanta. We choose a square-wave modulation signal, feed-forwarded from a signal generator to the intensity stabilizing circuit, whose bandwidth is tuned to be slower than the signal to prevent a distortion of the rectangular pulses. This enables us to achieve a controllable, full-depth modulation at a constant average intensity I_{to}. To test the quality of the pulse shape we Fourier-transform the recorded modulation signal observed by a fast photodiode, which yields additional peaks at odd multiples of the requested modulation frequency with their amplitudes falling off as f^{-1}, as we would expect for a square-wave pulse train. This is reflected by weaker, but clearly discernible peaks at one third and two thirds of f_z, where the atoms experience parametric heating via phase and amplitude modulation from the third harmonics. The relatively wide resonances and the noticeable shift of the observed center of the phase-modulation peak by $\simeq -18$ kHz compared to the longitudinal trap frequency of $f_z = 114.7(3)$ kHz obtained from the clock sideband spectra are a consequence of the relatively high initial temperature along the weakly confined axis of $T_r \simeq 25\,\mu$K, which allows the atoms to explore the individual lattice sites to a great extent, such that on average they experience a significantly weaker lattice. Notably, a signal in the fitted cloud size is barely visible, unlike for modulation spectroscopy in the bare magic lattice, which indicates that for this weak modulation depth the parametric heating leads to a comparably fast loss of individual atoms instead of a continuous, rethermalized heating response of the whole could. In addition, the limited spatial resolution of the absorption imaging setup prevents the detection of minuscule changes in the spatial extent.

For the atom loss detection measurement we select the resonance frequency at $2f_z = 178$ kHz, corresponding to $|n\rangle \rightarrow |n+2\rangle$ excitations, and modulate the tune-out lattice while the atoms are held in the $\simeq 730\,E_{\text{rec}}$ deep magic lattice for variable times. We then compare the resulting lifetime $\tau = 1/\Gamma$, obtained via a fit with a single exponential function, $N(t) = N_0 e^{-\Gamma t}$, to the lifetime without the tune-out lattice, τ_0, from which we can extract the excess loss rate $\Gamma_{\text{exc}} = 1/\tau - 1/\tau_0$. The lifetime with an unmodulated tune-out lattice at a constant intensity of I_{to} is also tested, but does not show any difference to the case where it is fully turned off. By toggling the tune-out lattice and randomizing the order of the selected wait times we ensure that the detected lifetime difference is not spuriously impaired by potential slow drifts of the lifetime due to, e.g., thermalization or changes in the lab environment during the data acquisition. We further carefully calibrate the photodiode at every frequency we choose for the tune-out lattice to account for the etaloning of the filter as discussed in the previous Section. To maximize the unmodulated lifetime signal, we reduce the initial occupation per lattice site

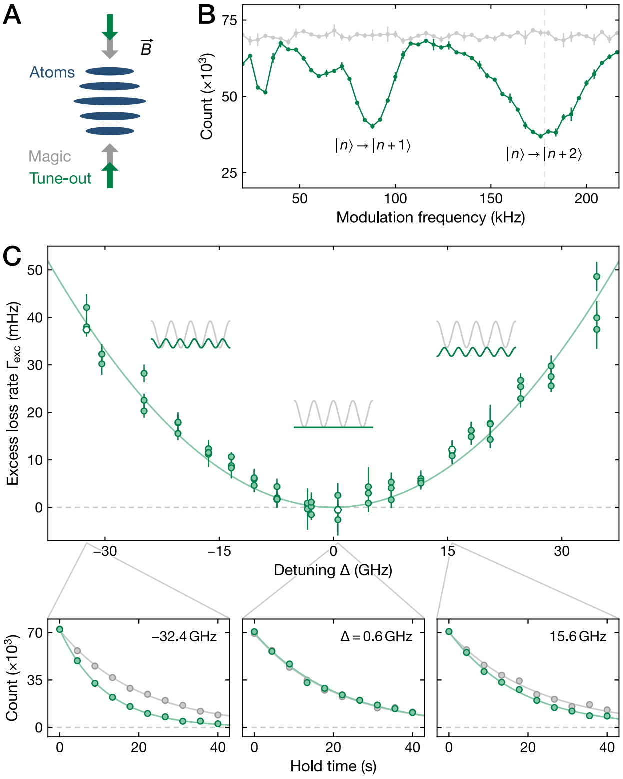

Figure 4.2 | Determination of the ground-state tune-out wavelength. A In contrast to the setup for the magic wavelength measurement depicted in Fig. 2.6 A, we superimpose the beam close to the tune-out wavelength onto the deep magic lattice (grey), such that a shallow tune-out lattice (green) is formed. **B** Loss spectrum of ground-state atoms for a variable modulation frequency (green) after 40×10^3 modulation periods at a detuning of $\Delta = 327$ GHz from the tune-out wavelength f_{to}, compared to a reference measurement without the tune-out lattice (grey). The error bar is the standard deviation from two averages. We can clearly identify the transitions at around 89 kHz and 178 kHz, corresponding to excitations by one or two harmonic oscillator quantum numbers, respectively. Owing to the square-pulse amplitude modulation, we also observe weak resonances at the third harmonics. The grey dashed vertical line indicates the modulation frequency used for the lifetime measurements. **C** As the tune-out lattice frequency is scanned across f_{to}, we observe a quadratic increase of the excess loss rate Γ_{exc}. This loss rate is determined from the lifetime difference between the modulated tune-out (green) and the bare magic lattice (grey, lower panels) by fitting to each lifetime curve with a single exponential function (solid line). The corresponding data points are highlighted by white hexagons in the upper panel. We can fit the dependence of excess loss rate on the detuning with a quadratic function without offset to determine the exact position of f_{to}. The error bars reflect the standard deviation of the fit uncertainties of the corresponding decay curves. Insets: Schematic of the amplitude of the two lattices and the polarizability sign flip around the tune-out wavelength.

by reducing the lattice loading depth to $\simeq 390\,E_{\mathrm{rec}}$, such that $\simeq 55$ atoms populate each layer on average. This way, we can suppress two-body interaction effects which otherwise dominate the loss rate for short wait times at larger loading lattice depths. While this reduces the amplitude of the lifetime curve, we achieve an overall better signal as the introduction of a two-body loss term as in Eq. (1.18) significantly increases the fit uncertainty. Since the two-body losses can also be inhibited by reducing the temperature of the atomic cloud, first attempts of longitudinal clock sideband cooling as discussed in Chapter 3.2.1 were performed prior to the measurement, but did not show a sufficient reduction of the total temperature to significantly increase the overall signal. We therefore maintain the simple experimental sequence with a 10 ms lattice ramp to the holding depth, followed by a 5 ms ramp of the tune-out lattice. We further note that a modulation at the $|n\rangle \to |n+1\rangle$ resonance frequency is found to yield a comparable loss rate, in agreement with the similarly deep resonance feature in the modulation spectrum. From a theoretical perspective, this can be understood as the comparable effect of the power spectra of lattice center position and amplitude fluctuations, $S_\mathrm{p}(f)$ and $S_\mathrm{a}(f)$, which both depend on the ratio of tune-out and deep lattice potential, i.e., are proportional to $\alpha^2 I_\mathrm{to}^2$, and determine the loss rates as [204, 312, 313]

$$\Gamma_\mathrm{exc,phase} = \pi^2 f_\mathrm{z}^2 \frac{S_\mathrm{p}(f_\mathrm{z})}{\langle x^2 \rangle}, \tag{4.3}$$

with $\langle x^2 \rangle$ the mean-square position of an atom in the trap, and

$$\Gamma_\mathrm{exc,amplitude} = \pi^2 f_\mathrm{z}^2 S_\mathrm{a}(2 f_\mathrm{z}), \tag{4.4}$$

respectively. The decision to choose the modulation at twice the trap frequency is therefore mostly based on a slightly larger loss response and a cleaner modulation signal. From the above equations we can also determine the expected loss rate trend around the tune-out wavelength, as the polarizability can again be approximated to be linear in frequency for a range much smaller than the detuning from the dominant transition, i.e., $\Gamma_\mathrm{exc} \propto \alpha^2(\Delta) \propto \Delta^2$ with Δ the detuning from the tune-out wavelength, where $\alpha = 0$.

This is indeed borne out by the data as the frequency of the tune-out lattice is scanned (Fig. 4.2 C). We further notice a vanishing excess loss rate at the tune-out frequency f_to, which is also in agreement with out expectations of a fully suppressed atom-light coupling without any vector or tensor shift contributions. Hence, we can fit the data with the quadratic function $\Gamma_\mathrm{exc} = A(f - f_\mathrm{to})^2$ and we obtain as a result

$$f_\mathrm{to} = 541832.49 \pm 0.23_\mathrm{stat} \left({}^{+0.05}_{-0.24}\right)_\mathrm{sys} \ \mathrm{GHz}. \tag{4.5}$$

However, the dependence of the loss rate on the tune-out potential appears to subtly deviate from the simple quadratic behavior for large detunings $\Delta > 20\,\mathrm{GHz}$, which thus introduces a systematic uncertainty to the measured tune-out frequency. A signature of this deviation is the occurrence of a non-zero offset of 1.46(41) mHz if this fit parameter is added to the fitting function. However, this offset is unphysical as it does not reflect the vanishing excess loss rate detected in the lifetime measurements at f_to. We first investigate this trend by fitting a partial dataset with and without offset and keep track of the fit results, starting with the datapoints closest to f_to and then increasing the detuning range within which we take datapoints into account. While the fit for very small datasets up until the fit threshold $|\Delta_\mathrm{c}| \simeq 11\,\mathrm{GHz}$ naturally yields very diffuse results with large error bars, the picture for the intermediate detuning regime up to $|\Delta_\mathrm{c}| \simeq 21\,\mathrm{GHz}$ shows a trend that is in agreement with our expectation of an offset consistent with zero (Fig. 4.3 B). At the same time, the fit result for the

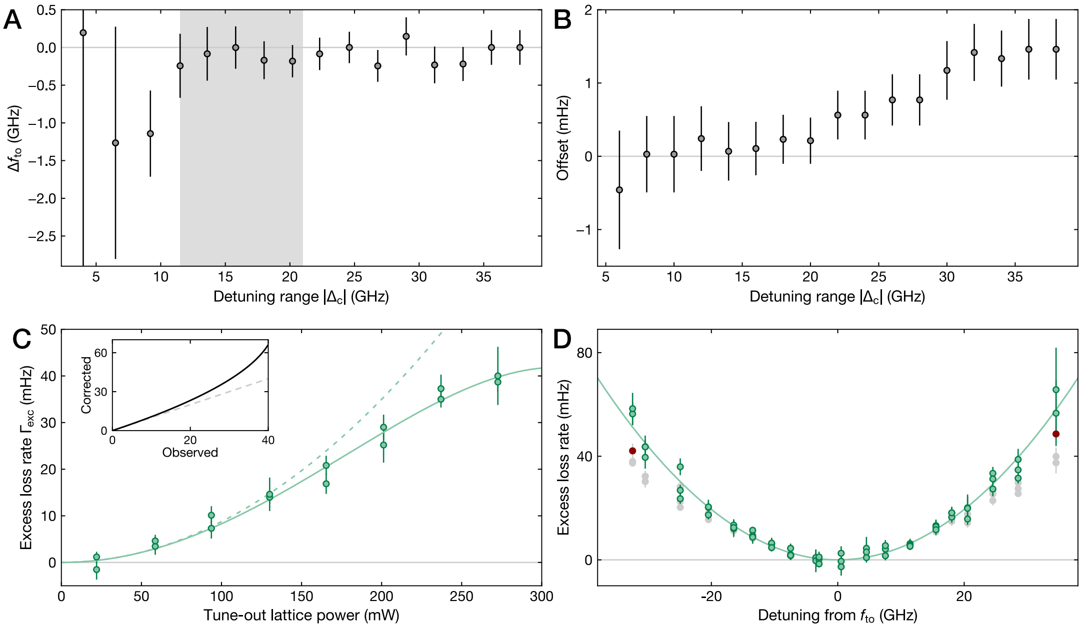

Figure 4.3 | Assessing the systematic error from the parametric heating saturation effect. **A** Fitted tune-out frequency for partial datasets in dependence of the frequency range $|\Delta_c|$ centered around f_{to}. Here, the quadratic fitting function does not include an offset. For small $|\Delta_c|$, the limited number of data points at asymmetrically spaced detunings lead to a bias towards lower frequencies, which changes as we include data points above 11.5 GHz. From this point on, the maximal deviation amounts to $\simeq -250$ MHz. The grey shaded area indicates the detuning range with a still marginal influence of the heating saturation, gauged via the fitted offset in **B**, but sufficiently many datapoints to extract a systematic uncertainty contribution. **B** Accumulation of an offset for growing datasets when we fit with a three-parameter quadratic function, indicative of the deviation from the expected quadratic behavior at larger detunings. **C** To further test this deviation, we measure Γ_{exc} at a constant detuning $\Delta \simeq 25$ GHz and vary the tune-out lattice power. For loss rates $\Gamma_{exc} \gtrsim 20$ mHz we observe a deviation from the expected quadratic behavior (dotted line). An empirical quartic function appears to capture the flattening behavior (solid line). Inset: Correction factor determined from the quartic fit to allow for rescaling of the saturated excess loss rates. **D** As we apply this correction to the tune-out data, we notice a vanishing offset even for the three-parameter fit function. Uncorrected values are shown in grey. We have to disregard two data points with a loss rate > 40 mHz (red), as they lie outside of the measured calibration range determined in **C**.

quadratic function without offset approaches f_{to}, but mostly remains below with a maximum deviation of -243 MHz at $|\Delta_c| \simeq 12$ GHz (Fig. 4.3 A). As we increase the fit threshold $|\Delta_c|$ further, the fitted offset almost continuously rises, while the extracted root mostly remains at a lower frequency than f_{to}. We therefore use the maximum deviation in the intermediate detuning range as one contribution to the systematic error. Simultaneously, we probe the loss rate deviation by varying the tune-out lattice power at a constant detuning of $\Delta \simeq 25$ GHz. Here, we observe a stark discrepancy to the simple loss model for the maximally attainable powers of $P \simeq 270$ mW where the loss rate appears to flatten, while we would again naively expect a quadratic increase, $\Gamma_{exc} \propto I_{to}^2$ (Fig. 4.3 C). This effect could be explained by a stronger influence of the lattice anharmonicity as the atoms experience fast heating to higher motional bands, such that the modulation is no longer resonant with the bulk of the atoms, likely accompanied by a change in the thermalization rate of hot atoms that can tunnel through the lattice and therefore redistribute their energy among colder atoms. However, we do not find any signature of the appearance of two-body losses at large detunings. A second potential explanation is the lattice potential modification introduced by a relatively strong tune-out lattice. However, the expected contribution is by far too weak to have an effect on the observed lattice frequency — over the probed frequency range of ±35 GHz the axial trap frequency does not exceed $\simeq 40$ Hz according to our empirical polarizability model — and an altered tunneling rate is expected to manifest in an increased two-body loss rate, as observed in [204]. We therefore attribute this deviation to a higher-order effect beyond the harmonic approximation underlying Eq. (4.4). To empirically compensate for this saturation effect, we introduce a quartic term to the fitting function, such that we can compute a correction to any measured loss rate in order to obtain the value we require for the quadratic model. Applying this correction on the tune-out data as shown in Fig. 4.3 D, we obtain a fit result with a root that deviates from f_{to} by +53 MHz, independent of the inclusion of an offset. Furthermore, the fitted offset for the corrected data is consistent with zero. Notably, two datapoints cannot be included in the corrected dataset as there the excess loss rate exceeds 40 mHz, which is the maximum that was measured in the calibration measurement in Fig. 4.3 C, and hence the correction model is not trustworthy beyond this threshold.

Knowing that the ground-state polarizability is zero, a spectroscopic measurement of the differential Stark shift thus yields a direct quantification of the clock-state light shift. We thus employ the same concept as for the magic measurements by tilting the tune-out beam away from the retro-reflecting mirror and determine the resonance shift as a function of the applied power. Despite the proximity to the magic wavelength, the enormous induced shifts of up to 4 kHz for the large powers of $P_{\text{to}} > 100$ mW result in an unwanted inhomogeneous broadening of the linewidth due to the finite extent of the tune-out dipole beam. To be able to obtain a robust light shift measurement, one can therefore adjust the magnetic field strength and clock power correspondingly to also broaden the unshifted linewidth to an extent that the spatial dipole beam inhomogeneity is outweighed. This is done in two different ways: We first employ a strong magnetic field of $B = 300$ G and a clock beam power of $P \simeq 100$ mW for all datapoints, leading to a constant linewidth of almost 3 kHz. This however reduces the sensitivity to small resonance shifts at low dipole beam powers. The second method thus utilizes an adaptive magnetic field strength, which is chosen to yield a constant ratio between the shift and linewidth of about 1 for all dipole beam strengths, which however entails additional systematic uncertainties from the magnetic field calibration. Alternatively, one can limit the tune-out power to $P \lesssim 35$ mW, where the broadening does not yet appear, and detect the light shift for the low-linewidth parameters as for the magic wavelength measurements. Since all three methods provide similar results, we use the latter method to obtain the final light shift value for reasons of comparability to the data presented in the previous Section. As a matter of fact, the small differences between the three results are largely outbalanced by the systematic uncertainties in the technically challenging determination of the dipole beam intensity, which is required to achieve the total light shift. By detecting its intensity-stabilized power in front of the glass cell with an integrating sphere for several dipole beam setpoints we can calibrate the applied optical power on the few-percent level, mostly limited by the specified powermeter uncertainty of 3%. While the glass cell windows are AR-coated and thus the surfaces reflect almost negibile fractions of the incident light, the absorption and diffuse scattering of light in the glass windows leads to a measurable reduction of the transmitted power. To quantify this reduction we detect the power in front and after the glass cell at a stabilized power of $P \simeq 180\,\mathrm{mW}$ with three different powermeters: the integrating sphere, a conventional photodiode sensor, and a thermal power head. In this vein, we measure a maximal decrease of 2.1% with the integrating sphere, compared to 1.6% and 0.2% detected by the conventional photodiode and the thermal head, respectively. We therefore multiply the calibrated power by 0.9895%, corresponding to identical losses at both windows. Taking the maximally conservative estimate for the systematic uncertainty, we instead assume this loss to either take only place at the first or the second window, while the other window is assumed to transmit 100%. This increases the uncertainty of the optical power at the atoms to $\simeq 6\%$, yielding a contribution of $\pm 0.24\,h\,\mathrm{Hz/Wcm^{-2}}$ to the total systematic uncertainty of the light shift. An estimate of the power at hand, we now turn to the determination of the intensity. Again using the camera to image the beam at the atomic plane, we confirm the beam size of $w_0 = 125(2)\,\mu\mathrm{m}$ by a fit to a 2D Gaussian distribution. We note that this deviates from the waist of $110\,\mu\mathrm{m}$ we would expect according to the propagation of a Gaussian beam. This indicates that either the focus of the dipole beam is not precisely at the atomic plane, the imaging plane of the camera is shifted, or the focusing lens introduces aberrations. Since it is not straightforward to disentangle these effects, we take the total discrepancy to the theoretically expected waist as an conservative estimate of the associated uncertainty. We can then repeat the fit to the absorption images of the atomic cloud with a 3D Gaussian as in Section 4.1 to obtain the mean atomic resonance shift and the corresponding systematic uncertainty from the beam waist, the fitted cloud size, and the relative angle to the imaging and lattice beam, amounting to $\pm 0.85\,h\,\mathrm{Hz/Wcm^{-2}}$. As the final source for systematic errors we assess the effect of the potential longitudinal mismatch of the dipole focus with respect to the atomic plane. Since the lattice and the dipole beam are focused by the same achromatic lens and we have established a reasonable agreement between the expected and measured lattice size, the axial overlap of their foci is mostly determined by the collimation accuracy of the dipole beam, and we assume a worst-case focus shift of 5 mm. This entails an asymmetric uncertainty contribution of $-0.48\,h\,\mathrm{Hz/Wcm^{-2}}$. Notably, here we do not take a radial pointing mismatch into account as we assume the Stark shift optimization prior to the measurement to yield reasonably overlapped beams. We therefore obtain a total light shift of the clock state at the ground-state tune-out wavelength of

$$V_{\mathrm{ac},e}/I = -3.8 \pm 0.07_{\mathrm{stat}} \left({}^{+1.1}_{-1.6}\right)_{\mathrm{sys}} h \times \mathrm{Hz/Wcm^{-2}}. \tag{4.6}$$

4.3 Measuring the clock-state tune-out wavelength

So far, no measurement of a tune-out wavelength for the excited state of an optical qubit has been reported. However, there is a number of interesting applications that require a potential at such a wavelength even beyond the LGT simulation scheme devised in Chapter 1.4, which will be discussed in the next Section. Unfortunately, the determination of this wavelength transpires to involve a plethora of complicating circumstances. The most obvious limitation is the minuscule polarizability slope as the tune-out wavelength is located almost exactly in between two comparably strong transitions spaced by $\simeq 200\,\mathrm{nm}$ (Fig. 1.3), which not only necessitates a larger frequency probing range during the measurement, but also the best theoretical predictions are associated with large error bars and disagree on the order of several nm [97, 152, 153]. Since our initial empirical model [101] appears to strongly agree with the $^3\mathrm{P}_0$ polarizability curve determined in [152], we presume the clock-state wavelength at the value of $\simeq 576\,\mathrm{nm}$ predicted by both models. However, the theoretical uncertainty causes the practical complication of purchasing a suitable laser that can be tuned far enough in case this expectation value turns out to be imprecise. The tuning ranges of typical commercially available high-power lasers are limited to few nm around the selected center wavelength, and the output power quickly drops outside of the specified range. Among these lasers, the VECSEL technology enables the largest tuning ranges of up to $\Delta\lambda \simeq 10\,\mathrm{nm}$ in the visible range with output powers of $P \simeq 2\,\mathrm{W}$ over large parts of this spectrum. Unfortunately, during the design of a new gain chip one cannot fully predetermine the eventual center wavelength. Therefore, the tuning range of the VECSEL we initially received was centered around 572 nm and exhibited a relatively steep power drop beyond 576.5 nm.

A second limitation is imposed by the shorter lifetime of clock-state atoms in the 759 nm lattice compared to atoms in the ground state. In typical experimental conditions, the predominant contributions, however, are lattice-induced losses from a Raman process via the $(6s7s)^3\mathrm{S}_1$ state [72, 110, 120, 314], which is surprising at first, given the enormous detuning of 67 THz,[3] and e-e inelastic collisions (Chapter 1.1.3). While the latter lead to mere atom loss, the former process leads to a expected reappearance of $\simeq 59\%$ of the clock-state atoms that undergo this Raman transition in the ground-state (Fig. 4.4 A), given by the comparison of branching ratios from the $^3\mathrm{S}_1$ state to the $^3\mathrm{P}_1$ and $^3\mathrm{P}_2$ states. Here, the remaining atoms end up in the untrapped $^3\mathrm{P}_2$ state and are also lost. For $^{171}\mathrm{Yb}$, this loss process has been characterized recently [120], with reported trap-depth-dependent loss rates of $\Gamma_{^3\mathrm{S}_1} = 9(1.2) \times 10^{-4}\,\mathrm{Hz}/E_\mathrm{rec}$, which is divided into atoms transferred to $^3\mathrm{P}_2$ with a rate of $\Gamma_{^3\mathrm{P}_2} = 3.3(5) \times 10^{-4}\,\mathrm{Hz}/E_\mathrm{rec}$ and to $^3\mathrm{P}_1$ and thus $^1\mathrm{S}_0$ eventually with $\Gamma_{^3\mathrm{P}_1} = 5.7(7) \times 10^{-4}\,\mathrm{Hz}/E_\mathrm{rec}$. We note that the inherent limit of vacuum background losses of $\Gamma_\mathrm{vac} \simeq 5\,\mathrm{mHz}$, which is shared with the ground state, is not a significant factor for this e tune-out measurement. Similarly, the loss of clock-state atoms due to a decay back to the ground state can be safely neglected for $^{174}\mathrm{Yb}$, while it can become relevant for the fermionic isotopes with loss rates of few tens of mHz.

Since the inelastic collisions lead to almost complete atom loss within few hundreds of ms, it is therefore impossible to achieve long clock-state lifetimes for a reasonably large number of atoms in the 1D lattice configuration used for the previous Sections. As the adversary effects of e-e collisions can only be prevented by separating atoms into individual sites, it is beneficial to use a higher-dimensional lattice to multiply the lattice site density — while $\simeq 1500$ layers are populated in the 1D lattice case, we typically reach a cloud size that corresponds to the occupation of $\simeq 25 \times 10^3$ tubes or $\simeq 140 \times 10^3$ 3D lattice sites. As this entails an average population of 0.5 atoms per 3D lattice site for typical MOT loading times, two-body losses would be mostly inhibited without the presence of tunneling. However, for uncooled atoms this necessitates the usage of deep lattices as otherwise the significant fraction of atoms in

---

[3] We note that in [120] a detuning of 64 THz is mentioned, which is in disagreement with the energy of the $^3\mathrm{S}_1$ state given by NIST [105].

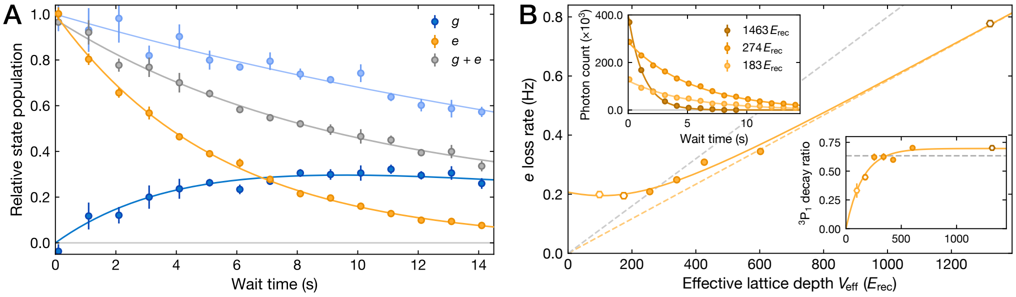

Figure 4.4 | Limits on the clock-state lifetime in a magic lattice. A We detect the fluorescence signal of a 2D-cooled cloud of *e* atoms for varying hold times in the magic 2D lattice with (orange) and without (grey) a second *g* atom removal pulse right before the repumping and imaging steps. This allows us to directly trace the *e* atom loss as well as the combined ground- and clock-state signal, and we can infer the ground state fraction (dark blue) from the difference between the two, showing the appearance of *g* atoms from the lattice-induced Raman process that transfers *e* atoms into the $^3P_1$ and $^3P_2$ state, which leads to a decay to the ground state for the former and losses for the latter. We fit the *g* and $g + e$ decay with an exponential function (solid lines) and use Eq. (4.7) to describe the ground-state trend with the relative strength of the Raman and inelastic collision losses as the only free parameter. To this end, we independently measure the lifetime of a pure *g* cloud at this lattice depth of 274 E_{rec} (light blue). **B** We find that the *e* lifetime of 5.3(1) s at this lattice depth is optimal by repeating this measurement for various lattice depths between 180 and 1500 E_{rec}. For deeper traps, the lattice-induced Raman process leads to a linearly increasing loss rate, while for shallower lattices two-body losses become dominant. We can model this competition via a fit with Eq. (4.9) (solid line), which also reveals the lattice depth dependence of the Raman loss rate (dotted line) and its deviation from the value measured in [120] (grey dotted line). Here, we account for the lower time-averaged lattice depth V_{eff} the radially hot atoms experience, but not for the Gaussian trap depth inhomogeneity, which likely explains the deviation. We also observe slightly dissenting ratio of atoms that undergo the Raman transition to the $^3P_1$ state and therefore reappear as *g* atoms (bottom right inset). For shallow lattices, two-body losses contribute significantly and lead to a reduced $^3P_1$ ratio, while for deep lattices, where tunneling and hence inelastic collisions are suppressed, we detect 70(3)% of the initial clock-state atoms returning in *g*, as determined by a fit to the data with an exponential saturation curve (solid line), which is slightly larger than the 63(8)% reported in [120] (grey dotted line). The lifetime trends for the various lattice depth regimes are illustrated in the top left inset. Here, we also observe the effect of fast initial losses in weak lattices due to spilling of radially hot atoms as well as quick tunneling-induced inelastic collisions, leading to a reduction of the early-time photon count. From wait times of 100 ms on, the remaining trend is well-captured by a single exponential fit. At the optimal lattice depth from **A**, this decrease amounts to ≃ 25% compared to deep lattices, which still yields the best signal-to-noise ratio at long wait times. The corresponding datapoints in the main plot are indicated by hexagons of matching color.

higher bands can propagate through the lattice, which in turn limits the lifetime to much less than a second because of the off-resonant Raman scattering process.

Hence, we have to resort to the cooling methods developed in the previous Chapter to suppress the tunneling of *e* atoms through a weak lattice. Here, we find that the swept 2D clock sideband cooling is sufficient to reach clock lifetimes of 5.3(1) s, which is not only larger than the 3D-cooled lifetimes reported in [120] for ^{171}Yb, but also exceeds the lifetime achieved in a BEC of ^{173}Yb atoms in a 90 E_{rec} deep, magic 3D lattice [110]. This value is found at a sweetspot between the onset of inelastic collisions and significant lattice-induced losses in a ≃ 250 E_{rec} deep 2D lattice (Fig. 4.4 B).

In order to understand this behavior better, we quantitatively compare the loss mechanisms for different lattice depths. For shallow lattices the *e* loss is defined by two strongly different timescales, with the first loss processes taking place within ms, such that they do not appear any longer after a wait time of 100 ms. From this point on, a slow decay sets in that is well described by an exponential fit. We ascribe the first process to spilling of radially hot atoms after the lattice is ramped down from the cooling depth of $\simeq 400\,E_{\mathrm{rec}}$ as well as two-body losses incurred from the few remaining atoms in higher motional bands that can tunnel through the lattice until they find a collisional partner. The slow exponential decay is then caused by Raman losses on top of inelastic collisions after tunneling of motional ground-state atoms. This is contrasted by the fully lattice-dominated loss behavior in deep lattices, where even higher-band tunneling is inhibited such that the initial photon count is large, but the Raman loss process leads to a fast clock-state decay.

Starting with an atomic sample purely consisting of atoms in the $^3\mathrm{P}_0$ state by removing remnant *g* atoms after the resonant π pulse with a first blow-away pulse on the $^1\mathrm{P}_1$ transition, we are informed of the relative ratio between the two loss mechanisms — two-body and Raman processes — by the relative number of *e* atoms that reappear in the ground state. We can detect this quantity by toggling the second blow-away pulse that removes all *g* atoms from the lattice before the clock-state atoms are repumped ahead of the fluorescence imaging sequence. In this vein, we can detect the mere *e* lifetime as well as the combined $e + g$ signal evolution, therefore allowing us to infer the appearance of ground-state atoms from the difference between the two measured curves (Fig. 4.4 A). We also determine the pure ground-state-atom loss rate at the corresponding lattice depth, which is found to be 26(2) s in the $250\,E_{\mathrm{rec}}$ deep lattice and vacuum-limited to 220(30) s beyond $\simeq 600\,E_{\mathrm{rec}}$. This at hand, we can describe the Raman-induced *g* evolution as

$$N_{\mathrm{g}}(t,V) = N_{\mathrm{e},0}\,\tilde{\zeta}(V)\,\left(1 - e^{-\Gamma_{\mathrm{e}}(V)t}\right)\,e^{-\Gamma_{\mathrm{g}}(V)t}, \tag{4.7}$$

which is a solution to the rate equations

$$\begin{aligned}\dot{N}_{\mathrm{g}} &= -\Gamma_{\mathrm{g}}(V)N_{\mathrm{g}} + \tilde{\zeta}(V)\Gamma_{\mathrm{e}}(V)N_{\mathrm{e}}\\ \dot{N}_{\mathrm{e}} &= -\Gamma_{\mathrm{e}}(V)N_{\mathrm{e}}.\end{aligned} \tag{4.8}$$

Here, we combine all loss channels for the clock state into a single lattice-depth-dependent decay rate, $\Gamma_{\mathrm{e}}(V) = V\Gamma_{^3\mathrm{S}_1} + \Gamma_0(V)$, where $\Gamma_{^3\mathrm{S}_1}$ is the Raman loss rate and Γ_0 contains the residual decay processes like off-resonant scattering or slow inelastic collision processes after lowest-band tunneling,[4] and the relative strength of these processes at a given lattice depth is captured in the prefactor $\tilde{\zeta}(V)$, which describes the ratio of atoms that are transferred to the $^3\mathrm{P}_1$ state, from where they can decay to *g*. Notably, any spontaneous decay from the $^3\mathrm{P}_0$ state is eliminated once the magnetic field is turned off. This then allows us to fit the ground-state fractions for various lattice depths with the single free parameter $\tilde{\zeta}$. For deep lattices, where the Raman-induced losses are predominant, this factor is expected to approach the $^3\mathrm{P}_1$ branching

---

[4] While this two-body process would typically require a different, N_{e}^2-dependent term in the rate equation, this effect is too weak to be differentiated from a single-body loss term for the conditions in this measurement.

ratio fraction from the $^3S_1$ state compared to the sum of the branching ratios to the $^3P_1$ and $^3P_2$ states. As was found in [120], this rate is slightly modified by off-resonant Raman transitions to further states, such that for ^{171}Yb the calculated value of $\zeta = 0.65$ was confirmed within the error bars of the measurement that yielded $\zeta = 0.63(8)$. For ^{174}Yb, we consistently find an even larger fraction of $\zeta = 0.70(3)$ for lattice depths above $700\,E_\mathrm{rec}$ (Fig. 4.4 B, bottom right inset). Furthermore, we notice a deviating lattice-dependent loss rate $\Gamma_{^3S_1}$ by tracing the total e loss rate for the different lattice depths by a fit with

$$\Gamma_\mathrm{e}(V) = \sqrt{V^2 {\Gamma_{^3S_1}}^2 + a\, e^{-2V/V_\mathrm{c}}}, \tag{4.9}$$

which reproduces the linear dependence on V for deep traps and takes the losses from exponentially faster tunneling in shallow lattices into account. Here, we also correct for the finite radial temperature along the vertical direction, which leads to a lower temporally averaged lattice depth [315, 316]

$$V_\mathrm{eff} = \frac{V}{1 + k_\mathrm{B} T_\mathrm{r}/V}. \tag{4.10}$$

This corresponds to the marked shift of the sideband maxima from f_1 towards the carrier for $T_\mathrm{r} \gtrsim 5\,\mu$K that we also observe in the sideband spectra. From this we obtain $\Gamma_{^3S_1} = 5.8(2) \times 10^{-4}\,\mathrm{Hz}/E_\mathrm{rec}$ and thus a ground-state quenching rate of $\Gamma_{^3P_1} = \zeta\Gamma_{^3S_1} = 4.1(2) \times 10^{-4}\,\mathrm{Hz}/E_\mathrm{rec}$. This is significantly lower than the measured values of $\Gamma_{^3S_1} = 9(1.2) \times 10^{-4}\,\mathrm{Hz}/E_\mathrm{rec}$ for ^{171}Yb [120] and $15(1) \times 10^{-4}\,\mathrm{Hz}/E_\mathrm{rec}$ for ^{173}Yb [110], which can at least partially be explained by the Gaussian trap depth inhomogeneity that is not accounted for in this calculation, as it is non-trivial to exactly quantify the relative sizes of atomic cloud and lattice beams without single-site resolution.

We further note that we do not find any sign of influence of the number of ground-state atoms on the e lifetime, consistent with the marginal inelastic collision rates β_eg for e-g atom pairs [142, 143]. Remarkably, any additional vertical confinement does not sufficiently help to retain multiple atoms within a tube from colliding and expelling each other to outweigh the damage incurred by the Raman losses. This can be understood as an effect of the comparably power-inefficient trap formed by the vertical lattice: In contrast to the second horizontal lattice the added number of sites is lower by a factor of $\simeq 4$, and owing to the shallow-angle geometry about an order of magnitude stronger beams are necessary to create the same separating potential. It is further not particularly crucial to reduce the vertical temperature of the atoms as we cannot effectively suppress the scattering of atoms in multiply occupied tubes in either case and the rethermalization, i.e., the redistribution of kinetic energy into the horizontal direction is only very weak due to the strongly differing trap frequencies. Thus, we do not expect significant lifetime improvements upon introducing 3D motional cooling at a later stage (Chapter 3.2.3). Moreover, we note that the 1D rethermalization cooling yields worse clock-state lifetimes despite an overall lower temperature. However, as the mean occupation number along the weakly confined horizontal direction is still large even after reaching the saturation of rethermalization, the ramp-up of the horizontal lattice leads to an increase of the

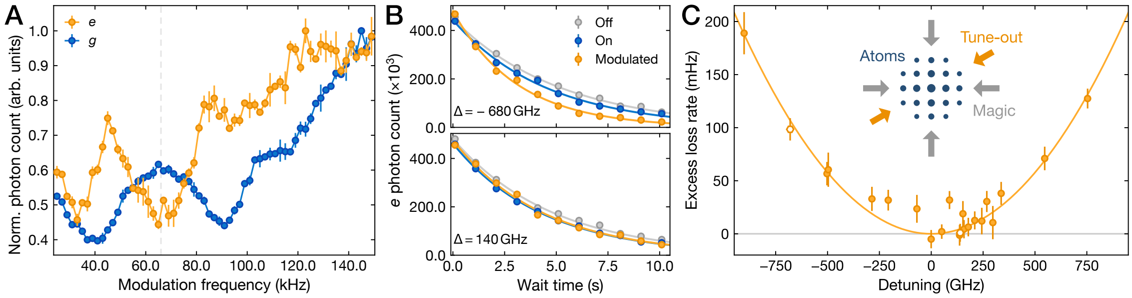

Figure 4.5 | Measurement of the tune-out wavelength for the clock state. A Modulating the amplitude of a retro-reflected beam close to the *e* tune-out wavelength leads to phase- and amplitude-modulation resonance features at the fundamental and harmonics of the 2D lattice trap frequency for atoms in the clock state (orange), similar to the *g* tune-out case. We choose the amplitude modulation resonance at 68 kHz (grey dotted line) for the lifetime tune-out measurements in **B** and **C**. With a considerably smaller modulation amplitude we can also resolve the trap frequencies experienced by ground-state atoms (blue), which are shifted and broadened due to the tune-out lattice itself. **B** A comparison of the lifetimes of *e* atoms in the 2D lattice with an additional tune-out lattice yields a reduction if the latter is modulated (orange) and detuned (upper panel) from the tune-out wavelength with respect to the case of a steady, unmodulated beam (blue). For comparably small detunings, the lifetime difference becomes negligible (lower panel). However, we consistently detect a longer lifetime if the tune-out lattice is fully turned off (grey), which is evaluated further in Fig. 4.6. Solid lines represent exponential fits to the data. **C** The excess loss rate determined from the difference in the fitted lifetimes for the modulated and constant tune-out lattice shows a quadratic dependence around the tune-out wavelength, allowing for a two-parameter fit without offset to extract $f_{\mathrm{to,e}}$. The datapoints corresponding to the lifetimes in **B** are indicated by white hexagons. In contrast to the *g* tune-out case, we do not find any indication on a parametric heating saturation effect at large excess loss rates. Inset: Illustration of the lattice geometry for this measurement, with the tune-out beam generating an irregular total pattern on top of the 2D magic lattice.

temperature along this second horizontal direction, and the atoms can tunnel more frequently to adjacent tubes, causing faster losses.

Long clock-state lifetimes at hand, we again retro-reflect the *e* tune-out beam to form a standing wave, in order to be able to induce strong parametric heating analogously to the measurement of the tune-out wavelength for the ground state. With the *e* tune-out lattice at a large angle between both horizontal lattice arms (Fig. 2.7 A), the combined lattice potential has a non-trivial shape, but can again be divided into sites that mostly observe center position or amplitude oscillations, such that we again expect both phase and amplitude modulation peaks in modulation spectroscopy measurements. We note that in this geometry pure phase modulation, induced by two independent beams with a relative detuning that is equal to the band gap and therefore generates a running wave, is expected to yield similar results since the disadvantage of the missing interference power enhancement is compensated by the addressing of atoms in every lattice site. However, the retro-reflected geometry directly allows for the search of a signal of ground-state atoms trapped inside a clock-tune-out lattice, which is why we continue with this method. Contrary to the *g* tune-out case, we can easily perform modulation spectroscopy of both ground- and clock-state atoms in this configuration. Here, the stark polarizability difference between the two states close to the *e* tune-out wavelength leads to a markedly higher $|n\rangle \rightarrow |n+2\rangle$ resonance frequency for the ground-state atoms in a deep tune-out lattice (Fig. 4.5 A). The observed shift from $f_z \simeq 68\,\mathrm{kHz}$ to $\simeq 91\,\mathrm{kHz}$ is in agreement with our expectation of an on average $\simeq 6\,\mu\mathrm{K}$ deep tune-out lattice for a ${}^1\mathrm{S}_0$ polarizability of $V_{\mathrm{ac},g}/I = -13\,h\,\mathrm{Hz/Wcm^{-2}}$ and an average tune-out power of $P = 0.7\,\mathrm{W}/2$ at this wavelength, with the factor of $1/2$ stemming from the modulation. We note that the $|n\rangle \rightarrow |n+1\rangle$ resonance does not shift as much and instead just appears to be smeared out towards larger frequencies, which is consistent with our picture of a fraction of lattice sites that mostly experience changes in the position of the potential minimum due to the tune-out lattice modulation, which thus does not result in a change of the local lattice depth up to first order. Upon a reduction of the tune-out lattice depth for the ground-state atoms we can retrieve the lower resonance frequencies measured for atoms in the ${}^3\mathrm{P}_0$ state.

For the lifetime measurements in the $240\,E_{\mathrm{rec}}$ deep 2D lattice we can observe a clean exponential decay from wait times of 20 ms after the π-pulse on. Up to this point, the fast initial loss processes, such as two-body losses on multiply occupied sites and spilling of atoms that are radially too fast for the lower lattice depth compared to the cooling depth of $400\,E_{\mathrm{rec}}$, have ebbed away and the dominant loss process is lattice-induced photon scattering. In a methodically similar fashion to the ground-state tune-out wavelength measurement we now iterate the frequency of the tune-out lattice, and we again observe a dependence compatible with a quadratic function. Crucially, the inversion point was found to be at the lower frequency edge of the laser tuning range, such that with this gain chip it was not possible to scan significantly beyond the tune-out wavelength. Therefore, the VECSEL was refitted with a different gain chip that exhibits a tuning range of $\pm 4\,\mathrm{nm}$ around 576.5 nm. Repeating the lifetime measurements with the updated laser over a large range of almost 2 THz, we can now probe the excess loss rate on both sides of the clock-state tune-out frequency, which is thus found to be at

$$f_{\mathrm{to},e} = 519.942(18)\,\mathrm{THz}. \tag{4.11}$$

This value is determined by fitting a quadratic function without offset to the excess loss rate induced by the lattice modulation compared to the case of a constant tune-out lattice at the same average power. If we instead use the bare e lifetime in the magic lattice as a reference, we observe a very similar quadratic trend, but with a finite offset of $\simeq 20(10)\,\mathrm{mHz}$ at the minimum, which is shifted by 3 GHz from $f_{\mathrm{to},e}$ (Fig. 4.6). We add this difference as a systematic uncertainty to the statistical uncertainty of 15 GHz given by the fit error. This offset motivates the study of the loss rate induced by the unmodulated tune-out lattice, which does not show any clear dependence on the detuning and is compatible with a constant additional loss rate. A weak dependence could likely be explained by relative intensity noise (RIN), corresponding to a weak, inherent modulation of the atoms, while a frequency-independent loss can be a consequence of Raman scattering via the same ${}^3\mathrm{S}_1$ transition that also causes losses at the magic wavelength, given the smaller detuning of 58 THz. We attempt to distinguish these two effects by quantifying the power dependence of the excess loss induced by the unmodulated light precisely at the tune-out wavelength. In agreement with the expectation of an off-resonant Raman process, the loss rate appears to increase monotonously as the tune-out lattice power is ramped up (Fig. 4.6 C). Due to limited tune-out beam power and the comparably small magnitude of this loss process, however, we cannot clearly discriminate between a linear and

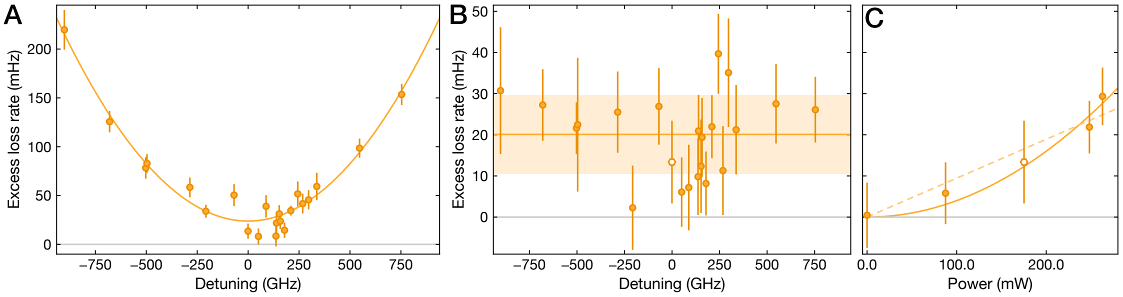

Figure 4.6 | Quantification of the finite unmodulated loss rate. A When compared to the case of the bare magic lattice without the tune-out beam the excess loss rate in the modulated tune-out lattice does not approach zero at the tune-out frequency and thus needs to be fitted with a quadratic function that includes an offset. The extracted minimum agrees with $f_{\mathrm{to},e}$ well within the statistical uncertainty. **B** The loss induced by the presence of a constant tune-out lattice appears to be frequency-independent, with an excess loss rate of 20(10) mHz, indicated by the solid orange line and the shaded region. **C** Probing the excess loss rate of an intensity stabilized tune-out lattice beam at the tune-out frequency for various powers shows an increase that is compatible with a linear dependence (dashed line), which would indicate that Raman scattering losses are the cause, but also a quadratic function fits to the data. Such a trend could be caused by RIN on the tune-out beam or e-g collisional effects.

a quadratic increase, where the latter would indicate a different loss process such as RIN or e-g collisions to be dominant. We note that we anticipate such collisions to be mostly frequency-independent, as they would be driven by heated ground-state atoms, which observe an effectively constant polarizability in this frequency regime.

A second approach to determine the tune-out wavelength is via a novel thermometric method that directly probes the parametric heating response via sideband spectroscopy instead of atom loss detection. This can be expected to provide a more time-efficient ascertainment, as the temperature increase can be measured at a constant, significantly shorter modulation time compared to the long durations necessary for the lifetime measurements, where the atoms are required to be heated up sufficiently to be able to leave the trap. Indeed, we find a modulation time of 0.5 s after the swept 2D sideband cooling sufficient to cause a visible increase in the longitudinal temperature of $\Delta T_{\mathrm{l}} \simeq 0.7\,\mu\mathrm{K}$ at a detuning of 754 GHz (Fig. 4.7 A). Close to the tune-out wavelength, we measure a negligibly small heating effect compared to the longitudinal temperature of $T_{\mathrm{l}} \simeq 960(70)\,\mathrm{nK}$ measured without tune-out lattice. This is consistent with our previous observation of very weak e-g interaction effects, since remnant or Raman-induced ground-state atoms are heated up fast in this far-from-tune-out lattice for this state. In contrast to the axial temperature, no change in temperature along the weakly confined vertical direction is recorded (Fig. 4.7 C), which is consistent with our expectation as the modulation takes place at a multiple of the longitudinal trap frequency. Fitting the overall longitudinal thermometry response around the tune-out wavelength with a three-parameter quadratic function yields a minimum at 519.86(5) THz, i.e., offset from $f_{\mathrm{to},e}$ measured by lifetime measurements by $\simeq$ 80 GHz. For future measurements, the efficiency of this measurement can be further enhanced by only probing a small part of the red and blue sideband around the modulation frequency instead of taking the whole first sideband spectrum.

We note that the measurements suffer from several systematic imperfections, which are

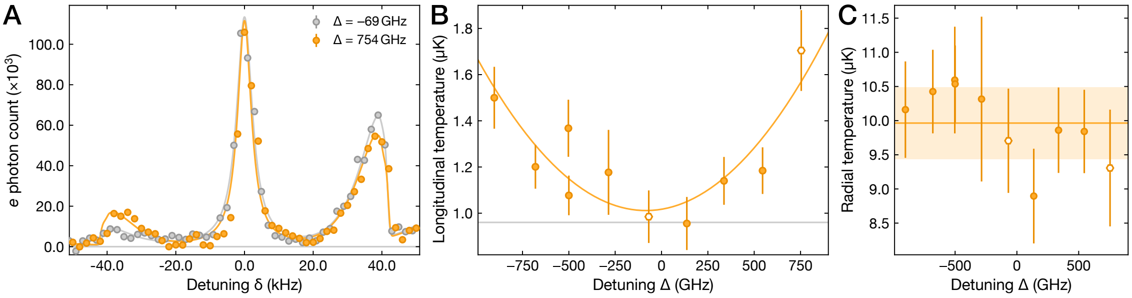

Figure 4.7 | Thermometry as an alternative to determine the clock-state tune-out wavelength. **A** We can detect the parametric heating directly by performing sideband spectroscopy in the $\simeq 250\,E_{\mathrm{rec}}$ deep holding lattice after a wait time of 500 ms with the modulated tune-out lattice active. The solid lines display the fits to the 2D sideband spectroscopy model discussed in Chapter 3.2.2 for a cloud size of $\sigma \simeq 10\,\mu\mathrm{m}$, from which we extract the longitudinal and radial temperatures. **B** Around $f_{\mathrm{to},e}$ the longitudinal temperatures remain close to the minimal temperature of $\simeq 1.0\,\mu\mathrm{K}$ recorded for the same wait time but in the bare 2D lattice, while a temperature increase is detected for larger detunings. The data appears to follow a quadratic dependence, allowing us to extract the minimum at a detuning of −80 GHz from $f_{\mathrm{to},e}$ from a corresponding fit (solid line). The temperatures obtained from the data in **A** are denoted as white hexagons. **C** The fitted radial temperatures remain within the error bar of the mean radial temperature $T_{\mathrm{r}} = 10.0(5)\,\mu\mathrm{K}$ (solid line and shaded area), which is in agreement with our expectation of a negigible coupling of longitudinal and vertical temperatures in the 2D lattice.

based upon the fact that this measurement was planned to only yield a good indication of the frequency range of interest for a carefully executed main measurement. This is then also the reason for the asymmetric and mostly coarse spacing of detunings as well as the limited number of overall datapoints. Furthermore, at each tune-out frequency only a single measurement is performed, such that the individual statistical uncertainties are quite large and explain the significant scatter of datapoints, causing a comparably large overall statistical uncertainty from the quadratic fits. In addition, the modulation was provided in a less controlled fashion compared to the g tune-out measurement as the intensity stabilization circuit could not be trimmed to not partially interfere with the feed-forwarded modulation signal from the signal generator. Therefore, the modulation amplitude could have changed between individual datapoints — a factor that is enhanced by an overall unstable laser output power despite efforts to choose the intensity stabilization setpoint at a conservative value. However, we assume that this affected all datapoints in a similar way, such that this does not cause a systematic shift but only contributes to the observed statistical uncertainty. While an upgrade to the modulation loop that allows for a stabilization to the modulated signal itself by using a fast *Toptica FALC 110* instead of home-built stabilization boxes was implemented and found to solve the former issue, instabilities in the longitudinal modes due to an unsuitably designed lasing cavity as well as suspected thermalization issues were found to lead to a strong deterioration of the laser output power within hours after the laser is turned on. A constant worsening of this problem, leading to output powers below 500 mW, required us to ship the laser back to the manufacturer for a second time to equip the laser with adjusted cavity mirrors, defering a more precise measurement of the clock-state tune-out wavelength beyond the completion of this work.

4.4 Quantum simulation and computation with tune-out potentials

Having determined the tune-out wavelengths for the optical qubit in Yb, this Section outlines prospects of simulation experiments and techniques that are enabled by this knowledge. Notably, the presented schemes are not restricted to Yb alone, but can also be used for other AEL atoms, in particular Sr.

One of the most exciting avenues enabled by tune-out wavelengths is the toolset it provides for tweezer arrays in the context of enhanced site-selective optical addressing or transporting abilities. The clock-state qubit is a key part in most quantum computing architectures based on AEL atoms and has found applications in particular for mid-circuit measurements and local shelving operations [72, 317, 318]. While the latter is so far performed by detuning the clock transition for atoms that are not to be shelved via the application of tweezer light at a non-magic wavelength for the clock state pair before a global clock pulse is sent, these tweezers also perturb the trapping potential for the detuned atoms, which can have detrimental effects on the coherence of the non-shelved atoms. In the protocols that have been demonstrated so far, this was not limiting as the unshelved ancilla qubits were imaged destructively as part of first mid-circuit operation demonstrations. However, the ability to not disturb atoms either in the ground- or clock-state manifold by applying tweezers at the respective tune-out wavelength to detune them ahead of a global rotation can open up new possibilities to reach, e.g., many-particle entanglement of atoms initially both in g and e via state-selective Rydberg interactions. A second method to achieve two-qubit gates that is made possible by tweezers at a tune-out wavelength is the locally adiabatic transport of atoms to an adjacent tweezer with an atom in the complimentary optical and nuclear qubit state [97]. By means of a spin-dependent light shift from a global beam close to the $^3\mathrm{P}_1$ transition one can precisely time the duration over which the two atoms can interact, which realizes a $\sqrt{\mathrm{SWAP}}$ gate for an interaction time equal to half a spin-exchange oscillation.

With the advent of hybrid tweezer-lattice systems, the possibility of resorting atoms to arbitrary initial configurations with dense spacings by means of movable tweezer arrays has appeared to be tantalizingly close, but yet out of reach so far. In optical lattices with typical spacings of $a \simeq 500\,\mathrm{nm}$ the comparably large size of a tweezer causes significant overlap with adjacent lattice sites, such that the total potential is distorted and the tweezer effectively pulls atoms from surrounding lattices sites into its center. Therefore, resorting of dense atom arrays in a lattice has only been demonstrated for anisotropic lattices with large constants of $a > 1\,\mu\mathrm{m}$ and low filling fractions, and abrupt onsets of near-unity atom loss probabilities are observed when a tweezer is moved past an occupied lattice site at a distance of $\lesssim 900\,\mathrm{nm}$ [75, 76]. However, in such lattices the tunneling rate of atoms in the lowest band is severely limited and thus not suitable for most quantum simulation approaches that rely on decently fast tunneling dynamics, in particular given the relatively large weight of AEL atoms. Notably, the usage of deep pinning tweezers to counteract the distortion of a nearby tweezer is mostly inhibited due to beating effects between adjacent AOD-generated tweezers owing to their frequency difference, which is typically in the realm of the radial trap frequency and its lowest harmonics for spacings below $1\,\mu\mathrm{m}$, causing fast heating and atom loss. Instead, one can make use of the orbital degree of freedom and a movable tweezer array at the tune-out wavelength to

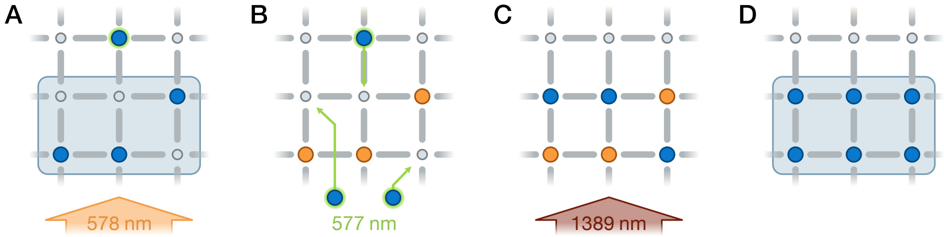

Figure 4.8 | Dense lattice resorting scheme based on tune-out tweezers. A To reach a uniform population of one atom per lattice site in a target region (blue shaded area) in an originally sparsely populated magic optical lattice (grey), we apply local shelving operations of *g* atoms (blue) to the clock state via a global π pulse or ARP sequence. Atoms that are not located at a target site are detuned from this global clock pulse via a weak local tune-out potential, induced via tweezers at either the ground- or clock-state tune-out wavelength. For clarity reasons we choose the latter for this illustration (green). **B** Using mobile *e* tune-out tweezers, we can rearrange ground-state atoms to empty lattice sites (small grey circles) in the target region. Shelved atoms in *e* (orange) remain unaffected due to the vanishing Stark shift of the tweezers for this state. **C** After the completion of the resorting step, we ramp the tweezer array down and unshelve the static atoms via a global repump pulse to the $^3D_1$ transition. Alternatively, one can perform a second clock pulse with weak tune-out tweezers at the position of the rearranged atoms in *g*. **D** In this vein, one can achieve arbitrary initial states even in lattices with small spacings. This method can also be inverted to shelve atoms that are to be moved, such that *g* tune-out tweezers are employed for this step, and is readily extendable to static magic-wavelength tweezer arrays and other AEL elements.

circumvent these issues. Starting with a sparsely loaded magic lattice in this scheme, atoms on lattice sites that shall remain occupied are shelved to the $^3P_0$ state via a global clock π-pulse. If a subset of atoms in the lattice is supposed to be moved, these atoms are detuned from the clock pulse via non-magic tweezer light, e.g., at a tune-out wavelength as described above. In the next step, atoms in the ground state from unshelved lattice sites or a different loading reservoir are moved to the desired lattice position in tweezers at the *e* tune-out wavelength, such that the shelved atoms do not experience any change in potential and thus remain unaffected. After ramping down the moving tweezer we can then bring the shelved stationary atoms back to the ground state via the repump transition to the $^3D_1$ state, which is very far detuned from any transition for ground-state atoms, such that the rearranged atoms are undisturbed and remain in g. We note that this scheme can also be inverted to move clock-state atoms in g tune-out tweezers, thus eventually repumping the resorted atoms, while the ground-state atoms in the lattice remain untouched. In Yb, the larger ground-state polarizability at the *e* tune-out wavelength compared to the *g* tune-out case renders a resorting beam at 577 nm more power-efficient, despite the slightly larger wavelength. As g tune-out tweezers would be only neglibily further detuned from the $(6s7s)^3S_1$ than the magic lattice and are instead closer to the higher-lying $(6s6d)^3D_1$ and $(6s8s)^3S_1$ transitions, they might therefore exhibit larger trap-induced losses on *e* atoms and thus make the resorting process less effective.

In order to avoid losses to the $^3P_2$ state or the necessity to use a second repumper, an alternative way to unshelve the *e* atoms is a resonant clock π-pulse. To this end, instead of fully turning off the tune-out tweezers after the rearrangement step we ramp them down to a lower depth such that it only induces a Stark shift on this particular site during the global clock pulse, but does not alter the lattice potential on adjacent sites to a significant extent.

Once this step is completed, the tune-out tweezers can be fully ramped down. With this resorting scheme, the limit on the distance between atoms in neighboring lattice sites after many rearrangement cycles is determined by its ratio to the tweezer extent, d/ξ, compared to the spectral resolution of the shelving clock pulse. As long as the induced Stark shift on the tweezer site is large compared to the resonance detuning from the weak light shift on the adjacent sites and the clock Rabi frequency,[5] a spectral separation is possible. Notably, this scheme is readily extendable to other AEL atoms such as Sr, but also to alkali metals as long as the resorting duration is kept much shorter than the inverse of the off-resonant scattering rate in the tune-out tweezers. Alternatively, for the latter, one can use different m_F states as an additional degree of freedom in combination with elliptically polarized tweezer light to shape the relative vector shift of the two target states.

---

[5] Although it is possible to push this boundary for very cold atoms with a clearly defined light shift from the nearby tweezer by, e.g., selecting a Rabi frequency whose nodes in the Rabi lineshape match this detuning, this appears practically unfeasible for high-fidelity applications.

Conclusions and outlook

The results in this thesis demonstrate the usefulness and versatility of ultracold ytterbium quantum gases in hybrid traps for quantum simulation and computation applications and set the stage for the implementation of first-of-its-kind lattice gauge theory simulations. Here, the combination of state-dependent tweezer arrays with a three-dimensional magic lattice does not only provide a tool to generate the necessary complex initial states, but also opens the door to realize elaborate, dynamical potential landscapes. While the hitherto demonstrated rearrangement schemes have been limited to relatively sparse fillings in optical lattices due to technical reasons [74, 75], the utilization of tweezers at a tune-out wavelength could reduce this intrinsic boundary to below typical lattice constants. The superposition of traps at different wavelengths, on the other hand, has found a large breadth of applications, from lattice depth homogenization and compensation of harmonic confinement [319] to the creation of sharp potential edges [33] and the scaling of trap sizes [30]. However, this has been barely used so far to extend the line-up of realizable trap geometries [185]. In this thesis we have illustrated methods to augment this scope to (anti-)Lieb lattices and discussed their suitability for two-dimensional LGT simulation schemes by adding state dependence to the total potential.

To this end, a key result presented herein is the determination of four previously unknown distinctive wavelengths. For the measurements of two new magic wavelengths at 459.6 nm and 552.6 nm we utilized a stable high-power clock laser setup, which allows us to drive fast clock Rabi cycles as well as perform narrow-linewidth resonance scans. As we anticipated [101], the magic wavelength at 459.6 nm has quickly found applications in quantum computation setups [162], owing to its larger polarizability and the shorter wavelength compared to the widely used 759.3 nm magic wavelength. The tune-out wavelengths at 553.3 nm for the ground and at 576.6 nm for the clock state will play an essential role in the envisioned fermionic U(1) LGT simulation measurements [179], but can also be used, e.g., in novel types of transport measurements with state-selective potentials. Here, one can use a deep ground-state tune-out tweezer to pin a single atom in the clock state to this lattice site, which then acts as an impurity for a bath of ground state atoms, while the latter do not observe a modification of the lattice potential [145, 320]. Using single-site resolution and coherent control over the impurity spin, this allows for a controlled study of the dynamics of the impurity as well as the bath and, hence, of non-Markovian processes in out-of-equilibrium systems. Furthermore, the impurity can be understood as disorder in the system, which could therefore also enable the observation of many-body localization [2]. We note that as a variation of such measurements the confinement of the clock-state atom can be tuned to extend to more than one lattice site by adjusting the tune-out potential accordingly, allowing for a controlled mobility of the impurity

[94]. Implementations of state-dependent potentials in AEL atoms are further expected to enable the study of twisted-bilayer models in two independent optical lattices at the tune-out wavelengths for the optical qubit with a small relative angle to simulate Moiré superlattices and graphene-like flat bands [321, 322], or to realize analog quantum chemistry simulation schemes, where a combination of magic lattices and non-magic tweezers emulates the behavior of electrons and their interaction with nuclei [323].

The measured state-dependent wavelengths could also find multiple applications in quantum computation, where tune-out wavelengths have been proposed to be used for fine control of collisional gates in tweezers [97] or the separation into storage and transport lattices and tweezer arrays [96, 324]. Here, the crucial feature is the ability to shuttle atoms in one state while leaving atoms in the other state unaffected.

Moreover, the report of experimentally determined distinctive wavelengths is relevant as accurate *ab initio* calculations of these quantities are typically highly intricate [299, 325–327], and especially elements with more than one valence electron and an accordingly rich energy level structure require a sophisticated theoretical treatment [204, 284, 298]. In the case of Yb, this is further complicated by the non-trivial interplay of well-understood LS transitions with core-excited states from the $4f$ subshell, which exceed the typical computational subspaces [152]. Here, measurements of distinctive wavelengths such as the magic and tune-out wavelengths that are reported in this thesis provide valuable feedback and can be used to improve the calculations of transition matrix elements [327], which can in turn inform on expected scattering rates as a second relevant key figure of a given trap wavelength beyond the ac polarizability [77, 110, 120].

A different direction that this experiment can explore involves the simulation of coupled 1D chains of spin-1/2 fermions, similar to [328], where antiferromagnetically ordered Li atoms have formed a synthetic ladder, coupled by strong orthogonal magnetic superexchange interactions $J_\perp$. In their system, the atoms can only tunnel along their chain with a rate t, but the strong singlet bonds along the rungs energetically penalize a broken spin order. Therefore, an initially prepared hole pair will attempt to prevent the formation of a string of displaced singlet bonds, inflicting an energy cost of $l J_\perp$ with the string length l, and instead move together. To prevent Pauli repulsion of the two holes along the rung, their system utilized a potential offset between the two chains. In our Yb setup, this ladder could be realized in a synthetic fashion, making use of the orbital degree of freedom and on-site interactions of ground- and clock-state atoms, where the superexchange interaction along rungs is given by the spin exchange energy between atoms in different spins, which could enable superexchange energies that are comparable to the tunneling energies. [189]. This study of bound states could shed light on the electronic behavior in pressurized nickelates, which have been found to host high-temperature superconductivity [329].

The second main result of this thesis, after the measurement of the magic and tune-out wavelengths, pertains to novel clock sideband cooling techniques in one- and two-dimensional lattices. The extension of this scheme to 3D lattices likely enables one to perform the initial state preparation almost two orders of magnitude faster than in previous ytterbium-based quantum simulators, which boosts the experimental cycle times and thus the accumulation of statistics. This further marks the first demonstration of sideband cooling in bosonic ytterbium, which is fundamentally impeded by the vanishing transition matrix element to the clock state. However, using acceptably large magnetic fields we have reached sub-μK temperatures along the strongly confined axes of one- and two-dimensional lattices within few hundreds of ms, with clear prospects of reaching a 3D-cooled cloud and further extending this scheme to the fermionic isotopes. Since for most quantum simulation or computation protocols only a maximal population in the absolute ground state is necessary, temperatures on the order of a few 100 nK are typically sufficient [330]. Here, we note that higher temperatures are not necessarily limiting, as erasure cooling on the hotter atoms leaves a pure sample in the motional ground state, but this step quickly reduces the lattice filling fraction too far to still be efficient. Furthermore, 3D sideband cooling on the clock transition could allow for the first Yb experiment with single-site resolution in a clock-magic lattice and the first quantum gas microscope with fermionic AEL atoms.

While fluorescence imaging on the intercombination line akin to magic tweezer experiments is expected to work well for ^{171}Yb [72], this thesis also presents an efficient molasses cooling technique during imaging on the broad 399 nm transition to prevent atom loss. Choosing this wavelength for imaging purposes allows for a resolution below the lattice spacing, which will benefit the signal-to-noise ratio of a ^{174}Yb quantum gas microscope. Due to the faster Rabi cycles that are possible in the fermionic isotopes, this clock sideband cooling method might also be useful for future quantum computation implementations in 459.6 nm clock-magic traps, where Raman sideband cooling is limited by the strong non-magicness of the $^3P_1$ transition because of the nearby $(6s6d)^3D$ transitions. In particular with the aid of a frequency-locked repump laser the clock sideband cooling duration could be reduced to few tens of ms to reach a 3D-cooled array.

In conclusion, the reported results showcase the enormous potential of state-dependent traps and optical cooling methods for ytterbium quantum gas experiments to allow for faster and more versatile measurements. The unification of optical lattices with tweezer arrays further promotes the realization of complex model Hamiltonians and the scaling of quantum processors. Hence, this thesis lays the foundation for a combination of all three modalities to contribute to understanding complex phenomena in condensed matter and high-energy physics.

Appendices

Appendix A Transition properties for the empirical polarizability model

Here, we collect the properties of the optical transitions from the ${}^1\mathrm{S}_0$, ${}^3\mathrm{P}_0$, and ${}^3\mathrm{P}_1$ states that are relevant for the empirical polarizability model (Chapter 1.2). Notably, we omit certain transitions from the two excited states compared to the model described in [110] that are instead captured by the empirical transitions.

$\lvert J\rangle$	$\lvert J'\rangle$	$\omega_{J'J}/2\pi$ (THz)	$\lambda_{J'J}$ (nm)	$\gamma_{J'J}$ (MHz)	τ (ns)	β	Ref.
${}^1\mathrm{S}_0$	$(6s6p)^3\mathrm{P}_1$	539.386800	555.802	0.183	869.6	1	[117, 122]
	$(6s6p)^1\mathrm{P}_1$	751.526389	398.911	29.127	5.464	1	[112]
	$(7/2, 5/2)_{J=1}$	865.111516	346.536	11.052	14.4	1	[117]
${}^3\mathrm{P}_0$	$(6s5d)^3\mathrm{D}_1$	215.870446	1388.761	0.308	329.3	0.639	[122]
	$(6s7s)^3\mathrm{S}_1$	461.867846	649.087	1.516*	15.9	0.151	[157]
	$(6s6d)^3\mathrm{D}_1$	675.141040	444.044	4.081*	22.7	0.582	[157]
	$(6s8s)^3\mathrm{S}_1$	729.293151	411.073	0.625*	34.3	0.135	[157]
	Empirical$_{J=1}$	797.204099	374.709	23.567			Fit
${}^3\mathrm{P}_1$	$(6s^2)^1\mathrm{S}_0$	−539.386800	−555.802	0.183	869.6	1	[117, 122]
	$(6s5d)^3\mathrm{D}_1$	194.778008	1539.149	0.170	329.3	0.352	[122]
	$(6s5d)^3\mathrm{D}_2$	202.657933	1479.303	0.280*	500	0.879	[113]
	$(6s7s)^3\mathrm{S}_1$	440.775408	680.148	3.954*	15.9	0.395	[157]
	$(6s6d)^3\mathrm{D}_1$	654.048602	458.364	2.783*	22.7	0.397	[157]
	$(6s6d)^3\mathrm{D}_2$	654.927593	457.749	5.215*	24.2	0.793	[157]
	$(6s8s)^3\mathrm{S}_1$	708.200713	423.316	1.718*	34.3	0.370	[157]
	Empirical$_{J=1}$	778.975785	384.855	22.313		0.378	Fit
	Empirical$_{J=2}$	778.975785	384.855	36.687		0.622	Fit

Table A.1 | Overview of the transition parameters for the ${}^1\mathrm{S}_0$, ${}^3\mathrm{P}_0$, and ${}^3\mathrm{P}_1$ empirical polarizability model. We denote the respective initial and final states as $\lvert J\rangle$ and $\lvert J'\rangle$ and highlight the used total electronic angular momentum of the effective transitions with a subscript. The transition frequencies and the corresponding vacuum wavelengths are taken from [155] unless mentioned otherwise in Fig. 1.1. Experimentally measured linewidths $\gamma_{J'J} = \Gamma_{J'J}/2\pi$ are given wherever possible, and we use the average of the linewidths measured in [117, 122] due to their comparably large error bars. For transitions where only the lifetime of the excited state is known we employ the *LS* model and calculate the branching ratios β following [110]. These linewidths are marked with an asterisk. The references for the linewidth measurements are given if applicable, otherwise the respective entry denotes the reference for the lifetime measurement. For the empirical $J = 1$ and $J = 2$ transitions to the ${}^3\mathrm{P}_1$ state, β describes their relative strength given by the computed branching ratios of the neglected nearby transitions.

Appendix B Finite-element simulation and optical design of the main breadboard

To understand and optimize the positioning of pillars to support the large main breadboard, we study its vulnerability to mechanical vibrations, which can affect the phase stability of the lattices, which is of importance for the relative stability between the tweezer array and the lattices, as discussed in Chapter 2.3.3. Using a finite-element simulation, we compute the lowest vibrational modes of the main breadboard and their frequencies by assuming a homogeneous gravitational force from its own weight, i.e., neglecting the placement of other components on it, and constraining the pillars to be infinitely stiff, such that the area of support is not flexible. We position the pillars such that the resonance frequencies for the critical areas around the glass cell, where the retro-reflecting lattice mirrors and the objective mounts reside, are maximized. The resulting configuration is displayed in Fig. B.1

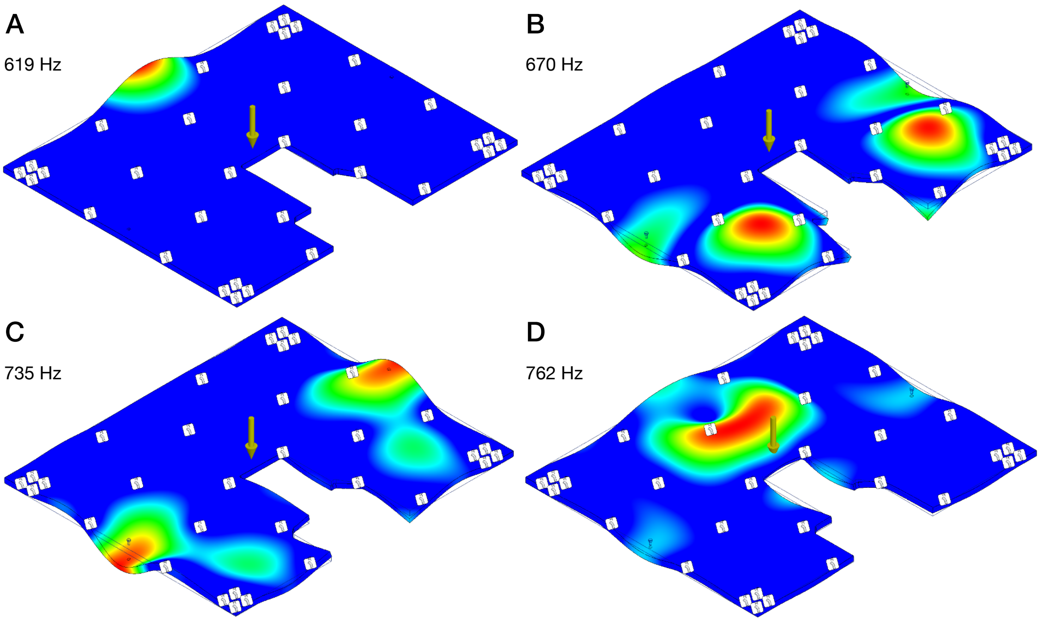

Figure B.1 | Acoustic modes of the main breadboard. Four out of the five lowest vibrational modes for the final breadboard configuration are displayed. The position of the pillars, which are assumed to be stable and possess identical heights, are indicated by white rectangles. The modes with the lowest frequencies mainly affect less relevant parts of the breadboard, and only for the resonance frequency of 762 Hz in **D** we expect a significant effect on the lattice and tweezer stability. Not depicted is the symmetric mode of the one in **C** with a resonance frequency of 737 Hz.

While Fig. 2.7 A shows a simplified optical setup on the main breadboard level around the glass cell, Fig. B.2 allows for a more detailed examination of the optical layout. We depict the setup to scale and with all relevant optical components and mounts included, apart from beam blocks and fibers and neglecting changes in the beam sizes of focused beams close to the glass cell.

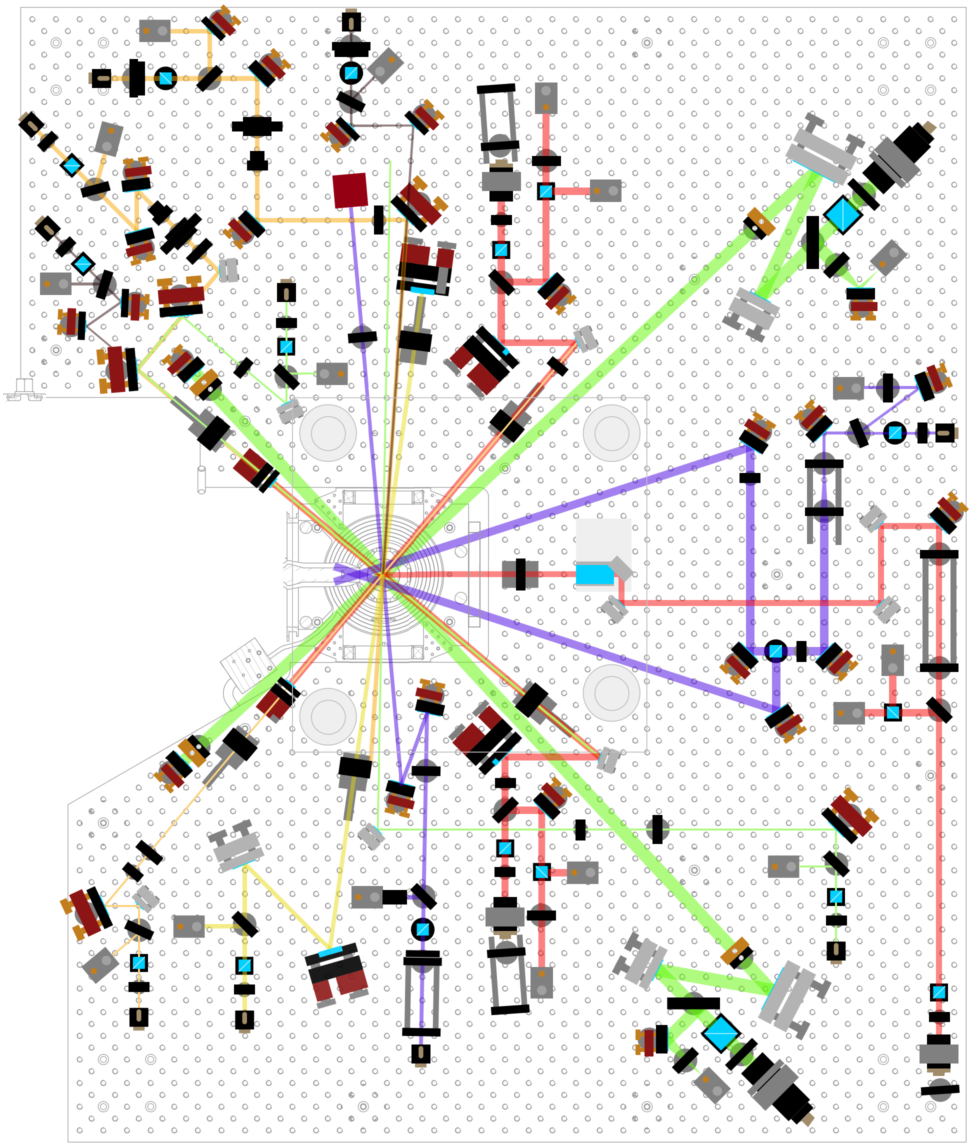

Figure B.2 | Complete optical layout on the main breadboard. To-scale illustration of the individual beam paths and placements of optics and optomechanics for the *e* tune-out wavelength measurements. The individual wavelengths are color-coded as follows: Blue: 399 nm, green: 556 nm, yellow: 577 nm, orange: 578 nm, red: 759 nm, brown: 1389 nm. The purpose of the individual beams is given in Fig. 2.7 A. In light gray the main breadboard outline as well as relevant components of the magnetic field coils are depticted. The position of the pillars for the top breadboard is indicated by solid grey circles, and the outline of the top breadboard is shown as a light grey rectangle.

References

[1] U. Schollwöck, *The density-matrix renormalization group in the age of matrix product states*, Annals of Physics **326**, January 2011 Special Issue, 96 (2011).

[2] D. A. Abanin, E. Altman, I. Bloch, and M. Serbyn, *Colloquium: Many-body localization, thermalization, and entanglement*, Rev. Mod. Phys. **91**, 021001 (2019).

[3] N. Y. Yao, A. C. Potter, I.-D. Potirniche, and A. Vishwanath, *Discrete Time Crystals: Rigidity, Criticality, and Realizations*, Phys. Rev. Lett. **118**, 030401 (2017).

[4] R. P. Feynman, *Simulating physics with computers*, Int. J. Theor. Phys. **21**, 467 (1982).

[5] I. Bloch, J. Dalibard, and W. Zwerger, *Many-body physics with ultracold gases*, Rev. Mod. Phys. **80**, 885 (2008).

[6] C. Gross and I. Bloch, *Quantum simulations with ultracold atoms in optical lattices*, Science **357**, 995 (2017).

[7] E. Altman et al., *Quantum Simulators: Architectures and Opportunities*, PRX Quantum **2**, 017003 (2021).

[8] A. J. Daley, I. Bloch, C. Kokail, S. Flannigan, N. Pearson, M. Troyer, and P. Zoller, *Practical quantum advantage in quantum simulation*, Nature **607**, 667 (2022).

[9] B. Hebbe Madhusudhana, S. Scherg, T. Kohlert, I. Bloch, and M. Aidelsburger, *Benchmarking a Novel Efficient Numerical Method for Localized 1D Fermi-Hubbard Systems on a Quantum Simulator*, PRX Quantum **2**, 040325 (2021).

[10] A. L. Shaw, Z. Chen, J. Choi, D. K. Mark, P. Scholl, R. Finkelstein, A. Elben, S. Choi, and M. Endres, *Benchmarking highly entangled states on a 60-atom analogue quantum simulator*, Nature **628**, 71 (2024).

[11] D. Deutsch and R. Jozsa, *Rapid solution of problems by quantum computation*, Proc. R. Soc. Lond. A **439**, 553 (1992).

[12] P. W. Shor, *Polynomial-Time Algorithms for Prime Factorization and Discrete Logarithms on a Quantum Computer*, SIAM Review **41**, 303 (1999).

[13] J. Preskill, *Quantum Computing in the NISQ era and beyond*, Quantum **2**, 79 (2018).

[14] F. Arute, K. Arya, R. Babbush, D. Bacon, J. C. Bardin, R. Barends, R. Biswas, S. Boixo, F. G. Brandao, and D. A. t. Buell, *Quantum supremacy using a programmable superconducting processor*, Nature **574**, 505 (2019).

[15] H.-S. Zhong et al., *Quantum computational advantage using photons*, Science **370**, 1460 (2020).

[16] M. Greiner, O. Mandel, T. Esslinger, T. W. Hänsch, and I. Bloch, *Quantum phase transition from a superfluid to a Mott insulator in a gas of ultracold atoms*, Nature **415**, 39 (2002).

[17] M. Greiner, C. A. Regal, and D. S. Jin, *Emergence of a molecular Bose–Einstein condensate from a Fermi gas*, Nature **426**, 537 (2003).

[18] S. Jochim, M. Bartenstein, A. Altmeyer, G. Hendl, S. Riedl, C. Chin, J. H. Denschlag, and R. Grimm, *Bose-Einstein Condensation of Molecules*, Science **302**, 2101 (2003).

[19] M. W. Zwierlein, C. A. Stan, C. H. Schunck, S. M. F. Raupach, S. Gupta, Z. Hadzibabic, and W. Ketterle, *Observation of Bose-Einstein Condensation of Molecules*, Phys. Rev. Lett. **91**, 250401 (2003).

[20] M. Aidelsburger, M. Atala, M. Lohse, J. T. Barreiro, B. Paredes, and I. Bloch, *Realization of the Hofstadter Hamiltonian with Ultracold Atoms in Optical Lattices*, Phys. Rev. Lett. **111**, 185301 (2013).

[21] M. Aidelsburger, M. Lohse, C. Schweizer, M. Atala, J. T. Barreiro, S. Nascimbene, N. Cooper, I. Bloch, and N. Goldman, *Measuring the Chern number of Hofstadter bands with ultracold bosonic atoms*, Nature Phys. **11**, 162 (2015).

[22] M. Schreiber, S. S. Hodgman, P. Bordia, H. P. Lüschen, M. H. Fischer, R. Vosk, E. Altman, U. Schneider, and I. Bloch, *Observation of many-body localization of interacting fermions in a quasi-random optical lattice*, Science **349**, 842 (2015).

[23] J.-y. Choi, S. Hild, J. Zeiher, P. Schauß, A. Rubio-Abadal, T. Yefsah, V. Khemani, D. A. Huse, I. Bloch, and C. Gross, *Exploring the many-body localization transition in two dimensions*, Science **352**, 1547 (2016).

[24] J. Vijayan, P. Sompet, G. Salomon, J. Koepsell, S. Hirthe, A. Bohrdt, F. Grusdt, I. Bloch, and C. Gross, *Time-resolved observation of spin-charge deconfinement in fermionic Hubbard chains*, Science **367**, 186 (2020).

[25] J. Léonard, S. Kim, J. Kwan, P. Segura, F. Grusdt, C. Repellin, N. Goldman, and M. Greiner, *Realization of a fractional quantum Hall state with ultracold atoms*, Nature **619**, 495 (2023).

[26] G. Semeghini et al., *Probing topological spin liquids on a programmable quantum simulator*, Science **374**, 1242 (2021).

[27] C. Chen et al., *Continuous symmetry breaking in a two-dimensional Rydberg array*, Nature **616**, 691 (2023).

[28] S. J. Evered, D. Bluvstein, M. Kalinowski, S. Ebadi, T. Manovitz, H. Zhou, S. H. Li, A. A. Geim, T. T. Wang, N. Maskara, H. Levine, G. Semeghini, M. Greiner, V. Vuletić, and M. D. Lukin, *High-fidelity parallel entangling gates on a neutral-atom quantum computer*, Nature **622**, 268 (2023).

[29] D. Bluvstein et al., *Logical quantum processor based on reconfigurable atom arrays*, Nature **626**, 58 (2024).

[30] H. J. Manetsch, G. Nomura, E. Bataille, K. H. Leung, X. Lv, and M. Endres, *A tweezer array with 6100 highly coherent atomic qubits*, 2024, arXiv:2403.12021.

[31] G. Pichard, D. Lim, E. Bloch, J. Vaneecloo, L. Bourachot, G.-J. Both, G. Mériaux, S. Dutartre, R. Hostein, J. Paris, B. Ximenez, A. Signoles, A. Browaeys, T. Lahaye, and D. Dreon, *Rearrangement of individual atoms in a 2000-site optical-tweezer array at cryogenic temperatures*, Phys. Rev. Appl. **22**, 024073 (2024).

[32] J. Mongkolkiattichai, L. Liu, D. Garwood, J. Yang, and P. Schauss, *Quantum gas microscopy of fermionic triangular-lattice Mott insulators*, Phys. Rev. A **108**, L061301 (2023).

[33] C. Braun, R. Saint-Jalm, A. Hesse, J. Arceri, I. Bloch, and M. Aidelsburger, *Real-space detection and manipulation of topological edge modes with ultracold atoms*, Nature Phys., 1 (2024).

[34] K. Viebahn, M. Sbroscia, E. Carter, J.-C. Yu, and U. Schneider, *Matter-Wave Diffraction from a Quasicrystalline Optical Lattice*, Phys. Rev. Lett. **122**, 110404 (2019).

[35] W. S. Bakr, J. I. Gillen, A. Peng, S. Fölling, and M. Greiner, *A quantum gas microscope for detecting single atoms in a Hubbard-regime optical lattice*, Nature **462**, 74 (2009).

[36] J. F. Sherson, C. Weitenberg, M. Endres, M. Cheneau, I. Bloch, and S. Kuhr, *Single-atom-resolved fluorescence imaging of an atomic Mott insulator*, Nature **467**, 68 (2010).

[37] M. F. Parsons, F. Huber, A. Mazurenko, C. S. Chiu, W. Setiawan, K. Wooley-Brown, S. Blatt, and M. Greiner, *Site-resolved imaging of fermionic Li 6 in an optical lattice*, Phys. Rev. Lett. **114**, 213002 (2015).

[38] J. Koepsell, S. Hirthe, D. Bourgund, P. Sompet, J. Vijayan, G. Salomon, C. Gross, and I. Bloch, *Robust Bilayer Charge Pumping for Spin- and Density-Resolved Quantum Gas Microscopy*, Phys. Rev. Lett. **125**, 010403 (2020).

[39] T. Hartke, B. Oreg, N. Jia, and M. Zwierlein, *Doublon-Hole Correlations and Fluctuation Thermometry in a Fermi-Hubbard Gas*, Phys. Rev. Lett. **125**, 113601 (2020).

[40] C. Chin, R. Grimm, P. Julienne, and E. Tiesinga, *Feshbach resonances in ultracold gases*, Rev. Mod. Phys. **82**, 1225 (2010).

[41] A. Browaeys and T. Lahaye, *Many-body physics with individually controlled Rydberg atoms*, Nature Phys. **16**, 132 (2020).

[42] S. Hollerith, J. Zeiher, J. Rui, A. Rubio-Abadal, V. Walther, T. Pohl, D. M. Stamper-Kurn, I. Bloch, and C. Gross, *Quantum gas microscopy of Rydberg macrodimers*, Science **364**, 664 (2019).

[43] J. Ye, H. J. Kimble, and H. Katori, *Quantum State Engineering and Precision Metrology Using State-Insensitive Light Traps*, Science **320**, 1734 (2008).

[44] V. A. Dzuba, V. V. Flambaum, and S. Schiller, *Testing physics beyond the standard model through additional clock transitions in neutral ytterbium*, Phys. Rev. A **98**, 022501 (2018).

[45] A. Kawasaki, T. Kobayashi, A. Nishiyama, T. Tanabe, and M. Yasuda, *Observation of the* $4f^{14}6s^2$ $^1S_0 - 4f^{13}5d6s^2(J = 2)$ *clock transition at 431* nm *in* ^{171}Yb, Phys. Rev. A **107**, L060801 (2023).

[46] A. Kawasaki, T. Kobayashi, A. Nishiyama, T. Tanabe, and M. Yasuda, *Isotope-shift analysis with the* $4f^{14}6s^{21}S_0$–$4f^{13}5d6s^2(J = 2)$ *transition in ytterbium*, Phys. Rev. A **109**, 062806 (2024).

[47] L. Tarruell and L. Sanchez-Palencia, *Quantum simulation of the Hubbard model with ultracold fermions in optical lattices*, C. R. Phys. **19**, 365 (2018).

[48] A. E. Leanhardt, T. A. Pasquini, M. Saba, A. Schirotzek, Y. Shin, D. Kielpinski, D. E. Pritchard, and W. Ketterle, *Cooling Bose-Einstein Condensates Below 500 Picokelvin*, Science **301**, 1513 (2003).

[49] J. Koepsell, *Quantum simulation of doped two-dimensional Mott insulators*, Ph.D. thesis, Ludwig-Maximilians-Universität München (2021).

[50] P. A. Lee, N. Nagaosa, and X.-G. Wen, *Doping a Mott insulator: Physics of high-temperature superconductivity*, Rev. Mod. Phys. **78**, 17 (2006).

[51] R. Jördens, N. Strohmaier, K. Günter, H. Moritz, and T. Esslinger, *A Mott insulator of fermionic atoms in an optical lattice*, Nature **455**, 204 (2008).

[52] M. Boll, T. A. Hilker, G. Salomon, A. Omran, J. Nespolo, L. Pollet, I. Bloch, and C. Gross, *Spin- and density-resolved microscopy of antiferromagnetic correlations in Fermi-Hubbard chains*, Science **353**, 1257 (2016).

[53] L. W. Cheuk, M. A. Nichols, K. R. Lawrence, M. Okan, H. Zhang, E. Khatami, N. Trivedi, T. Paiva, M. Rigol, and M. W. Zwierlein, *Observation of spatial charge and spin correlations in the 2D Fermi-Hubbard model*, Science **353**, 1260 (2016).

[54] E. Gull, O. Parcollet, and A. J. Millis, *Superconductivity and the Pseudogap in the Two-Dimensional Hubbard Model*, Phys. Rev. Lett. **110**, 216405 (2013).

[55] G. A. Phelps, A. Hébert, A. Krahn, S. Dickerson, F. Öztürk, S. Ebadi, L. Su, and M. Greiner, *Sub-second production of a quantum degenerate gas*, 2020, arXiv:2007.10807.

[56] G. Pasqualetti, *Probing the thermodynamics of SU(N)-symmetric Fermi gases with ultracold atoms*, Ph.D. thesis, Ludwig-Maximilians-Universität München (2023).

[57] A. M. Kaufman and K.-K. Ni, *Quantum science with optical tweezer arrays of ultracold atoms and molecules*, Nature Phys. **17**, 1324 (2021).

[58] M. Endres, H. Bernien, A. Keesling, H. Levine, E. R. Anschuetz, A. Krajenbrink, C. Senko, V. Vuletić, M. Greiner, and M. D. Lukin, *Atom-by-atom assembly of defect-free one-dimensional cold atom arrays*, Science **354**, 1024 (2016).

[59] D. Bluvstein, H. Levine, G. Semeghini, T. T. Wang, S. Ebadi, M. Kalinowski, A. Keesling, N. Maskara, H. Pichler, M. Greiner, V. Vuletić, and M. D. Lukin, *A quantum processor based on coherent transport of entangled atom arrays*, Nature **604**, 451 (2022).

[60] A. M. Kaufman, B. J. Lester, and C. A. Regal, *Cooling a Single Atom in an Optical Tweezer to Its Quantum Ground State*, Phys. Rev. X **2**, 041014 (2012).

[61] J. D. Thompson, T. G. Tiecke, A. S. Zibrov, V. Vuletić, and M. D. Lukin, *Coherence and Raman Sideband Cooling of a Single Atom in an Optical Tweezer*, Phys. Rev. Lett. **110**, 133001 (2013).

[62] M. A. Norcia, A. W. Young, and A. M. Kaufman, *Microscopic Control and Detection of Ultracold Strontium in Optical-Tweezer Arrays*, Phys. Rev. X **8**, 041054 (2018).

[63] A. Jenkins, J. W. Lis, A. Senoo, W. F. McGrew, and A. M. Kaufman, *Ytterbium Nuclear-Spin Qubits in an Optical Tweezer Array*, Phys. Rev. X **12**, 021027 (2022).

[64] A. Cooper, J. P. Covey, I. S. Madjarov, S. G. Porsev, M. S. Safronova, and M. Endres, *Alkaline-Earth Atoms in Optical Tweezers*, Phys. Rev. X **8**, 041055 (2018).

[65] R. Tao, M. Ammenwerth, F. Gyger, I. Bloch, and J. Zeiher, *High-Fidelity Detection of Large-Scale Atom Arrays in an Optical Lattice*, Phys. Rev. Lett. **133**, 013401 (2024).

[66] A. Omran et al., *Generation and manipulation of Schrödinger cat states in Rydberg atom arrays*, Science **365**, 570 (2019).

[67] A. L. Shaw, R. Finkelstein, R. B.-S. Tsai, P. Scholl, T. H. Yoon, J. Choi, and M. Endres, *Multi-ensemble metrology by programming local rotations with atom movements*, Nature Phys. **20**, 195 (2024).

[68] W. J. Eckner, N. Darkwah Oppong, A. Cao, A. W. Young, W. R. Milner, J. M. Robinson, J. Ye, and A. M. Kaufman, *Realizing spin squeezing with Rydberg interactions in an optical clock*, Nature **621**, 734 (2023).

[69] G. Bornet, G. Emperauger, C. Chen, B. Ye, M. Block, M. Bintz, J. A. Boyd, D. Barredo, T. Comparin, F. Mezzacapo, T. Roscilde, T. Lahaye, N. Y. Yao, and A. Browaeys, *Scalable spin squeezing in a dipolar Rydberg atom array*, Nature **621**, 728 (2023).

[70] K. Singh, S. Anand, A. Pocklington, J. T. Kemp, and H. Bernien, *Dual-Element, Two-Dimensional Atom Array with Continuous-Mode Operation*, Phys. Rev. X **12**, 011040 (2022).

[71] Y. Nakamura, T. Kusano, R. Yokoyama, K. Saito, K. Higashi, N. Ozawa, T. Takano, Y. Takasu, and Y. Takahashi, *Hybrid Atom Tweezer Array of Nuclear Spin and Optical Clock Qubits*, Phys. Rev. X **14**, 041062 (2024).

[72] J. W. Lis, A. Senoo, W. F. McGrew, F. Rönchen, A. Jenkins, and A. M. Kaufman, *Midcircuit Operations Using the omg Architecture in Neutral Atom Arrays*, Phys. Rev. X **13**, 041035 (2023).

[73] A. W. Young, W. J. Eckner, N. Schine, A. M. Childs, and A. M. Kaufman, *Tweezer-programmable 2D quantum walks in a Hubbard-regime lattice*, Science **377**, 885 (2022).

[74] A. W. Young, S. Geller, W. J. Eckner, N. Schine, S. Glancy, E. Knill, and A. M. Kaufman, *An atomic boson sampler*, Nature **629**, 311 (2024).

[75] F. Gyger, M. Ammenwerth, R. Tao, H. Timme, S. Snigirev, I. Bloch, and J. Zeiher, *Continuous operation of large-scale atom arrays in optical lattices*, Phys. Rev. Res. **6**, 033104 (2024).

[76] M. A. Norcia et al., *Iterative Assembly of* ^{171}Yb *Atom Arrays with Cavity-Enhanced Optical Lattices*, PRX Quantum **5**, 030316 (2024).

[77] D. A. Steck, *Quantum and Atom Optics*, available online at http://steck.us/teaching (revision 0.16, 26 April 2024).

[78] A. D. Ludlow, M. M. Boyd, J. Ye, E. Peik, and P. O. Schmidt, *Optical atomic clocks*, Rev. Mod. Phys. **87**, 637 (2015).

[79] J. McKeever, J. R. Buck, A. D. Boozer, A. Kuzmich, H.-C. Nägerl, D. M. Stamper-Kurn, and H. J. Kimble, *State-Insensitive Cooling and Trapping of Single Atoms in an Optical Cavity*, Phys. Rev. Lett. **90**, 133602 (2003).

[80] R. Yamamoto, J. Kobayashi, T. Kuno, K. Kato, and Y. Takahashi, *An ytterbium quantum gas microscope with narrow-line laser cooling*, New J. Phys. **18**, 023016 (2016).

[81] J. P. Covey, I. S. Madjarov, A. Cooper, and M. Endres, *2000-Times Repeated Imaging of Strontium Atoms in Clock-Magic Tweezer Arrays*, Phys. Rev. Lett. **122**, 173201 (2019).

[82] A. W. Young, W. J. Eckner, W. R. Milner, D. Kedar, M. A. Norcia, E. Oelker, N. Schine, J. Ye, and A. M. Kaufman, *Half-minute-scale atomic coherence and high relative stability in a tweezer clock*, Nature **588**, 408 (2020).

[83] S. Ma, A. P. Burgers, G. Liu, J. Wilson, B. Zhang, and J. D. Thompson, *Universal Gate Operations on Nuclear Spin Qubits in an Optical Tweezer Array of* ^{171}Yb *Atoms*, Phys. Rev. X **12**, 021028 (2022).

[84] L. Förster, M. Karski, J.-M. Choi, A. Steffen, W. Alt, D. Meschede, A. Widera, E. Montano, J. H. Lee, W. Rakreungdet, and P. S. Jessen, *Microwave Control of Atomic Motion in Optical Lattices*, Phys. Rev. Lett. **103**, 233001 (2009).

[85] X. Li, T. A. Corcovilos, Y. Wang, and D. S. Weiss, *3D Projection Sideband Cooling*, Phys. Rev. Lett. **108**, 103001 (2012).

[86] C. Robens, J. Zopes, W. Alt, S. Brakhane, D. Meschede, and A. Alberti, *Low-Entropy States of Neutral Atoms in Polarization-Synthesized Optical Lattices*, Phys. Rev. Lett. **118**, 065302 (2017).

[87] B. Yang, H. Sun, C.-J. Huang, H.-Y. Wang, Y. Deng, H.-N. Dai, Z.-S. Yuan, and J.-W. Pan, *Cooling and entangling ultracold atoms in optical lattices*, Science **369**, 550 (2020).

[88] H. Sun, B. Yang, H.-Y. Wang, Z.-Y. Zhou, G.-X. Su, H.-N. Dai, Z.-S. Yuan, and J.-W. Pan, *Realization of a bosonic antiferromagnet*, Nat. Phys. **17**, 990 (2021).

[89] O. Mandel, M. Greiner, A. Widera, T. Rom, T. W. Hänsch, and I. Bloch, *Coherent Transport of Neutral Atoms in Spin-Dependent Optical Lattice Potentials*, Phys. Rev. Lett. **91**, 010407 (2003).

[90] S. Trotzky, P. Cheinet, S. Fölling, M. Feld, U. Schnorrberger, A. M. Rey, A. Polkovnikov, E. A. Demler, M. D. Lukin, and I. Bloch, *Time-Resolved Observation and Control of Superexchange Interactions with Ultracold Atoms in Optical Lattices*, Science **319**, 295 (2008).

[91] C. Weitenberg, M. Endres, J. F. Sherson, M. Cheneau, P. Schauß, T. Fukuhara, I. Bloch, and S. Kuhr, *Single-spin addressing in an atomic Mott insulator*, Nature **471**, 319 (2011).

[92] T. Fukuhara, A. Kantian, M. Endres, M. Cheneau, P. Schauß, S. Hild, D. Bellem, U. Schollwöck, T. Giamarchi, C. Gross, I. Bloch, and S. Kuhr, *Quantum dynamics of a mobile spin impurity*, Nat. Phys. **9**, 235 (2013).

[93] H.-N. Dai, B. Yang, A. Reingruber, H. Sun, X.-F. Xu, Y.-A. Chen, Z.-S. Yuan, and J.-W. Pan, *Four-body ring-exchange interactions and anyonic statistics within a minimal toric-code Hamiltonian*, Nat. Phys. **13**, 1195 (2017).

[94] L. Riegger, N. Darkwah Oppong, M. Höfer, D. R. Fernandes, I. Bloch, and S. Fölling, *Localized Magnetic Moments with Tunable Spin Exchange in a Gas of Ultracold Fermions*, Phys. Rev. Lett. **120**, 143601 (2018).

[95] N. Darkwah Oppong, G. Pasqualetti, O. Bettermann, P. Zechmann, M. Knap, I. Bloch, and S. Fölling, *Probing Transport and Slow Relaxation in the Mass-Imbalanced Fermi-Hubbard Model*, Phys. Rev. X **12**, 031026 (2022).

[96] A. J. Daley, M. M. Boyd, J. Ye, and P. Zoller, *Quantum Computing with Alkaline-Earth-Metal Atoms*, Phys. Rev. Lett. **101**, 170504 (2008).

[97] G. Pagano, F. Scazza, and M. Foss-Feig, *Fast and Scalable Quantum Information Processing with Two-Electron Atoms in Optical Tweezer Arrays*, Adv. Quantum Tech. **2**, 1800067 (2019).

[98] W.-Y. Zhang et al., *Scalable Multipartite Entanglement Created by Spin Exchange in an Optical Lattice*, Phys. Rev. Lett. **131**, 073401 (2023).

[99] H. Labuhn, S. Ravets, D. Barredo, L. Béguin, F. Nogrette, T. Lahaye, and A. Browaeys, *Single-atom addressing in microtraps for quantum-state engineering using Rydberg atoms*, Phys. Rev. A **90**, 023415 (2014).

[100] H. Levine, A. Keesling, G. Semeghini, A. Omran, T. T. Wang, S. Ebadi, H. Bernien, M. Greiner, V. Vuletić, H. Pichler, and M. D. Lukin, *Parallel Implementation of High-Fidelity Multiqubit Gates with Neutral Atoms*, Phys. Rev. Lett. **123**, 170503 (2019).

[101] T. O. Höhn, E. Staub, G. Brochier, N. Darkwah Oppong, and M. Aidelsburger, *State-dependent potentials for the* $^1S_0$ *and* $^3P_0$ *clock states of neutral ytterbium atoms*, Phys. Rev. A **108**, 053325 (2023).

[102] T. O. Höhn, R. A. Villela, E. Zu, L. Bezzo, R. M. Kroeze, and M. Aidelsburger, *Determining the* $^3P_0$ *excited-state tune-out wavelength of* ^{174}*Yb in a triple-magic lattice*, 2024, arXiv:2412.14163.

[103] R. M. Kroeze, T. O. Höhn, R. A. Villela, E. Zu, and M. Aidelsburger, *Clock sideband cooling of ytterbium to the 3D motional ground state*, in preparation.

[104] J. Emsley, *The elements* (Oxford University Press, New York, 1998).

[105] A. Kramida, Yu. Ralchenko, J. Reader, and NIST ASD Team, *NIST Atomic Spectra Database*, available online at https://physics.nist.gov/asd (version 5.8).

[106] A. V. Gorshkov, M. Hermele, V. Gurarie, C. Xu, P. S. Julienne, J. Ye, P. Zoller, E. Demler, M. D. Lukin, and A. M. Rey, *Two-orbital* $SU(N)$ *magnetism with ultracold alkaline-earth atoms*, Nat. Phys. **6**, 289 (2010).

[107] F. Schäfer, T. Fukuhara, S. Sugawa, Y. Takasu, and Y. Takahashi, *Tools for quantum simulation with ultracold atoms in optical lattices*, Nat. Rev. Phys. **2**, 10.1038/s42254-020-0195-3 (2020).

[108] A. Lurio, M. Mandel, and R. Novick, *Second-Order Hyperfine and Zeeman Corrections for an (*sl*) Configuration*, Phys. Rev. **126**, 1758 (1962).

[109] B. H. Bransden and C. J. Joachain, *Physics of atoms and molecules* (Pearson Education, Essex, 2003).

[110] L. Riegger, *Interorbital spin exchange in a state-dependent optical lattice*, Ph.D. thesis, Ludwig-Maximilians-Universität München (2019).

[111] M. Kleinert, M. E. Gold Dahl, and S. Bergeson, *Measurement of the Yb I $^1S_0$–$^1P_1$ transition frequency at 399 nm using an optical frequency comb*, Phys. Rev. A **94**, 052511 (2016).

[112] Y. Takasu, K. Komori, K. Honda, M. Kumakura, T. Yabuzaki, and Y. Takahashi, *Photoassociation Spectroscopy of Laser-Cooled Ytterbium Atoms*, Phys. Rev. Lett. **93**, 123202 (2004).

[113] J. W. Cho, H.-g. Lee, S. Lee, J. Ahn, W.-K. Lee, D.-H. Yu, S. K. Lee, and C. Y. Park, *Optical repumping of triplet-P states enhances magneto-optical trapping of ytterbium atoms*, Phys. Rev. A **85**, 035401 (2012).

[114] M. M. Boyd, T. Zelevinsky, A. D. Ludlow, S. Blatt, T. Zanon-Willette, S. M. Foreman, and J. Ye, *Nuclear spin effects in optical lattice clocks*, Phys. Rev. A **76**, 022510 (2007).

[115] T. L. Nicholson, S. L. Campbell, R. B. Hutson, G. E. Marti, B. J. Bloom, R. L. McNally, W. Zhang, M. D. Barrett, M. S. Safronova, G. F. Strouse, W. L. Tew, and J. Ye, *Systematic evaluation of an atomic clock at 2×10^{-18} total uncertainty*, Nat. Commun. **6**, 6896 (2015).

[116] F. Scazza, *Probing SU(N)-symmetric orbital interactions with ytterbium Fermi gases in optical lattices*, Ph.D. thesis, Ludwig-Maximilians-Universität München (2015).

[117] K. Blagoev and V. Komarovskii, *Lifetimes of Levels of Neutral and Singly Ionized Lanthanide Atoms*, Atomic Data and Nuclear Data Tables **56**, 1 (1994).

[118] P. E. Atkinson, J. S. Schelfhout, and J. J. McFerran, *Hyperfine constants and line separations for the $^1S_0 -^3 P_1$ intercombination line in neutral ytterbium with sub-Doppler resolution*, Phys. Rev. A **100**, 042505 (2019).

[119] M. Pizzocaro, F. Bregolin, P. Barbieri, B. Rauf, F. Levi, and D. Calonico, *Absolute frequency measurement of the 1S0–3P0 transition of ^{171}Yb with a link to international atomic time*, Metrologia **57**, 035007 (2020).

[120] J. L. Siegel, W. F. McGrew, Y. S. Hassan, C.-C. Chen, K. Beloy, T. Grogan, X. Zhang, and A. D. Ludlow, *Excited-Band Coherent Delocalization for Improved Optical Lattice Clock Performance*, Phys. Rev. Lett. **132**, 133201 (2024).

[121] S. G. Porsev and A. Derevianko, *Hyperfine quenching of the metastable $^3P_{0,2}$ states in divalent atoms*, Phys. Rev. A **69**, 042506 (2004).

[122] K. Beloy, J. A. Sherman, N. D. Lemke, N. Hinkley, C. W. Oates, and A. D. Ludlow, *Determination of the 5d6s $^3D_1$ state lifetime and blackbody-radiation clock shift in Yb*, Phys. Rev. A **86**, 051404(R) (2012).

[123] D. Ai, T. Jin, T. Zhang, L. Luo, L. Liu, M. Zhou, and X. Xu, *Erratum: Absolute frequency measurement of the $6s6p^3P_0 \rightarrow 5d6s^3D_1$ transition based on ultracold ytterbium atoms [Phys. Rev. A 107, 063107 (2023)]*, Phys. Rev. A **109**, 039902 (2024).

[124] A. V. Taichenachev, V. I. Yudin, C. W. Oates, C. W. Hoyt, Z. W. Barber, and L. Hollberg, *Magnetic Field-Induced Spectroscopy of Forbidden Optical Transitions with Application to Lattice-Based Optical Atomic Clocks*, Phys. Rev. Lett. **96**, 083001 (2006).

[125] Z. W. Barber, C. W. Hoyt, C. W. Oates, L. Hollberg, A. V. Taichenachev, and V. I. Yudin, *Direct Excitation of the Forbidden Clock Transition in Neutral* ^{174}Yb *Atoms Confined to an Optical Lattice*, Phys. Rev. Lett. **96**, 083002 (2006).

[126] X. Zhang, K. Beloy, Y. S. Hassan, W. F. McGrew, C.-C. Chen, J. L. Siegel, T. Grogan, and A. D. Ludlow, *Subrecoil Clock-Transition Laser Cooling Enabling Shallow Optical Lattice Clocks*, Phys. Rev. Lett. **129**, 113202 (2022).

[127] A. Derevianko, *Feasibility of Cooling and Trapping Metastable Alkaline-Earth Atoms*, Phys. Rev. Lett. **87**, 023002 (2001).

[128] V. Klüsener, S. Pucher, D. Yankelev, J. Trautmann, F. Spriestersbach, D. Filin, S. G. Porsev, M. S. Safronova, I. Bloch, and S. Blatt, *Long-Lived Coherence on a* µHz *Scale Optical Magnetic Quadrupole Transition*, Phys. Rev. Lett. **132**, 253201 (2024).

[129] A. Aeppli, K. Kim, W. Warfield, M. S. Safronova, and J. Ye, *Clock with* 8×10^{-19} *Systematic Uncertainty*, Phys. Rev. Lett. **133**, 023401 (2024).

[130] W. F. McGrew, X. Zhang, R. J. Fasano, S. A. Schäffer, K. Beloy, D. Nicolodi, R. C. Brown, N. Hinkley, G. Milani, M. Schioppo, T. H. Yoon, and A. D. Ludlow, *Atomic clock performance enabling geodesy below the centimetre level*, Nature **564**, 87 (2018).

[131] F. Le Kien, P. Schneeweiss, and A. Rauschenbeutel, *Dynamical polarizability of atoms in arbitrary light fields: general theory and application to cesium*, Eur. Phys. J. D **67** (2013).

[132] J. He, B. Pasquiou, R. G. Escudero, S. Zhou, M. Borkowski, and F. Schreck, *Coherent Three-Photon Excitation of the Strontium Clock Transition*, 2024, arXiv:2406.07530.

[133] S. P. Carman, J. Rudolph, B. E. Garber, M. J. V. de Graaff, H. Swan, Y. Jiang, M. Nantel, M. Abe, R. L. Barcklay, and J. M. Hogan, *Collinear three-photon excitation of a strongly forbidden optical clock transition*, 2024, arXiv:2406.07902.

[134] T. Akatsuka, M. Takamoto, and H. Katori, *Optical lattice clocks with non-interacting bosons and fermions*, Nat. Phys. **4**, 954 (2008).

[135] M. Baumann and G. Wandel, g_J *Factors of the 6s6p* $^3P_1$ *and 6s6p* $^1P_1$ *states of ytterbium*, Phys. Lett. A **28**, 200 (1968).

[136] M. Höfer, L. Riegger, F. Scazza, C. Hofrichter, D. R. Fernandes, M. M. Parish, J. Levinsen, I. Bloch, and S. Fölling, *Observation of an Orbital Interaction-Induced Feshbach Resonance in* ^{173}Yb, Phys. Rev. Lett. **115**, 265302 (2015).

[137] G. Pagano, M. Mancini, G. Cappellini, L. Livi, C. Sias, J. Catani, M. Inguscio, and L. Fallani, *Strongly Interacting Gas of Two-Electron Fermions at an Orbital Feshbach Resonance*, Phys. Rev. Lett. **115**, 265301 (2015).

[138] N. Poli, Z. W. Barber, N. D. Lemke, C. W. Oates, L. S. Ma, J. E. Stalnaker, T. M. Fortier, S. A. Diddams, L. Hollberg, J. C. Bergquist, A. Brusch, S. Jefferts, T. Heavner, and T. Parker, *Frequency evaluation of the doubly forbidden* $^1S_0 \rightarrow ^3 P_0$ *transition in bosonic* ^{174}Yb, Phys. Rev. A **77**, 050501 (2008).

[139] J. J. Sakurai and J. Napolitano, *Modern quantum mechanics* (Cambridge University Press, 2020).

[140] N. Darkwah Oppong, *Probing many-body physics with multiorbital quantum gases*, Ph.D. thesis, Ludwig-Maximilians-Universität München (2021).

[141] M. Kitagawa, K. Enomoto, K. Kasa, Y. Takahashi, R. Ciuryło, P. Naidon, and P. S. Julienne, *Two-color photoassociation spectroscopy of ytterbium atoms and the precise determinations of s-wave scattering lengths*, Phys. Rev. A **77**, 012719 (2008).

[142] L Franchi, L. F. Livi, G Cappellini, G Binella, M Inguscio, J Catani, and L Fallani, *State-dependent interactions in ultracold ^{174}Yb probed by optical clock spectroscopy*, New J. Phys. **19**, 103037 (2017).

[143] R Bouganne, M. B. Aguilera, A Dareau, E Soave, J Beugnon, and F Gerbier, *Clock spectroscopy of interacting bosons in deep optical lattices*, New J. Phys. **19**, 113006 (2017).

[144] O. Bettermann, N. Darkwah Oppong, G. Pasqualetti, L. Riegger, I. Bloch, and S. Fölling, *Clock-line photoassociation of strongly bound dimers in a magic-wavelength lattice*, Phys. Rev. A **108**, L041302 (2023).

[145] F. Scazza, C. Hofrichter, M. Höfer, P. C. De Groot, I. Bloch, and S. Fölling, *Observation of two-orbital spin-exchange interactions with ultracold SU(N)-symmetric fermions*, Nat. Phys. **10**, 779 (2014).

[146] G. Pagano, M. Mancini, G. Cappellini, P. Lombardi, F. Schäfer, H. Hu, X.-J. Liu, J. Catani, C. Sias, M. Inguscio, and L. Fallani, *A one-dimensional liquid of fermions with tunable spin*, Nat. Phys. **10**, 198 (2014).

[147] S. Taie, R. Yamazaki, S. Sugawa, and Y. Takahashi, *An SU (6) Mott insulator of an atomic Fermi gas realized by large-spin Pomeranchuk cooling*, Nature Physics **8**, 825 (2012).

[148] G. Pasqualetti, O. Bettermann, N. Darkwah Oppong, E. Ibarra-García-Padilla, S. Dasgupta, R. T. Scalettar, K. R. A. Hazzard, I. Bloch, and S. Fölling, *Equation of State and Thermometry of the 2D* $\mathrm{SU}(N)$ *Fermi-Hubbard Model*, Phys. Rev. Lett. **132**, 083401 (2024).

[149] C. Hofrichter, *Probing the SU(N) Fermi-Hubbard model with ytterbium atoms in an optical lattice*, Ph.D. thesis, Ludwig-Maximilians-Universität München (2016).

[150] J. Weiner, V. S. Bagnato, S. Zilio, and P. S. Julienne, *Experiments and theory in cold and ultracold collisions*, Rev. Mod. Phys. **71**, 1 (1999).

[151] S. Saskin, J. T. Wilson, B. Grinkemeyer, and J. D. Thompson, *Narrow-Line Cooling and Imaging of Ytterbium Atoms in an Optical Tweezer Array*, Phys. Rev. Lett. **122**, 143002 (2019).

[152] V. A. Dzuba and A Derevianko, *Dynamic polarizabilities and related properties of clock states of the ytterbium atom*, J. Phys. B: At. Mol. Opt. Phys. **43**, 074011 (2010).

[153] K. Guo, G. Wang, and A. Ye, *Dipole polarizabilities and magic wavelengths for a Sr and Yb atomic optical lattice clock*, J. Phys. B: At. Mol. Opt. Phys. **43**, 135004 (2010).

[154] V. A. Dzuba, *Private communications*.

[155] W. Meggers and J. Tech, *The First Spectrum of Ytterbium (Yb I)*, J. Res. Natl. Bur. Stand. (1977) **83**, 13 (1978).

[156] R. Grimm, M. Weidemüller, Y. B. Ovchinnikov, B. Bederson, and H. Walther, *Optical Dipole Traps for Neutral Atoms*, in *Advances in atomic, molecular, and optical physics*, Vol. 42 (Academic Press, 2000), 95.

[157] M Baumann, M Braun, A Gaiser, and H Liening, *Radiative lifetimes and* g_J *factors of low-lying even-parity levels in the Yb I spectrum*, J. Phys. B: Atom. Mol. Phys. **18**, L601 (1985).

[158] W. C. Martin, R Zalubas, and L Hagan, *Atomic energy levels - the rare earth elements*, (1978).

[159] W. F. McGrew, *An Ytterbium Optical Lattice Clock with Eighteen Digits of Uncertainty, Instability, and Reproducibility*, PhD thesis, University of Colorado, Boulder (2020).

[160] I. S. Madjarov, *Entangling, Controlling, and Detecting Individual Strontium Atoms in Optical Tweezer Arrays*, Ph.D. thesis, California Institute of Technology (2021).

[161] S. L. Campbell, R. B. Hutson, G. E. Marti, A. Goban, N. Darkwah Oppong, R. L. McNally, L. Sonderhouse, J. M. Robinson, W. Zhang, B. J. Bloom, and J. Ye, *A Fermi-degenerate three-dimensional optical lattice clock*, Science **358**, 90 (2017).

[162] M. A. Norcia et al., *Midcircuit Qubit Measurement and Rearrangement in a* ^{171}Yb *Atomic Array*, Phys. Rev. X **13**, 041034 (2023).

[163] Z.-M. Tang, Y.-M. Yu, J. Jiang, and C.-Z. Dong, *Magic wavelengths for the* $6s^{21}S_0$–$6s6p^3P_1^o$ *transition in ytterbium atom*, J. Phys. B: At. Mol. Opt. Phys. **51**, 125002 (2018).

[164] X. Zheng, J. Dolde, M. C. Cambria, H. M. Lim, and S. Kolkowitz, *A lab-based test of the gravitational redshift with a miniature clock network*, Nature Communications **14**, 4886 (2023).

[165] H. J. Metcalf and P. Van der Straten, *Laser cooling and trapping* (Springer, New York, 1999).

[166] S. Blatt, J. W. Thomsen, G. K. Campbell, A. D. Ludlow, M. D. Swallows, M. J. Martin, M. M. Boyd, and J. Ye, *Rabi spectroscopy and excitation inhomogeneity in a one-dimensional optical lattice clock*, Phys. Rev. A **80**, 052703 (2009).

[167] W. Kohn, *Analytic Properties of Bloch Waves and Wannier Functions*, Phys. Rev. **115**, 809 (1959).

[168] G. B. Airy, *On the diffraction of an object-glass with circular aperture*, Transactions of the Cambridge Philosophical Society **5**, 283 (1835).

[169] D. Gröters, *Diffraction-limited Imaging and Trapping of Ultracold Ytterbium Atoms in Optical Tweezer Arrays*, Master thesis, Ludwig-Maximilians-Universität München (2023).

[170] T. Latychevskaia, *Lateral and axial resolution criteria in incoherent and coherent optics and holography, near- and far-field regimes*, Appl. Opt. **58**, 3597 (2019).

[171] C. Schweizer, F. Grusdt, M. Berngruber, L. Barbiero, E. Demler, N. Goldman, I. Bloch, and M. Aidelsburger, *Floquet approach to* $\mathbb{Z}_2$ *lattice gauge theories with ultracold atoms in optical lattices*, Nat. Phys. **15**, 1168 (2019).

[172] A. Mil, T. V. Zache, A. Hegde, A. Xia, R. P. Bhatt, M. K. Oberthaler, P. Hauke, J. Berges, and F. Jendrzejewski, *A scalable realization of local U(1) gauge invariance in cold atomic mixtures*, Science **367**, 1128 (2020).

[173] H. Bernien, S. Schwartz, A. Keesling, H. Levine, A. Omran, H. Pichler, S. Choi, A Zibrov, M. Endres, M. Greiner, V. Vuletić, and M. D. Lukin, *Probing many-body dynamics on a 51-atom quantum simulator*, Nature **551**, 579 (2017).

[174] F. M. Surace, P. P. Mazza, G. Giudici, A. Lerose, A. Gambassi, and M. Dalmonte, *Lattice Gauge Theories and String Dynamics in Rydberg Atom Quantum Simulators*, Phys. Rev. X **10**, 021041 (2020).

[175] B. Yang, H. Sun, R. Ott, H.-Y. Wang, T. V. Zache, J. C. Halimeh, Z.-S. Yuan, P. Hauke, and J.-W. Pan, *Observation of gauge invariance in a 71-site Bose–Hubbard quantum simulator*, Nature **587**, 392 (2020).

[176] Z.-Y. Zhou, G.-X. Su, J. C. Halimeh, R. Ott, H. Sun, P. Hauke, B. Yang, Z.-S. Yuan, J. Berges, and J.-W. Pan, *Thermalization dynamics of a gauge theory on a quantum simulator*, Science **377**, 311 (2022).

[177] H.-Y. Wang, W.-Y. Zhang, Z. Yao, Y. Liu, Z.-H. Zhu, Y.-G. Zheng, X.-K. Wang, H. Zhai, Z.-S. Yuan, and J.-W. Pan, *Interrelated Thermalization and Quantum Criticality in a Lattice Gauge Simulator*, Phys. Rev. Lett. **131**, 050401 (2023).

[178] A. Frölian, C. S. Chisholm, E. Neri, C. R. Cabrera, R. Ramos, A. Celi, and L. Tarruell, *Realizing a 1D topological gauge theory in an optically dressed BEC*, Nature **608**, 293 (2022).

[179] F. M. Surace, P. Fromholz, N. Darkwah Oppong, M. Dalmonte, and M. Aidelsburger, *Ab initio derivation of lattice gauge theory dynamics for cold gases in optical lattices*, PRX Quantum **4**, 020330 (2023).

[180] J. Kogut and L. Susskind, *Hamiltonian formulation of Wilson's lattice gauge theories*, Phys. Rev. D **11**, 395 (1975).

[181] L. Susskind, *Lattice fermions*, Phys. Rev. D **16**, 3031 (1977).

[182] M. Aidelsburger, M. Atala, S. Nascimbène, S. Trotzky, Y.-A. Chen, and I. Bloch, *Experimental Realization of Strong Effective Magnetic Fields in an Optical Lattice*, Phys. Rev. Lett. **107**, 255301 (2011).

[183] G.-B. Jo, J. Guzman, C. K. Thomas, P. Hosur, A. Vishwanath, and D. M. Stamper-Kurn, *Ultracold Atoms in a Tunable Optical Kagome Lattice*, Phys. Rev. Lett. **108**, 045305 (2012).

[184] D. Bourgund, T. Chalopin, P. Bojović, H. Schlömer, S. Wang, T. Franz, S. Hirthe, A. Bohrdt, F. Grusdt, I. Bloch, and T. A. Hilker, *Formation of stripes in a mixed-dimensional cold-atom Fermi-Hubbard system*, 2023, arXiv:2312.14156.

[185] D. Wei, D. Adler, K. Srakaew, S. Agrawal, P. Weckesser, I. Bloch, and J. Zeiher, *Observation of Brane Parity Order in Programmable Optical Lattices*, Phys. Rev. X **13**, 021042 (2023).

[186] J. Sebby-Strabley, M. Anderlini, P. S. Jessen, and J. V. Porto, *Lattice of double wells for manipulating pairs of cold atoms*, Phys. Rev. A **73**, 033605 (2006).

[187] A Rauschenbeutel, H Schadwinkel, V Gomer, and D Meschede, *Standing light fields for cold atoms with intrinsically stable and variable time phases*, Opt. Commun. **148**, 45 (1998).

[188] F. M. Surace, P. Fromholz, F. Scazza, and M. Dalmonte, *Scalable, ab initio protocol for quantum simulating SU(N)×U(1) Lattice Gauge Theories*, Quantum **8**, 1359 (2024).

[189] L. Homeier, *Private communications*.

[190] U.-J. Wiese, *Ultracold quantum gases and lattice systems: quantum simulation of lattice gauge theories*, Ann. d. Phys. **525**, 777 (2013).

[191] L. Homeier, A. Bohrdt, S. Linsel, E. Demler, J. C. Halimeh, and F. Grusdt, *Realistic scheme for quantum simulation of Z 2 lattice gauge theories with dynamical matter in (2+ 1) D*, Commun. Phys. **6**, 127 (2023).

[192] Y. Takasu, K. Maki, K. Komori, T. Takano, K. Honda, M. Kumakura, T. Yabuzaki, and Y. Takahashi, *Spin-Singlet Bose-Einstein Condensation of Two-Electron Atoms*, Phys. Rev. Lett. **91**, 040404 (2003).

[193] M. Miranda, A. Nakamoto, Y. Okuyama, A. Noguchi, M. Ueda, and M. Kozuma, *All-optical transport and compression of ytterbium atoms into the surface of a solid immersion lens*, Phys. Rev. A **86**, 063615 (2012).

[194] S. Dörscher, A. Thobe, B. Hundt, A. Kochanke, R. Le Targat, P. Windpassinger, C. Becker, and K. Sengstock, *Creation of quantum-degenerate gases of ytterbium in a compact 2D-/3D-magneto-optical trap setup*, Review of Scientific Instruments **84**, 10.1063/1.4802682 (2013).

[195] G. Cappellini, M. Mancini, G. Pagano, P. Lombardi, L. Livi, M. Siciliani de Cumis, P. Cancio, M. Pizzocaro, D. Calonico, F. Levi, C. Sias, J. Catani, M. Inguscio, and L. Fallani, *Direct Observation of Coherent Interorbital Spin-Exchange Dynamics*, Phys. Rev. Lett. **113**, 120402 (2014).

[196] A. Dareau, M. Scholl, Q. Beaufils, D. Döring, J. Beugnon, and F. Gerbier, *Doppler spectroscopy of an ytterbium Bose-Einstein condensate on the clock transition*, Phys. Rev. A **91**, 023626 (2015).

[197] M.-S. Kim, M. Lee, J. H. Han, and Y.-i. Shin, *Experimental apparatus for generating quantum degenerate gases of ytterbium atoms*, Journal of the Korean Physical Society **67**, 1719 (2015).

[198] M. Miranda, R. Inoue, Y. Okuyama, A. Nakamoto, and M. Kozuma, *Site-resolved imaging of ytterbium atoms in a two-dimensional optical lattice*, Phys. Rev. A **91**, 063414 (2015).

[199] K.-N. Schymik, S. Pancaldi, F. Nogrette, D. Barredo, J. Paris, A. Browaeys, and T. Lahaye, *Single Atoms with 6000-Second Trapping Lifetimes in Optical-Tweezer Arrays at Cryogenic Temperatures*, Phys. Rev. Appl. **16**, 034013 (2021).

[200] R. R. Hultgren, P. D. Desai, D. T. Hawkins, M. Gleiser, K. K. Kelley, and D. D. Wagman, *Selected values of the thermodynamic properties of the elements*, 1973.

[201] E. Staub, *Developing a High-Flux Atomic Beam Source for Experiments with Ultracold Strontium Quantum Gases*, Master thesis, Ludwig-Maximilians-Universität München (2019).

[202] T. M. Klostermann, *Construction of a Caesium Quantum Gas Microscope*, Ph.D. thesis, Ludwig-Maximilians-Universität München (2021).

[203] S. Campbell, *A Fermi-degenerate three-dimensional optical lattice clock*, Ph.D. thesis, University of Colorado, Boulder (2017).

[204] A. Heinz, A. J. Park, N. Šantić, J. Trautmann, S. G. Porsev, M. S. Safronova, I. Bloch, and S. Blatt, *State-dependent optical lattices for the strontium optical qubit*, Phys. Rev. Lett. **124**, 203201 (2020).

[205] C. E. Staub, *A New Hybrid Lattice-Tweezer Experiment for Quantum Simulation with Ytterbium Atoms*, Ph.D. thesis, Ludwig-Maximilians-Universität München (2024).

[206] J. H. A. Park, *Towards Quantum Simulations with Strontium in Cavity-enhanced Optical Lattices*, Ph.D. thesis, Ludwig-Maximilians-Universität München (2021).

[207] M. Sohmen, M. J. Mark, M. Greiner, and F. Ferlaino, *A ship-in-a-bottle quantum gas microscope setup for magnetic mixtures*, SciPost Phys. **15**, 182 (2023).

[208] M. Höfer, *A two-orbital quantum gas with tunable interactions*, Ph.D. thesis, Ludwig-Maximilians-Universität München (2017).

[209] Z. W. Barber, J. E. Stalnaker, N. D. Lemke, N. Poli, C. W. Oates, T. M. Fortier, S. A. Diddams, L. Hollberg, C. W. Hoyt, A. V. Taichenachev, and V. I. Yudin, *Optical Lattice Induced Light Shifts in an Yb Atomic Clock*, Phys. Rev. Lett. **100**, 103002 (2008).

[210] M. M. Boyd, A. D. Ludlow, S. Blatt, S. M. Foreman, T. Ido, T. Zelevinsky, and J. Ye, ^{87}Sr *Lattice Clock with Inaccuracy below* 10^{-15}, Phys. Rev. Lett. **98**, 083002 (2007).

[211] AZO Materials, *Titanium Alloys - Physical Properties*, available online at https://www.azom.com/article.aspx?articleid=1341; accessed 20.06.2024, 2002.

[212] I. Shakir Abbood, S. aldeen Odaa, K. F. Hasan, and M. A. Jasim, *Properties evaluation of fiber reinforced polymers and their constituent materials used in structures – A review*, Materials Today: Proceedings **43**, International Conference on Advanced Materials Behavior and Characterization (ICAMBC 2020), 1003 (2021).

[213] F. Brislee, *A redetermination of the elastic modulus of aluminium*, Transactions of the Faraday Society **9**, 155 (1913).

[214] The Engineering Toolbox, *Metals - Temperature Expansion Coefficients*, available online at https://www.engineeringtoolbox.com/thermal-expansion-metals-d-859.html; accessed 20.06.2024, 2005.

[215] P. E. Ciddor, *Refractive index of air: new equations for the visible and near infrared*, Appl. Opt. **35**, 1566 (1996).

[216] L. Asteria, H. P. Zahn, M. N. Kosch, K. Sengstock, and C. Weitenberg, *Quantum gas magnifier for sub-lattice-resolved imaging of 3D quantum systems*, Nature **599**, 571 (2021).

[217] N. Lorenz, *A Rydberg tweezer platform with potassium atoms*, Ph.D. thesis, Ludwig-Maximilians-Universität München (2021).

[218] H. von Raven, *A new Caesium quantum gas microscope with precise magnetic field control*, Ph.D. thesis, Ludwig-Maximilians-Universität München (2022).

[219] D. Wei, *Microscopy of spin hydrodynamics and cooperative light scattering in atomic Hubbard systems*, Ph.D. thesis, Ludwig-Maximilians-Universität München (2023).

[220] S. V. Tovstonog, S. Kurimura, I. Suzuki, K. Takeno, S. Moriwaki, N. Ohmae, N. Mio, and T. Katagai, *Thermal effects in high-power CW second harmonic generation in Mg-doped stoichiometric lithium tantalate*, Opt. Express **16**, 11294 (2008).

[221] M. Cladera Rosselló, *Laser Cooling of Rb atoms in a MOT and SHG for Tweezer generation*, Master thesis, Ludwig-Maximilians-Universität München (2023).

[222] S. Burd, D. Leibfried, A. C. Wilson, and D. J. Wineland, *Optically pumped semiconductor lasers for atomic and molecular physics*, in Vertical external cavity surface emitting lasers (vecsels) v, Vol. 9349, edited by M. Guina (International Society for Optics and Photonics, 2015), 93490P.

[223] S. C. Burd, D. T. C. Allcock, T. Leinonen, J. P. Penttinen, D. H. Slichter, R. Srinivas, A. C. Wilson, R. Jördens, M. Guina, D. Leibfried, and D. J. Wineland, *VECSEL systems for the generation and manipulation of trapped magnesium ions*, Optica **3**, 1294 (2016).

[224] C. Gross, *Private communications*.

[225] J. Poirson, F. Bretenaker, M. Vallet, and A. L. Floch, *Analytical and experimental study of ringing effects in a Fabry–Perot cavity. Application to the measurement of high finesses*, J. Opt. Soc. Am. B **14**, 2811 (1997).

[226] D. R. Huber and J. B. Carroll, *Time domain response of an optically frequency swept Fabry-Perot interferometer*, Appl. Opt. **25**, 2386 (1986).

[227] M. J. Martin, *Quantum Metrology and Many-Body Physics: Pushing the Frontier of the Optical Lattice Clock*, Ph.D. thesis, University of Colorado, Boulder (2013).

[228] J. I. Thorpe, K. Numata, and J. Livas, *Laser frequency stabilization and control through offset sideband locking to optical cavities*, Opt. Express **16**, 15980 (2008).

[229] L. Bezzo, *in preparation*, Master thesis, Ludwig-Maximilians-Universität München (2024).

[230] J. Lee, J. H. Lee, J. Noh, and J. Mun, *Core-shell magneto-optical trap for alkaline-earth-metal-like atoms*, Phys. Rev. A **91**, 053405 (2015).

[231] W. Huie, L. Li, N. Chen, X. Hu, Z. Jia, W. K. C. Sun, and J. P. Covey, *Repetitive Readout and Real-Time Control of Nuclear Spin Qubits in* ^{171}Yb *Atoms*, PRX Quantum **4**, 030337 (2023).

[232] T. H. Loftus, T. Ido, M. M. Boyd, A. D. Ludlow, and J. Ye, *Narrow line cooling and momentum-space crystals*, Phys. Rev. A **70**, 063413 (2004).

[233] A. Urech, I. H. A. Knottnerus, R. J. C. Spreeuw, and F. Schreck, *Narrow-line imaging of single strontium atoms in shallow optical tweezers*, Phys. Rev. Res. **4**, 023245 (2022).

[234] C. Hölzl, A. Götzelmann, M. Wirth, M. S. Safronova, S. Weber, and F. Meinert, *Motional ground-state cooling of single atoms in state-dependent optical tweezers*, Phys. Rev. Res. **5**, 033093 (2023).

[235] M. A. Norcia, J. R. Cline, J. P. Bartolotta, M. J. Holland, and J. K. Thompson, *Narrow-line laser cooling by adiabatic transfer*, New J. Phys. **20**, 023021 (2018).

[236] S. Snigirev, A. J. Park, A. Heinz, I. Bloch, and S. Blatt, *Fast and dense magneto-optical traps for strontium*, Phys. Rev. A **99**, 063421 (2019).

[237] T. Kuwamoto, K. Honda, Y. Takahashi, and T. Yabuzaki, *Magneto-optical trapping of Yb atoms using an intercombination transition*, Phys. Rev. A **60**, R745 (1999).

[238] T. Na Narong, T. Liu, N. Raghuram, and L. Hollberg, *Stimulated slowing of Yb atoms on the narrow* $^1S_0 \to {}^3P_1$ *transition*, Phys. Rev. A **104**, 053117 (2021).

[239] B. Plotkin-Swing, A. Wirth, D. Gochnauer, T. Rahman, K. E. McAlpine, and S. Gupta, *Crossed-beam slowing to enhance narrow-line ytterbium magneto-optic traps*, Rev. Sci. Instrum. **91**, 093201 (2020).

[240] P. Ilzhöfer, G. Durastante, A. Patscheider, A. Trautmann, M. J. Mark, and F. Ferlaino, *Two-species five-beam magneto-optical trap for erbium and dysprosium*, Phys. Rev. A **97**, 023633 (2018).

[241] F. Scazza, *Private communications*.

[242] G. Reinaudi, T. Lahaye, Z. Wang, and D. Guéry-Odelin, *Strong saturation absorption imaging of dense clouds of ultracold atoms*, Opt. Lett. **32**, 3143 (2007).

[243] O. Bettermann, *Private communications*.

[244] G. Pasqualetti, *Design and characterization of a repump laser for clock state detection using the* $^3P_0 \to {}^3D_1$ *transition in* ^{173}*Yb*, Praktikumsbericht, Aug. 2017.

[245] Y. Takata, S. Nakajima, J. Kobayashi, K. Ono, Y. Amano, and Y. Takahashi, *Current-feedback-stabilized laser system for quantum simulation experiments using* Yb *clock transition at 578 nm*, Rev. Sci. Instrum. **90**, 083002 (2019).

[246] E. Haller, J. Hudson, A. Kelly, D. A. Cotta, B. Peaudecerf, G. D. Bruce, and S. Kuhr, *Single-atom imaging of fermions in a quantum-gas microscope*, Nat. Phys. **11**, 738 (2015).

[247] G. J. Edge, R. Anderson, D. Jervis, D. C. McKay, R. Day, S. Trotzky, and J. H. Thywissen, *Imaging and addressing of individual fermionic atoms in an optical lattice*, Phys. Rev. A **92**, 063406 (2015).

[248] M.-D. Li, W. Lin, A. Luo, W.-Y. Zhang, H. Sun, B. Xiao, Y.-G. Zheng, Z.-S. Yuan, and J.-W. Pan, *High-powered optical superlattice with robust phase stability for quantum gas microscopy*, Opt. Express **29**, 13876 (2021).

[249] A. Omran, M. Boll, T. A. Hilker, K. Kleinlein, G. Salomon, I. Bloch, and C. Gross, *Microscopic Observation of Pauli Blocking in Degenerate Fermionic Lattice Gases*, Phys. Rev. Lett. **115**, 263001 (2015).

[250] L. W. Cheuk, M. A. Nichols, M. Okan, T. Gersdorf, V. V. Ramasesh, W. S. Bakr, T. Lompe, and M. W. Zwierlein, *Quantum-gas microscope for fermionic atoms*, Phys. Rev. Lett. **114**, 193001 (2015).

[251] J. Yang, L. Liu, J. Mongkolkiattichai, and P. Schauss, *Site-Resolved Imaging of Ultracold Fermions in a Triangular-Lattice Quantum Gas Microscope*, PRX Quantum **2**, 020344 (2021).

[252] A. Impertro, J. F. Wienand, S. Häfele, H. von Raven, S. Hubele, T. Klostermann, C. R. Cabrera, I. Bloch, and M. Aidelsburger, *An unsupervised deep learning algorithm for single-site reconstruction in quantum gas microscopes*, Commun. Phys. **6**, 166 (2023).

[253] J. L. Ville, T. Bienaimé, R. Saint-Jalm, L. Corman, M. Aidelsburger, L. Chomaz, K. Kleinlein, D. Perconte, S. Nascimbène, J. Dalibard, and J. Beugnon, *Loading and compression of a single two-dimensional Bose gas in an optical accordion*, Phys. Rev. A **95**, 013632 (2017).

[254] P. T. Brown, D. Mitra, E. Guardado-Sanchez, P. Schauß, S. S. Kondov, E. Khatami, T. Paiva, N. Trivedi, D. A. Huse, and W. S. Bakr, *Spin-imbalance in a 2D Fermi-Hubbard system*, Science **357**, 1385 (2017).

[255] S. Buob, J. Höschele, V. Makhalov, A. Rubio-Abadal, and L. Tarruell, *A strontium quantum-gas microscope*, PRX Quantum **5**, 020316 (2024).

[256] A. F. Impertro, *Preparation and Study of 1D and 2D Many-Body Systems with Fermionic Ytterbium*, Master thesis, Ludwig-Maximilians-Universität München (2020).

[257] R. Tao, *Near-resonant Dipole Traps and Lattices for Ultracold Molecules*, Master thesis, Ludwig-Maximilians-Universität München (2020).

[258] M. Ammenwerth, R. Tao, F. Gyger, and J. Zeiher, *Private communications*.

[259] M. von Melchner, L. Festa, D. Tsevas, R. Eberhard, and J. Zeiher, *Private communications*.

[260] D. Okuno, Y. Nakamura, T. Kusano, Y. Takasu, N. Takei, H. Konishi, and Y. Takahashi, *High-resolution Spectroscopy and Single-photon Rydberg Excitation of Reconfigurable Ytterbium Atom Tweezer Arrays Utilizing a Metastable State*, J. Phys. Soc. Jpn. **91**, 084301 (2022).

[261] T. Grünzweig, A. Hilliard, M. McGovern, and M. F. Andersen, *Near-deterministic preparation of a single atom in an optical microtrap*, Nat. Phys. **6**, 951 (2010).

[262] B. J. Lester, N. Luick, A. M. Kaufman, C. M. Reynolds, and C. A. Regal, *Rapid Production of Uniformly Filled Arrays of Neutral Atoms*, Phys. Rev. Lett. **115**, 073003 (2015).

[263] M. O. Brown, T. Thiele, C. Kiehl, T.-W. Hsu, and C. A. Regal, *Gray-Molasses Optical-Tweezer Loading: Controlling Collisions for Scaling Atom-Array Assembly*, Phys. Rev. X **9**, 011057 (2019).

[264] J. Ang'ong'a, C. Huang, J. P. Covey, and B. Gadway, *Gray molasses cooling of* ^{39}K *atoms in optical tweezers*, Phys. Rev. Res. **4**, 013240 (2022).

[265] C. Tuchendler, A. M. Lance, A. Browaeys, Y. R. P. Sortais, and P. Grangier, *Energy distribution and cooling of a single atom in an optical tweezer*, Phys. Rev. A **78**, 033425 (2008).

[266] J. Dalibard and C. Cohen-Tannoudji, *Laser cooling below the Doppler limit by polarization gradients: simple theoretical models*, J. Opt. Soc. Am. B **6**, 2023 (1989).

[267] B. Darquié, M. P. A. Jones, J. Dingjan, J. Beugnon, S. Bergamini, Y. Sortais, G. Messin, A. Browaeys, and P. Grangier, *Controlled Single-Photon Emission from a Single Trapped Two-Level Atom*, Science **309**, 454 (2005).

[268] G. Morigi, J. Eschner, and C. H. Keitel, *Ground State Laser Cooling Using Electromagnetically Induced Transparency*, Phys. Rev. Lett. **85**, 4458 (2000).

[269] A. T. Grier, I. Ferrier-Barbut, B. S. Rem, M. Delehaye, L. Khaykovich, F. Chevy, and C. Salomon, *Λ-enhanced sub-Doppler cooling of lithium atoms in D_1 gray molasses*, Phys. Rev. A **87**, 063411 (2013).

[270] S. E. Hamann, D. L. Haycock, G. Klose, P. H. Pax, I. H. Deutsch, and P. S. Jessen, *Resolved-Sideband Raman Cooling to the Ground State of an Optical Lattice*, Phys. Rev. Lett. **80**, 4149 (1998).

[271] A. J. Kerman, *Raman sideband cooling and cold atomic collisions in optical lattices*, Ph.D. thesis, Stanford University (2002).

[272] Y. Yu, N. R. Hutzler, J. T. Zhang, L. R. Liu, J. D. Hood, T. Rosenband, and K.-K. Ni, *Motional-ground-state cooling outside the Lamb-Dicke regime*, Phys. Rev. A **97**, 063423 (2018).

[273] S. S. Phatak, K. N. Blodgett, D. Peana, M. R. Chen, and J. D. Hood, *Generalized theory for optical cooling of a trapped atom with spin*, Phys. Rev. A **110**, 043116 (2024).

[274] W. Huie, X. Hu, L. Li, Z. Jia, and J. Covey, *Time-bin encoded atom-photon entanglement in a* ^{171}Yb *atom array*, Bulletin of the American Physical Society (2024).

[275] C. Shu, S. Colombo, Z. Li, A. Adiyatullin, E. Mendez, E. Pedrozo-Peñafiel, and V. Vuletić, *Increased atom-cavity coupling through cooling-induced atomic reorganization*, Phys. Rev. Res. **6**, L032049 (2024).

[276] C.-C. Chen, J. L. Siegel, B. D. Hunt, T. Grogan, Y. S. Hassan, K. Beloy, K. Gibble, R. C. Brown, and A. D. Ludlow, *Clock-Line-Mediated Sisyphus Cooling*, Phys. Rev. Lett. **133**, 053401 (2024).

[277] T. Ido, M. Kuwata-Gonokami, and H. Katori, *Sideband cooling and spectroscopy of strontium atoms in the Lamb-Dicke confinement*, in *Laser spectroscopy* (2002), 337.

[278] N. Nemitz, T. Ohkubo, M. Takamoto, I. Ushijima, M. Das, N. Ohmae, and H. Katori, *Frequency ratio of Yb and Sr clocks with* 5×10^{-17} *uncertainty at 150 seconds averaging time*, Nat. Photon. **10**, 258 (2016).

[279] P. Scholl, A. L. Shaw, R. B.-S. Tsai, R. Finkelstein, J. Choi, and M. Endres, *Erasure conversion in a high-fidelity Rydberg quantum simulator*, Nature **622**, 273 (2023).

[280] R. Journet, F. Faisant, S. Lee, and M. Cheneau, *Differential polarizability of the strontium intercombination transition at 1064.7 nm*, Phys. Rev. A **110**, 032819 (2024).

[281] A. W. Young, *Programmable arrays of alkaline earth atoms: qubits, clocks, and the Bose-Hubbard model*, Ph.D. thesis, University of Colorado, Boulder (2023).

[282] A. J. Park, J. Trautmann, N. Šantić, V. Klüsener, A. Heinz, I. Bloch, and S. Blatt, *Cavity-Enhanced Optical Lattices for Scaling Neutral Atom Quantum Technologies to Higher Qubit Numbers*, PRX Quantum **3**, 030314 (2022).

[283] L. Su, A. Douglas, M. Szurek, A. H. Hebert, A. Krahn, R. Groth, G. A. Phelps, O. Markovic, and M. Greiner, *Fast single atom imaging in optical lattice arrays*, 2024, arXiv:2404.09978.

[284] D. S. Grün, S. J. M. White, A. Ortu, A. Di Carli, H. Edri, M. Lepers, M. J. Mark, and F. Ferlaino, *Optical Tweezer Arrays of Erbium Atoms*, Phys. Rev. Lett. **133**, 223402 (2024).

[285] A. Bergschneider, V. M. Klinkhamer, J. H. Becher, R. Klemt, G. Zürn, P. M. Preiss, and S. Jochim, *Spin-resolved single-atom imaging of* ^{6}Li *in free space*, Phys. Rev. A **97**, 063613 (2018).

[286] Y. S. Hassan, T. Kobayashi, T. Bothwell, J. L. Siegel, B. D. Hunt, K. Beloy, K. Gibble, T. Grogan, and A. Ludlow, *Ratchet loading and multi-ensemble operation in an optical lattice clock*, Quantum Science and Technology (2024).

[287] M. T. DePue, C. McCormick, S. L. Winoto, S. Oliver, and D. S. Weiss, *Unity Occupation of Sites in a 3D Optical Lattice*, Phys. Rev. Lett. **82**, 2262 (1999).

[288] J. Hu, A. Urvoy, Z. Vendeiro, V. Crépel, W. Chen, and V. Vuletić, *Creation of a Bose-condensed gas of* ^{87}Rb *by laser cooling*, Science **358**, 1078 (2017).

[289] N. Lundblad, M. Schlosser, and J. V. Porto, *Experimental observation of magic-wavelength behavior of* ^{87}Rb *atoms in an optical lattice*, Phys. Rev. A **81**, 031611 (2010).

[290] T. Bothwell, C. J. Kennedy, A. Aeppli, D. Kedar, J. M. Robinson, E. Oelker, A. Staron, and J. Ye, *Resolving the gravitational redshift across a millimetre-scale atomic sample*, Nature **602**, 420 (2022).

[291] I. Ushijima, M. Takamoto, M. Das, T. Ohkubo, and H. Katori, *Cryogenic optical lattice clocks*, Nat. Photon. **9**, 185 (2015).

[292] N. Schine, A. W. Young, W. J. Eckner, M. J. Martin, and A. M. Kaufman, *Long-lived Bell states in an array of optical clock qubits*, Nature Phys. **18**, 1067 (2022).

[293] A. Cao, W. J. Eckner, T. Lukin Yelin, A. W. Young, S. Jandura, L. Yan, K. Kim, G. Pupillo, J. Ye, N. Darkwah Oppong, and A. M. Kaufman, *Multi-qubit gates and Schrödinger cat states in an optical clock*, Nature **634**, 315 (2024).

[294] G. Kestler, K. Ton, D. Filin, C. Cheung, P. Schneeweiss, T. Hoinkes, J. Volz, M. Safronova, A. Rauschenbeutel, and J. Barreiro, *State-Insensitive Trapping of Alkaline-Earth Atoms in a Nanofiber-Based Optical Dipole Trap*, PRX Quantum **4**, 040308 (2023).

[295] T Topcu and A Derevianko, *Possibility of triple magic trapping of clock and Rydberg states of divalent atoms in optical lattices*, J. Phys. B: At. Mol. Opt. Phys. **49**, 144004 (2016).

[296] A. Bhowmik, M. Gaudesius, G. Biedermann, and D. Blume, *Double, triple, and quadruple magic wavelengths for cesium ground, excited, and Rydberg states*, Phys. Rev. A **110**, 043114 (2024).

[297] W. F. Holmgren, R. Trubko, I. Hromada, and A. D. Cronin, *Measurement of a Wavelength of Light for Which the Energy Shift for an Atom Vanishes*, Phys. Rev. Lett. **109**, 243004 (2012).

[298] C. D. Herold, V. D. Vaidya, X. Li, S. L. Rolston, J. V. Porto, and M. S. Safronova, *Precision Measurement of Transition Matrix Elements via Light Shift Cancellation*, Phys. Rev. Lett. **109**, 243003 (2012).

[299] R. H. Leonard, A. J. Fallon, C. A. Sackett, and M. S. Safronova, *High-precision measurements of the* ^{87}Rb *D-line tune-out wavelength*, Phys. Rev. A **92**, 052501 (2015).

[300] R. Trubko, M. D. Gregoire, W. F. Holmgren, and A. D. Cronin, *Potassium tune-out-wavelength measurement using atom interferometry and a multipass optical cavity*, Phys. Rev. A **95**, 052507 (2017).

[301] B. Décamps, J. Vigué, A. Gauguet, and M. Büchner, *Measurement of the 671-nm tune-out wavelength of* ^{7}Li *by atom interferometry*, Phys. Rev. A **101**, 033614 (2020).

[302] A. Ratkata, P. D. Gregory, A. D. Innes, J. A. Matthies, L. A. McArd, J. M. Mortlock, M. S. Safronova, S. L. Bromley, and S. L. Cornish, *Measurement of the tune-out wavelength for* ^{133}Cs *at 880 nm*, Phys. Rev. A **104**, 052813 (2021).

[303] B. M. Henson, R. I. Khakimov, R. G. Dall, K. G. H. Baldwin, L.-Y. Tang, and A. G. Truscott, *Precision Measurement for Metastable Helium Atoms of the 413 nm Tune-Out Wavelength at Which the Atomic Polarizability Vanishes*, Phys. Rev. Lett. **115**, 043004 (2015).

[304] F. Schmidt, D. Mayer, M. Hohmann, T. Lausch, F. Kindermann, and A. Widera, *Precision measurement of the* ^{87}Rb *tune-out wavelength in the hyperfine ground state* $F = 1$ *at 790 nm*, Phys. Rev. A **93**, 022507 (2016).

[305] W. Kao, Y. Tang, N. Q. Burdick, and B. L. Lev, *Anisotropic dependence of tune-out wavelength near Dy 741-nm transition*, Opt. Express **25**, 3411 (2017).

[306] R. Bause, M. Li, A. Schindewolf, X.-Y. Chen, M. Duda, S. Kotochigova, I. Bloch, and X.-Y. Luo, *Tune-Out and Magic Wavelengths for Ground-State* ^{23}Na^{40}K *Molecules*, Phys. Rev. Lett. **125**, 023201 (2020).

[307] B. M. Henson, J. A. Ross, K. F. Thomas, C. N. Kuhn, D. K. Shin, S. S. Hodgman, Y.-H. Zhang, L.-Y. Tang, G. W. F. Drake, A. T. Bondy, A. G. Truscott, and K. G. H. Baldwin, *Measurement of a helium tune-out frequency: an independent test of quantum electrodynamics*, Science **376**, 199 (2022).

[308] L. W. Clark, L.-C. Ha, C.-Y. Xu, and C. Chin, *Quantum Dynamics with Spatiotemporal Control of Interactions in a Stable Bose-Einstein Condensate*, Phys. Rev. Lett. **115**, 155301 (2015).

[309] J. Catani, G. Barontini, G. Lamporesi, F. Rabatti, G. Thalhammer, F. Minardi, S. Stringari, and M. Inguscio, *Entropy Exchange in a Mixture of Ultracold Atoms*, Phys. Rev. Lett. **103**, 140401 (2009).

[310] E. Copenhaver, K. Cassella, R. Berghaus, and H. Müller, *Measurement of a* ^{7}Li *tune-out wavelength by phase-patterned atom interferometry*, Phys. Rev. A **100**, 063603 (2019).

[311] H. Xia, C. O'Brien, S. Suckewer, and M. O. Scully, *Beam propagation near the dispersionless wavelength at 790 nm in rubidium*, Phys. Rev. A **93**, 053810 (2016).

[312] T. A. Savard, K. M. O'Hara, and J. E. Thomas, *Laser-noise-induced heating in far-off resonance optical traps*, Phys. Rev. A **56**, R1095 (1997).

[313] M. E. Gehm, K. M. O'Hara, T. A. Savard, and J. E. Thomas, *Dynamics of noise-induced heating in atom traps*, Phys. Rev. A **58**, 3914 (1998).

[314] S. Dörscher, R. Schwarz, A. Al-Masoudi, S. Falke, U. Sterr, and C. Lisdat, *Lattice-induced photon scattering in an optical lattice clock*, Phys. Rev. A **97**, 063419 (2018).

[315] I. Ushijima, M. Takamoto, and H. Katori, *Operational Magic Intensity for Sr Optical Lattice Clocks*, Phys. Rev. Lett. **121**, 263202 (2018).

[316] K. Beloy, W. F. McGrew, X. Zhang, D. Nicolodi, R. J. Fasano, Y. S. Hassan, R. C. Brown, and A. D. Ludlow, *Modeling motional energy spectra and lattice light shifts in optical lattice clocks*, Phys. Rev. A **101**, 053416 (2020).

[317] S. Ma, G. Liu, P. Peng, B. Zhang, S. Jandura, J. Claes, A. P. Burgers, G. Pupillo, S. Puri, and J. D. Thompson, *High-fidelity gates and mid-circuit erasure conversion in an atomic qubit*, Nature **622**, 279 (2023).

[318] Z. Jia, W. Huie, L. Li, W. K. C. Sun, X. Hu, Aakash, H. Kogan, A. Karve, J. Y. Lee, and J. P. Covey, *An architecture for two-qubit encoding in neutral ytterbium-171 atoms*, npj Quantum Inf **10**, 106 (2024).

[319] N. Navon, R. P. Smith, and Z. Hadzibabic, *Quantum gases in optical boxes*, Nature Phys. **17**, 1334 (2021).

[320] K. Ono, Y. Amano, T. Higomoto, Y. Saito, and Y. Takahashi, *Observation of spin-exchange dynamics between itinerant and localized* ^{171}Yb *atoms*, Phys. Rev. A **103**, L041303 (2021).

[321] A. González-Tudela and J. I. Cirac, *Cold atoms in twisted-bilayer optical potentials*, Phys. Rev. A **100**, 053604 (2019).

[322] X.-W. Luo and C. Zhang, *Spin-Twisted Optical Lattices: Tunable Flat Bands and Larkin-Ovchinnikov Superfluids*, Phys. Rev. Lett. **126**, 103201 (2021).

[323] J. Argüello-Luengo, A. González-Tudela, T. Shi, P. Zoller, and J. I. Cirac, *Analogue quantum chemistry simulation*, Nature **574**, 215 (2019).

[324] D. González-Cuadra, D. Bluvstein, M. Kalinowski, R. Kaubruegger, N. Maskara, P. Naldesi, T. V. Zache, A. M. Kaufman, M. D. Lukin, H. Pichler, B. Vermersch, J. Ye, and P. Zoller, *Fermionic quantum processing with programmable neutral atom arrays*, Proc. Natl. Acad. Sci. USA **120**, e2304294120 (2023).

[325] J. Mitroy, M. S. Safronova, and C. W. Clark, *Theory and applications of atomic and ionic polarizabilities*, J. Phys. B: At. Mol. Opt. Phys. **43**, 202001 (2010).

[326] B. Arora, M. S. Safronova, and C. W. Clark, *Tune-out wavelengths of alkali-metal atoms and their applications*, Phys. Rev. A **84**, 043401 (2011).

[327] M. S. Safronova, Z. Zuhrianda, U. I. Safronova, and C. W. Clark, *Extracting transition rates from zero-polarizability spectroscopy*, Phys. Rev. A **92**, 040501 (2015).

[328] S. Hirthe, T. Chalopin, D. Bourgund, P. Bojović, A. Bohrdt, E. Demler, F. Grusdt, I. Bloch, and T. A. Hilker, *Magnetically mediated hole pairing in fermionic ladders of ultracold atoms*, Nature **613**, 463 (2023).

[329] H. Sun, M. Huo, X. Hu, J. Li, Z. Liu, Y. Han, L. Tang, Z. Mao, P. Yang, B. Wang, J. Cheng, D.-X. Yao, G.-M. Zhang, and M. Wang, *Signatures of superconductivity near 80 K in a nickelate under high pressure*, Nature **621**, 493 (2023).

[330] M. Olshanii and D. Weiss, *Producing Bose-Einstein Condensates Using Optical Lattices*, Phys. Rev. Lett. **89**, 090404 (2002).

Acknowledgements

At the end of this thesis, I would first like to thank Monika Aidelsburger for her supervision and the opportunity to set up this exciting experiment. I especially appreciate her trust in me and the freedom to pursue my own ideas — be it unnecessarily complicated mechanical designs or crazy-sounding ideas for new measurement techniques. I also admire her positive attitude and calmness, especially in difficult moments, and her unbridled flow of new ideas.

I would also like to appreciate the support of the International Max Planck Research School for Quantum Science and Technology (IMPRS-QST) and especially thank Sonya Gzyl for her coordination and Fabian Grusdt-Bohrdt as the second member of my advisory board for his supervision. I further thank Immanuel Bloch for convincing me to come back to Munich and pursue my Ph.D. in Monika's group.

A heartfelt thank you goes to all my colleagues who worked with me on this machine. I am particularly indebted to our fantastic post-docs Nelson Darkwah Oppong and Ronen M. Kroeze, who did not only bring the experiment to whole new levels, but also taught me invaluable lessons about physics and life in general, never refusing to answer even the dumbest questions. I also wish to thank Etienne Staub, my lab mate from the beginning. I am grateful for the many hours we worked together to design the experiment, to set up the lab infrastructure, and to reach a good vacuum, and for many rounds of Sporcle during long measurement nights. Now that the control of the experiment is being passed on to the next generation, I am convinced that René Villela and Er Zu (Aki) will greatly advance the machine, and I am happy that our Ph.D.s still overlapped so significantly. We were also lucky to have had many fantastic and highly motivated master students, starting with Daniel Adler, David Gröters, Martí Cladera Rosselló, and currently Leonardo Bezzo, and I feel very happy to see how they have continued their outstanding work after graduating. Similarly, I had the great pleasure of working with the very talented and jolly internship students Tobias Maroszak, Guillaume Brochier, and Semyon Zarutskiy. I also wish to express my gratitude to Giulio Pasqualetti, who not only helped me with many Docker issues and ytterbium troubles, but was also a great friend in the office next door I could always talk to. Moreover, I want to thank my fellow Ph.D. students, the master students, post-docs, and group leaders in the Bloch group and especially the ones at LMU, who made me feel part of a big team. Furthermore, I am extremely happy to have been part of the IPCC workshop team led by Raphaël Saint-Jalm, which has further shaped my idea of what I want to fight for after my Ph.D.

A very big thanks goes to Ildiko Kecskesi for her unweary efforts to coordinate and sort out our endless line of orders and her incredible talent to straighten out the various delivery and customs affairs. I know how much troubles we have caused, and I am deeply grateful for her persistently lighthearted and thorough attitude. We also would not have been able to construct this experiment without the help of Mr. Aust and the LMU workshop, and I am still particularly impressed by the craftsmanship of Mr. Etterer who realized an extremely fragile center piece within hours. Likewise, I am grateful for Anton Mayer to teach me how to use Inventor and the MPQ workshop for also manufacturing several delicate parts. We further appreciate the help from Stefan Karsch, who allowed us to use their Zygo.

I further have to thank Aléna Birzele, who hunted down our single intact glass cell after it was delivered to an innocent lady in Berlin. I would not like to thank FedEx for not letting me sleep for a few days until then.

A special thanks goes to Nelson, Aki, Ronen, Giulio, my family, and in particular Marie Semmler and Daniel for proof-reading my thesis.

Eventually and most importantly, I would like to thank my family for their unconditional support and great advice throughout my graduate education, and Marie for her incredible patience, understanding, and backing during scientific ups and downs and especially during late-night-measurement phases and the final weeks of writing this thesis.